Towards an Improved Neutrino Cross Section Landscape: First Measurements of ν_e-Argon and Monoenergetic ν_μ Interactions

by

Rory Shea Fitzpatrick

A dissertation submitted in partial fulfillment
of the requirements for the degree of
Doctor of Philosophy
(Physics)
in the University of Michigan
2021

Doctoral Committee:

Associate Professor Joshua Spitz, Chair
Professor Christine Aidala
Professor Myron Campbell
Professor Igor Jovanovic
Professor James Liu

Rory Shea Fitzpatrick

roryfitz@umich.edu

ORCID iD: 0000-0002-1896-6386

© Rory Shea Fitzpatrick 2021

To the books, bookstores, libraries, and cafes that got me through.

ACKNOWLEDGEMENTS

The work presented here is a credit to a great number of people. Josh made Michigan the right place for me to be, and is the reason it was possible to work on such a wide variety of projects throughout grad school. He gave me the freedom to pursue topics I found interesting and went out of his way to find new opportunities to explore.

The ArgoNeuT result would not have come to fruition without Tingjun, who has been an invaluable teacher, mentor, and advocate during these five years. Much of the way I've learned to think about problems was shaped by our ArgoNeuT discussions.

Thanks are also due to the rest of the ArgoNeuT team, each of whom played a role in making ArgoNeuT one of the highlights of my time in grad school: Ornella, Bruce, Mitch, Corey, Xiao, Ivan, and Wanwei. Thanks to Shekhar, Dave C., and the rest of the ICEBERG team for the fantastic and fun learning environment. There were always reasons to smile while working at PAB. The Wire-Cell team was incredibly welcoming and is constantly showing me new ways to tackle questions. I look forward to each week's discussions. Thanks also to Ralitsa, Bryan, Matt T., and Linda, all of whom could be relied on for fruitful advice pertaining to all things photon detectors (and noise, often noise).

I'm lucky to have had the company of several other longstanding Spitz group members. Working with Johnathon on the KDAR analysis produced some of my favorite memories of Ann Arbor, and I could not have asked for a better person to share/celebrate reaching every milestone alongside. Chris always made sure we all took the time to celebrate successes and was a great neighbor to have on WH12. Joel consistently manages to teach while providing a good laugh; the SBND chapter of this thesis is a credit to him. I am especially thankful for the wonderful Spitz group undergrads. Claire, Polina, and Daniel have each made summers at Fermilab brighter. The rest of my extended UM cohort, Garrett, Elizabeth, Rachel, Bradley, Matt, Kara, Owen, Karley, Jennifer, Abigail, made finding excuses to come back to Ann Arbor easy (present circumstances aside).

I could not reasonably claim that any part of this endeavor would have been possible without my mother. Thanks, Mom.

And I'll be forever grateful for Kelsey, Curtis, JC, and Smyles, the only people with whom I'd willingly spend even more time on zoom. Here's one for Mahler.

PREFACE

Work spanning several different experiments, all based at Fermilab, is presented in this dissertation. My contributions to each are summarized below.

Chapter 4 presents the first measurement of the electron neutrino cross section on argon using data from ArgoNeuT. It was published in the following paper: *Phys. Rev. D* **102** 011101(R) (2020) and I am listed as the sole corresponding author. While I was the primary investigator on this analysis, I worked in close collaboration with Tingjun Yang and Josh Spitz throughout, each of them regularly providing teaching, insight, and suggestions. The chapter is adapted directly from a technical note that I wrote summarizing the analysis during the collaboration review of the paper, in addition to including some of the text written in response to reviewer questions.

Chapter 5 describes the Wire-Cell reconstruction algorithm developed for MicroBooNE and its application to the low energy electron-like excess search, in addition to the wide-ranging potential for high-statistics measurements of neutrino-argon cross sections. I joined the Wire-Cell team in 2020 and contributed primarily to the development and validation of the electron neutrino selection, which builds on the already efficient flavor-agnostic neutrino selection that had been developed by Wire-Cell prior to my joining the group.

Chapter 6 is meant to provide a complete picture of how the design of the photon detector system for SBND came to be. The X-ARAPUCA group was led by Joel Mousseau. Throughout my time in grad school, I was typically responsible for testing new SiPM carrier board prototype designs, in addition to training and advising undergraduates doing work for the group during summers. I've made a point to highlight the undergraduate projects in sections of this chapter, as appropriate, and indicated in the footnote at the start of the chapter.

Chapter 7 describes the DUNE single phase far detector photon detection system. I have presented in detail my R&D responsibilities as a grad student. The first is the initial test of an ultrasound ADC-based readout electronics prototype for comparison to what was at the time the planned, but far more expensive, readout electronics design. This test was directly responsible for DUNE's decision to switch to the more cost-effective readout system, as it demonstrated single photoelectron resolution with a comparable signal to noise ratio. I was also responsible for installing and coordinating the photon detector system in the initial runs of the ICEBERG LArTPC test stand at Fermilab, which was designed to test DUNE prototype components in a small-scale and adaptable environment.

Chapter 8 presents the first measurement of monoenergetic muon neutrinos from kaon decay at rest using data from MiniBooNE. The analysis was published in the following paper: *Phys. Rev. Lett.* **120** 141802 (2018), which was selected as an Editors' Suggestion and featured in *Physics*. I am a corresponding author along with fellow collaborators Johnathon Jordan, Joe Grange, and Josh Spitz. The text in this chapter comes largely from a technical note that we produced as a group, but I have focused on my own contributions, while still providing a complete summary of the analysis. I was responsible for developing (in close collaboration with Johnathon and Josh) and implementing the χ^2 minimization procedure for extracting the final result and the fake data studies for determining the significance of the selection.

TABLE OF CONTENTS

Chapter

LIST OF FIGURES

FIGURE

LIST OF TABLES

TABLE

LIST OF APPENDICES

APPENDIX

ABSTRACT

Knowledge of neutrino cross sections is critical for understanding neutrino oscillation experiments. Existing theoretical interaction models can be improved by data-driven constraints measured across a variety of neutrino-nucleus interaction mechanisms and energies. However, neutrino cross section measurements are complicated by a number of factors, including detector limitations and challenges to neutrino energy reconstruction. Improving neutrino flavor identification and reconstruction in now popular liquid argon time projection chamber (LArTPC) detectors operating with GeV-scale neutrino sources is critical for success in upcoming large-scale neutrino experiments like the Deep Underground Neutrino Experiment (DUNE), aiming to further illuminate our picture of the neutrino. Specifically, the value of the charge-parity violating phase governing neutrino mixing and the mass ordering of the neutrinos are yet unknown. In parallel, studies of unique known energy neutrinos from decays at rest can eliminate one source of uncertainty to improve our understanding of neutrino-nucleus interactions in the MeV range and aid detector energy calibration.

The topics covered in this dissertation are broad. They traverse multiple collaborations, analysis, hardware tests, electron neutrinos, muon neutrinos, and photon detectors. Foremost are the two published results. The first is a measurement of the electron neutrino cross section on argon with ArgoNeuT (at the time the only measurement of its kind). This electron neutrino sample, albeit low in statistics, is unique as the only currently available GeV-scale neutrino beam electron neutrino data collected by a LArTPC. The GeV-scale energy region presents distinct challenges for electron neutrino identification and reconstruction driven by increased hadron multiplicities that obscure vertex information traditionally used to classify electron neutrinos. The ArgoNeuT analysis demonstrates novel strategies for GeV-scale electron neutrino searches. The second result is a measurement of monoenergetic muon neutrino interactions in MiniBooNE from kaon decay at rest in the NuMI neutrino beam dump. Neutrino energy reconstruction is famously difficult and this monoenergetic neutrino source is a valuable tool for probing neutrino-nucleus interactions. The distinct timing and direction information of these events make it possible to extract signal shape and rate above background and the resulting measurements can be used to constrain interaction models. Between these two bookends, we consider first MicroBooNE's low energy excess search and cross section program through the lens of the Wire-Cell tomographic reconstruction toolbox. And finally, we discuss photon detection in LArTPCs. The design and testing of the photon detection system for the Short Baseline Near Detector (SBND) and recent research and development efforts for DUNE are summarized.

CHAPTER 1

The Neutrino and its Properties

On December 4, 1930, Wolfgang Pauli wrote a letter that was sent in his place to a physics meeting in Tübingen, Germany. He claimed, to the attending "radioactive ladies and gentleman" to "have hit upon a desperate remedy" to explain the continuous electron energy spectrum observed in the beta decay of heavy nuclei — an observation that seemed to contradict conservation of energy (see Figure 1.1). Pauli continued, "in the nuclei there could exist electrically neutral particles, which I will call neutrons, that have spin 1/2 and obey the exclusion principle and that further differ from light quanta in that they do not travel with the velocity of light." He was hesitant about suggesting that such a particle existed. "I admit that my remedy may seem almost improbable because one probably would have seen those neutrons, if they exist, for a long time." But Pauli had hit the mark exactly. What is today known as the neutron, the composite neutral nucleon composed of quarks, was discovered before Pauli's neutron. Pauli's neutral particle became, as Enrico Fermi proposed in his theory of weak interactions [1], the "little neutral one": the neutrino. It was first observed in 1956 [2].

In 1960, John Updike published a poem in the *New Yorker* (see Figure 1.2). *Cosmic Gall* reported that neutrinos "are very small.... have no charge ... no mass ... and do not interact at all." He was wrong on two counts. Yes, the neutrino is very small in the context of the rest of the Standard Model particles. Yes, it has no electric charge. But the neutrino is massive, a property (still somewhat mysterious) that is directly linked to the fact that neutrinos oscillate. And the neutrino does interact via the weak force.

But we can give Updike partial credit: for all intents and purposes, the neutrino does not interact – tens of billions pass through the tip of your thumb undetected every second. This is

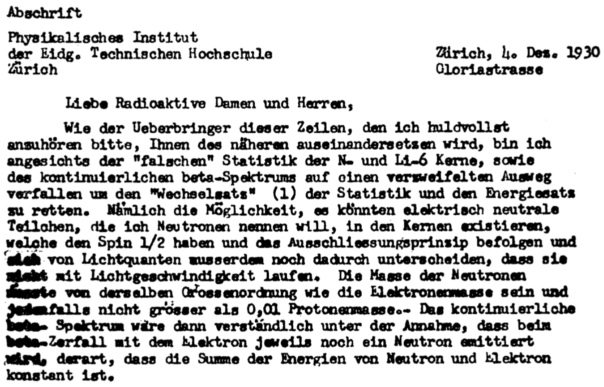

Abschrift

Physikalisches Institut
der Eidg. Technischen Hochschule
Zürich

Zürich, 4. Dez. 1930
Gloriastrasse

Liebe Radioaktive Damen und Herren,

Wie der Ueberbringer dieser Zeilen, den ich huldvollst anzuhören bitte, Ihnen des näheren auseinandersetzen wird, bin ich angesichts der "falschen" Statistik der N- und Li-6 Kerne, sowie des kontinuierlichen beta-Spektrums auf einen verzweifelten Ausweg verfallen um den "Wechselsatz" (1) der Statistik und den Energiesatz zu retten. Nämlich die Möglichkeit, es könnten elektrisch neutrale Teilchen, die ich Neutronen nennen will, in den Kernen existieren, welche den Spin 1/2 haben und das Ausschliessungsprinzip befolgen und sich von Lichtquanten ausserdem noch dadurch unterscheiden, dass sie nicht mit Lichtgeschwindigkeit laufen. Die Masse der Neutronen müsste von derselben Grossenordnung wie die Elektronenmasse sein und jedenfalls nicht grösser als 0,01 Protonenmasse.- Das kontinuierliche beta- Spektrum wäre dann verständlich unter der Annahme, dass beim beta-Zerfall mit dem Elektron jeweils noch ein Neutron emittiert wird, derart, dass die Summe der Energien von Neutron und Elektron konstant ist.

"I have hit upon a desperate remedy.... [T]here could exist electrically neutral particles ... that have spin 1/2 and obey the exclusion principle."

— Wolfgang Pauli, 1930

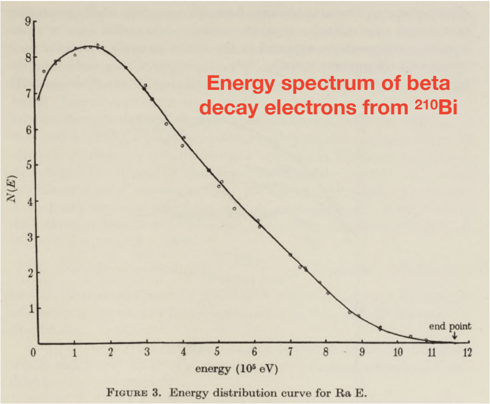

Figure 1.1: (left) The opening of Pauli's letter to his colleagues at the Tübingen conference. Image and translation courtesy of Ref. [3]. (right) The (at the time) anomalous continuous electron energy spectrum for beta decay of ^{210}Bi to ^{210}Po [4].

why physicists have gone to such great lengths to study the ghostly particle. And at the time the poem was published, physicists themselves believed the neutrino to be massless. It would take another several decades to observe definite proof of neutrino mass via neutrino oscillations (published in 1998). And to this day, we are still unable to measure the absolute mass of the neutrino, though the community has made great strides in the right direction. This document is an exploration of the many challenges associated with studying the neutrino, through the lens of a number of past, present, and future Fermilab-based neutrino beam experiments.

1.1 A Brief History of the Neutrino

Neutrinos are enigmatic, yet abundant. Natural and artificial sources generate neutrinos with energies that span several orders of magnitude. The earliest neutrino experiments studied naturally abundant solar neutrinos (produced by interactions in the Sun), cosmic neutrinos (produced as cosmic rays strike the Earth's atmosphere), and high-intensity neutrino fluxes from nuclear reactors. They were closely followed by experiments using dedicated high-intensity neutrino beams, searches for signals from ultra-high energy cosmogenic neutrinos, and observation of geoneutrinos produced by radioactive elements in the earth's interior [5]. Future neutrino experiments

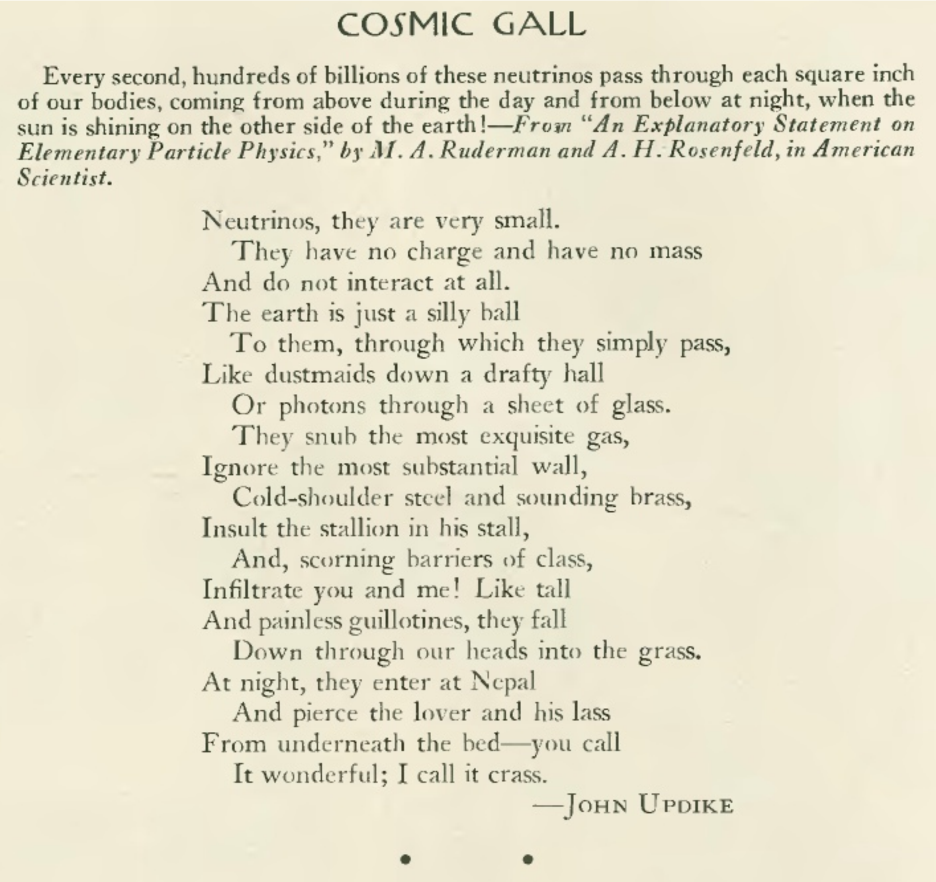

COSMIC GALL

Every second, hundreds of billions of these neutrinos pass through each square inch of our bodies, coming from above during the day and from below at night, when the sun is shining on the other side of the earth!—*From "An Explanatory Statement on Elementary Particle Physics," by M. A. Ruderman and A. H. Rosenfeld, in American Scientist.*

Neutrinos, they are very small.
They have no charge and have no mass
And do not interact at all.
The earth is just a silly ball
To them, through which they simply pass,
Like dustmaids down a drafty hall
Or photons through a sheet of glass.
They snub the most exquisite gas,
Ignore the most substantial wall,
Cold-shoulder steel and sounding brass,
Insult the stallion in his stall,
And, scorning barriers of class,
Infiltrate you and me! Like tall
And painless guillotines, they fall
Down through our heads into the grass.
At night, they enter at Nepal
And pierce the lover and his lass
From underneath the bed—you call
It wonderful; I call it crass.

—John Updike

• •

Figure 1.2: John Updike's 1960 poem *Cosmic Gall*, published in *The New Yorker*.

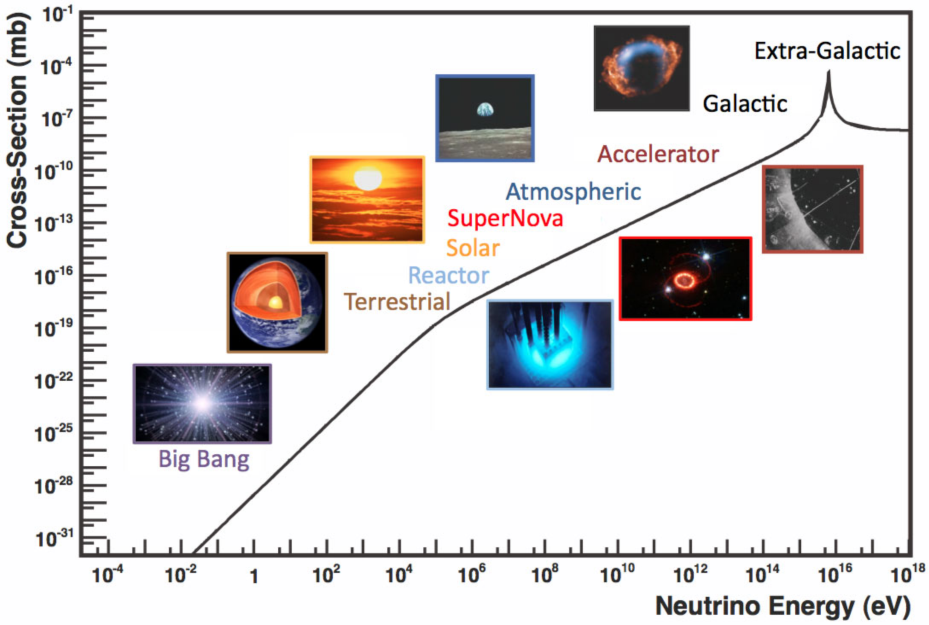

Figure 1.3: Neutrino sources as a function of energy. Image from Ref. [6].

aim to observe the heretofore undetectable meV-scale cosmic neutrino background (a remnant from the universe's infancy like the cosmic microwave background). Figure 1.3 illustrates a wide variety of neutrino sources as a function of the characteristic neutrino energy produced in each environment.

The neutrino was conceived as a solution to an apparent anomaly in conservation of energy during beta decays. If beta decay were a two-body decay ($X \to X' + e^-$) where the parent nucleus decays from rest the exiting electron would be monoenergetic, with an energy determined by the three particle masses m:

$$E_{e^-} = (m_X^2 - m_{X'}^2 + m_{e^-}^2)/2m_X. \tag{1.1}$$

Having never observed an additional product in beta decays, physicists were mired by the observed range in energies for electrons emitted in these decays.

After Pauli proposed the neutrino and Fermi formalized its place in his theory of weak interactions, the existence of the neutrino was confirmed in 1956, when Cowan, Reines, and colleagues reported the first observation of (anti)neutrinos produced by beta decay in a nuclear reactor [2] a mere three years after they first proposed the method of detection [7]. At the Savannah River Site in South Carolina, they set up an experiment to measure inverse beta decay ($\overline{\nu}_e + p \to n + e^+$)

interactions in a detector composed of two tanks of water doped with $CdCl_2$ placed between three scintillation detectors ("club-sandwich" style, per the report). Both interaction products could be detected: the positron annihilates to produce two gamma rays that are detected by the scintillator layers, and the neutron captures via $n + ^{108}\mathrm{Cd} \rightarrow ^{109}\mathrm{Cd} + \gamma$ (the resulting gamma from this capture is recorded by the scintillator layers). The prompt gamma rays from positron annihilation are observed several microseconds prior to the gamma ray from the neutron capture process, producing a distinct signature for inverse beta decays in Cowan and Reines's detector. The measured power-dependent neutrino rate was consistent with the theoretical prediction of $\sigma \sim 10^{-44}$ cm^2. In 1995 Frederick Reines was awarded the Nobel Prize.

During the same year that the Savannah River experiment was being conducted, T. D. Lee and C. N. Yang suggested that parity might not be conserved in the weak sector [8]. Their theory was confirmed a year later, in 1957, by C. S. Wu and colleagues [9]. The helicity of the neutrino was determined shortly thereafter: neutrinos are "left-handed" and antineutrinos are "right-handed" [10].

Today we have a more complete, albeit unfinished, picture of the neutrino: it is a spin-1/2 lepton that comes in three flavors; it only interacts weakly via the $W^{\pm}$ (charged current) and Z^0 (neutral current) bosons, yielding a very small interaction cross section; and it has non-zero mass. The remaining two neutrino flavors were directly detected in 1962 (muon neutrino) [11] and 2000 (tau neutrino) [12] at Brookhaven and Fermilab, respectively. (The tau particle itself, the charged lepton partner of the tau neutrino, was not discovered until 1975 [13].) Additional measurements of the Z-boson decay width strongly suggest that these three are the only flavors of neutrinos which actively participate in weak interactions [14].

But the story of the neutrino wasn't over. In 1964 Ray Davis and John Bahcall proposed a new kind of solar neutrino detector to measure the rate of neutrinos produced by the Sun [15], made feasible by Bahcall's recent theoretical work showing that the neutrino capture rate on chlorine was an order of magnitude larger than previously thought [16]. Davis and his team set up a 390,000 liter tank of C_2Cl_4 in the Homestake mine in South Dakota, 4400 meters underground. They were then able to count the number of argon isotopes produced by inverse beta decay ($\nu_e + ^{37}\mathrm{Cl} \rightarrow ^{37}\mathrm{Ar} + e^-$) and measure the solar neutrino flux. But the solar neutrino flux they observed was only about one-third the rate expected [17, 18]. This newly unearthed "solar neutrino problem" would plague physicists for another 30 years.

The solar neutrino deficit observed at the Homestake experiment was independently confirmed by the Kamiokande experiment in 1989 [19, 20] via measurements of neutrino elastic scattering ($\nu_x + e^- \to \nu_x + e^-$, where $x = e, \mu, \tau$) and similar deficits were observed by SAGE [21] and GALLEX [22] using inverse beta decay with gallium targets ($\nu_e + {}^{71}$Ga $\to {}^{71}$Ge + e^-).

In parallel with the solar neutrino measurement, theorists were developing a model of neutrino flavor oscillations. The theory was formalized between 1957 and 1967 by Pontecorvo [23, 24] and Maki, Nakagawa, and Sakata [25] (the namesakes of the PMNS matrix which houses the paremeters that govern neutrino mixing), culminating in an explanation of the solar neutrino deficit put forward by Pontecorvo and Gribov in 1969 [26]. Additional work by Wolfenstein, Smirnov, and Mikheyev showed that traveling through matter rather than in a vacuum can further impact neutrino oscillation probabilities, an effect known as the MSW effect [27–30]. Neutrino oscillations will be discussed in more formal detail in Section 1.3.3.

The Sudbury Neutrino Observatory (SNO) provided the first unambiguous explanation for the solar neutrino deficit in 2001 [31]. Previous results had been sensitive primarily or exclusively to electron neutrino flux. SNO was able to independently measure two interaction channels: flavor-dependent charged current interactions and flavor-independent neutral current interactions:

$$\nu_e + d \to p + p + e^- \quad \text{(charged current)} \tag{1.2}$$

$$\nu_{e,\mu,\tau} + d \to p + n + \nu_{e,\mu,\tau} \quad \text{(neutral current)} \tag{1.3}$$

Solar neutrino energies ($<$ 18 MeV) are too low to produce muon ($m_\mu = 106$ MeV) and tau ($m_\tau = 1780$ MeV) particles, so the charged current interaction can only occur with electron neutrinos. However, the neutral current interaction is flavor-blind. SNO found that the total neutrino flux, measured via neutral current interactions, was three times greater than the electron neutrino flux, measured via charged current interactions and equivalent to the Homestake, Kamiokande, SAGE, and GALLEX measurements. The solar model predictions for neutrino flux were correct. The missing electron neutrinos had transformed ("oscillated") into muon and tau neutrinos. Remnants of the solar neutrino puzzle still exist in physics nomeclature today: we continue to refer to oscillations away from a detected neutrino flavor as neutrino "disappearance."

On February 23, 1987, light from a supernova in the Large Magellanic Cloud, 168,000 light-years away, reached Earth. Several hours before the visible light arrived, neutrino detectors around the world saw a spike in activity. The Kamiokande [32], IMB [33], and Baksan [34] experiments observed 12, 8, and 5 electron antineutrinos over the course of about 13 seconds at 7:35 UT. The core collapse during the type-II supernova 1987A had produced an enormous number of neutrinos that were now passing through the earth.

Kamiokande, originally designed as a proton decay experiment, was a Cherenkov detector capable of detecting both solar and atmospheric neutrinos. As noted previously, the experiment provided independent confirmation of the solar neutrino deficit. Neutrinos incident on the detector elastically scattered with electrons and the resulting charged particle information could be used to reconstruct incoming neutrino direction, confirming that the neutrino flux did come from the Sun. Note also that neutrino elastic scattering is enhanced for electron neutrino scattering; the electron neutrino elastic scattering cross section is about six times higher for electron neutrinos as it is for muon or tau neutrinos.

Another abundant natural source of neutrinos is the Earth's atmosphere. Pions are produced and then decay via a chain that yields muon and electron neutrinos ($\pi^{\pm} \to \mu + \nu_{\mu}$, $\mu \to e + \nu_{\mu} + \nu_{e}$). In addition to reproducing Homestake's solar neutrino deficit, the Kamiokande experiment observed evidence of neutrino oscillations in atmospheric neutrinos [35]. The subsequent Super-Kamiokande experiment was designed as a larger version of Kamiokande to definitively resolve the atmospheric neutrino problem [36]. Super-Kamiokande consisted of a 50 kiltoton tank of pure water surrounded by 11,200 photomultiplier tubes. Data showed a zenith angle-dependent deficit of muon neutrinos. Fewer muon neutrinos were observed coming from below the detector (produced in the atmosphere on the opposite side of the Earth) than from directly above the detector location. Given the small neutrino cross section, this deficit could not be explained simply by neutrino interactions with the Earth as they passed through. Instead, more of the muon neutrinos traversing through the Earth had oscillated into tau neutrinos ($\nu_{\mu} \to \nu_{\tau}$). It was clear from the results that neutrinos did oscillate. It also meant neutrinos had mass, a paradigm-shifting discovery. The original result was published in 1998 [36], followed by increased statistics [37] and modest evidence of tau-neutrino-like appearance [38]. In 2002, Ray Davis and Masatoshi Koshiba (of the Kamiokande collaboration) shared the Nobel Prize in Physics for their observations of solar,

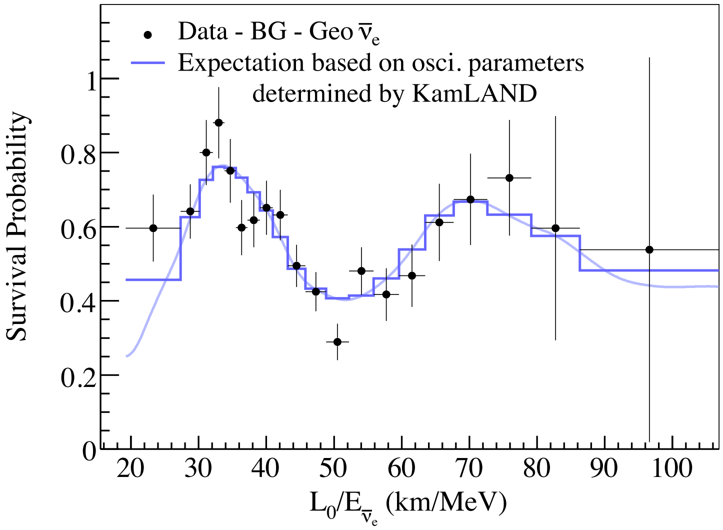

Figure 1.4: The KamLAND reactor antineutrino disappearance spectrum as a function of L/E. Figure from Ref. [41].

cosmic, and supernova neutrinos.

Reactor neutrino experiments were quick on the heels of Super-Kamiokande to see evidence of electron neutrino disappearance. The KamLAND experiment is a liquid scintillator neutrino detector located in the Kamioka mine in Japan and it observes flux incident from just over 50 reactors, though nearly 80% of the ν_e flux comes from 26 reactors ranging in distance from 138-214 km. The average baseline is $\sim$180 km. Like other scintillator detectors, KamLAND identifies inverse beta decays from neutrinos using the distinct two-part event signature. First, prompt scintillation light from the positron provides a measurement of neutrino energy, then neutron capture occurs $\sim$200 μs later, producing a second scintillation signal. In 2003, KamLAND published first results citing evidence for reactor electron antineutrino disappearance [39] followed up with additional statistics a year later [40] and again in 2008 [41]. The neutrino spectrum observed by KamLAND as a function of L/E is shown in Figure 1.4. These results, in combination with the Super-Kamiokande and SNO solar neutrino observations being published during the same years provide unambiguous evidence for the neutrino oscillation paradigm. KamLAND was also the first experiment to observe geoneutrinos: electron antineutrinos produced by natural radioactive elements inside the earth [5]. In 2015, Taakaki Kajita of Super-Kamiokande and Art McDonald of SNO were awarded the Nobel Prize for the discovery of neutrino oscillations.

parameter	ν_e **best fit** $\pm 1\sigma$	3σ **range**	**best suited exp. for measuring**
$\sin^2(\theta_{12})$ $[10^{-1}]$	$3.10^{+0.13}_{-0.12}$	$2.75 \rightarrow 3.50$	solar, LBL reactor
θ_{12} $[°]$	$33.82^{+0.78}_{-0.76}$	$31.61 \rightarrow 36.27$	
$\sin^2(\theta_{23})$ $[10^{-1}]$	$5.63^{+0.18}_{-0.24}$	$4.33 \rightarrow 6.09$	LBL accel. ν_μ, ν_e, atm.
θ_{23} $[°]$	$48.6^{+1.0}_{-1.4}$	$41.1 \rightarrow 51.3$	
$\sin^2(\theta_{13})$ $[10^{-1}]$	$2.237^{+0.066}_{-0.065}$	$2.044 \rightarrow 2.435$	reactor, solar, atm. LBL accel. ν_e
θ_{13} $[°]$	$8.60^{+0.13}_{-0.13}$	$8.22 \rightarrow 8.98$	
δ_{CP} $[°]$	221^{+39}_{-28}	$144 \rightarrow 357$	LBL accel. ν_e, atm.
Δm^2_{21} $[10^{-5}\ \mathrm{eV}^2]$	$7.39^{+0.21}_{-0.20}$	$6.79 \rightarrow 8.01$	LBL reactor, solar
Δm^2_{32} $[10^{-3}\ \mathrm{eV}^2]$	$2.353^{+0.029}_{-0.031}$	$2.362 \rightarrow 2.544$	MBL reactor, LBL accel. ν_μ, atm.

Table 1.1: Current best fit three-neutrino oscillation parameters assuming normal ordering (the current best fit ordering). Values from Ref. [42].

In the past decade, a sharper image of the neutrino has come into focus, through a comprehensive international experimental program spanning a large range of baselines and energies. Though open questions remain (and will be discussed in more detail below), the parameters governing neutrino oscillations in the three-neutrino paradigm have been measured with precision and validated across many experiments (excluding, until recently, the phase δ_{CP}). A summary of the current best fits for each of the neutrino parameters is shown in Table 1.1 along with the best neutrino sources and baselines, where relevant, for measuring each parameter.

Before further exploring the properties of the neutrino and its many mysteries, it is worthwhile to take a step back and review the theoretical context in which the neutrino resides. The Standard Model of Particle Physics describes the world we live in more accurately and completely than any other model physicists have imagined. Its predictions are verified time and again — most notably in recent history with the discovery of the Higgs boson. However, despite the Standard Model's repeated successes, it remains incomplete: it does not include gravity, it has no mechanism for describing dark matter, it cannot explain the dark energy we observe in the universe, and it does not provide a full description of the neutrino.

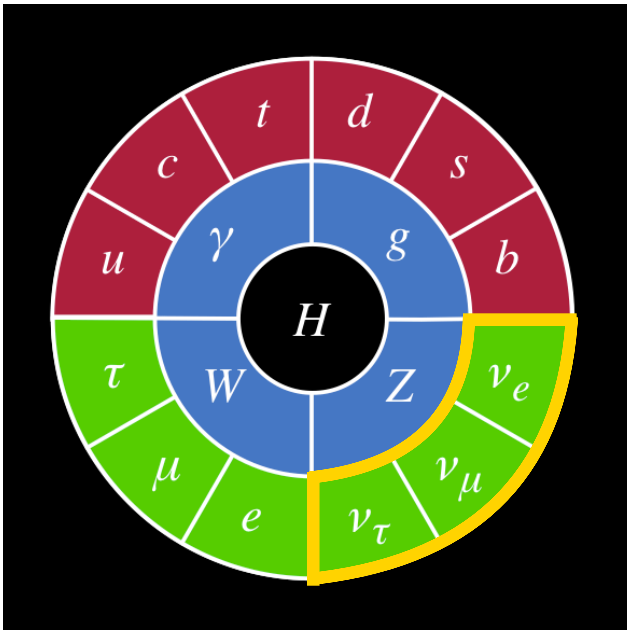

Figure 1.5: The particles in the Standard Model.

1.2 Neutrinos and the Standard Model

In the Standard Model there are three kinds of particles: leptons, quarks, and mediators. The six leptons (plus their antileptons) further separate into three generations, from lightest to heaviest:

$$\begin{pmatrix} \nu_e \\ e \end{pmatrix} \begin{pmatrix} \nu_\mu \\ \mu \end{pmatrix} \begin{pmatrix} \nu_\tau \\ \tau \end{pmatrix} \tag{1.4}$$

In each generation, there is one neutral and one charged lepton (the electron neutrino and the electron, respectively, for the first and lightest lepton generation) There are also six quarks (up, down, charm, strange, top, and bottom, plus their antiquarks), again grouped into three generations:

$$\begin{pmatrix} u \\ d \end{pmatrix} \begin{pmatrix} c \\ s \end{pmatrix} \begin{pmatrix} t \\ b \end{pmatrix} \tag{1.5}$$

Quarks are additionally characterized by color — red, green, or blue — a property analogous to electric charge, but for the strong force. As such there are 36 individually distinct quarks: six quarks plus six antiquarks each in three different color varieties. While leptons have integer charge (0 for neutrinos, -1 for charged leptions and 1 for charged antileptons) quarks have fractional charge ($\pm 2/3$ for up, charm, and top quarks/antiquarks and $\mp 1/3$ for down, strange, and bottom quarks/antiquarks). Finally, there are mediators for each force/interaction between particles: the photon mediates the electromagnetic force, $W^{\pm}$'s and Z^0's the weak force, eight gluons mediate the strong force, and the graviton mediates gravity. Figure 1.5 shows all the particles in the Standard Model (for details about the role of the Higgs boson, see Appendix A). To add even more nomenclature, particles with half-integer spin are fermions (quarks and leptons) and particles with integer spin are bosons (mediators).

Formally, the Standard Model is an $SU(3) \otimes SU(2)_L \otimes U(1)_Y$ gauge theory that describes all elementary particle interactions with the exception of gravity. A detailed overview of the Standard Model formalism focusing on neutrinos and the electroweak sector is provided in Appendix A. Here, we jump straight to neutrino masses and mixing, interrelated mechanisms that do not automatically spring from the current Standard Model formalism, but must instead be added explicitly. That neutrinos are only partially described by the minimal Standard Model is part of what makes them such a fascinating particle to study.

1.3 Neutrino Masses and Mixing

Neutrino mass and neutrino oscillations are inseparable. As we will see, the observation of neutrino oscillations directly implies that neutrinos have mass. But first, we review mechanisms for introducing neutrino mass to the Standard Model.

1.3.1 Neutrino Masses

All fermions in the Standard Model can exist with both left- and right-handed helicity. The neutrino is the only exception, existing only with left-handed helicity (the antineutrino is right-handed). To accommodate massive neutrinos, we must introduce right-handed neutrino fields ν_l^R corresponding to each lepton flavor l. These are $SU(2)_L$ singlets with hypercharge $Y = 0$. The right-handed neutrino singlets (ν_R) couple to the left-handed SM doublets (ψ_L) and the Higgs doublet (ϕ) via a Yukawa coupling with strength f_ν:

$$\begin{aligned}\mathcal{L}_D &= f_\nu \bar{\psi}_L \phi \nu_R + \text{h.c.} \\ &\overset{\text{ssb}}{=} f_\nu v \bar{\nu}_L \nu_R + \text{h.c.} \\ &\equiv m_D \bar{\nu}_L \nu_R + \text{h.c.}\end{aligned} \tag{1.6}$$

After spontaneous symmetry breaking, this gives the neutrino a (Dirac) mass:

$$m_D = f_\nu v \tag{1.7}$$

formed by the coupling of a chirally left-handed neutrino to a chirally right-handed neutrino with a dimensionless coupling f_ν and Higgs vacuum expectation value v. However, this mass mechanism does not explain the apparent discrepancy between the charged and neutral lepton mass couplings. In the quark sector, the components of each doublet have masses that are similar (e.g. $m_u \simeq m_d$) where as the charged and neutral leptons have couplings that generate masses that differ by several orders of magnitude (e.g. $m_{\nu_e} \simeq 10^{-6} m_e$). Why is f_{ν_e} so much smaller than f_e despite the fact that they are partners in the same lepton generation?

Consider neutrino mass terms that arise from two left-handed or two right-handed neutrinos, known as Majorana mass terms:

$$\mathcal{L}_M = \frac{m_L}{2} \overline{(\nu_L)^C} \nu_L + \frac{m_R}{2} \overline{(\nu_R)^C} \nu_R + \text{h.c.} \tag{1.8}$$

where for a field ψ, $\psi^C = C\bar{\psi}^T$ is the charge-conjugate field, and C is the charge conjugation matrix. Also note that $(\nu_L)^C$ is a right-handed neutrino field and $(\nu_R)^C$ is a left-handed neutrino field.

Dirac mass terms conserve the lepton number L that distinguishes leptons from antileptons. They keep neutrinos coupled exclusively with neutrinos and antineutrinos with antineutrinos. The alternative Majorana mass term does not and couples neutrinos with antineutrinos. See Section 1.4.5 for a discussion of the experimental ramifications of Dirac versus Majorana masses.

Introducing Majorana mass terms gives a potential hint toward the nature of neutrino mass.

Suppose the neutrino sector of the Standard Model contains a Dirac mass as well as a right-handed Majorana mass. The neutrino mass terms in the Lagrangian are then given by

$$\begin{aligned}\mathcal{L}_{m_\nu} &= m_D \bar{\nu}_L \nu_R + \frac{1}{2} m_R \overline{(\nu_R)^C} \nu_R + \text{h.c.} \qquad (1.9)\\ &= \frac{1}{2} \overline{\nu^C} \mathcal{M} \nu + \text{h.c.}\end{aligned}$$

where in the second line we have defined

$$\nu \equiv \begin{pmatrix} \nu_L \\ \nu_R^C \end{pmatrix} \qquad (1.10)$$

and

$$\mathcal{M} = \begin{pmatrix} 0 & m_D \\ m_D & m_R \end{pmatrix} \qquad (1.11)$$

and used the identity

$$\overline{(\nu_L)^C} m_D (\nu_R)^C = \bar{\nu}_L m_D \nu_R. \qquad (1.12)$$

Diagonalizing the mass matrix $\mathcal{M}$ in this equation yields

$$m_{1,2} = \frac{m_R \pm \sqrt{m_R^2 + 4m_D^2}}{2} \qquad (1.13)$$

which gives us $m_1 \approx m_R$ and $m_2 \approx m_D^2/m_R$ (in the limit where $m_R \gg m_D$). This so-called seesaw mechanism yields one heavy right-handed neutrino and a light left-handed neutrino that could explain the observed neutrino mass scale. The heavy neutrino in this scenario has not yet been observed, if it exists. Alternatives and variations of the seesaw mechanism exist, but this outlines well the type of extension to the Standard Model that could be used to explain neutrino masses as we unveil more of their properties.

1.3.2 Two-Neutrino Oscillations

Experimental evidence has shown that the three observed neutrinos can oscillate between flavor types over a variety of distance and energy scales.

To understand the mechanics of neutrino mixing, we can simplify the problem to two neutrinos. This version of the problem can provide valuable insight into the nature of neutrino oscillations while avoiding complex results that obfuscate key characteristics of the oscillations. To start we can write the flavor eigenstates ν_α ($\alpha = e, \mu$) in terms of the mass eigenstates ν_i ($i = 1, 2$).

$$|\nu_e\rangle = \cos\theta|\nu_1\rangle + \sin\theta|\nu_2\rangle$$
$$|\nu_\mu\rangle = -\sin\theta|\nu_1\rangle + \cos\theta|\nu_2\rangle$$

where θ is the mixing angle. To put this more concisely, we may write

$$|\nu_\alpha\rangle = \sum_i U^*_{\alpha i}|\nu_i\rangle \tag{1.14}$$

where U^* is the unitary matrix

$$U = \begin{pmatrix} \cos\theta & \sin\theta \\ -\sin\theta & \cos\theta \end{pmatrix} \tag{1.15}$$

We can then compute the probability of ν_e oscillating to ν_μ at some later time:

$$P(\nu_e \to \nu_\mu) = |\langle\nu_\mu|\nu_e(t)\rangle|^2. \tag{1.16}$$

The time dependence of the mass states can be written in terms of the initial state as:

$$|\nu_i(t)\rangle = e^{-i(E_i t - p_i L)}|\nu_i(0)\rangle \tag{1.17}$$

and expanding the inner product using this time dependence gives:

$$\begin{aligned}\langle \nu_\mu(t)|\nu_e(0)\rangle &= (-\sin\theta\langle\nu_1(t)| + \cos\theta\langle\nu_2(t)|)\cdot(\cos\theta|\nu_1\rangle + \sin\theta|\nu_2\rangle)\\ &= (-\sin\theta e^{i\phi_1}\langle\nu_1| + \cos\theta e^{i\phi_2}\langle\nu_2|)\cdot(\cos\theta|\nu_1\rangle + \sin\theta|\nu_2\rangle) \\ &= -\sin\theta\cos\theta e^{i\phi_1} + \sin\theta\cos\theta e^{i\phi_2}\end{aligned} \tag{1.18}$$

where $\phi_i = E_i t - p_i L$. Next, let $c = 1$ and $t \approx L$ (the relativistic limit, relevant for neutrinos) where L is the distance from a neutrino source to a detector. In the limit where neutrino momentum is much larger than its mass, $E_i = \sqrt{p_i^2 + m_i^2} \approx p_i + m_i^2/(2p_i)$. Thus, we can write $\phi_i = [m_i^2/(2E)]L$ and we find

$$\begin{aligned}P(\nu_e \to \nu_\mu) &= \sin^2(2\theta)\sin^2\left(\frac{\phi_1 - \phi_2}{2}\right)\\ &= \sin^2(2\theta)\sin^2\left(\frac{\Delta m_{12}^2 L}{4E}\right)\\ &= \sin^2(2\theta)\sin^2\left(1.27\frac{\Delta m_{12}^2}{\text{eV}^2}\frac{L}{\text{km}}\frac{\text{GeV}}{E}\right)\end{aligned} \tag{1.19}$$

where we have reintroduced the missing constants and converted to reasonable units in the last step. It is now immediately clear that oscillations require neutrinos to have mass, otherwise $P(\nu_e \to \nu_\mu) = 0$. As neutrino mixing has been observed, conclusively, we require that $P(\nu_e \to \nu_\mu)$ is nonzero. Thus, the mass mixing Δm_{12}^2 must be nonzero for the oscillation probability to be nonzero.

For generic two-neutrino oscillations, the probability can be written

$$P(\nu_\alpha \to \nu_\beta)_{\alpha\neq\beta} = \sin^2(2\theta)\sin^2\left(\frac{1.27\Delta m_{\alpha\beta}^2 L}{E}\frac{[\text{eV}^2][\text{km}]}{[\text{GeV}]}\right). \tag{1.20}$$

Furthermore, we can define an oscillation length

$$L = \frac{4\pi E}{\Delta m_{\alpha\beta}^2} \tag{1.21}$$

which gives the distance scale over which the oscillation effects are appreciable.

1.3.3 Three-Neutrino Oscillations

We may now expand this approach to the three-neutrino case. Once again, the neutrino flavor states ν_α ($\alpha = e, \mu, \tau$) can be written as linear combinations of the three mass mass ν_i ($i = 1, 2, 3$).

$$|\nu_\alpha\rangle = \sum_i U^*_{\alpha i}|\nu_i\rangle \tag{1.22}$$

The mixing matrix U, known as the PMNS matrix, in the three-neutrino case is written as

$$U = \begin{bmatrix} U_{e1} & U_{e2} & U_{e3} \\ U_{\mu 1} & U_{\mu 2} & U_{\mu 3} \\ U_{\tau 1} & U_{\tau 2} & U_{\tau 3} \end{bmatrix} \tag{1.23}$$

and the probability of oscillation from flavor α to β is given by

$$P(\nu_\alpha \to \nu_\beta) = |\langle\nu_\beta|\nu_\alpha(L)\rangle|^2 \tag{1.24}$$

where we have already imposed the relativistic limit where $t \approx L$. The evolution of a flavor state over time can be written out in terms of the PMNS matrix

$$|\nu_\alpha(L)\rangle = \sum_\beta \Big[\sum_i U^*_{\alpha i} e^{-i(m_i^2/2E)L} U_{\beta_i}\Big]|\nu_\beta\rangle. \tag{1.25}$$

Inserting this into Eq. 1.24 gives

$$\begin{aligned}
P(\nu_\alpha \to \nu_\beta) =& \Big| \sum_i U^*_{\alpha i} e^{-i(m_i^2/2E)L} U_{\beta_i} \Big|^2 \\
&= \delta_{\alpha\beta} - 4\sum_{i>j} \mathrm{Re}(U^*_{\alpha i} U_{\beta i} U_{\alpha j} U^*_{\beta j}) \sin^2\left(\frac{\Delta m^2_{ij} L}{4E}\right) \\
&\quad + 2\sum_{i>j} \mathrm{Im}(U^*_{\alpha i} U_{\beta i} U_{\alpha j} U^*_{\beta j}) \sin\left(\frac{\Delta m^2_{ij} L}{2E}\right) \\
&= \delta_{\alpha\beta} - 4\sum_{i>j} \mathrm{Re}(U^*_{\alpha i} U_{\beta i} U_{\alpha j} U^*_{\beta j}) \sin^2\left(1.27 \frac{\Delta m^2_{ij}}{\mathrm{eV}^2} \frac{L}{\mathrm{km}} \frac{\mathrm{GeV}}{E}\right) \\
&\quad + 2\sum_{i>j} \mathrm{Im}(U^*_{\alpha i} U_{\beta i} U_{\alpha j} U^*_{\beta j}) \sin\left(2.54 \frac{\Delta m^2_{ij}}{\mathrm{eV}^2} \frac{L}{\mathrm{km}} \frac{\mathrm{GeV}}{E}\right)
\end{aligned} \tag{1.26}$$

The three-neutrino mixing matrix can be rewritten in terms of six independent parameters: three mixing angles, two mass squared differences ($\Delta m^2_{12} + \Delta m^2_{23} + \Delta m^2_{31} = 0$ is imposed) and a phase. We often write the mixing matrix in terms of three component matrices:

$$\begin{aligned}
U =& \begin{bmatrix} 1 & 0 & 0 \\ 0 & \mathrm{c}_{23} & \mathrm{s}_{23} \\ 0 & -\mathrm{s}_{23} & \mathrm{c}_{23} \end{bmatrix}
\begin{bmatrix} \mathrm{c}_{13} & 0 & \mathrm{s}_{13e^{-i\delta}} \\ 0 & 1 & 0 \\ -\mathrm{s}_{13}e^{i\delta} & 0 & \mathrm{c}_{13} \end{bmatrix}
\begin{bmatrix} \mathrm{c}_{12} & \mathrm{s}_{12} & 0 \\ -\mathrm{s}_{12} & \mathrm{c}_{12} & 0 \\ 0 & 0 & 1 \end{bmatrix}
\begin{bmatrix} e^{i\alpha_1/2} & 0 & 0 \\ 0 & e^{i\alpha_2/2} & 0 \\ 0 & 0 & 1 \end{bmatrix} \\
=& \begin{bmatrix} \mathrm{c}_{12}\mathrm{c}_{13} & \mathrm{s}_{12}\mathrm{c}_{13} & \mathrm{s}_{13}e^{-i\delta} \\ -\mathrm{s}_{12}\mathrm{c}_{23} - \mathrm{c}_{12}\mathrm{s}_{23}\mathrm{s}_{13}e^{i\delta} & \mathrm{c}_{12}\mathrm{c}_{23} - \mathrm{s}_{12}\mathrm{s}_{23}\mathrm{s}_{13}e^{i\delta} & \mathrm{s}_{23}\mathrm{c}_{13} \\ \mathrm{s}_{12}\mathrm{s}_{23} - \mathrm{c}_{12}\mathrm{c}_{23}\mathrm{s}_{13}e^{i\delta} & -\mathrm{c}_{12}\mathrm{s}_{23} - \mathrm{s}_{12}\mathrm{c}_{23}\mathrm{s}_{13}e^{i\delta} & \mathrm{c}_{23}\mathrm{c}_{13} \end{bmatrix}
\begin{bmatrix} e^{i\alpha_1/2} & 0 & 0 \\ 0 & e^{i\alpha_2/2} & 0 \\ 0 & 0 & 1 \end{bmatrix}
\end{aligned} \tag{1.27}$$

Expanding the oscillation matrix in such a way isolates the mixing parameters governing the mixing between each individual pair of mass eigenstates.

1.3.4 Matter Effects

To this point, our treatment of neutrino oscillations has been done in a vacuum. Realistically, many neutrino experiments observe neutrino oscillations that occur as neutrinos traverse through the earth, subject to matter effects [27, 29].

The MSW effect describes the impact of matter on neutrino flavor oscillations with a mechanism analogous to indices of refraction in optics. Electron flavor neutrinos experience different refractive indices while traveling through matter than muon and tau neutrinos. More intuitively, this is related to the fact that matter is made up of electrons rather than muons and taus, so electron neutrinos have the opportunity to interact via charged current with the matter they travel through. Matter effects impact the oscillation probabilities between flavor states, an effect that is observable in neutrinos that pass through the earth.

Another interesting result of the MSW effect is the nature of the neutrinos exiting the Sun. The electron neutrinos produced in the Sun's core oscillate in such a such a way that by the time they exit the Sun they are entirely in the ν_2 mass state.

1.3.5 Other Experimental Constraints

Additional constraints on the number and mass of neutrinos arise from empirical measurements outside of dedicated neutrino physics experiments.

Colliders The neutrino is an invisible product of interactions that occur inside of colliders, but their presence can be inferred through studying missing energy and decay rates. In particular, the decay width of the Z boson, the neutral mediator of the weak force, provides a strong limit on the number of neutrino flavors that can participate in weak interactions. Data collected by the ALEPH, DELPHI, L3, and OPAL collaborations at LEP and by the SLD experiment at SLC (LEP and SLC are both electron-positron colliders) yielded $\Gamma_Z = 2.4952 \pm 0.0023$ [14]. The decay width can be written as the sum of all possible decay modes:

$$\Gamma_Z = \Gamma_{ee} + \Gamma_{\mu\mu} + \Gamma_{\tau\tau} + \Gamma_{\text{hadronic}} + \Gamma_{\text{invisible}} \tag{1.28}$$

where $\Gamma_{\text{invisible}}$ is the decay width contribution from neutrinos. Assuming lepton universality, the decay width can be related to the number of active (participating in the weak force) "light" neutrinos N_ν by:

$$\frac{\Gamma_{\text{invisible}}}{\Gamma_{ll}} = N_\nu \left(\frac{\Gamma_{\nu\bar{\nu}}}{\Gamma_{ll}} \right) \tag{1.29}$$

which gives $N_\nu = 2.9840 \pm 0.0082$. Any additional neutrinos beyond the three known flavors cannot participate in the weak force. We call these inactive neutrinos "sterile" neutrinos.

Cosmology The universe is pervaded by a cosmic neutrino background (CνB) analogous to the cosmic microwave background (CMB). These "relic" neutrinos have not yet been observed, but their impact has been measured indirectly through several observations, including the abundance of light elements in the early universe, CMB anisotropies, and large-scale clustering of cosmological structures. These measurements can place limits on both the number of neutrinos and their total mass. Today, the CνB neutrinos have energy of $T_\nu \simeq 1.7 \times 10^{-4}$ eV $\simeq 1.9$ K and an average number density $n_\nu = 339.5\ \nu/\mathrm{cm}^3$ [42]. Future experiments like PTOLEMY hope to directly observe relic neutrinos via capture on tritium [43].

1.4 Open Questions

A number of open questions remain in neutrino physics. Future dedicated experiments are underway to answer many of these questions, pioneering new technology along the way.

1.4.1 Sterile Neutrinos

The LSND experiment at Los Alamos National Laboratory was a short baseline (30 m, $L/E \sim 0.4 - 1.2\mathrm{m/MeV}$) liquid scintillator detector designed to measure $\overline{\nu}_\mu \to \overline{\nu}_e$ oscillations. Approximately 95% of the flux came from π^+ ($\pi^+ \to \mu^+ + \nu_\mu$) and μ^+ ($\mu^+ \to e^+ + \overline{\nu}_\mu + \nu_e$) decays at rest in the copper beam stop. LSND, like many experiments before it, detected neutrinos through inverse beta decay by tagging events based on the unique timing signature of the prompt positron scintillation followed by neutron capture a few microseconds later. LSND measured a 3.8σ excess of $\overline{\nu}_e$-like interactions above the background expectation [44]. However, taken in combination with the characteristic baseline for the experiment, this indicated a neutrino oscillation with mass squared difference around $\Delta m^2 = 0.2 - 10\ \mathrm{eV}^2$ and neutrino mass greater than 0.4 eV. This was completely inconsistent with the oscillation parameters measured by previous atmospheric, solar, and reactor experiments (these all indicated Δm^2 values of order $10^{-3}\ \mathrm{eV}^2$ and $10^{-5}\ \mathrm{eV}^2$).

Because independent collider-based measurements of the Z boson decay width constrained

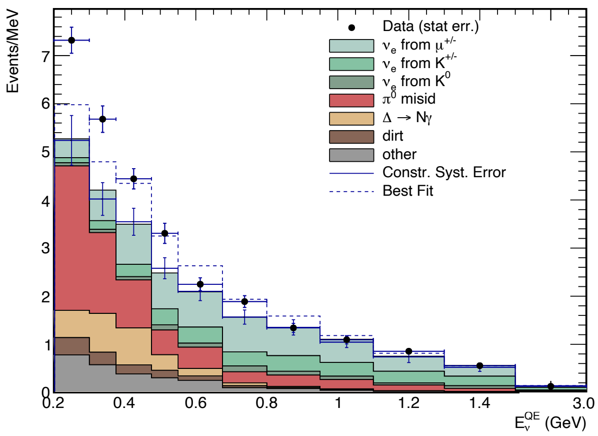

Figure 1.6: MiniBooNE observes a 4.8σ excess of low-energy ν_e-like events in the most recent results reporting on 18.75×10^{20} POT of data collected in neutrino mode from the NuMI beam. Figure from Ref. [45].

the number of weakly interacting neutrinos to three (see Section 1.3.5), if a fourth neutrino existed to participate in the oscillation observed by LSND, it would be a so-called "sterile" neutrino. These neutrinos would readily mix with the three known neutrino states via an expanded mixing matrix, but would not participate in the weak interactions and would therefore be invisible to direct detection experiments except through oscillations inferred based on the three known flavor states.

The MiniBooNE experiment was designed to shed light on the LSND results. MiniBooNE is a spherical mineral oil Cherenkov detector surrounded by about 1300 photomultiplier tubes and located in the BNB neutrino source at Fermilab, capable of operating in both neutrino and antineutrino modes. MiniBooNE's most recent result reports a 4.8σ (638.0 ± 132.8 event) excess of low-energy ν_e-like events consistent with the LSND anomaly [45]. The result is shown in Figure 1.6.

Today, the MicroBooNE experiment in operation at Fermilab seeks to illuminate the source of the anomaly observed by both LSND and MinBooNE. MicroBooNE has the added advantage of precision topological and vertex calorimetry information that give it the ability to distinguish electrons produced in ν_e interactions from photon backgrounds that are most prominent in MiniBooNE's selected ν_e-like interactions (see Chapter 2 for more details). A discussion of MicroBooNE's capabilities and progress to understand this anomaly can be found in Chapter 5.

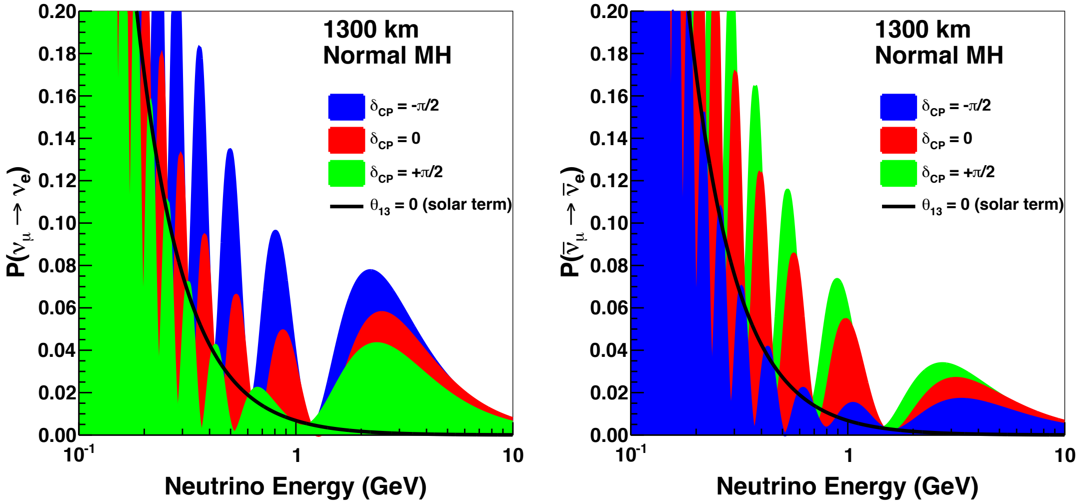

Figure 1.7: Neutrino oscillation probability in DUNE as a function of neutrino energy and δ_{CP}. Normal mass ordering is assumed. Figure from Ref. [49].

1.4.2 CP Phase

Precision measurements of the final parameter governing three-neutrino oscillations are also in reach. The CP-violating phase of the PMNS matrix, δ_{CP}, is slowly being constrained by several experiments, though no consensus has arisen. Recent preliminary constraints on the value of δ_{CP} from T2K [46] and NOνA [47] are in slight tension with one another [48], though neither has yet been able to provide a strong constraint. Notably, a non-zero value would have significant implications for the larger CP violation picture in the universe, possibly providing hints toward understanding the reasons for the matter-antimatter asymmetry we observe today. The future Deep Underground Neutrino Experiment (DUNE) aims to measure the value definitively in the next few decades. The change in neutrino oscillation probability in DUNE as a function of neutrino energy and δ_{CP} is shown in Figure 1.7. Both the amplitude and position of each peak changes a function of δ_{CP}, giving DUNE a handle for extracting the value from ν_e interaction rates observed by the far detector. A more detailed discussion of DUNE can be found in Chapter 7.

1.4.3 Mass Hierarchy

The absolute mass, and therefore the order of the three neutrino masses, also remains a mystery. Oscillation experiments allow us to measure mass-squared splitting, but without a conclusive sign

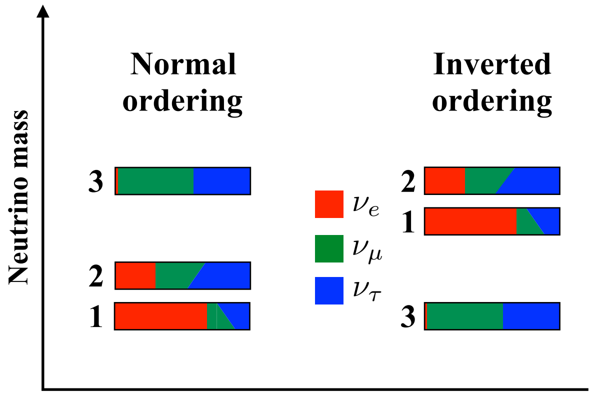

Figure 1.8: Possible neutrino mass hierarchies. Based on current data, these two orderings are degenerate. Image from Ref. [49].

on Δm^2_{23}, there are degeneracies in the possible order of increasing mass states. DUNE and other experiments are slowly constraining the allowed phase space in each hierarchy. An illustration of the two possible mass hierarchies is shown in Figure 1.8.

1.4.4 Absolute Mass Scale

Closely related to the neutrino mass hierarchy is the absolute scale of neutrino masses. At present only measurements of mass squared difference exist. These measurements provide an obvious lower limit on the heavier mass in each mass splitting ($|m_i| \geq \sqrt{\Delta m^2_{ij}}$), but not an upper limit. Observations of tritium decay from KATRIN place an upper limit on the effective electron neutrino mass: $m^{\text{eff}}_{\nu_e} < 1.1$ eV [50]. Other experiments use ^{163}Ho to perform similar measurements to constrain the effective masses of the flavor states [51–53]. Cosmological observations constrain the sum of the neutrino masses to $\sum m_\nu < 0.11$ eV at 95% confidence [42]. All that said, efforts to measure absolute neutrino mass are still in their nascency and future improvements in precision are inevitable.

1.4.5 Majorana vs. Dirac Neutrinos

Finally, there is the question of the nature of neutrino mass, or how we go about actually writing down the terms for neutrino mass in the formalism of the Standard Model. Do neutrinos behave as their own antiparticles? The best probe as to whether neutrino masses are Majorana or Dirac are searches for neutrinoless double beta decay. The Feynman diagram for the interaction is shown in

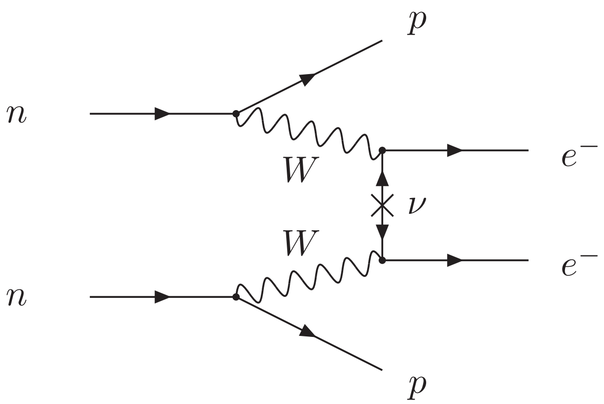

Figure 1.9: The Feynman diagram for neutrinoless double beta decay.

Figure 1.9. If neutrinos have non-zero Majorana mass, neutrinoless double beta decay is a viable interaction. Neutrinos with non-zero Dirac mass cannot take part in neutrinoless double beta decay. Observation of neutrinoless double beta decay would provide conclusive evidence that neutrinos are their own antiparticles.

CHAPTER 2

Neutrino Beams, Time Projection Chambers, and Cross Sections: An Introduction

xThroughout this work, we will return over and over again two the two main components necessary for studying neutrinos: a neutrino source and a neutrino detector. Many neutrino experiments make an appearance throughout this work, some currently taking data, others finished running, and some still being designed and built. The NuMI neutrino beam, the Booster Neutrino Beam, and the future Long Baseline Neutrino Facility act as the primary neutrino sources for the neutrino experiments discussed, all based at Fermilab in Batavia, Illinois. Each of the experiments (with the exception of MiniBooNE) uses liquid argon time projection chamber detection technology, with key differences between experiments described in later chapters.

Here we provide a broad overview of neutrino beam and neutrino detector technology as the foundation for future experiment-specific discussions. Figure 2.1 lists the Fermilab-based neutrino experiments and their operational status, with the experiments covered in this document highlighted.

2.1 Neutrino Beams

Though there is much to learn from natural (cosmic, solar, geo) and pre-existing (reactor) neutrino sources, accelerator neutrino beams have the added benefit of being tunable to physics goals. Another advantage is a precisely known arrival time for neutrino signals which can dramatically reduce asynchronous backgrounds. Current active neutrino beams include the Booster Neutrino Beam (BNB) and Neutrinos at the Main Injector (NuMI) beam at Fermilab, and the T2K neutrino

Operating

- NOvA
- MicroBooNE
- MINERvA
- LArIAT

Designing and Building

- DUNE
- Short-Baseline Neutrino Program (SBN)
  - SBND
  - ICARUS

Analyzing, Finished Running

- ArgoNeuT
- MiniBooNE
- MINOS / MINOS+

Figure 2.1: A list of the neutrino experiments at Fermilab by operational status. The experiments highlighted will be discussed in subsequent chapters.

beam produced at J-PARC in Tokai, Japan [54].

To produce a neutrino beam, protons are accelerated into a fixed target where they interact to produce mesons like pions and kaons. The charged mesons can be focused using magnetic horns to impact the composition of the resulting neutrino beam. When the mesons decay, neutrinos are produced.

Neutrino beams must be highly intense, given the neutrino's small cross section. They must also be pure, as it is significantly easier to measure an oscillation (e.g. $\nu_\mu \to \nu_e$) when there are fewer intrinsic backgrounds with which to contend. Additionally, it is critical to understand the energy characteristics of the neutrino flux. It is difficult to reconstruct neutrino energy, and precise knowledge of flux often requires empirical testing. To wit, neutrino experiments often have a near detector, whose goal is to measure the unoscillated flux from the neutrino source, and a far detector to measure the beam composition after oscillations, where the rate of oscillation is dependent on the ratio L/E, in which L is the distance traveled by the neutrino (often referred to as "baseline") and E is the energy of the neutrino. The Short Baseline Neutrino Program (SBN, which includes MicroBooNE, SBND, and ICARUS) and DUNE are both designed with this kind of setup. ArgoNeuT benefitted from detailed studies by the MINERνA experiment to understand the NuMI on-axis flux [55].

Fermilab's accelerator complex begins with a hydrogen ion source fed into a 4.5 m radio fre-

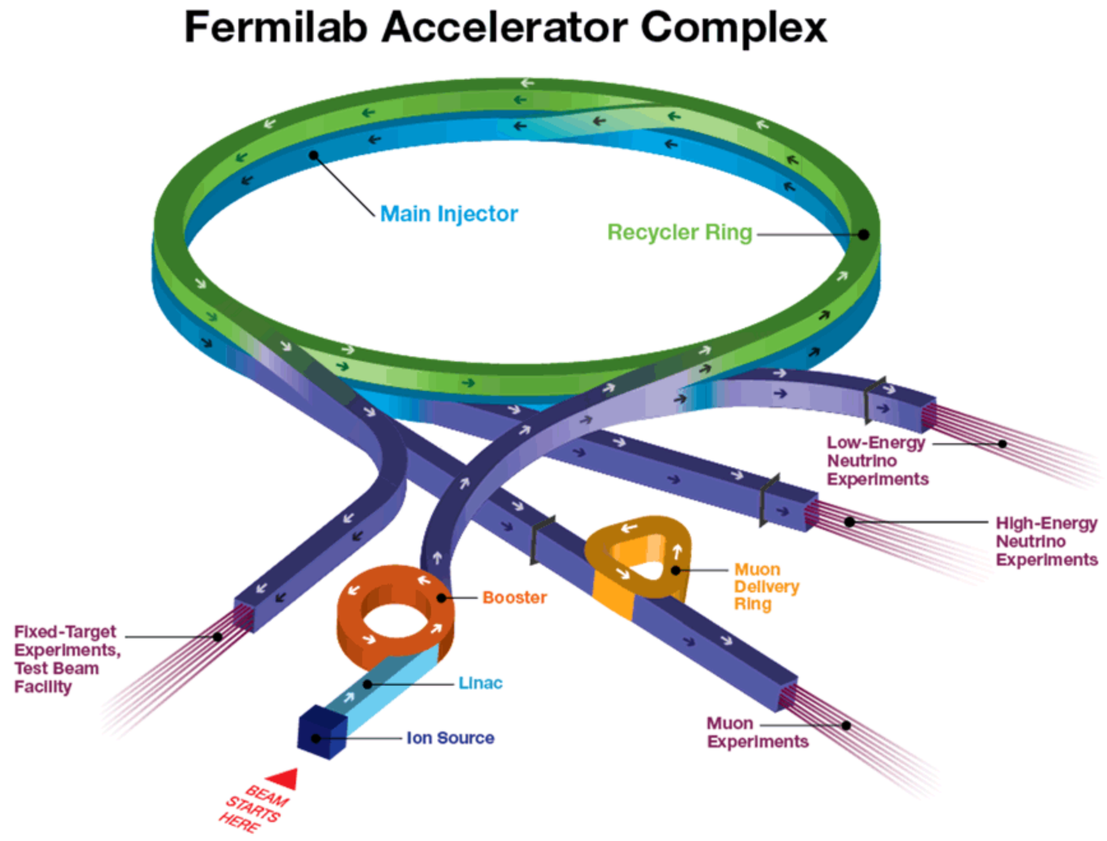

Figure 2.2: Diagram of the particle beams originating from the accelerator complex at Fermilab. The future beam intended for DUNE is not shown. Image courtesy of Ref. [56].

quency quadropole (RFQ) that accelerates the ions from 35 keV to 750 keV (prior to 2012 this task was done by a Cockroft-Walton generator). Then an Alvarez linear accelerator (the Linac), operating at 201.25 MHz (producing bunches about 5 ns apart), further accelerates the ions to approximately 400 MeV. After exiting the Linac, the ions enter the Booster (operating at 15 Hz), a synchrotron that accelerates them to 8 GeV in less than 67 ms. It is at this stage that the H^- ions are converted to pure protons with a thin carbon foil. After up to 10 turns in the Booster, the proton batches (about 5×10^{12} protons are in each batch) are either delivered to the BNB target, or delivered to the Main Injector for further acceleration up to 120 GeV.

An illustration of the Fermilab accelerator complex is shown in Figure 2.2. The beams labeled for low- and high-energy neutrino experiments are the BNB and NuMI sources, respectively.

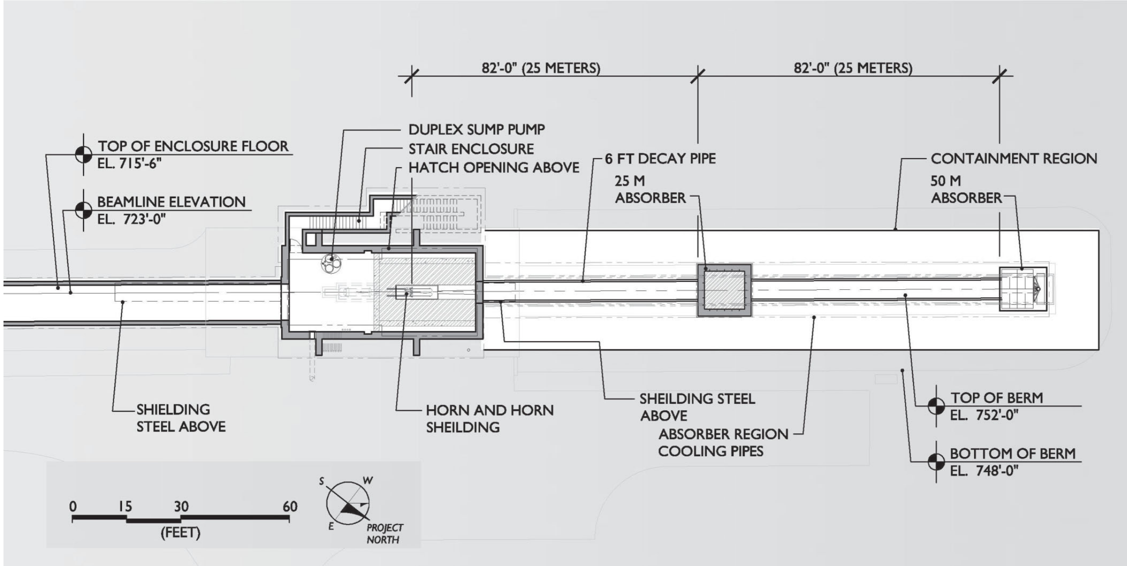

Figure 2.3: Schematic of the Booster Neutrino Beam. Image from Ref. [57].

2.1.1 The Booster Neutrino Beam

The Booster Neutrino Beam (BNB) neutrino source is a primarily muon neutrino beam with neutrino energies that peak at $\mathcal{O}(1)$ GeV. The BNB target is a 70 cm cylinder made of seven beryllium segments. Over 80% of the 8 GeV protons incident on the target interact to produce charged hadrons such as pions and kaons. The composition and energy spectrum of this collection of hadrons is the largest source of uncertainty in the final neutrino beam composition. A 185 cm magnetic horn with reversible polarity focuses the charged hadrons, which then pass through a 214 cm block of concrete, the collimator, which absorbs any particles that don't contribute to the neutrino flux. The polarity of the horn impacts beam composition and is the mechanism by which the beam is set to be in neutrino mode or antineutrino mode. Finally, the charged hadrons enter the 45 m cylindrical air-filled decay pipe with a 3 ft radius ending at a concrete and steel beam dump at the downstream end. Hadrons that do not decay in flight come to rest in the beam dump. A diagram of the BNB is shown in Figure 2.3.

The Booster Neutrino Beam is a predominantly ν_μ source with small contamination from $\overline{\nu}_\mu$ and ν_e. The BNB ν_μ flux comes primarily from pion decays, with small contributions from muon and kaon decays. The BNB neutrino mode flux and the ν_μ flux from each parent meson observed by MiniBooNE are shown in Figure 2.4.

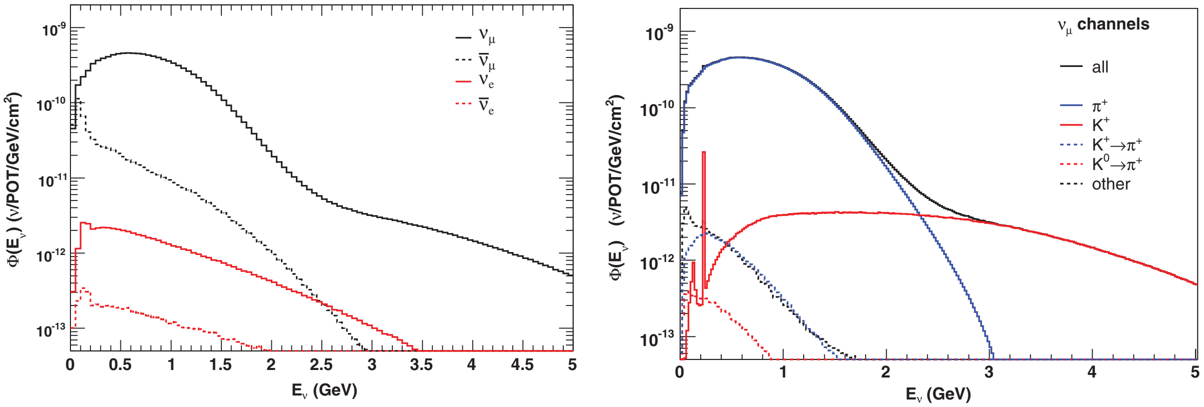

Figure 2.4: (left) The total predicted BNB neutrino mode flux at MiniBooNE by neutrino species. (right) Predicted BNB neutrino mode ν_μ flux by parent meson species. Figures from Ref. [57].

2.1.2 The Neutrinos at the Main Injector Beam

The NuMI beam is the higher energy neutrino beam at Fermilab, capable of producing proton energies up to 120 GeV and subsequent neutrino energies up to $\sim$20 GeV. To reach higher proton energy, the 8 GeV protons provided by the Booster are fed to the Main Injector synchrotron that accelerates the protons up to 120 GeV (and once upon a time also up to 150 GeV for the Tevatron and collider experiments). The NuMI beam is more configurable than the BNB, capable of running in multiple energy modes. The flux observed by the MINOS far detector at Soudan mine in Minnesota is shown in Figure 2.5. The NuMI beam has operated primarily in low energy neutrino and antineutrino modes, which are the only samples relevant in the analyses described in subsequent chapters.

The NuMI beam differs from the BNB in several respects: 1) the location of the 1 m graphite target is adjustable, 2) there are two focusing horns to accommodate the higher energy hadrons exiting the target as a result of the higher energy incident protons, and 3) the helium-filled decay pipe is much longer at 675 m. Any hadrons that have not decayed by the end of the decay pipe are stopped at the end by an aluminum/steel/concrete absorber (also referred to, interchangeably, as the beam dump). A diagram of the NuMI beam is shown in Figure 2.6. Notably, the NuMI beam dump is a high intensity source of monoenergetic muon neutrinos from kaon decay at rest that can be observed by several experiments at Fermilab. The first observation of these special neutrinos with MiniBooNE is discussed in Chapter 8.

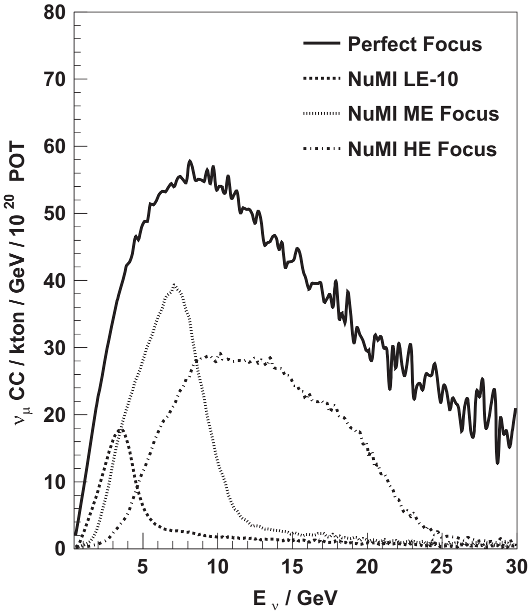

Figure 2.5: Predicted NuMI neutrino mode flux in each mode at the MINOS far detector. The beam has operated primarily in low energy mode. Figure from Ref. [58].

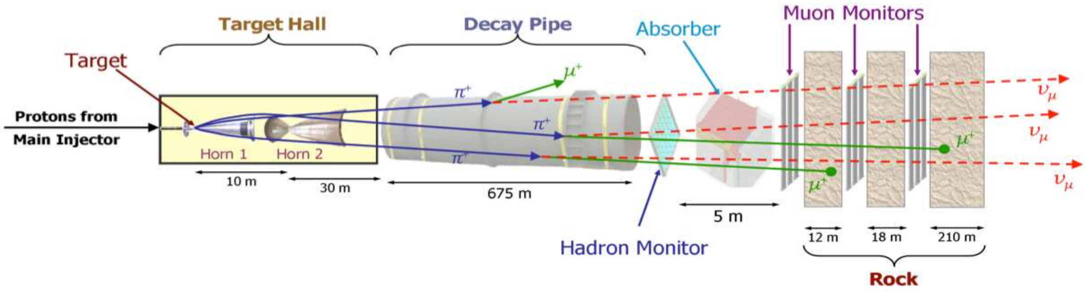

Figure 2.6: Schematic of the NuMI neutrino beam. Image from Ref. [58].

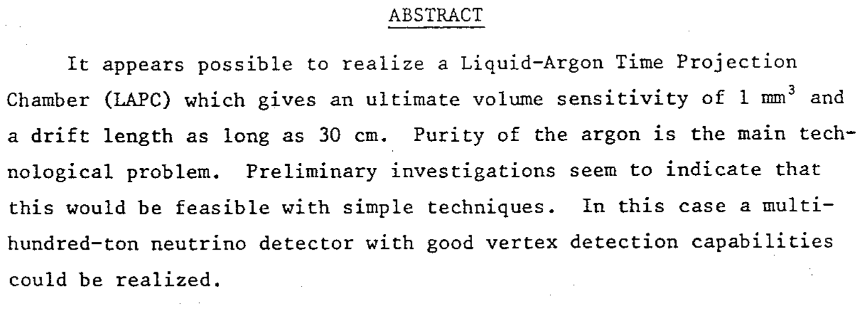
ABSTRACT

It appears possible to realize a Liquid-Argon Time Projection Chamber (LAPC) which gives an ultimate volume sensitivity of 1 mm^3 and a drift length as long as 30 cm. Purity of the argon is the main technological problem. Preliminary investigations seem to indicate that this would be feasible with simple techniques. In this case a multi-hundred-ton neutrino detector with good vertex detection capabilities could be realized.

Figure 2.7: The abstract of Rubbia's report advocating for the use of LArTPCs in neutrino physics. Image of Ref. [61].

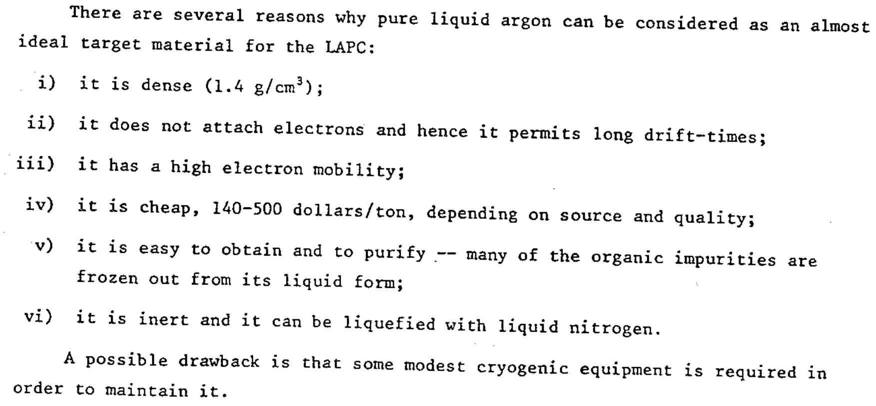
There are several reasons why pure liquid argon can be considered as an almost ideal target material for the LAPC:

i) it is dense (1.4 $\mathrm{g/cm}^3$);

ii) it does not attach electrons and hence it permits long drift-times;

iii) it has a high electron mobility;

iv) it is cheap, 140-500 dollars/ton, depending on source and quality;

v) it is easy to obtain and to purify -- many of the organic impurities are frozen out from its liquid form;

vi) it is inert and it can be liquefied with liquid nitrogen.

A possible drawback is that some modest cryogenic equipment is required in order to maintain it.

Figure 2.8: Rubbia's list of reasons for using liquid argon in TPC neutrino detectors. Image of Ref. [61].

2.2 Time Projection Chambers

The time projection chamber is a powerful detector that records high resolution images of neutrino interactions, providing both detailed topological and calorimetric information about the charged particles traversing the detector. Neutrino experiments have typically used liquid argon as the gaseous noble element inside these detectors, but dark matter experiments like XENON [59] have used alternatives (perhaps it's overkill to state explicitly that they use xenon).

Invented in 1974 [60], the time projection chamber (TPC) quickly caught the eyes of neutrino physicists. In 1977, Carlo Rubbia published a report describing the applications of TPC technology in neutrino physics (see the abstract in Figure 2.7) [61]. In particular, he advocates for the use of liquid argon as a target material, for a number of reasons, outlined concisely in a bulleted listed (see Figure 2.8).

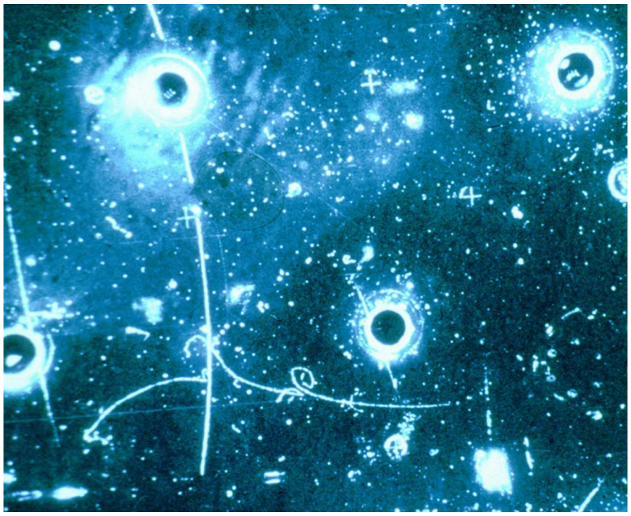

Figure 2.9: An electron neutral current interaction observed by the Gargamelle bubble chamber. Image courtesy of CERN/Gargamelle.

At the time, the world of high resolution particle detection was dominated by bubble chambers. These detectors produced beautifully clear images of charged particles that passed through the heated liquid inside a magnetized chamber, producing visible ionization tracks. A bubble chamber at CERN named Gargamelle had just discovered direct evidence of weak neutral currents [62, 63]. An example of one of the Gargamelle neutral current interactions is shown in Figure 2.9. Despite their incredible resolution, bubble chambers had several disadvantages. They provide no calorimetric information, only the charge of a particle could be inferred from its curvature while traversing the magnetic field. In addition, bubble chambers were not self-triggered and the data collection was not digitized. Both of these aspects make identifying interactions of interest far more challenging. Given the amount of data required in neutrino experiments today, the bubble chamber becomes an inviable option.

Enter, the liquid argon time projection chamber. LArTPCs provide close to bubble chamber image quality, adding calorimetric information, while also being self-triggered and fully digitized. As yet they have not been magnetized.

2.2.1 The LArTPC Concept

When a neutrino interacts with an argon atom in the detector, the products of the interaction (muons, electrons, pions, protons, neutrons, etc.) travel away from the interaction vertex through the detector volume. In order to identify the flavor and energy of the neutrino that interacted, the interaction products must be efficiently reconstructed. Particles with electric charge ionize the argon atoms in the detector as they pass through. The amount of ionization depends on both the mass and momentum of each particle. Neutral particles like photons and neutrons do not ionize the argon as they travel, but can interact with argon atoms at any point to produce charged particles that are visible to the detector. Neutrons scattering off argon nuclei often yield visible proton tracks, and photons[1] participate in Compton scattering and pair production to generate distinct electromagentic showers (photons are particularly pesky backgrounds when looking for electron neutrino interactions in a LArTPC, see Chapter 4).

The trail of ionization electrons produced by the traveling charged particle is free to move about the detector, surrounded by inert noble argon atoms. An electric field applied to the TPC causes the electrons to drift in the direction of instrumented wire planes that record the signal of the electrons as they arrive. LArTPCs typically have two (ArgoNeuT) or three (MicroBooNE, SBND) wire planes each oriented at different angles with wires separated by a few millimeters (e.g. 4 mm in ArgoNeuT, 3 mm in MicroBooNE). As ionized charge drifts across the the first "induction" wire planes, it induces a current in the wires, yielding a bipolar signal. The charge is collected by the final "collection" wire plane, producing unipolar signals.

Combining information from all planes makes it possible to reconstruct a two-dimensional projection of the interaction with mm-scale position resolution. An illustration of the LArTPC detection concept is shown in Figure 2.10. An example interaction recorded by ArgoNeuT is shown in Figure 2.11, where two neutral pions, each of which decays to a pair of photons, are clearly visible. The photons each generate distinctive electromagnetic showers. Three additional track-like particles (typically muons, charged pions, or protons) are also visible. The projection of the interaction collected on each of ArgoNeuT's wire planes is shown. The combination of high resolution position and charge information makes LArTPCs incredibly powerful tools for probing neutrino interactions.

Timing information provides a handle for reconstructing position in the third (drift) direction. And charge deposited on the wire planes is proportional to the amount of energy deposited in the detector and can be used to reconstruct particle energy and identity. Energy reconstruction is

---

[1] Throughout this document, the terms photon and gamma are used interchangeably.

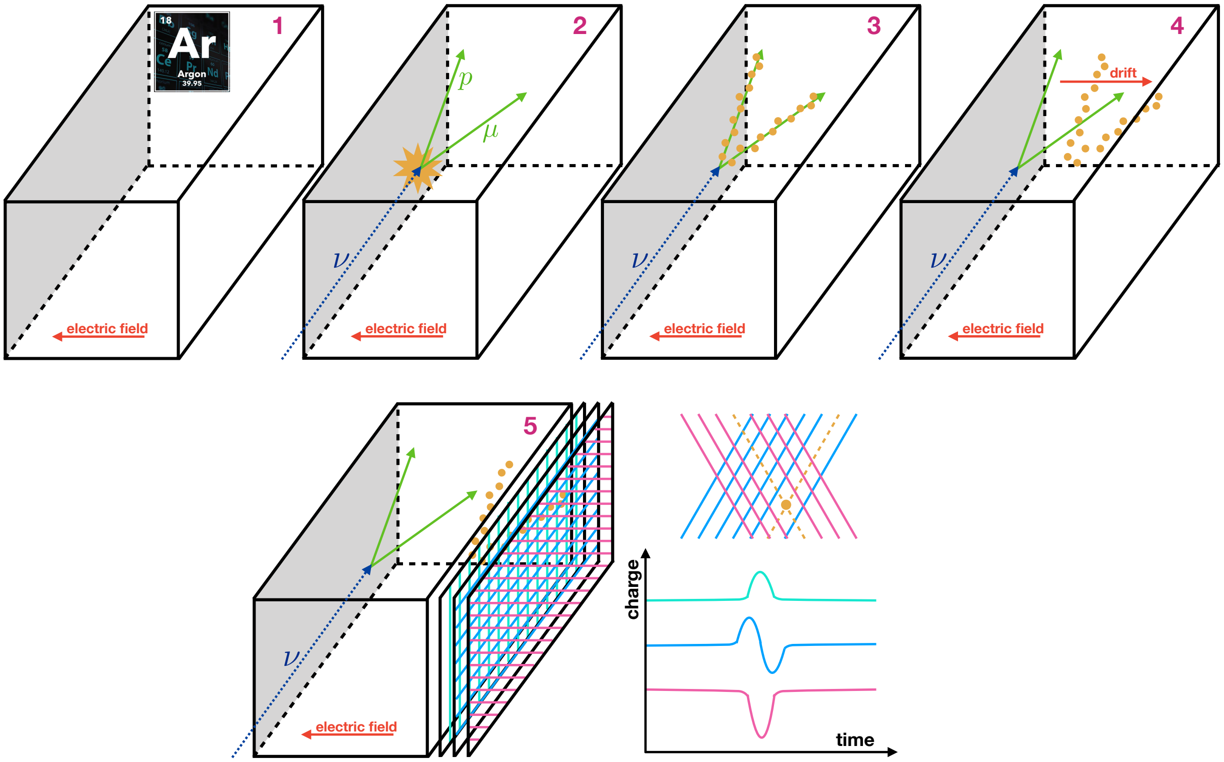

Figure 2.10: An illustration of particle detection in a LArTPC.

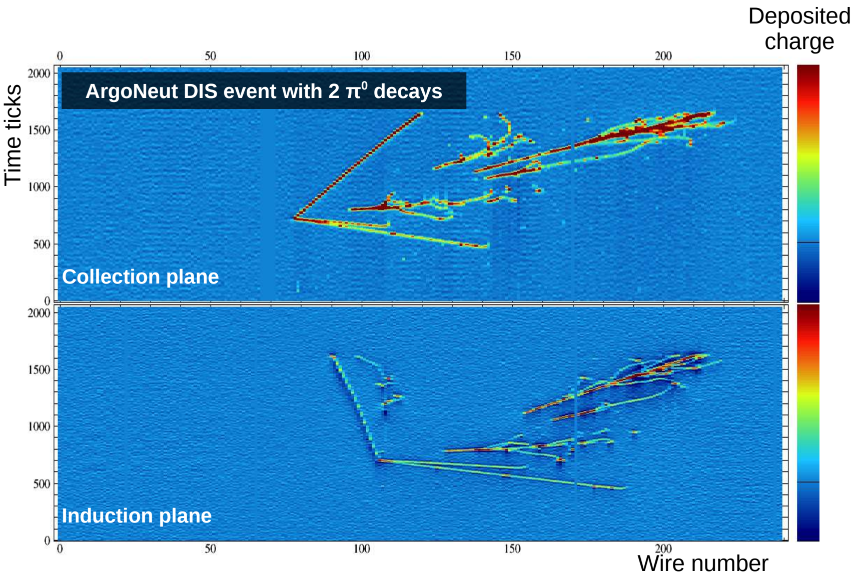

Figure 2.11: An event display from ArgoNeuT with two neutral pions, each decaying to a pair of photons. Each photon generates a distinctive electromagnetic shower. Three additional track-like particles (typically muons, charged pions, or protons) are also visible.

complicated by a number of effects including electron recombination [64] and build up of space charge in larger detectors [65].

To date, neutrino experiments using LArTPCs have traditionally applied horizontal drift fields to send electrons toward instrumented wire planes on one side of the detector. Alternative configurations are also possible, and new innovations are actively being pursued for implementation in at least one of the future DUNE far detector modules. For example, the dark matter experiment DarkSide has a two-phase TPC design using argon [66, 67]. A vertical drift field draws the ionization electrons toward the top of the detector, where they move from the liquid argon into gaseous argon and the signal is amplified via electroluminescence in the gaseous argon. DUNE's ProtoDUNE-DP will prototype this kind of dual phase detector for use in neutrino experiments.

2.2.2 Photon Detection in LArTPCs

The electron drift times in LArTPCs are typically on the order of microseconds (determined by the strength of the drift field and the size of the detector), yielding large uncertainty in the absolute position of an interaction along the drift direction of a detector. The addition of a light collection system to detect scintillation light produced in the argon makes it possible to measure the start time of an interaction, significantly reducing the uncertainty in the position along the drift direction. Prompt scintillation light produced during interactions with argon targets can be used in combination with the ionized charge collected by the wire planes in a LArTPC to fully reconstruct an interaction three dimensions.

In addition to producing ionization electrons, charged particles traversing through an argon detector excite argon atoms into the dimer state Ar_2^*. To return to a ground state configuration, the excited argon atoms undergo photon emission through de-excitation, a process that occurs with characteristic time of order 6 ns. There is also a second excited state that de-excites at much longer time scales ($\mathcal{O}(1.5)$ μs). In both cases, the photons are emitted in the VUV range at around 127 nm [68]. The combination of prompt and delayed de-excitation scintillation actually provides a second tool for particle identification under certain circumstances. The relative intensity of the prompt and delayed scintillation signals is dependent on the type of ionizing particle [69]. In large detectors at the scales of those used in neutrino experiments, where most interactions involved multiple particles, the utility is minimal. However, these scintillation signatures have been used

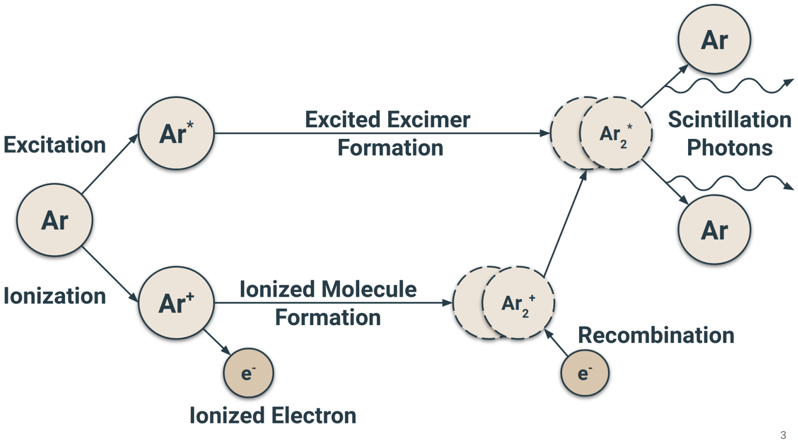

Figure 2.12: Schematic of ionization and scintillation processes in argon. Image from [70].

very effectively for particle identification in smaller detectors like DarkSide-50 [66]. A schematic illustrating the scintillation and ionization processes in argon is shown in Figure 2.12.

A number of photon detection methods are popular, including photomultiplier tube- and silicon photomultiplier-based systems. Photon detection systems in LArTPCs can provide critical temporal and spatial information that can be used to isolate neutrino activity among significant background or complement charge-based calorimetry. They can also be used as an independent trigger system for events not in time with the beam, like possible supernova burst neutrinos.

2.3 Cherenkov Detectors

We will back up briefly with an interlude on Cherenkov detectors, still a popular neutrino detection technology. They are advantageous in that they use relatively cheap detector material, making it easier to create very large-volume detectors. Cherenkov detectors make observation of electron flavor neutrinos possible, but it can be difficult to distinguish electrons from prominent photon backgrounds. Figure 2.13 shows example muon and electron neutrino interactions simulated in Super-K, which illustrates that muons produce much smoother rings than electrons and other electromagnetic activity. Figure 2.14 shows an example event display in MiniBooNE (a Cherenkov detector) compared to MicroBooNE (a LArTPC) to illustrate the wealth of additional topological information recorded with LArTPCs, including particle vertex location, noting that a photon would be displaced from the neutrino vertex while an electron would not, a distinction

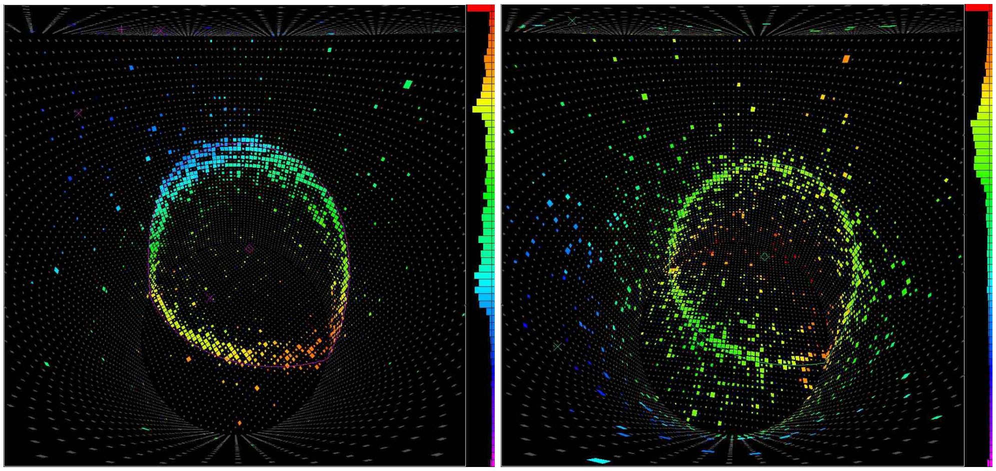

Figure 2.13: Example neutrino interactions simulated in Super-K. (left) A muon event and (right) an electron event. The muon produces a much cleaner Cherenkov ring. Images from Ref. [71].

that is invisible to Cherenkov detectors. Additionally, Cherenkov detectors are unable to observe hadrons in the final state interaction, as their energies fall below the detector threshold.

Nonetheless, Cherenkov detectors have been absolutely critical to the last half-century of neutrino physics. The early Kamiokande, current Super-K, and future Hyper-K experiments are all water Cherenkov detectors. SNO was a heavy water (D_2O) Cherenkov detector. IceCube uses Cherenkov signals to detect highly energetic (TeV scale) extragalactic cosmogenic neutrinos [72]. And MiniBooNE was a Fermilab-based mineral oil Cherenkov detector that will feature prominently here.

2.4 Neutrino Cross Sections

Neutrino oscillation measurements would not be possible without detailed understanding of how the neutrino interacts. Neutrino cross sections for neutral and charged current channels have been measured over a range of energies on a number of target nuclei in the past several decades. A summary of the current landscape of neutrino cross section measurements is shown in Figure 2.15 [6]. Notably, neutrino cross sections on argon have only started to be measured in the past decade with ArgoNeuT and now MicroBooNE, but are the most relevant to the future long baseline Deep Underground Neutrino Experiment (DUNE). However, measuring neutrino cross sections is uniquely challenging [73, 74], primarily because the energy of the incident neutrino is

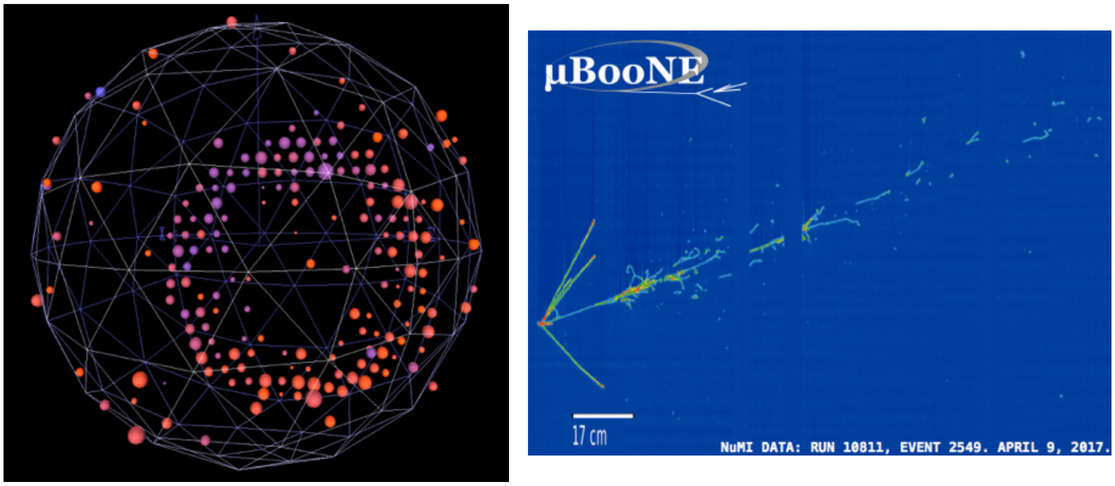

Figure 2.14: (left) An example event display from MiniBooNE and (right) an example event display from MicroBooNE.

almost never known precisely; uncertainties in neutrino flux (both flavor composition and energy spectrum) dominate current accelerator based neutrino interaction measurements.

Taking into account multi-nucleon effects, final state interactions, and detector effects impacting observed final state topologies all makes sorting through and fully quantifying the different mechanisms that govern neutrino-nucleus scattering extremely difficult. In particular, nuclear models, (describing what occurs when a neutrino interacts with a multi-nucleon target), inject a large degree of uncertainty (this is directly related to the effects that cause high uncertainty in neutrino beam composition). Given the number of degrees of freedom, existing models span a wide range of possible total interaction cross sections that can only be further constrained with dedicated data-based studies. As illustrated by Figure 2.15, nuclear effects become more prominent at higher energies as deep inelastic scattering becomes a prominent effect. Understanding final state multiplicities (i.e. the number of hadrons produced in a neutrino-nucleus interaction) is one of the major challenges for GeV-scale LArTPC-based neutrino experiments where so many particles are visible to the detector. In particular, GeV-scale neutrino interactions, where deep inelastic scattering contributions are prominent, yield complex interaction topologies with many tracks and showers that can obfuscate one another. Part of the challenge includes developing efficient tools for automated reconstruction of high-multiplicity interactions (see next section).

Another tool for better understanding neutrino nucleus interactions are monoenergetic neu-

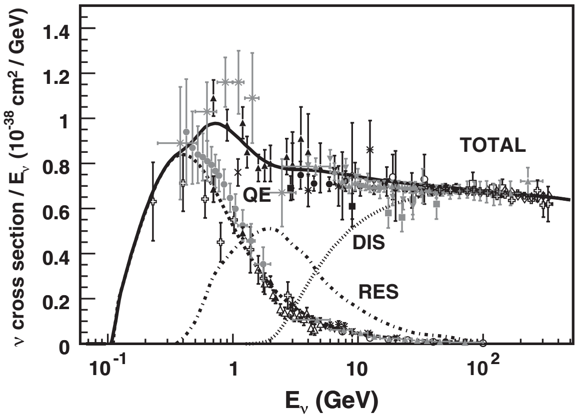

Experiment	beam	$\langle E_\nu \rangle$, $\langle E_{\overline{\nu}} \rangle$ GeV	neutrino target(s)	run period
ArgoNeuT	$\nu, \overline{\nu}$	4.3, 3.6	Ar	2009 – 2010
ICARUS (at CNGS)	ν	20.0	Ar	2010 – 2012
K2K	ν	1.3	CH, H_2O	2003 – 2004
MicroBooNE	ν	0.8	Ar	2015 –
MINERvA	$\nu, \overline{\nu}$	3.5 (LE), 5.5 (ME)	He, C, CH, H_2O, Fe, Pb	2009 – 2019
MiniBooNE	$\nu, \overline{\nu}$	0.8, 0.7	CH_2	2002 – 2019
MINOS	$\nu, \overline{\nu}$	3.5, 6.1	Fe	2004 – 2016
NOMAD	$\nu, \overline{\nu}$	23.4, 19.7	C–based	1995 – 1998
NOvA	$\nu, \overline{\nu}$	2.0, 2.0	CH_2	2010 –
SciBooNE	$\nu, \overline{\nu}$	0.8, 0.7	CH	2007 – 2008
T2K	ν, $\overline{\nu}$	0.6, 0.6	CH, H_2O, Fe	2010 –

Figure 2.15: (left) Total per nucleon neutrino charged current cross section as a function of neutrino energy. Contributions from quasielastic scattering, resonance production, and deep inelastic scattering are shown. Figure from Ref. [6]. (right) Recent accelerator-based neutrino experiments with beam properties and target nuclei listed. Table from Ref. [42].

trino sources. These are one of the few cases where incident neutrino energy is known with complete certainty. Pion and kaon decays at rest both produce monoenergetic muon neutrinos. The higher energy (236 MeV) muon neutrino from kaon decay at rest is the focus of Chapter 8. LArTPCs like MicroBooNE that observe point source-like fluxes of monoenergetic neutrinos (in the case they come from the NuMI beam dump) can use them to calibrate detector energy response and reconstruction.

2.5 Neutrino Flavor Identification and Reconstruction in LArTPCs

One of the biggest technical challenges in measuring neutrino cross sections is automated reconstruction and selection of signal interactions. LArTPCs provide unprecedented detail of information, but the fully-digitized data remains challenging to reconstruct. However, given the size of the datasets being collected by today's neutrino experiments, automated reconstruction and selection tools are the only practical path forward. Imperfect reconstruction and identification of neutrino flavor and interaction type affect both efficiency and purity of selections and impact the statistical significance of a measurement. ArgoNeuT, and now MicroBooNE, ICARUS, and soon SBND, are all simultaneously pursuing valuable physics programs while also acting as research and development environments for future detectors. In particular, the reconstruction of GeV-scale electron neutrino interactions in DUNE is critical to measuring δ_{CP} and inferring the neutrino mass ordering. Reconstruction tools that are being developed for currently operating LArTPC experiments will all be valuable foundation for DUNE to build on.

Significant progress is being made in developing the computer vision software required for deep learning-based event reconstruction [75–77], but data-based studies at the GeV-scale have been largely absent. Interpreting neutrino data has many challenges that can never be fully anticipated with simulation, so data-based studies in concert with high-statistics simulation are required. Chapters 3 and 4, describing the ν_e-argon cross section measured with ArgoNeuT data, discuss these challenges in detail and provides novel strategies for overcoming them that have since been adopted by other LArTPC experiments.

2.6 Experiments Making an Appearance

We'll visit the following experiments in the chapters to come. Provided here is a short introduction to the detectors and topics covered with each.

ArgoNeuT. ArgoNeuT was a small LArTPC that sat directly in front of the MINOS near detector in the NuMI beam and took antineutrino mode data for six months in 2009-2010. It was the first LArTPC deployed at Fermilab and has produced a wealth of physics results, including many neutrino on argon cross sections [78–83] and beyond the Standard Model searches [84, 85]. Though its run was short, ArgoNeuT has led the way in paving the landscape of neutrino-argon cross section measurements. It has also provided a wealth of insight into the calibration and reconstruction of TPCs, invaluable knowledge for future massive detectors like DUNE. Chapters 3 and 4 present the first measurement of the electron neutrino cross section on argon, with particular emphasis on challenges and strategies for reconstructing electron neutrino data from GeV-scale neutrino beams — the energy regime most critical to DUNE's primary physics goals. The reconstruction strategies put forth in Chapter 4 are now being adopted as part of reconstruction efforts in larger TPCs like MicroBooNE and DUNE, and ArgoNeuT's GeV-scale dataset is currently being used in combination with the cross section measurement reported here to validate deep learning-based reconstruction tools being designed for DUNE.

MicroBooNE. MicroBooNE is a school bus-sized (170-ton) LArTPC that is designed, along with the rest of the SBN Program (consisting of SBND, MicroBooNE, and ICARUS) to shed light on the low energy excess anomalies observed in both LSND [44] and MiniBooNE [45]. It began taking data in 2015. The LArTPC's unmatched ability to differentiate between electrons and photons using both topological and calorimetric information is critical in this task. It sits in line with the BNB and is also sensitive to off-axis flux from NuMI, which is used both for standalone physics measurements and validation of MicroBooNE forthcoming low energy excess results. MicroBooNE is also equipped with a cosmic ray veto, because it sits at surface-level rather than underground and observes significant cosmic background, and a PMT-based photon detection system. In particular, MicroBooNE is providing the first high statistics neutrino on argon scattering data and is quickly ramping up its cross section program. Chapter 5 will discuss the novel Wire-Cell tomographic reconstruction developed for MicroBooNE and its application to MicroBooNE's capstone low energy excess result. In particular, we focus on validation of the BNB-blinded electron neutrino selection using data from NuMI in a similar energy range. Additionally, we discuss the application of Wire-Cell's reconstruction toolkit on a broad range of novel cross section measurements (including a measurement of monoenergetic muon neutrinos from the NuMI beam dump).

SBND. The Short Baseline Near Detector (SBND) is a LArTPC deployed upstream of MicroBooNE in the BNB neutrino source. One of its primary goals is to empirically characterize the neutrino flux observed by MicroBooNE to reduce flux-related systematic uncertainties. SBND's photon detection system is comprised of a combination of more traditional PMTs and new ARAPUCA technology, which combines SiPM photon detectors with an efficient light-trapping device to increase the active area of the system. Chapter 6 will describe the hardware testing and development that has been done in the past five years for the SBND photon detection system, which is slated for installation later in 2021. As the near detector of the SBN Program, SBND will observe the largest flux of neutrinos, making it ideal for studying neutrino-argon interactions with high-statistics datasets. For example, in one year of exposure, SBND will record around 12,000 ν_e interactions, or six to seven times the number observed in MicroBooNE's full Run 1 dataset (also roughly one year of exposure) [86]. This ν_e data will provide a heretofore unprecedented sample on which to test and optimize electron neutrino reconstruction in LArTPCs. Not only will SBND reduce the systematic uncertainties on measurements made by MicroBooNE and ICARUS, it will, more generally, provide a wealth of neutrino interaction information across multiple inclusive and exclusive final state topologies that are extremely relevant to future DUNE physics on a target nucleus that has only recently entered the landscape of neutrino cross sections.

DUNE. The future Deep Underground Neutrino Experiment (DUNE) is a massive international collaboration with the goal of measuring the outstanding parameter governing neutrino behavior: the phase δ_{CP}. To that end, Chapter 7 will provide an overview of DUNE's physics goals and the wealth of prototype testing environments, like ProtoDUNE, being used to finalize the design of detector components for DUNE's far detector. It will focus on tests performed to quantify the performance of the now-nominal photon detector readout electronics, culminating in its integration with the small-scale ICEBERG LArTPC located at Fermilab.

MiniBooNE. The MiniBooNE experiment is an outlier in this list, but in many ways it is the natural predecessor to all the LArTPC-based experiments listed above. MiniBooNE was a mineral oil Cherenkov detector. 1280 PMTs surround the 12 m spherical tank to collect Cherenkov light from particles traversing the detector faster than the speed of light in that medium [87]. MiniBooNE, which began taking data in 2002, is most famous for its independent observation of a low energy excess in electron-like events after LSND reported the anomaly, and has since taken enough data to yield a 4.8σ excess over the Standard Model. MiniBooNE has also published limits on sub-GeV dark matter [88]. Like MicroBooNE, MiniBooNE sat in the BNB neutrino source, but was also less than 100 m from the NuMI beam dump. As such, it is subject to a large flux of monoenergetic muon neutrinos from kaon decay at rest in the dump. Chapter 8 will describe the first observation of these monoenergetic neutrinos.

CHAPTER 3

ArgoNeuT: Neutrinos in a Liquid Argon Time Projection Chamber

3.1 The ArgoNeuT Detector

The ArgoNeuT LArTPC experiment at Fermilab collected data in the NuMI beamline just upstream of the MINOS near detector [89] in 2009-2010, with the vast majority (1.25×10^{20} POT) taken in low-energy antineutrino mode ($\langle E_{\bar{\nu}_e} \rangle = 4.3$ GeV with 68% falling between 1.0 and 6.5 GeV and $\langle E_{\nu_e} \rangle = 10.5$ GeV with 68% falling between 2.5 and 21.5 GeV) [55]. ArgoNeuT was a $40 \times 47 \times 90$ cm^3 [vertical, drift, horizontal (beam)] TPC filled with 170 liters of active volume liquid argon. It operated with an electric field of 481 V/cm with 240 induction and 240 collection wires separated by 4 mm and sampled at a rate of 5 MHz by the readout electronics. The detector is described in detail in Ref. [90]. Neutrino interactions in ArgoNeuT are simulated using the GENIE [91] neutrino event generator in combination with GEANT4-based [92] detector and particle propagation models. Neutrino and antineutrino fluxes from the NuMI beam are provided by the MINERνA Collaboration [55]. (The MINERνA detector sat directly upstream of ArgoNeuT in the detector hall.) After event simulation, interactions in the ArgoNeuT detector are first reconstructed using the LArSoft software package [93]. The algorithms, described in detail in Ref. [82], proceed in the following steps: 1) noise removal and deconvolution of raw wire signals to correct for electronics and field response, 2) hit finding, 3) clustering of hits on each plane based on proximity to one another, 4) reconstruction of three-dimensional (3D) tracks by matching clusters across wire planes with temporal consistency, and 5) calorimetric reconstruction.

ArgoNeuT's placement in the MINOS near detector hall is shown in Figure 3.1. A more de-

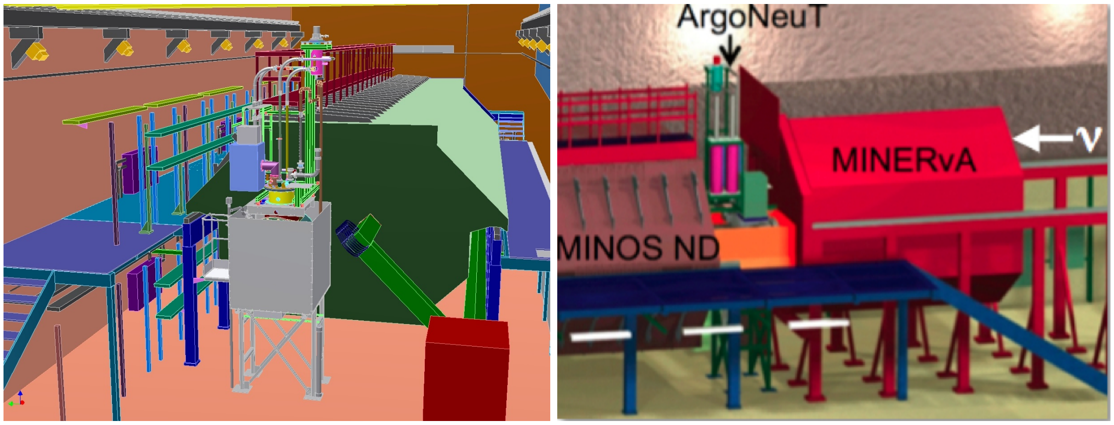

Figure 3.1: Illustrations of the MINOS near detector Hall. (left) ArgoNeuT (grey box) sat directly upstream of the MINOS near detector (green vessel), roughly centered on the NuMI neutrino beam. (right) The MINVERνA detector was installed upstream of ArgoNeuT while ArgoNeuT was completing its physics run. Images from Ref. [90].

tailed diagram is shown in Figure 3.2. The MINERνA detector was being installed in front of ArgoNeuT in the same beam line during a majority of ArgoNeuT's physics run. ArgoNeuT's nominal physics operating conditions are summarized in Figure 3.3. The POT collected from the NuMI beam as a function of time is shown in Figure 3.4.

3.2 The MINOS Detector

ArgoNeuT sat directly in front of the MINOS near detector [94]. MINOS was a magnetized steel/scintillator tracking calorimeter split into two halves. The upstream half was a calorimeter designed for hadronic energy reconstruction and vertex identification, while the downstream half was a muon spectrometer. The MINOS detector is shown in Figure 3.5. Most muons in ArgoNeuT enter the MINOS detector, and its magnetic field can be used to sign-select muon neutrino interactions. Alternatively, MINOS data can be used to filter muon neutrino charged current interactions from ArgoNeuT data when searching for electron neutrino interactions, as discussed in Chapter 4.

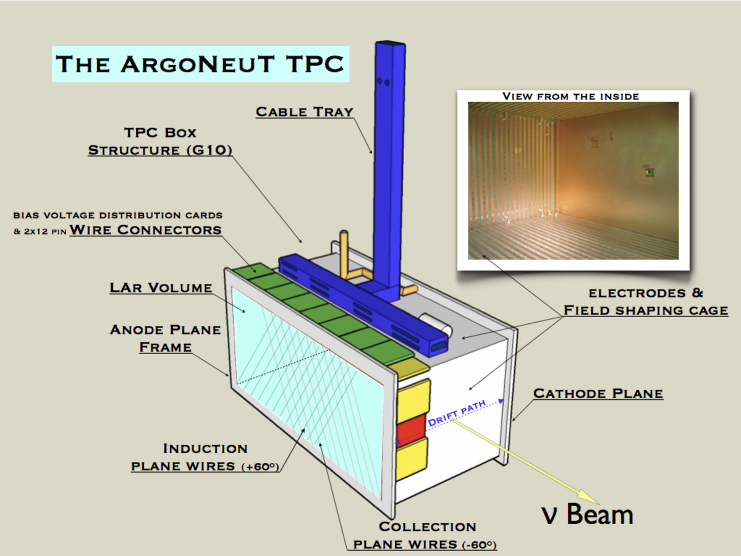

Figure 3.2: Diagram of the ArgoNeuT TPC. The insert shows the cathode plane inside the detector volume and the copper strips of the field cage. Image from Ref. [90].

TPC dimensions	$40\ h \times 47\ w \times 90\ l$ cm^3
TPC (active) volume	170 liters
Max. Drift Length (TPC width)	$\ell_d = 470$ mm
# of wire-planes	3 (2 instrumented - I, C)
Interplane gaps width	$\ell_g = 4$ mm
Wire pitch (normal to wire direction)	$\delta s = 4$ mm (all planes)
Wire Type	Be-Cu Alloy #25, diam. 152 μm
# of wires (total)	705
Shield plane (S)	225 (non-instrumented)
Induction plane (I)	240 (instrumented - w-index: n_w^I)
Collection plane (C)	240 (instrumented - w-index: n_w^C)
Wire Orientation (w.r.t. horizontal)	90^o, $+60^o$, -60^o (S, I, C)
Non-destructive Configuration	EF nominal (Transparency Ratio)
Drift volume	$E_d = 500$ V/cm
S-I gap	E_{g1}=700 V/cm ($r_T = 1.4$)
I-C gap	E_{g2}=900 V/cm ($r_T = 1.3$)
Drift Velocity (at nominal field)	1.59 mm/μs
Max. Drift Time (at nominal field)	$t_d = 295$ μs

Figure 3.3: Nominal specifications and features in ArgoNeuT. Operational values differed slightly after further experimental optimization during the physics run. Table from Ref. [90].

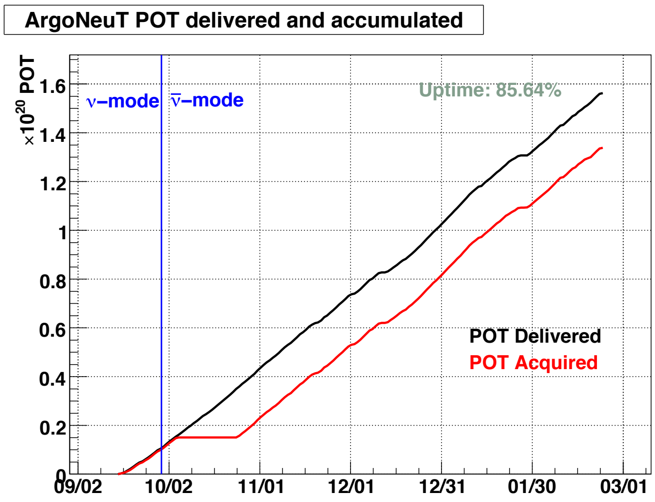

Figure 3.4: Delivered and accumulated POT during the ArgoNeuT physics run as a function of time. The ∼2-week downtime in October was the result of a commercial component failure in the cooling system. Plot from Ref. [90].

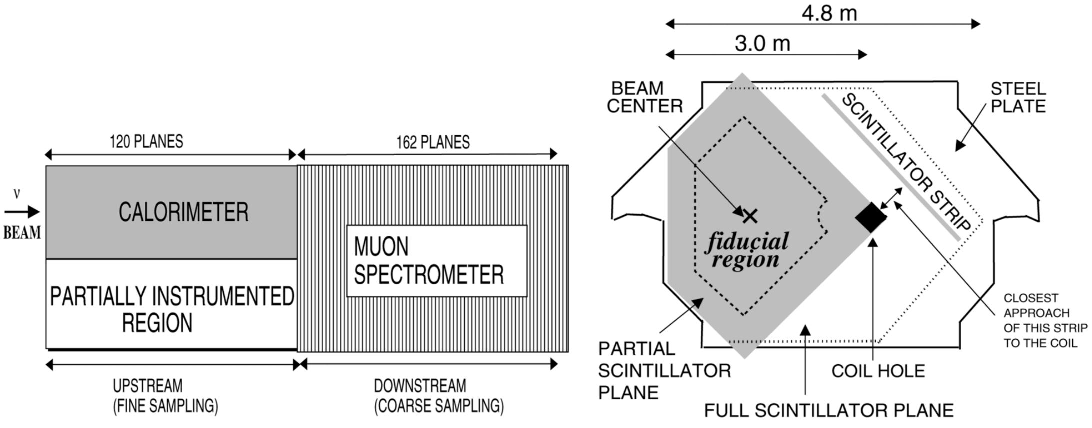

Figure 3.5: The MINOS near detector. Images from Ref. [90].

3.3 Physics in ArgoNeuT

ArgoNeuT has had a fruitful physics program, despite its short run time. A decade after the detector was decommissioned (it has now been repurposed as the LArIAT detector) it is still producing novel new physics measurements and limits. ArgoNeuT successfully characterized the recombination response of a LArTPC [64] and produced the first charged current inclusive muon neutrino cross sections on argon [78, 79], in addition to several exclusive final state topologies [80, 82]. Recently, ArgoNeuT pioneered techniques for studying MeV-scale physics in LArTPCs [84], including setting new limits on millicharged particles [85]. Finally, ArgoNeuT achieved several milestones in identifying and reconstructing neutrino-induced electrons and photons in LArTPCs: 1) a measurement of neutral current $\pi^0 \to \gamma\gamma$ production, 2) the first observation of electron neutrinos and rejection of photons backgrounds using vertex topology and calorimetry in the GeV regime [95], and 3) the first measurement of the electron neutrino cross section on argon, the subject of the next chapter [83]. Currently, ArgoNeuT is being used to develop a deep learning-based region-of-interest (ROI) finder for raw wire waveforms with very promising results. A beyond-the-Standard-Model search for heavy neutral leptons with dimuon signatures is also in preparation for publication.

CHAPTER 4

First Measurement of the Electron Neutrino Scattering Cross Section on Argon[1]

4.1 Motivation

While neutrino mass and mixing has enjoyed a bounty of rich discoveries over the past few decades, a number of questions remain. Most notably, the ordering of the neutrino mass states, the value of the CP-violating phase (δ_{CP}), and the possibility of new degrees of freedom driving oscillations (e.g. $\nu_{e,\mu,\tau} \to \nu_s$), are still mysterious. Electron neutrino identification and characterization is essential to the $\nu_\mu \to \nu_e$ and $\overline{\nu}_\mu \to \overline{\nu}_e$ appearance based short- and long-baseline experiments seeking answers to these questions. The precision required for these subtle measurements calls for high-resolution detection techniques, including liquid argon time projection chamber (LArTPC) technology, which is currently being pursued by the SBN Program at Fermilab [96], seeking to study the possibility of a sterile flavor participating in oscillations, and DUNE [97], seeking to determine the neutrino mass hierarchy and extract δ_{CP}.

Despite their importance for completing the mixing picture and searching for beyond-Standard-Model physics with accelerator-based neutrinos, the hundreds-of-MeV and GeV-scale $\nu_e/\overline{\nu}_e$ present in these experiments are difficult to reconstruct[2]. Even with LArTPC technology and its ability to provide mm-scale-resolution pictures of the events in question, the density of stereoscopic position and calorimetric information in these images, often including multiple and overlapping

---

[1] The work presented in this chapter was published in the following paper: *Phys. Rev. D* **102** 011101(R) (2020) [83]. R. S. Fitzpatrick is the corresponding author. The text here is adapted from an internal note describing the analysis that was written by R. S. Fitzpatrick.

[2] For simplicity and because ArgoNeuT cannot distinguish between electron-flavor neutrinos and antineutrinos, ν_e will be used to refer to both ν_e and $\overline{\nu}_e$ in this chapter.

tracks and showers, decays, missing energy due to neutrons, and other complications, makes hit and cluster finding, shower formation, and finally neutrino energy reconstruction and flavor identification an enormous challenge. This is particularly true for DUNE, which will rely on the inclusive set of all ν_e charged current (CC) events [97], rather than an exclusive CC quasi-elastic-like, signal channel in the few-GeV energy range, with substantial contributions from the varying event topologies associated with quasi-elastic, resonant, and deep inelastic scattering, and significantly affected by nuclear physics, including multi-nucleon correlations and final state interactions. Background presents a difficulty as well: even for underground detectors with low or negligible cosmic contamination, the electromagnetic showers characteristic of ν_e CC events are readily mimicked by numerous neutrino-induced background processes, especially $\nu_\mu/\overline{\nu}_\mu$ CC and neutral current events featuring $\pi^0 \to \gamma\gamma$ and $\Delta \to \mathrm{N}\gamma$ (with a branching ratio of 0.55-0.65% [42]) production.

These energy reconstruction and background issues directly affect oscillation measurements. For example, while DUNE is expected to be statistics-limited early on with exposures less than 100 kt·MW·year, energy-scale, flux, and interaction model systematic uncertainties will quickly take the lead in the δ_{CP} measurement uncertainty budget [97]. Although significant progress has been made in building the computer vision software required for the multi-layered and extensive task [75–77] on the way to efficient electron-flavor reconstruction with minimal background in LArTPC neutrino experiments, data-based studies at the GeV-scale are largely absent.

Traditional exclusive quasi-elastic-like ν_e CC searches have relied on calorimetric and topological information near the neutrino interaction vertex to distinguish electron neutrino interactions from photon-producing background processes [95, 98], but an inclusive selection strategy must expand the scope of these techniques to include information about the entire electromagnetic shower.

4.2 Electron Neutrinos in ArgoNeuT

ArgoNeuT expected to observe roughly 100 ν_e CC interactions in the six months of data collected by the detector. These neutrinos have energies that peak in the few-GeV region most relevant to DUNE oscillation physics. The neutrino flux at the ArgoNeuT detector from NuMI and the energy spectrum of electron neutrinos observed by ArgoNeuT in antineutrino mode are shown in Figure 4.1.

Previously, ArgoNeuT demonstrated that topological information alone could be used to identify electron neutrino candidates by rejecting gamma backgrounds based on the characteristic gap expected between the neutrino interaction vertex and the beginning of a gamma-induced shower due to the large (relative to LArTPC spatial resolution) conversion length of 18 cm in liquid argon [95]. It was further shown, using samples of events selected by visual scanning methods containing either an electron or gamma candidate, that vertex dE/dx could be used to separate electrons from gammas, a notable milestone in LArTPC reconstruction for exploiting the wealth of charge and spatial detail provided by the technology. However, these strategies are quickly complicated by interactions with high multiplicity where hadronic overlap with EM showers can obscure the essential gap and dE/dx information close to the vertex. This analysis expands upon that work with the development of an automated electron neutrino selection designed to incorporate charge and topological information from the full reconstructed shower to better handle higher energy interactions where deep inelastic scattering is prominent and can obscure vertex information despite the high resolution of LArTPC detectors. At the time this work was published, the electron neutrino cross section had never been measured before on argon. Recently, MicroBooNE published its first measurement of the ν_e cross section on argon, also with NuMI (off-axis) data [99].

4.3 Reconstruction

The reconstruction in this analysis consists of two parts. First, standard LArSoft [93] reconstruction is used to identify hits, clusters, and 3D tracks in each event. Then, a custom shower reconstruction algorithm builds candidate shower objects from the reconstructed tracks and clusters within each ArgoNeuT event.

4.3.1 Standard Reconstruction

The first step in the reconstruction for this analysis is standard to many prior ArgoNeuT analyses and is described, most recently, in Ref. [82]. Here we provide a brief overview of the steps in stan-

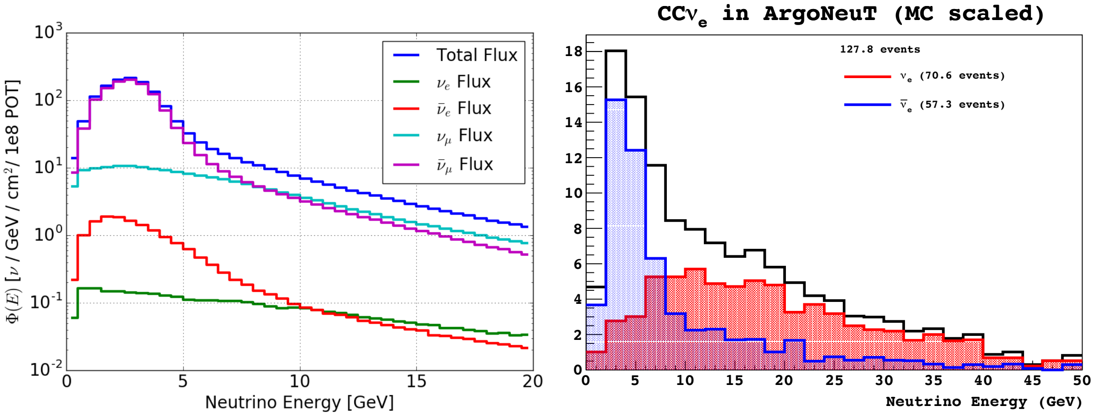

Figure 4.1: (left) The neutrino flux at the ArgoNeuT detector in antineutrino mode. Figure from Ref. [95]. (right) The spectrum of electron neutrino energies for charged current electron neutrino interactions observed by ArgoNeuT in antineutrino mode, POT-scaled to data. Note that this plot was generated using the fiducial volume (in cm) $3 < x < 44, -16 < y < 16, 6 < z < 86$. The analysis uses $6 < z < 70$ cm (see Section 4.4.2 for details).

dard reconstruction, highlighting the components that are most critical to the subsequent shower reconstruction.

Noise Filtering and Deconvolution. First, noise filtering is applied to raw wire signal. After noise filtering deconvolution removes electric field effects and the electronics response. Unique to this analysis is the addition of coherent noise filtering, which is employed to remove noise in data that is correlated to each electronic readout board. Each correlated channel group consists of 24 channels. There are ten channel groups on each plane. The channels in each channel group are mapped to adjacent readout channels (i.e. channels 0-23 are one, 24-47 another, etc.). In addition, signal protection is included to ensure that very flat tracks do not get inadvertently subtracted out of the event. Hits with > 6 (6) ADC on the collection plane and > 4 (6) ADC on the induction plane in data (MC) are masked from being included in the coherent noise calculation.

Hit Finding. To reconstruct hits the GausHitFinder module is used to fit Gaussians to the deconvoluted wire signals.

Clustering. Next, clusters of hits are reconstructed on each wire plane by the TrajCluster algorithm [100] based on proximity of hits to one another. Additionally, TrajCluster tags each cluster as "track-like" or "shower-like" based on the MCS (multiple Coulomb scattering) momentum measured for the cluster and the proximity of the cluster to other clusters.

3D Track Building. Finally, three-dimensional tracks are constructed using the Projection Matching Algorithm (PMA) [101] which takes as input the clusters generated by TrajCluster. PMA assigns a vertex and direction to each track, which is used to define the vertex and direction of subsequently reconstructed showers (see Section 4.3.2).

Calorimetry Calibration. The measured pulse area (ADC) observed on wire channels in the detector must be converted to charge via a scale factor that is measured using known-energy through-going muons. The conversion factor in data is found using muons tagged by the MINOS detector, which possesses a magnetic field that can be used to accurately measure muon momentum. The MC and data calibration are done using the methods (and the same tools, in fact) that had been used previously to recalibrate the constants. They are summarized below:

- **MC:** We generate a sample of 10k 8 GeV muons and tune the calibration constant such that the most probable value is 1.75 MeV/cm. The resulting proton dE/dx vs residual range on the collection plane is shown in Figure 4.2.

- **Data:** We find well-matched muons in MINOS and use MINOS information to determine the muon momentum. dE/dx is measured immediately prior to the track exiting the detector. The calibration constant is tuned such that measured dE/dx matches expectation as a function of energy with the data separated into 1 GeV bins. The result for the collection plane (the only plane from which charge information is used), in data is shown in Figure 4.2.

4.3.2 Shower Reconstruction

The shower reconstruction algorithm used in this analysis is designed to reconstruct electrons. While the subsequently described selection procedure could be applied to any population of electron neutrino candidate events with photon contamination, we focus here on reconstructing only the leading shower in each neutrino interaction in ArgoNeuT. Particularly, we rely on the reliable three-dimensional track reconstruction by TrajCluster and PMA for defining the vertex and direction of a shower candidate. The shower reconstruction builds candidate electron showers around

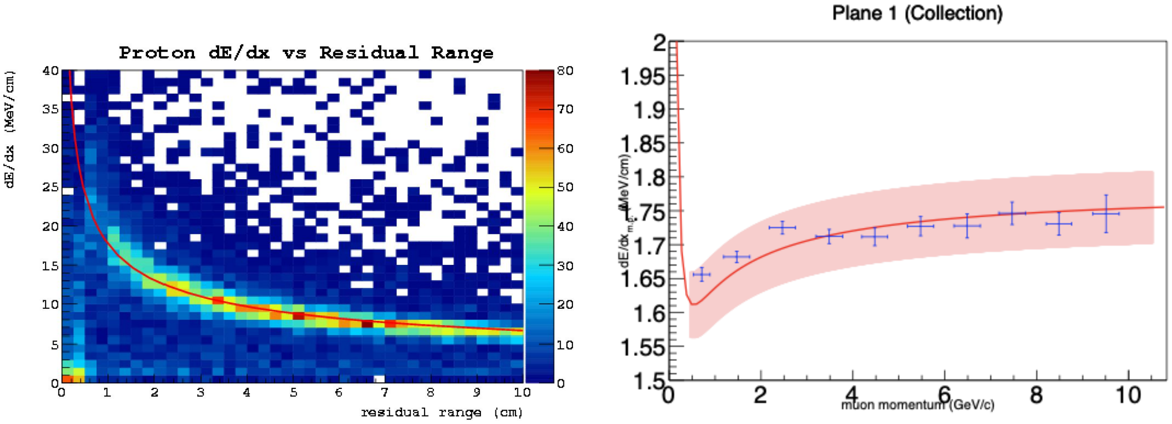

Figure 4.2: (left) Proton dE/dx vs residual range in MC after calibration. The expected distribution is indicated by the red curve. (right) dE/dx vs muon momentum in data. The expected distribution in shown in red.

reconstructed 3D tracks by looking for shower-like clusters of hits in close proximity to the track axis; the hit and proximity thresholds for finding candidate showers were optimized to maximize reconstruction completeness, purity, and efficiency for electrons specifically.

First, tracks are sorted into "long" and "short" groups ($<$ 20 cm, $>$ 20 cm) and then by z position within each group such that the upstream-most long tracks are at the top of the list. In ArgoNeuT, this takes advantage of the fact that photons, which may also be present in the events being reconstructed, typically start further downstream than electrons given the neutrino energies observed in ArgoNeuT and the characteristic gap between the interaction vertex and the start of the photon shower in LArTPCs. For each track, the number of shower-like hits contained in shower-like clusters in close proximity to the track axis is counted. The maximum distance is a progressive threshold determined by the length of the candidate electron track. If the number of shower-like hits exceeds a threshold (again, this threshold is progressive and defined based on the length of the track), the track and the additional clusters are considered to be a "shower candidate". Additional requirements include: even distribution of shower-like hits around the track, exclusion of shower-like clusters near the vertex of the track, and exclusion of shower-like clusters upstream of the track vertex.

If a candidate shower is found, a second round of hit/cluster selection is done to add missed clusters (that failed to be tagged as "shower-like" by TrajCluster) and unclustered hits to the candidate shower in order to catch charge contributions potentially missed in earlier reconstruction

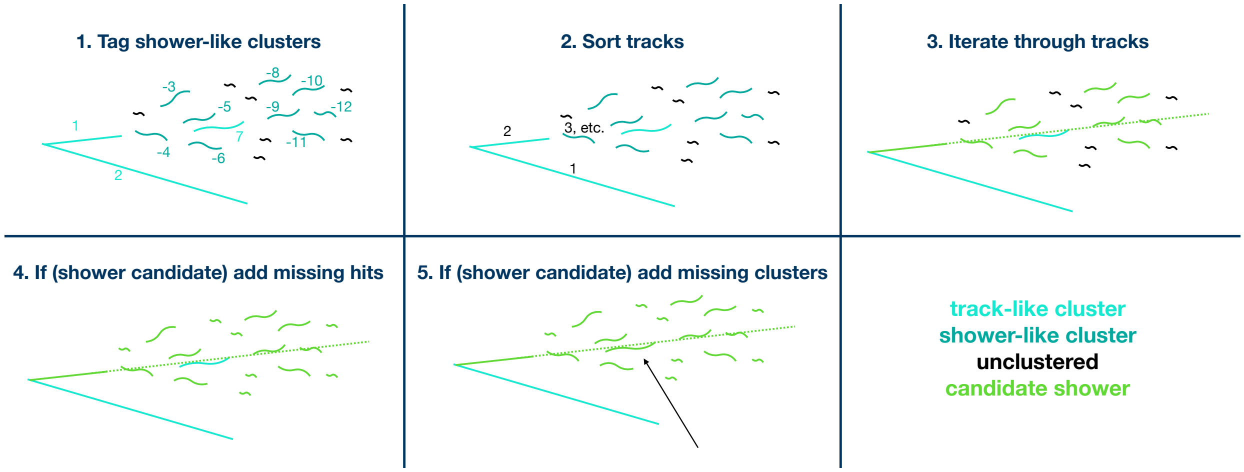

Figure 4.3: An illustration of the shower reconstruction algorithm used in ArgoNeuT, which builds on information reconstructed by TrajCluster and PMA.

steps. The algorithm halts after finding the first shower in an event. A cartoon diagram illustrating this reconstruction procedure is shown in Figure 4.3. The shower vertex and direction are defined as the vertex and direction of the candidate electron track produced by PMA around which the shower was constructed.

The shower-like tag is assigned to a particular 2D cluster based on whether it complies with a set of TrajCluster thresholds defined by the user. The decision takes into account the number of hits in the 2D cluster, the measured MCS momentum of the cluster, and its proximity to other clusters. The threshold for each of these parameters was optimized for ArgoNeuT using a combination of hand scanning and maximizing shower completeness, purity, and reconstruction efficiency for a large sample (∼1000) simulated ν_e interactions.

In addition, while the "shower-like" tag is used to determine which hit clusters can be used in the initial formation of candidate showers, a second round of hit selection occurs after a candidate shower has been deemed viable to further add missing hits — typically unclustered to begin with or mis-identified as track-like. Whether to include hits during this second iteration of hit selection is determined based on number of clustered hits and proximity to the candidate shower vertex and axis.

4.3.3 Reconstruction Performance

The efficiency of the shower reconstruction algorithm on a sample of simulated ν_e CC-only interactions as a function of neutrino and electron energy is shown in Figure 4.4. In relying on the vertex and direction information provided by PMA, we take advantage of the high resolution reconstructed position information that PMA can provide. The vertex and and direction reconstruction performance of reconstructed showers is also shown in Figure 4.4. It should be noted that no quality cuts are applied to the entries to these plots, so they include all attempts at reconstruction in ν_e CC interactions, including easily identifiable failures of reconstruction often due to track reconstruction failures. The quality cuts described in Section 4.4.2 aim to mitigate many reconstruction failures. The completeness and purity of these reconstructed electron showers is shown in Figure 4.5, where completeness is defined as the fraction of energy in the simulated electron shower included in the reconstructed shower. Purity is defined as the fraction of energy in the reconstructed shower contributed by the true simulated electron.

It is worth examining the makeup of the candidate showers reconstructed by this algorithm. As noted, we did not seek to design a generic electromagnetic shower reconstruction algorithm. Rather, we have intentionally designed an algorithm that reconstructs electrons well but does not necessarily perform well for the reconstruction of photons for a variety of reasons. The purity and completeness of the objects deemed "candidate showers" are shown in Figure 4.6. In the figure a shower candidate is labeled to be the simulated particle that contributes the largest fraction of energy to the reconstructed shower candidate. Most notably, when an electron is reconstructed the reconstructed object tends to be very pure in electron hits. That is, the electron is well reconstructed. However, other reconstructed objects, or backgrounds in this analysis, tend to be poorly reconstructed and often come from neutrino interactions with a significant number of particles produced. With that in mind, we must think about rejecting background as a process for rejecting interaction channels (e.g. CC/NCπ^0) in addition to being a process for rejecting interactions based on a particular particle (e.g. a single photon present in an interaction). That said, a short discussion of the electron/gamma separation power of the methods described in this note is provided in Section 4.5.5.

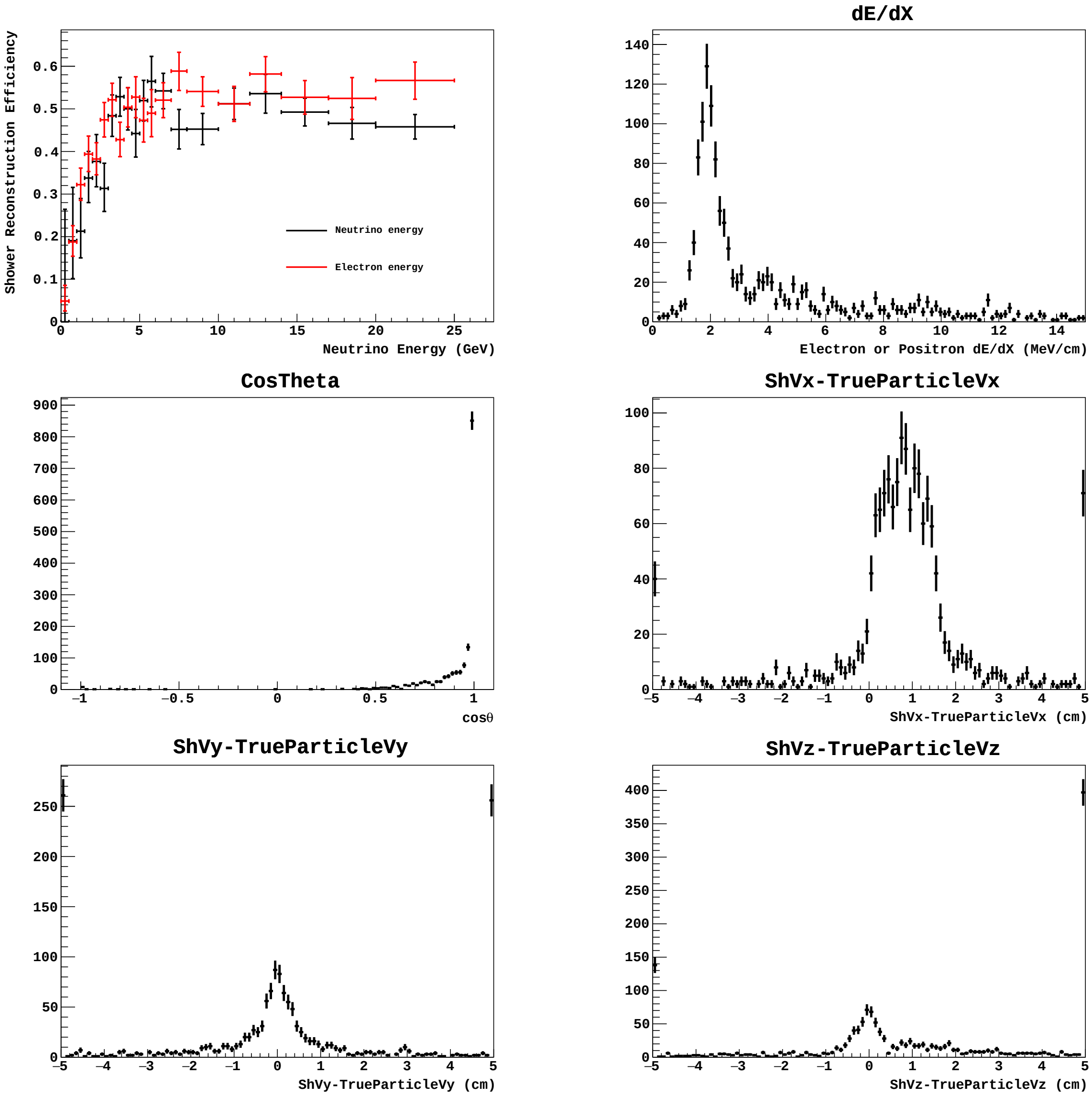

Figure 4.4: The performance of the shower reconstruction on a sample of three thousand simulated ν_e interactions including (top left) The efficiency of the shower reconstruction algorithm as a function of neutrino and electron energy, (top right) the dE/dx measured as the median charge in the first for cm of reconstructed showers, (middle left) the cosine of the angle between the true and reconstructed electron, and the difference between the reconstructed and true electron vertex in (middle right) x, (bottom left) y, and (bottom right) z. No additional quality cuts were applied to mitigate known failure modes.

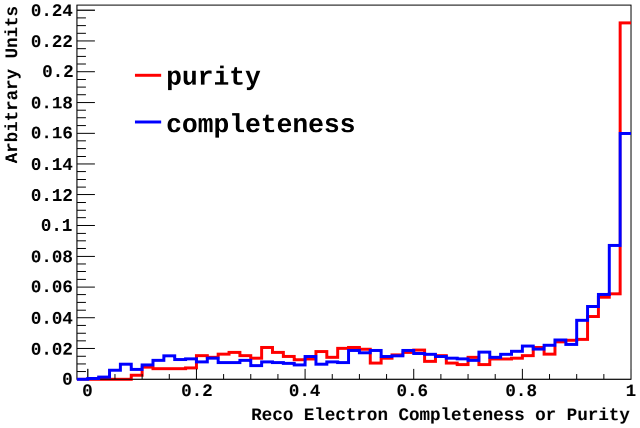

Figure 4.5: The purity and completeness of reconstructed electron showers from a sample of ν_e interactions. Completeness is defined as the fraction of energy in the simulated electron shower included in the reconstructed shower. Purity is defined as the fraction of energy in the reconstructed shower contributed by the true simulated electron.

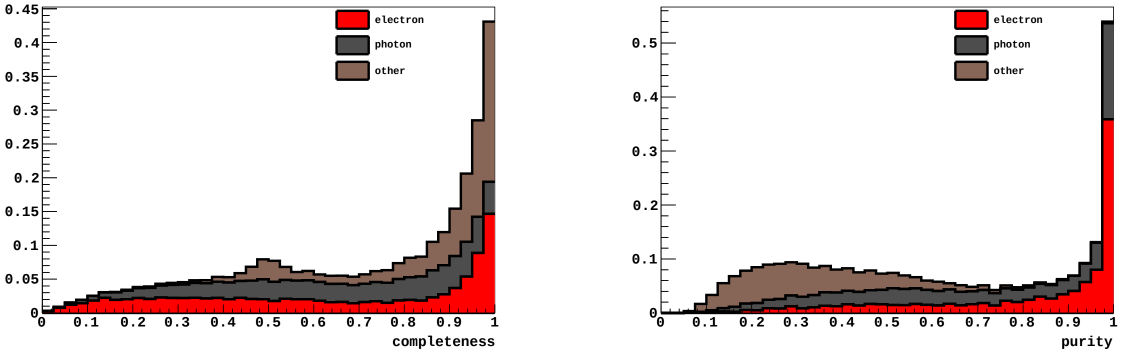

Figure 4.6: The (left) completeness and (right) purity for shower candidates reconstructed in all MC interactions including both signal events (ν_e CC) and backgrounds (primarily NC π_0 and external backgrounds with EM activity), labeled by the MC particle that contributes the largest fraction of energy to the reconstructed object.

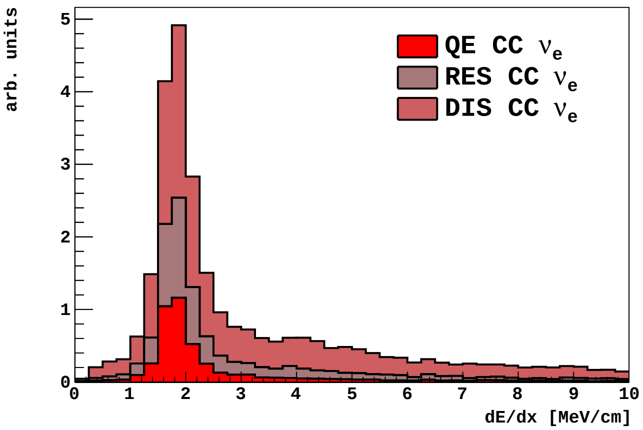

Figure 4.7: The distribution of dE/dx for electron showers reconstructed in a sample of simulated ν_e events, broken down into interaction channels. We can demonstrate that this tail is almost entirely composed of deep inelastic scattering interactions with messy vertices, further motivating the need to use more extensive topological information to select electron neutrinos.

4.3.4 Reconstructed dE/dx

The dE/dx for each shower is measured by taking the median charge collected in the first 4 cm of the track constructed by PMA. This is consistent with one of the methods described in [95]. However, it is worth noting that previous ArgoNeuT analyses of vertex dE/dx for electromagnetic showers relied on hand selected hits near the vertex of the shower. The distribution of dE/dx for electrons reconstructed in ArgoNeuT is shown in Figure 4.7, which includes a breakdown into quasi-elastic, resonant, and deep inelastic scattering channels. The figure illustrates that the tail to high dE/dx is comprised almost entirely of deep inelastic scattering events, where there is significant activity around the neutrino interaction vertex, obscuring the electron hits.

4.4 ν_e Charged Current Selection

The selection of ν_e CC interactions proceeds in three steps. First, an anti-MINOS filter is applied to reject a significant portion of the ν_μ CC interactions that produce muons which can be detected by MINOS. Second, a set of cuts is applied to remove reconstruction failures and to handle several known differences between data and MC. Finally, a boosted decision tree is used to classify candidate showers as electron-like or background-like. Each component of the selection is discussed in detail below.

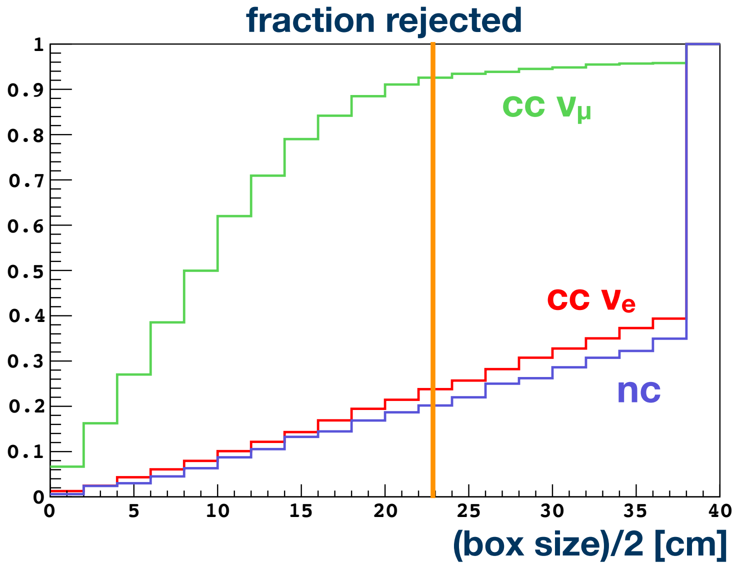

Figure 4.8: The fraction of events rejected (based on true vertex information) for a box centered in the detector. The current cut sits at ∼23 cm (the detector is not an exact square, so this plot illustrates an approximate model). The volume in z is always $0 < z < 90$ cm.

4.4.1 Anti-MINOS Filtering

To reject ν_μ CC events, we project tracks in MINOS backward toward ArgoNeuT and check if the track crosses within the volume defined by $3 < x < 44, -16 < y < 16, 0 < z < 90$ (cm) in the ArgoNeuT detector. If any MINOS track crosses this volume in ArgoNeuT, the event is rejected. This was demonstrated to be more effective than matching ArgoNeuT tracks to MINOS before rejecting an event (i.e. we're not interested in only rejecting "golden muons", we want to reject all ν_μ CC interactions). A toy model (in which the detector is square in x and y) was used to determine the optimal rejection volume in the x, y plane. The result is shown Figure 4.8 along with the approximate volume, which lies 3 cm inside the edge of the detector in the x, y plane.

4.4.2 Basic Cuts

The following cuts are applied to both data and MC prior to performing a multivariate analysis. They are designed to improve agreement between data and MC and remove obvious reconstruction failures.

- **fiducial volume:** The candidate shower vertex must be within the volume defined by (in cm) $3 < x < 44, -16 < y < 16, 6 < z < 70$. We require that the z vertex be at least 20 cm from the back of the detector to give candidate electrons enough space to begin exhibiting shower-like qualities, motivated by the 14 cm interaction length in argon.

- **shower angle:** $\cos(\theta_z) > 0.05$. The area-normalized distribution of shower z angle for data and MC is shown in Figure 4.9. While we acknowledge that there may exist backward-going electron showers in the data, we accept this negligible loss of phase space in favor of improving the agreement between data and MC and reducing the external background contribution.

- **nearest $z > 2.5$:** To reject events with through-going particles in data, we remove events with clusters of hits < 2.5 cm from upstream face of the detector. The area-normalized data and MC distributions for the "nearestz" variable are shown in Figure 4.9. This cut was initially defined in [102]; the value has been updated slightly for this analysis based on Figure 4.9.

- **vertex-hit minimum distance:** We require that closest shower hit on each plane be within 2 cm of the 3D reconstructed vertex projected onto that plane. This removes track reconstruction failures typically due to a failure to accurately match clusters between planes. The distribution of the vertex-hit minimum distance is shown in Figure 4.10 along with a typical failure of this kind.

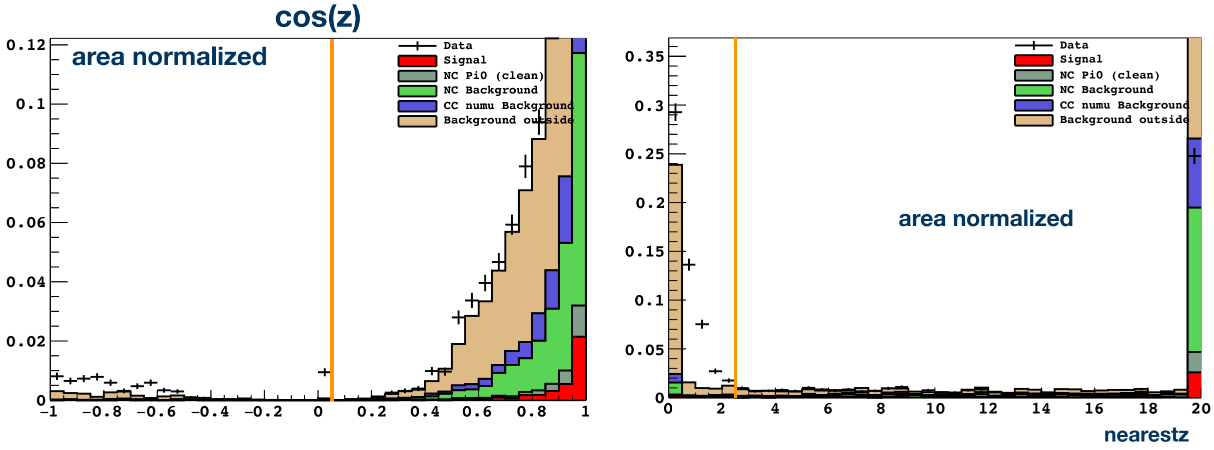

Figure 4.9: (left) The area normalized distribution of $\cos(\theta_z)$ in data and MC. A cut is placed such that candidate showers must have $\cos(\theta_z) > 0.5$. (right) The area normalized distribution of the nearest z variable in data and MC. A cut is placed at such that no event can have a cluster within 2.5 cm up the upstream face of the detector to reduce through-going backgrounds in data.

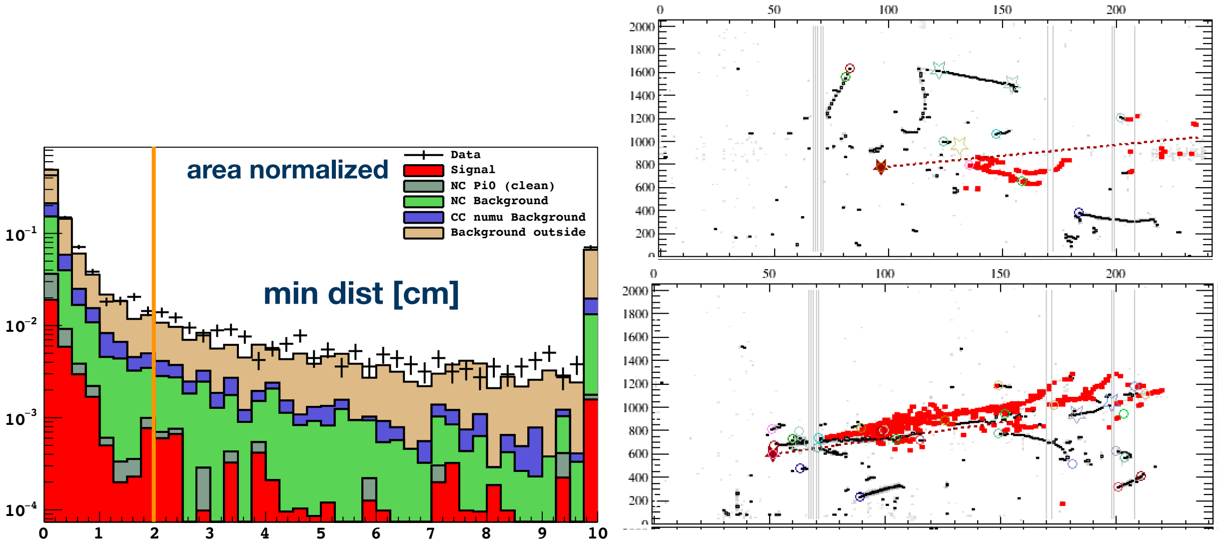

Figure 4.10: (left) The minimum distance between a candidate shower hit and the 3D candidate shower vertex projected onto the collection plane. A cut is placed such that this value must be less than 2 cm on both planes to remove failures of track matching. (right) A typical reconstruction failure removed by the minimum distance cut. The vertex reconstructed by PMA is indicated on both planes by the red star. The hits selected as part of the candidate shower are highlighted in red.

4.4.3 Boosted Decision Tree

The calorimetric discrimination techniques described here could be applied to any reconstructed shower object, independent of the reconstruction algorithm. We simply assume a reconstructed shower contains 1) a collection of hits on at least one plane, 2) a vertex, and 3) a direction. In ArgoNeuT lack of containment prohibits the use of absolute charge for characterizing electrons. Instead, we have adapted these concepts to use charge-normalized quantities. Topological regions of charge are defined as shown in Figure 4.11 which can then be used to define ratios of charge that characterize the shape of each candidate shower. For example, we can model the longitudinal development of the shower by defining the ratios $Q_n / \sum Q_i$ where $n = 1, 2, 3, 4$. Similarly, the transverse shower development can be modeled with $Q_{\text{core}}/Q_{\text{shower}}$. Such ratios have been shown to be powerful discriminators for categorizing ν_e CC events when used along with vertex dE/dx as inputs for multivariate classification tools like boosted decision trees (BDTs).

Input Variables. The following quantities are used as input for the boosted decision tree. All charge variables are defined using the collection plane only.

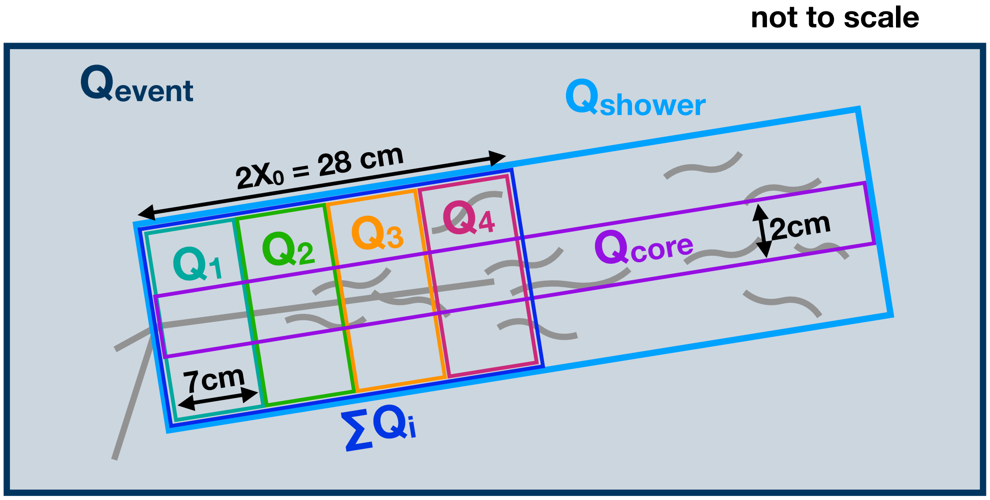

Figure 4.11: The topological charge regions defined for each reconstructed shower, intended to characterize the transverse and longitudinal development of the reconstructed shower.

- three angles ($\cos(\theta_x), \cos(\theta_y)$, and $\cos(\theta_z)$)
- dE/dx (collection plane)
- $Q_{\text{shower}}/Q_{\text{event}}$ (collection plane)
- $\sum_i Q_i/Q_{\text{shower}}$ (collection plane)
- $Q_{\text{core}}/Q_{\text{shower}}$ (collection plane)
- $Q_1/\sum_i Q_i$ (collection plane)
- $Q_2/\sum_i Q_i$ (collection plane)
- $Q_4/\sum_i Q_i$ (collection plane)[3]

The distance between the neutrino vertex and EM shower start is not used in this analysis for signal identification; the high neutrino energies and resulting large track multiplicities complicate automated gap reconstruction, yielding weak separation power between electrons and gammas.

Area-normalized comparisons between signal and background in MC for each of these variables can be seen in Figures 4.12 and 4.13.[4] Data/MC comparisons with final POT and background

---

[3] NB: $Q_3/\sum_i Q_i$ is not used because it provides no additional separation power when used in combination with the other quantities on this list.

[4] The shower vertices are included in Figure 4.13 for completeness but are not used to train the BDT.

scaling are shown in Figures 4.14 and 4.15 (see Section 4.5.1 for details on background scaling). The correlations between each variable in signal and background samples is shown in Figure 4.16.

BDT Performance. The distribution of BDT scores for signal and background are shown in Figure 4.17. The distribution of BDT scores in data is shown in Figure 4.18 along with the selection significance, adjusted to included a 20% systematic uncertainty in the background, motivated primarily by the known limitations in the model of backgrounds produced outside the cryostat (see Section 4.5.1 for details). The variables are ranked in importance toward the final selection as follows (from most important to least): $Q_{\text{shower}}/Q_{\text{event}}$, $Q_{\text{core}}/Q_{\text{shower}}$, dE/dx, $Q_1/\sum_i Q_i$, $\cos(\theta_y)$, $\sum_i Q_i/Q_{\text{shower}}$, $Q_4/\sum_i Q_i$, $Q_2/\sum_i Q_i$, $\cos(\theta_z)$, $\cos(\theta_x)$.

The BDT is performing two jobs: 1) it is selecting well reconstructed electrons from the events passing all pre-selection cuts, and 2) it is rejecting reconstruction failures that don not look like any kind of real EM shower. The second role is the reason the inclusion of all topological variables performs so much better than just using dE/dx. The vertex dE/dx measure has no sense of whether or not the reconstructed object itself resembles a real electromagnetic shower, instead of just being a collection of track-like and shower-like energy deposits that have been grouped together erroneously.

Given the difficulty of reconstructing EM activity in LArTPCs and in particular for DIS interactions, the reconstruction was designed to be open to producing a large number of failures in favor of increasing the efficiency of reconstructing the signal channel as much as possible, knowing that the BDT itself would be able to distinguish between a well-reconstructed object and a reconstruction failure in addition to distinguishing between well-reconstructed objects. A discussion of the BDT inputs and performance as a function of ν_e interaction mechanism (quasielastic, resonant pion production, and deep inelastic scattering) is included in Appendix B.

4.4.4 Summary of Selection Impact

A summary of the impact of each cut on the selection is shown in Table 4.1. The values are normalized to data POT but do not include the additional external background correction described in Section 4.5.1.

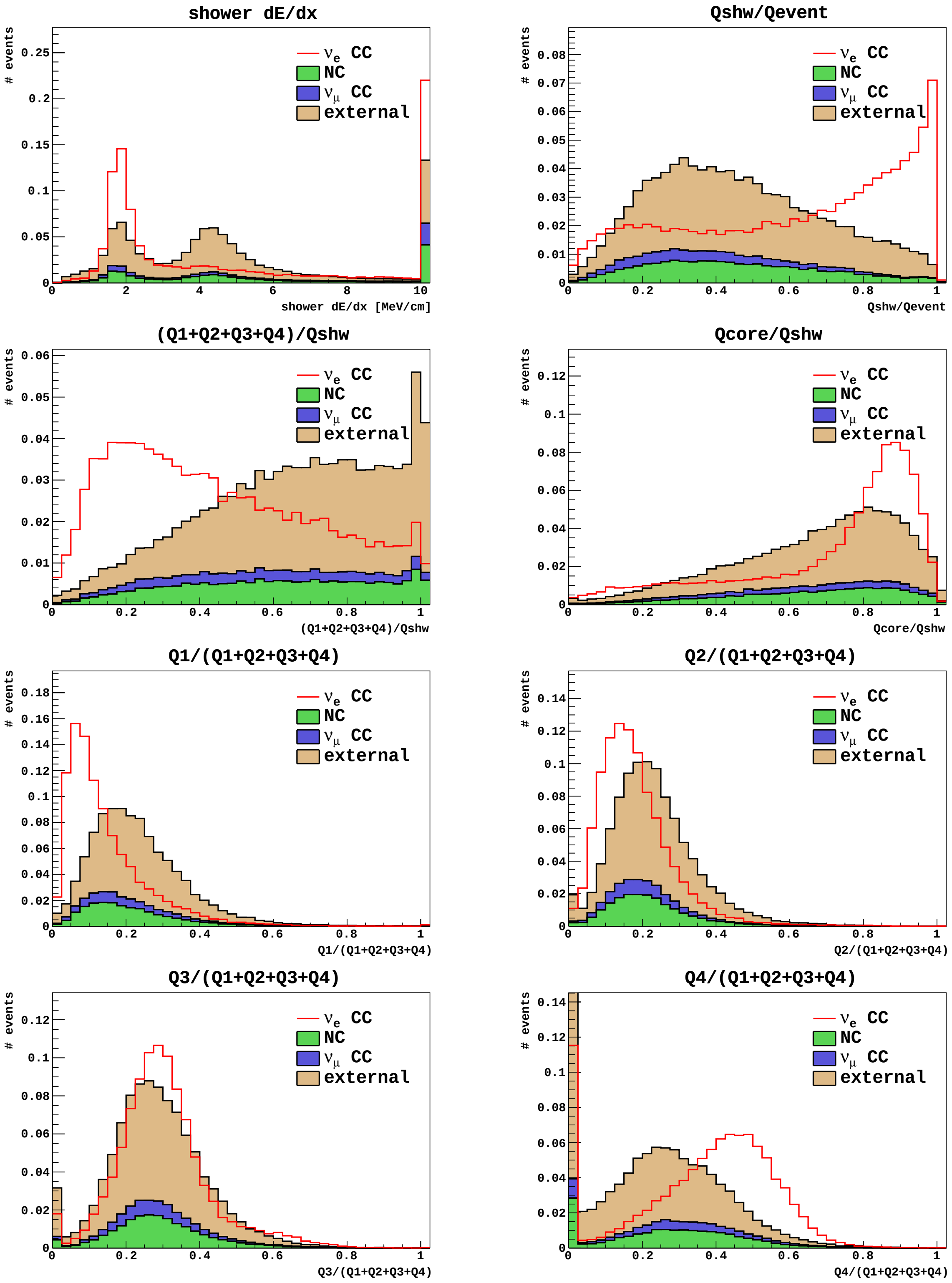

Figure 4.12: Area normalized distributions comparing candidate shower charge and topological variables. Note that an additional reweighting is applied to the outside background, as described in Section 4.5.1.

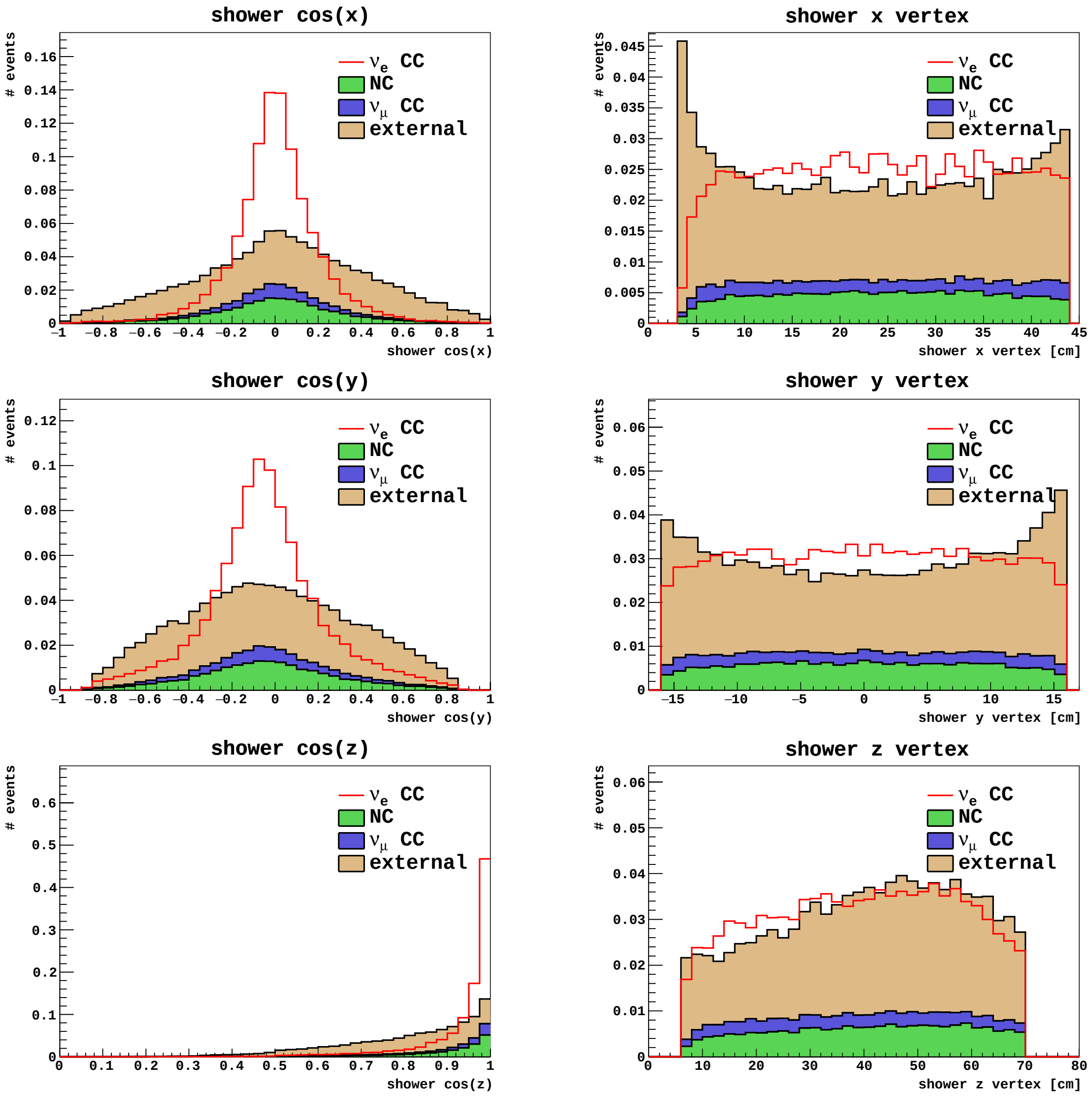

Figure 4.13: Area normalized distributions comparing candidate shower charge and topological variables. Note that an additional reweighting is applied to the outside background, as described in Section 4.5.1.

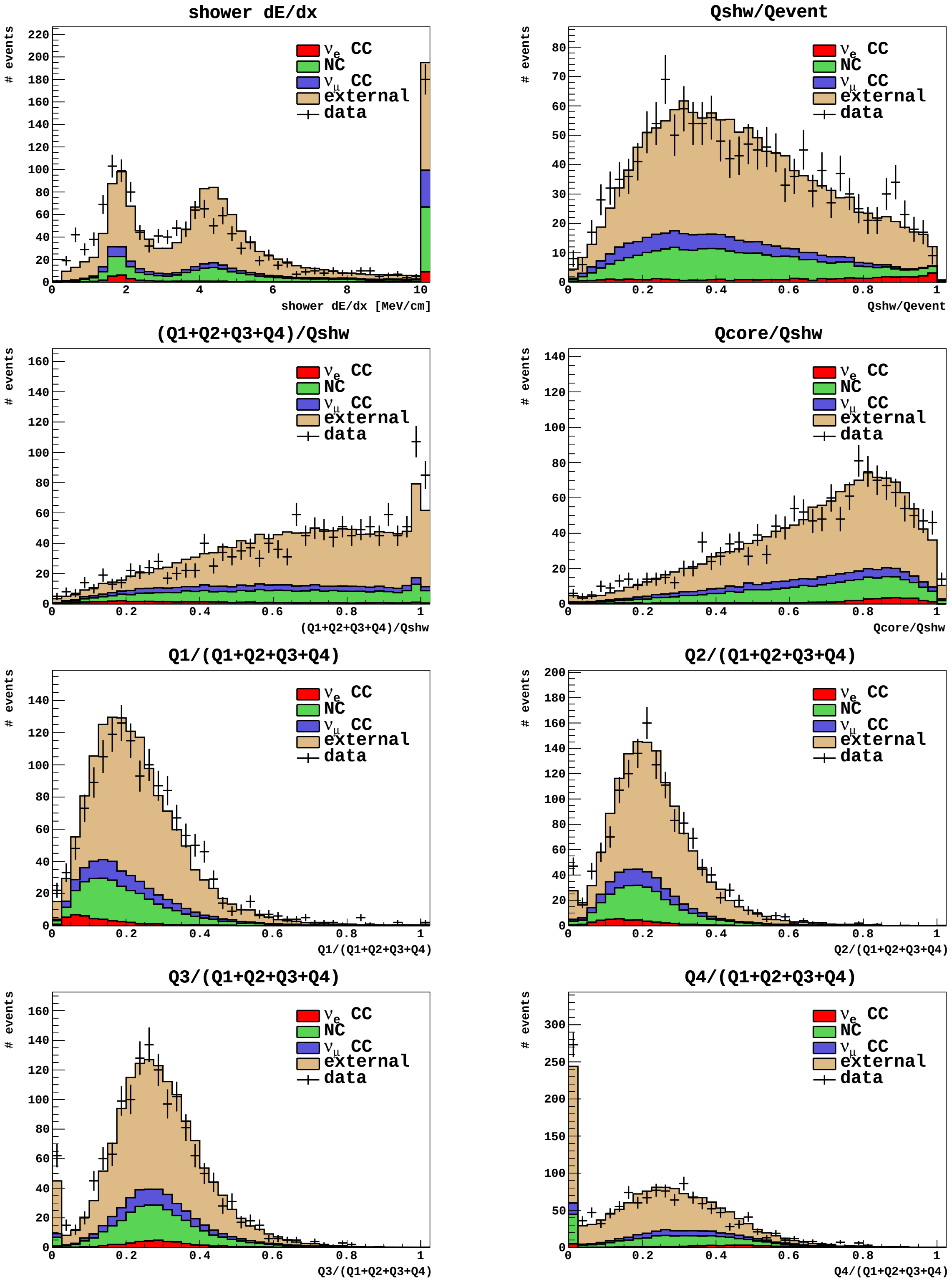

Figure 4.14: POT normalized (with additional external background scaling) comparison of candidate shower charge and topological variables in data and MC.

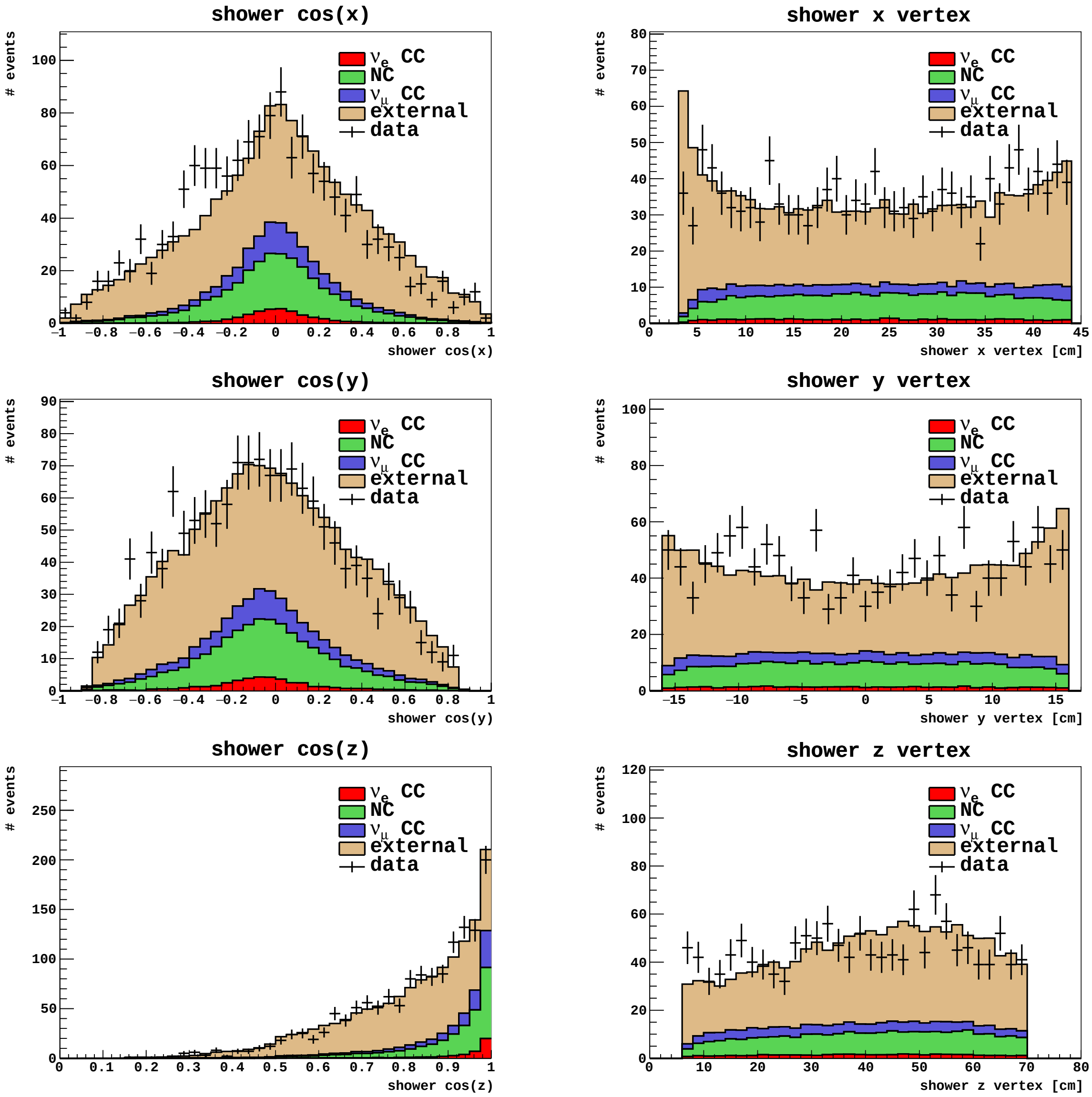

Figure 4.15: POT normalized (with additional external background scaling) comparison of candidate shower charge and topological variables in data and MC.

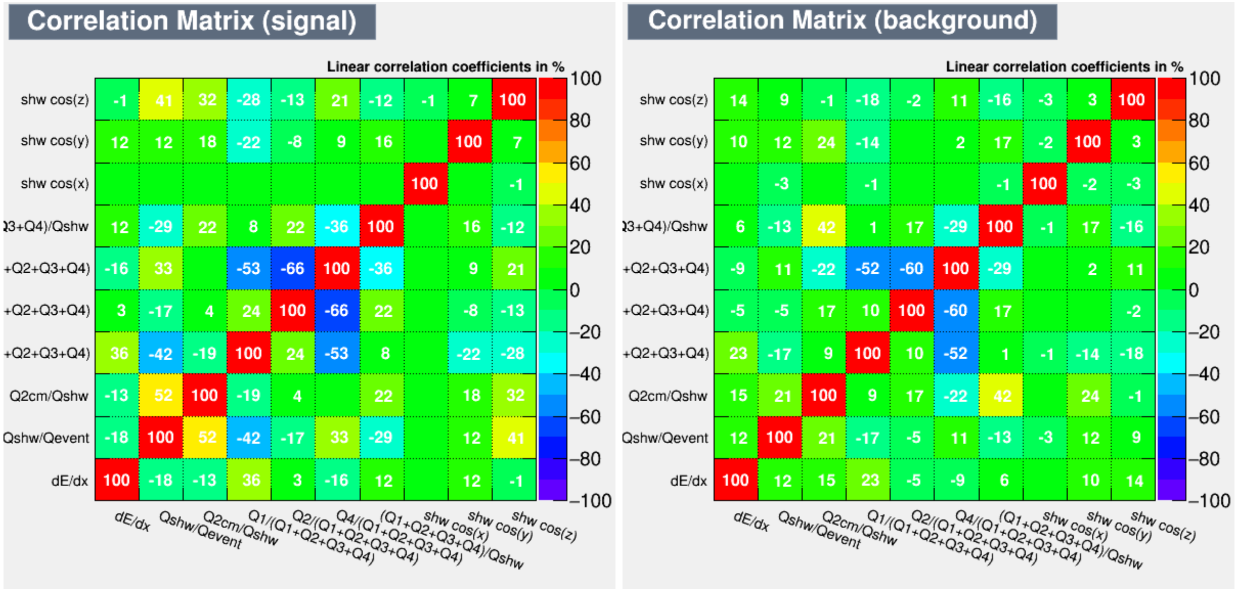

Correlation Matrix (signal)

	dE/dx	Qshw/Qevent	Q2cm/Qshw	Q1/(Q1+Q2+Q3+Q4)	Q2/(Q1+Q2+Q3+Q4)	Q4/(Q1+Q2+Q3+Q4)	(Q1+Q2+Q3+Q4)/Qshw	shw cos(x)	shw cos(y)	shw cos(z)
shw cos(z)	-1	41	32	-28	-13	21	-12	-1	7	100
shw cos(y)	12	12	18	-22	-8	9	16		100	7
shw cos(x)								100		-1
3+Q4)/Qshw	12	-29	22	8	22	-36	100		16	-12
+Q2+Q3+Q4)	-16	33		-53	-66	100	-36		9	21
+Q2+Q3+Q4)	3	-17	4	24	100	-66	22		-8	-13
+Q2+Q3+Q4)	36	-42	-19	100	24	-53	8		-22	-28
Q2cm/Qshw	-13	52	100	-19	4		22		18	32
Qshw/Qevent	-18	100	52	-42	-17	33	-29		12	41
dE/dx	100	-18	-13	36	3	-16	12		12	-1

Correlation Matrix (background)

	dE/dx	Qshw/Qevent	Q2cm/Qshw	Q1/(Q1+Q2+Q3+Q4)	Q2/(Q1+Q2+Q3+Q4)	Q4/(Q1+Q2+Q3+Q4)	(Q1+Q2+Q3+Q4)/Qshw	shw cos(x)	shw cos(y)	shw cos(z)
shw cos(z)	14	9	-1	-18	-2	11	-16	-3	3	100
shw cos(y)	10	12	24	-14		2	17	-2	100	3
shw cos(x)		-3		-1			-1	100	-2	-3
3+Q4)/Qshw	6	-13	42	1	17	-29	100	-1	17	-16
+Q2+Q3+Q4)	-9	11	-22	-52	-60	100	-29		2	11
+Q2+Q3+Q4)	-5	-5	17	10	100	-60	17			-2
+Q2+Q3+Q4)	23	-17	9	100	10	-52	1	-1	-14	-18
Q2cm/Qshw	15	21	100	9	17	-22	42		24	-1
Qshw/Qevent	12	100	21	-17	-5	11	-13	-3	12	9
dE/dx	100	12	15	23	-5	-9	6		10	14

Figure 4.16: The correlations between BDT input variables in the signal and background samples. Note that in the list of variables, $Q_{2\mathrm{cm}}/Q_{\mathrm{shw}}$ is equivalent to $Q_{\mathrm{core}}/Q_{\mathrm{shw}}$.

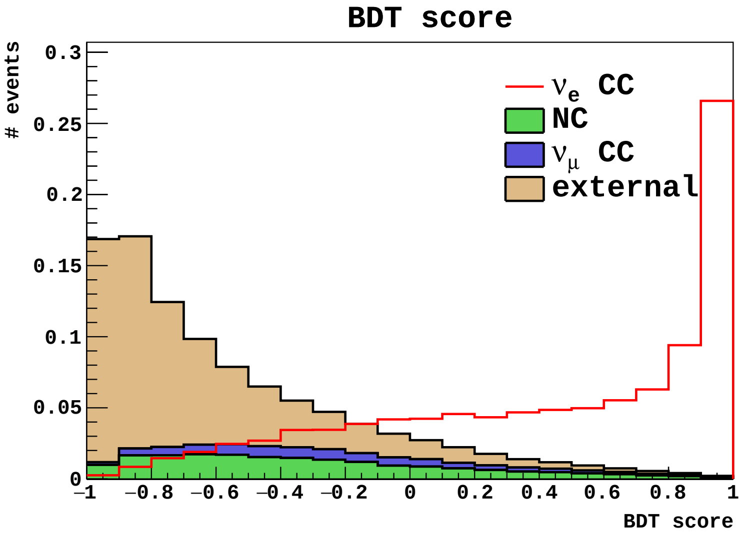

Figure 4.17: The distribution of BDT score for signal and background interactions.

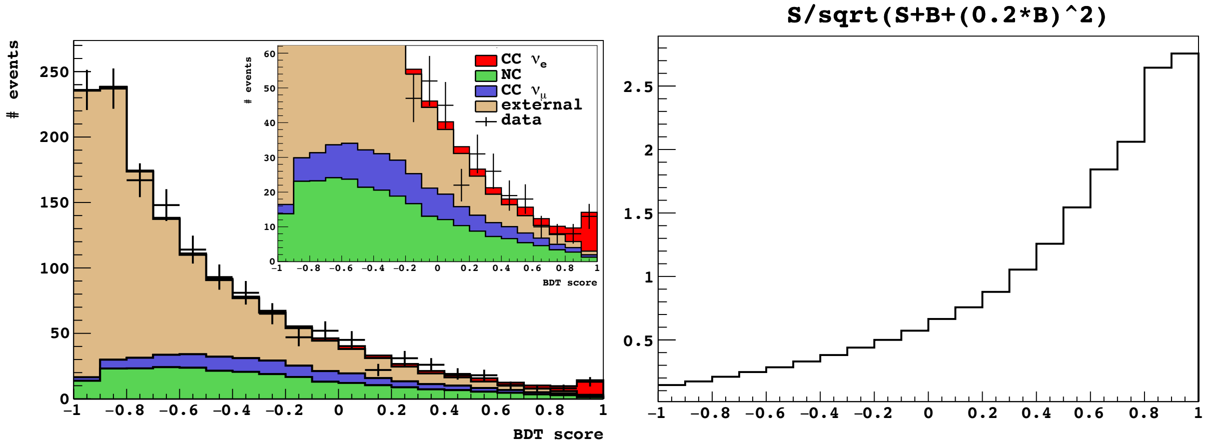

Figure 4.18: (left) The POT normalized (including an additional background scale factor) distribution of BDT score in data and MC. (right) The observation significance for selecting above a part BDT score. A rough 20% systematic error on the background is included.

Cut	ν_e **CC**	ν_μ **CC**	**NC**	**external**	**data**
All MC	128.5	6508	2398	72589	4056940
Anti-MINOS	104.4	755.8	2032	56231	3688222
Shower Reco	73.1	225.1	465.6	3034	14264
Fiducial Volume	57.0	166.1	358.9	874.8	5427
Shower θ_z	56.9	164.7	356.3	847.0	5083
Nearest z	53.6	149.7	327.8	489.3	2233
Vtx-Hit Min. Dist.	40.4	107.6	239.5	320.4	1440
BDT score > 0.9	11.2	0.65	1.26	1.08	13 ± 3.6(stat)

Table 4.1: A summary of the impact each cut of this analysis has on each category of interaction considered. All counts are normalized to data POT but no additional external background correction is applied. Additionally, no flux reweighting is applied (except on the last line).

4.5 Signal Candidates and Background Treatment

One difficulty in this analysis is the small size of the ArgoNeuT detector. We find that a significant background comes from EM-like activity in the detector produced by interactions originating outside of the detector active volume. This is a complication unique to ArgoNeuT, where it is impossible to move sufficiently far from the edge of the detector to reject a significant fraction of these outside backgrounds while simultaneously maintaining satisfactory signal statistics. Additionally, we find that the external background is underestimated in the ArgoNeuT simulation, which only generates neutrino interactions that occur with and inside the cryostat. While the simulation reproduces the energy and topological characteristics of external EM-like backgrounds in the detector, it misrepresents the total quantity of these backgrounds. To correct for this deficit and constrain the external background contribution in the strict $\nu_e/\overline{\nu}_e$ selection region, the external background is scaled as a linear function of BDT score, derived using a data-simulation comparison sideband with score < 0. The data-driven function is motivated by the fact that external backgrounds tend to look topologically distinct from signal, a characteristic which is quantitatively described by decreasing BDT score, a proxy for event topology.

Given the high degree of uncertainty associated with the backgrounds in this analysis, we have chosen to define our signal to be only events with an BDT score greater than 0.9. However, a BDT score-dependent scale factor is applied to each background event produced by an interaction outside the cryostat to bring data and MC into agreement. The rationale and procedure for finding this scale factor are described in this section along with the final selection of candidate charged current electron neutrino interactions.

4.5.1 External Background

The deficit in MC relative to data is due to an excess of backgrounds produced outside the detector volume. It was apparent that there was a significant excess of events in data relative to MC after the basic cuts were applied. Hand scanning the events with candidate showers reconstructed in data indicated that this excess was comprised of energy depositions in the crystotat produced by interactions outside the detector volume. Many of these outside background are not simulated. ArgoNeuT simulates neutrino interactions inside the cryostat but not neutrino interactions with the surrounding rock. For example, a neutrino-rock interaction produces a neutron which enters the cryostat and is captured on an argon nucleus in the TPC, producing low-energy photons, would not be simulated but may be present in data. To account for this known limitation, we define a linear scale factor for reweighting outside background events based on BDT score using a side band of data defined by BDT score < 0. This is done by fitting a line to the quantity $(N_{\rm data} - N_{\rm sig} - N_{\nu_\mu \rm CC} - N_{\rm NC})/N_{\rm out}$. The result of this fit is shown in Figure 4.19 along with the ratio of data to MC as a function of BDT score after the correction is applied. After the correction is applied, the are 1440 data events and 1437.6 MC events after POT scaling. The systematic errors associated with the outside background in the selection are assigned to be a conservatie 100%, which is consistent with the 1σ errors to the linear fit, as shown in Figure 4.19, and corresponding to $\sim \pm\, 1$ background event in the final selection.

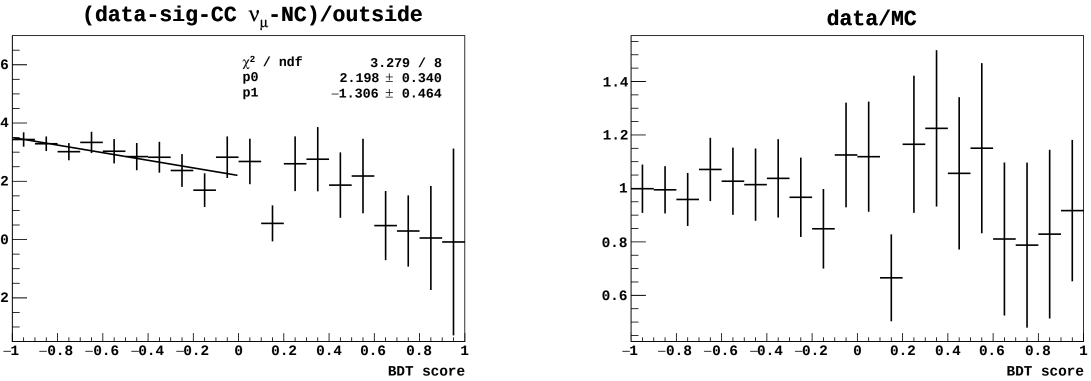

Figure 4.19: (left) The linear fit to outside background scale factor as a function of BDT score. (right) The ratio of data to MC after the outside background correction is applied.

The candidate shower angle with respect to the neutrino beam also provides independent validation of the effectiveness of this scaling procedure. Figure 4.20 shows the distribution of this quantity for all events in data and MC immediately prior to applying the BDT selection. The outside background is scaled on an event-by-event basis according to the procedure defined above, which brings the data and MC into satisfactory shape agreement.

4.5.2 Validation of External Background Correction

While working out how best to handle the external background, multiple methods for scaling were tested, and all yield similar results. Applying a uniform scale factor to the external back-

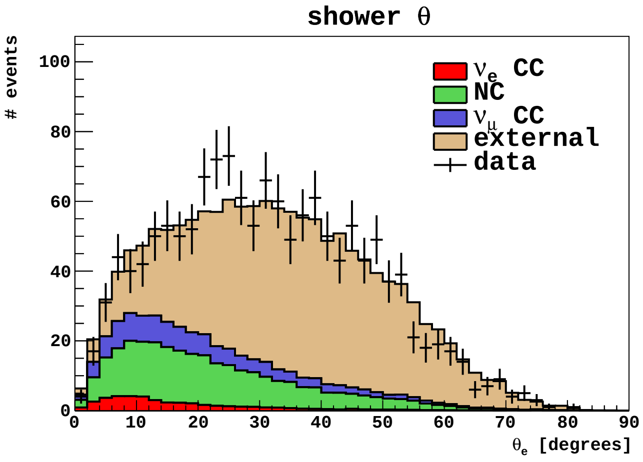

Figure 4.20: The candidate shower angle with respect to beam direction immediately prior to the BDT cut. The BDT score-dependent correction is applied to the outside background contribution.

ground is comparable, but consistently overestimates simulation at higher BDT scores and, more importantly, is physically unmotivated (more on this in next paragraph). A scale factor based on the total charge in the event was also tested, yielding comparable results to the BDT-based scale factor. To validate the use of BDT-based scaling, a hand scan was done at several regions from low to high BDT scores in both data and MC. The scaling applied was consistent with the number of external background events observed in data at low- and mid-BDT score regions in a random sample of scanned events.

We emphasize that topologically the external backgrounds that are not simulated do not look like signal (that is — if we think about it conversely — an electron neutrino that interacts just upstream of the ArgoNeuT detector does look like signal, but these kinds of events are fully simulated, as they are interactions that occur inside the cryostat). Thus we expect the underestimation to be more egregious at lower BDT scores and scaling as a function of BDT score is therefore well-motivated. To illustrate this, we include two external backgrounds in ArgoNeuT that have BDT score < -0.9 (extremely background-like) shown in Figure 4.21.

4.5.3 Candidate Electrons

We select only events with BDT score above 0.9 to reduce the systematic uncertainty associated with the quantity of background in the final selection. After including a rough 20% systematic uncertainty in the background this selection yields the highest significance. There are 13 data

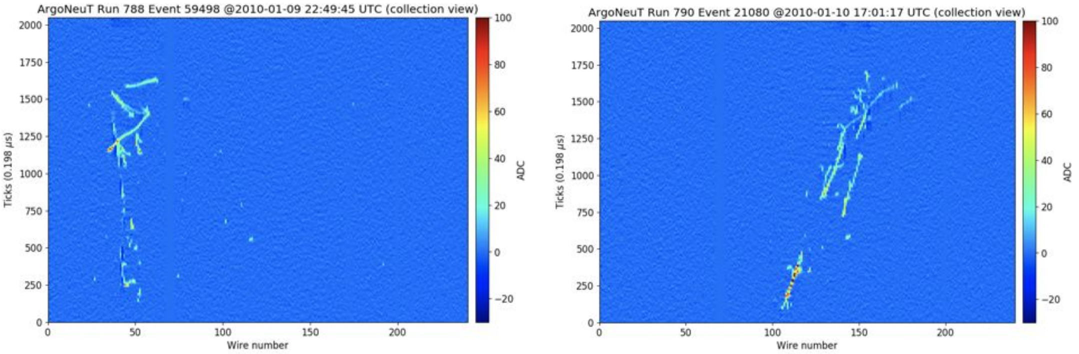

Figure 4.21: Two example external EM backgrounds in ArgoNeuT.

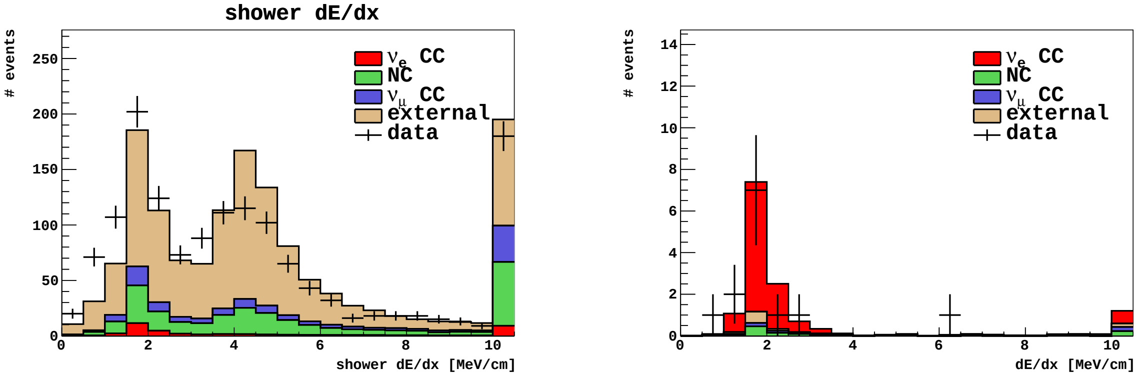

Figure 4.22: The distribution of dE/dx for all events (left) immediately prior to cutting on BDT score and (right) in the final selection. Note the the last bin in these plots contain all events with $dE/dx > 10$ MeV/cm.

events in the final selection. We expect 11.2 signal events and 2.99 background events, 1.08 of which are expected to come from interactions outside the cryostat (plus 1.26 NC and 0.63 ν_μ CC backgrounds). The distributions of dE/dx and electron angle with respect to the neutrino beam before and after the BDT score cut are shown in Figures 4.22 and 4.23.

Figures 4.24-4.27 show the full set of 13 candidate events selected in the ArgoNeuT automated search for $\nu_e/\overline{\nu}_e$ charged current interactions. The induction plane (left) and collection plane (right) views are both shown. These images scale to approximately 90 cm in the wire direction, which increases along the beam direction, and approximately 62 cm in the drift direction (measured in time sample number, noting that the time range is larger than the size of the detector in the drift direction, 47 cm). The color is proportional to the charge collected. Coherent noise is present in some images around approximately wire 200-250, sample number 1750. Other images

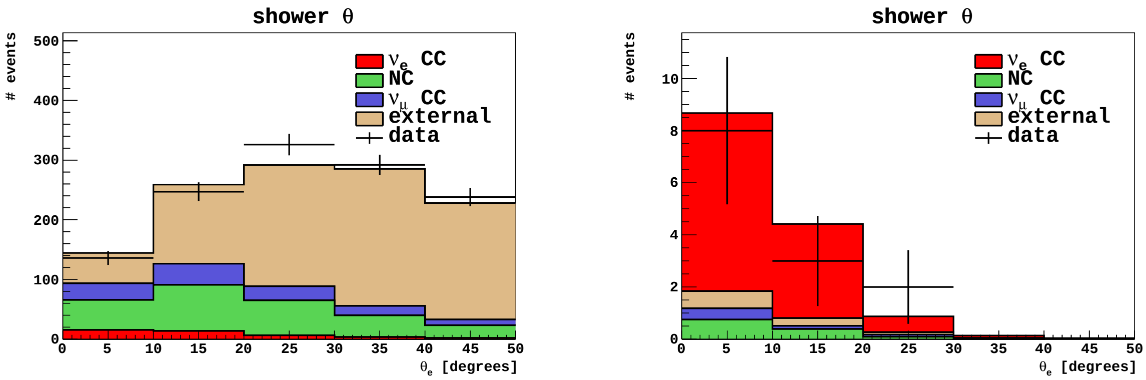

Figure 4.23: The distribution of electron angle with respect to the neutrino beam for all events (left) immediately prior to cutting on BDT score and (right) in the final selection.

contain bursts of charge due to activity on the opposite side of the wire planes in approximately wire 230, sample number 0-500 region.

The final set, in Figure 4.27, shows the obvious-by-eye background interactions spuriously identified as signal in the final selection. The first background event shows a single gamma-induced shower separated from the interaction vertex. The second is a through-going muon, and the third is track-like. These backgrounds and the event rate are consistent with expectations from simulation.

4.5.4 A Note on Selection Efficiency

While the efficiency is sufficient for exploring the data-driven classification techniques and performing the measurements reported here, it is limited by ArgoNeuT's intrinsic reconstruction capabilities. First, ArgoNeuT's size is such that EM shower containment is a rarity, which leads to difficulty in event classification. Poor track containment, in general, also affects vertex reconstruction and event classification. Second, the signal selection in ArgoNeuT is necessarily very strict since we cannot move sufficiently far away from the detector walls in the fiducial volume definition to reduce background events produced by interactions external to the active volume of the detector, most notably single gammas. With improvements to these issues, as expected in future detectors, like DUNE, we expect a significant increase in inclusive $\nu_e/\overline{\nu}_e$ CC signal selection efficiency.

The topology of selected events is consistent with expectation and the strict cut on BDT score

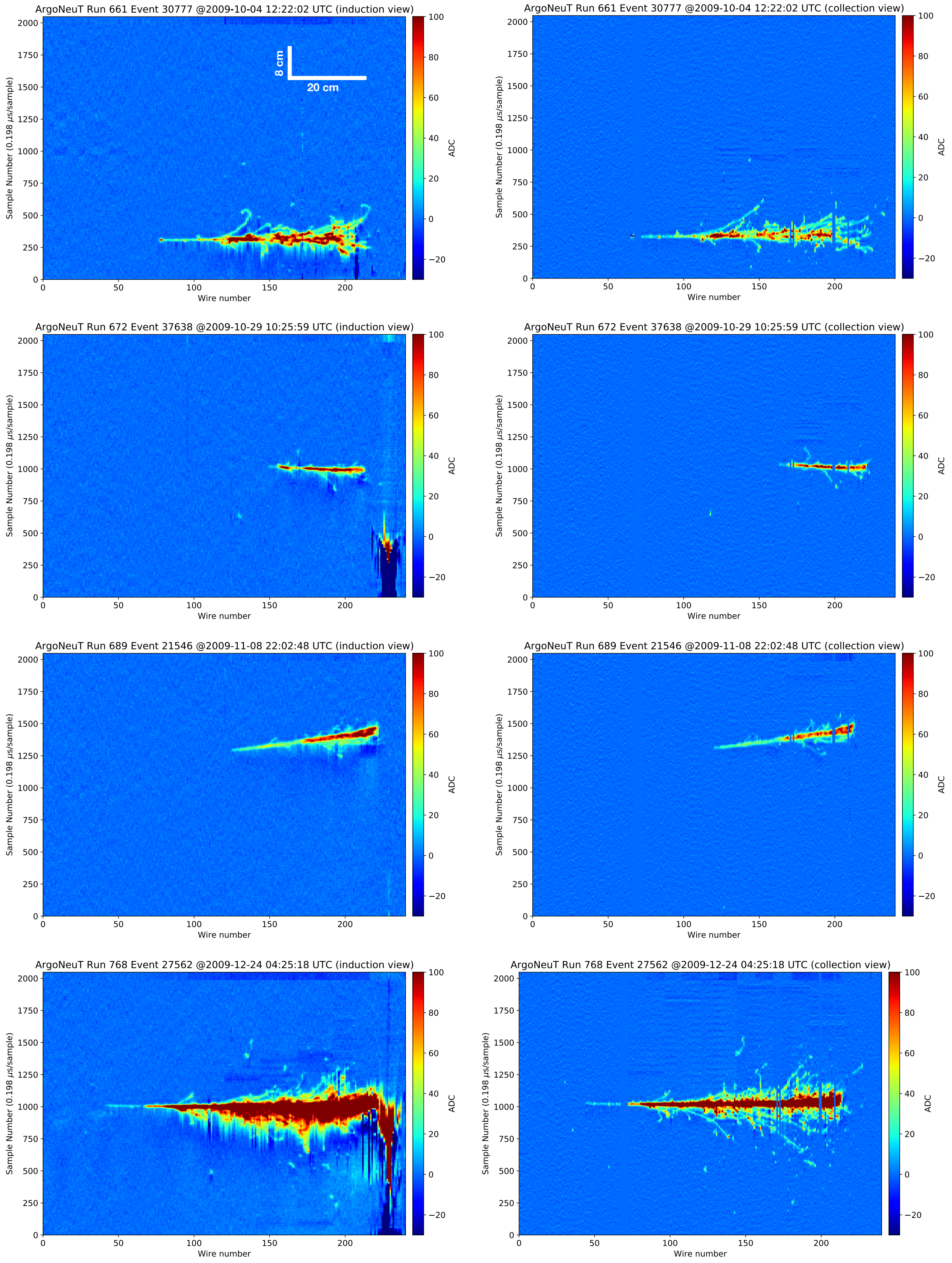

Figure 4.24: The thirteen candidate electron events selected in ArgoNeuT. Continued in Figures 4.25-4.27.

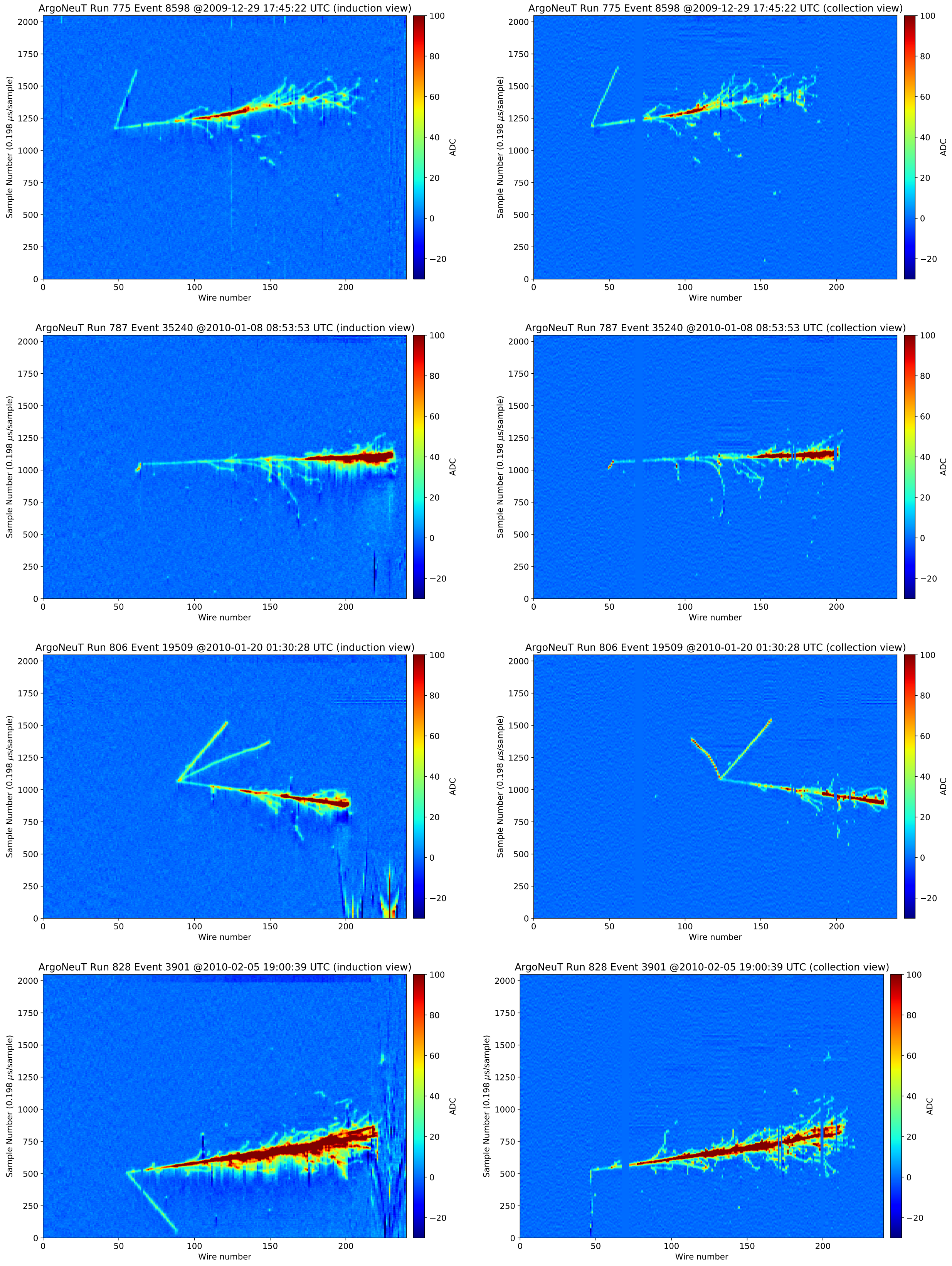

Figure 4.25: Continued from Figure 4.24. The thirteen candidate electron events selected in ArgoNeuT. Continued in Figures 4.26 and 4.27.

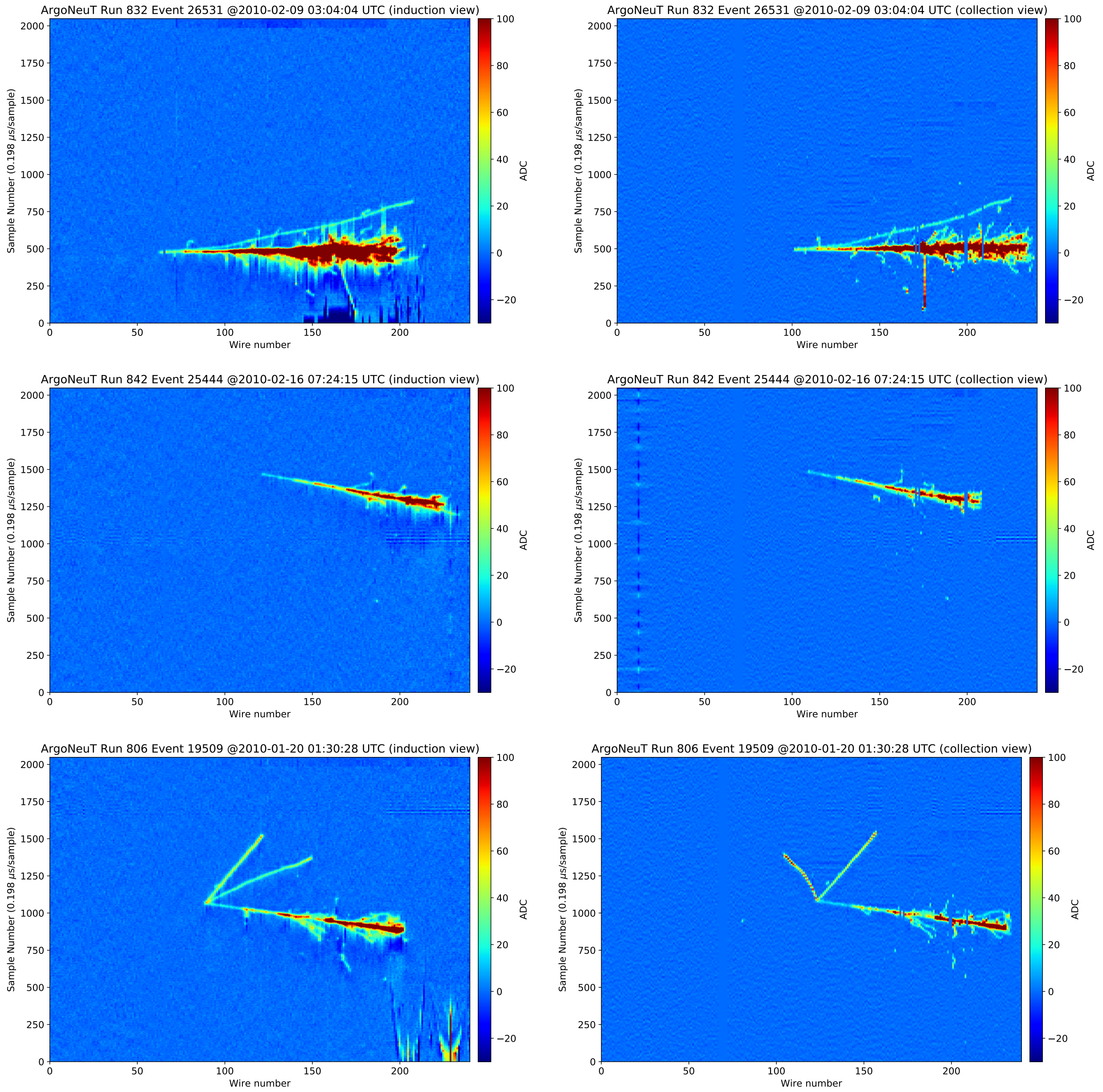

Figure 4.26: Continued from Figure 4.24. The thirteen candidate electron events selected in ArgoNeuT. Continued in Figure 4.27.

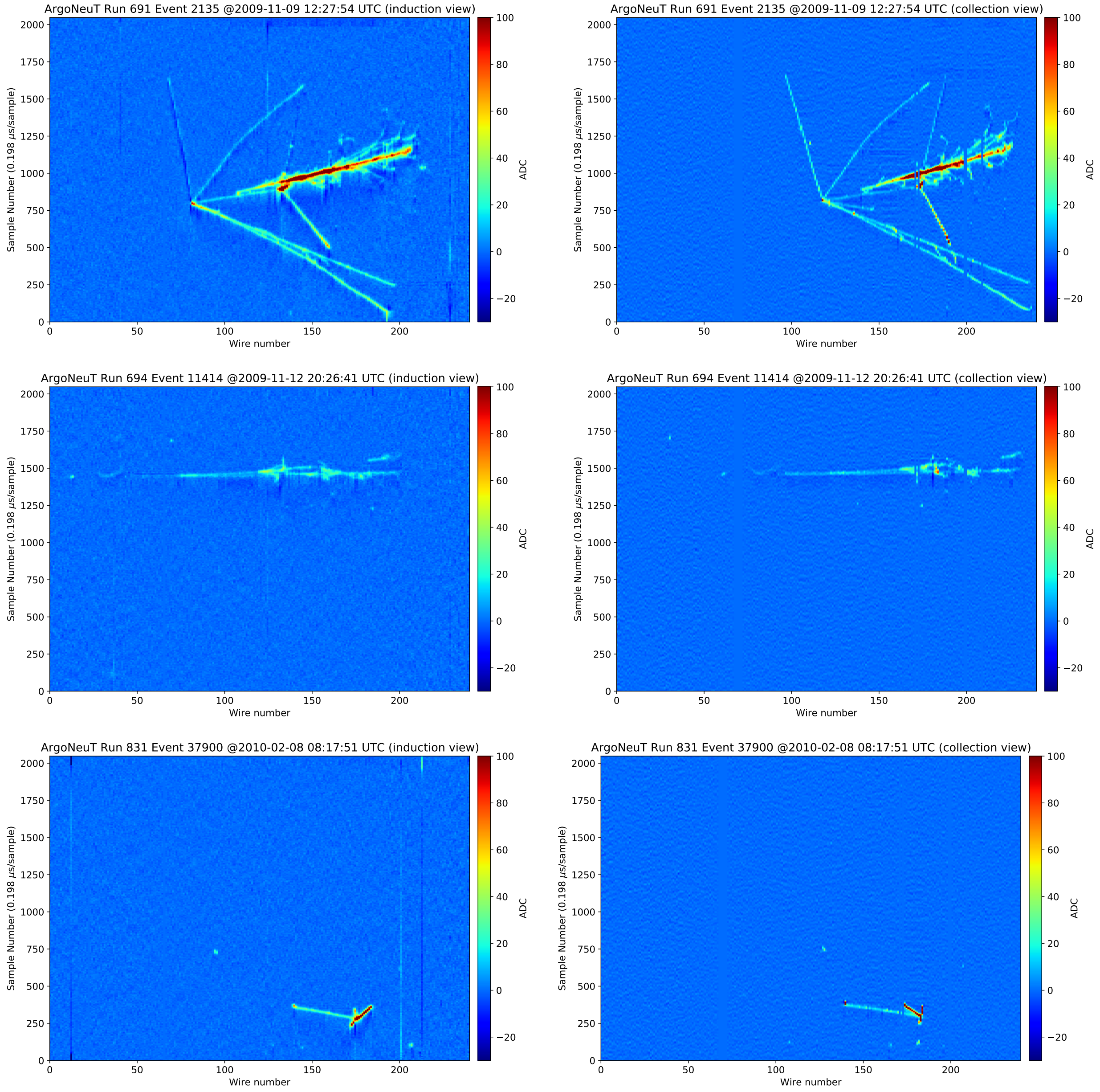

Figure 4.27: Continued from Figure 4.26. The obvious-by-eye background interactions spuriously identified as signal in the final selection. The first background event shows a single gamma-induced shower separated from the interaction vertex. The second is a through-going muon, and the third is track-like. These backgrounds and the event rate are consistent with expectations from simulation. In addition, the third event shown on the next page is the one event with the largest vertex dE/dx in the final selection (∼6 MeV/cm). There is only a single shower visible in this event and it may be a single gamma background, which is consistent with the background expectation.

means the selection is more efficient for quasielastic events than deep inelastic scattering (DIS) events. We expect 3.6 quasi-elastic events, 3.4 resonant events, and 4.1 DIS events in the final sample, and note that many of the interactions selected have simple topologies. This is unsurprising given the stringent cut on BDT score and the size of the data sample. While it is difficult to make definitive statements about the initial interaction of the selected events based on final state topology, a hand scan of DIS events in simulation was done to confirm the topologies that are selected could be consistent with DIS interactions. Additionally, there is a non-negligible probability that there are zero or one DIS events in the final selection. A subsequent scan was done of all events in data with BDT score > 0.7, which was also consistent with the signal and background expectations and yielded many more clear, high-multiplicity examples of DIS signal-like interactions in data. The full collection of events with BDT score > 0.7 is included in Appendix C.

4.5.5 Electron/Photon Seperation: An Aside

As has been noted, the shower reconstructed employed in this analysis is designed to reconstruct electrons well, but often fails when attempting to reconstruct photons (see Section 4.3.3 and Figure 4.6 in particular). However, we can still ask how this selection method would perform if given a sample of well-reconstructed photons; or photons that were reconstructed as well as typical electrons (see Figure 4.6 for reference). To explore this question, we define “well-reconstructed photons” as reconstructed photon showers identified by truth information that have completeness greater than 80% and purity greater than 90%. The BDT performance for this photon sample relative to all ν_e CC interactions is shown in Figure 4.28 along with the dE/dx for these events. Both are area-normalized. These distributions demonstrate that the shower reconstruction and the selection method used in this analysis maintain the strong separation between electrons and gammas that has been shown to be achievable with hand scan-based analysis like in previous ArgoNeuT work [95].

4.6 Flux

The NuMI $\nu_e + \overline{\nu}_e$ low-energy antineutrino mode flux used in this analysis is drawn directly from the supplemental materials in [55]. We have reproduced the relevant details here for ease of access.

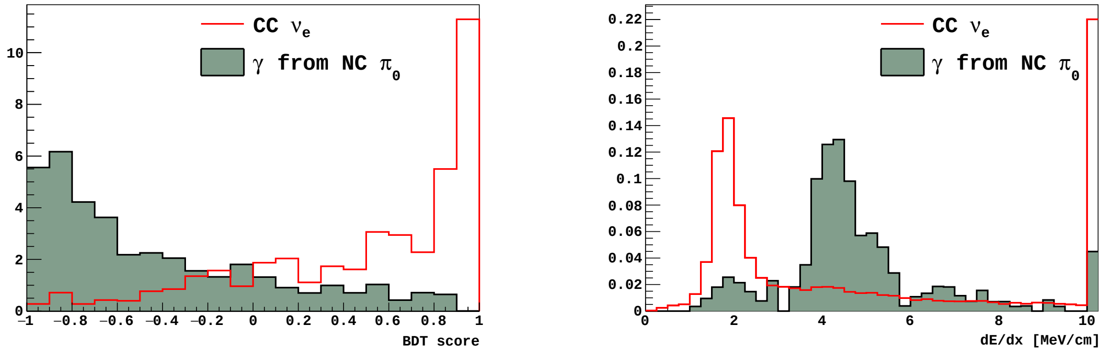

Figure 4.28: (left) The area-normalized BDT score of electrons compared to a sample of well reconstructed gammas. (right) The area-normalized dE/dx of reconstructed electrons and well reconstructed gammas.

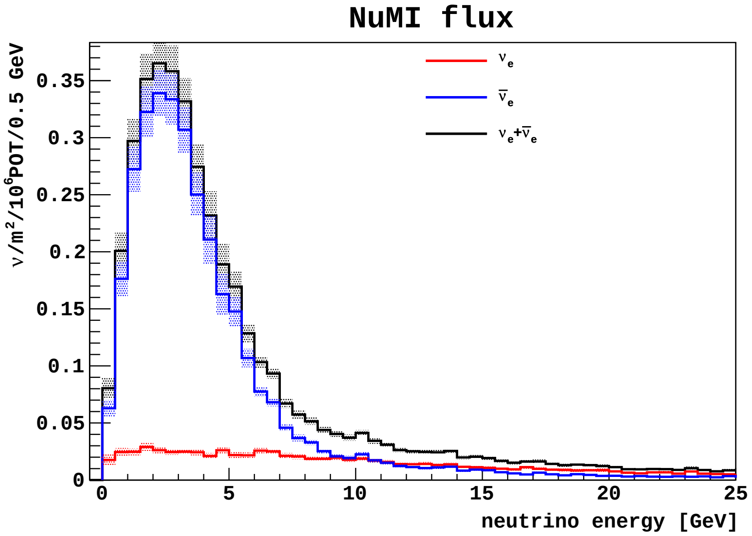

Figure 4.29: The NuMI ν_e and $\overline{\nu}_e$ flux as a function of energy in low-energy antineutrino mode.

The NuMI ν_e flux in low-energy antineutrino mode as a function of energy is shown in Figure 4.29. The contribution to each energy bin and its errors are shown in Figure 4.30.

4.7 Systematics

While the statistical errors associated with this measurement exceed the contribution of systematic errors, we describe and quantify the systematic uncertainties associated with the analysis below. To measure the effect of each uncertainty on the final result, the analysis is repeated (except in noted cases where the uncertainty only affects the final cross section calculation), varying each

TABLE VII: The ν_e flux in units of $\nu/m^2/10^6 POT$ for the RHC beam.

E (GeV)	ϕ	$\delta\phi$ (%)	E (GeV)	ϕ	$\delta\phi$ (%)
0.0-0.5	1.76e-02	28.3	0.5-1.0	2.45e-02	14.4
1.0-1.5	2.47e-02	11.7	1.5-2.0	2.90e-02	11.5
2.0-2.5	2.61e-02	12.6	2.5-3.0	2.45e-02	9.1
3.0-3.5	2.48e-02	9.6	3.5-4.0	2.43e-02	10.4
4.0-4.5	2.11e-02	12.0	4.5-5.0	2.61e-02	11.6
5.0-5.5	2.19e-02	11.6	5.5-6.0	2.17e-02	10.1
6.0-6.5	2.58e-02	9.2	6.5-7.0	2.51e-02	8.4
7.0-7.5	2.12e-02	10.9	7.5-8.0	2.06e-02	10.6
8.0-8.5	1.86e-02	10.9	8.5-9.0	1.86e-02	8.3
9.0-9.5	1.96e-02	9.9	9.5-10.0	1.76e-02	10.0
10.0-10.5	1.88e-02	9.3	10.5-11.0	1.69e-02	9.7
11.0-11.5	1.58e-02	9.1	11.5-12.0	1.40e-02	10.3
12.0-12.5	1.38e-02	10.6	12.5-13.0	1.41e-02	10.7
13.0-13.5	1.32e-02	10.2	13.5-14.0	1.38e-02	9.2
14.0-14.5	1.16e-02	10.1	14.5-15.0	1.12e-02	10.3
15.0-15.5	1.07e-02	9.8	15.5-16.0	9.93e-03	10.1
16.0-16.5	9.34e-03	11.3	16.5-17.0	1.13e-02	10.7
17.0-17.5	9.80e-03	12.8	17.5-18.0	9.07e-03	10.9
18.0-18.5	8.86e-03	11.7	18.5-19.0	8.36e-03	11.6
19.0-19.5	8.56e-03	11.4	19.5-20.0	8.61e-03	13.0

TABLE VIII: The $\bar{\nu}_e$ flux in units of $\nu/m^2/10^6 POT$ for the RHC beam.

E (GeV)	ϕ	$\delta\phi$ (%)	E (GeV)	ϕ	$\delta\phi$ (%)
0.0-0.5	6.28e-02	11.3	0.5-1.0	1.76e-01	8.7
1.0-1.5	2.72e-01	7.1	1.5-2.0	3.22e-01	6.9
2.0-2.5	3.39e-01	6.0	2.5-3.0	3.34e-01	6.6
3.0-3.5	3.07e-01	6.6	3.5-4.0	2.50e-01	7.6
4.0-4.5	2.11e-01	10.0	4.5-5.0	1.63e-01	10.9
5.0-5.5	1.48e-01	8.6	5.5-6.0	1.07e-01	7.2
6.0-6.5	7.75e-02	5.7	6.5-7.0	6.82e-02	5.3
7.0-7.5	4.58e-02	7.0	7.5-8.0	3.67e-02	7.7
8.0-8.5	3.29e-02	7.3	8.5-9.0	2.53e-02	7.2
9.0-9.5	2.08e-02	7.0	9.5-10.0	1.94e-02	8.9
10.0-10.5	2.25e-02	8.1	10.5-11.0	1.74e-02	9.4
11.0-11.5	1.51e-02	7.2	11.5-12.0	1.22e-02	9.3
12.0-12.5	1.14e-02	8.7	12.5-13.0	1.05e-02	8.8
13.0-13.5	1.11e-02	10.1	13.5-14.0	1.17e-02	9.4
14.0-14.5	8.22e-03	10.3	14.5-15.0	9.14e-03	8.3
15.0-15.5	8.59e-03	9.4	15.5-16.0	6.84e-03	9.0
16.0-16.5	5.83e-03	13.0	16.5-17.0	4.87e-03	9.6
17.0-17.5	6.44e-03	10.3	17.5-18.0	5.04e-03	9.2
18.0-18.5	4.13e-03	12.1	18.5-19.0	5.13e-03	10.5
19.0-19.5	4.48e-03	8.2	19.5-20.0	3.62e-03	11.9

Figure 4.30: The NuMI ν_e and $\overline{\nu}_e$ flux and errors as a function of energy in low-energy antineutrino mode. These tables come directly from the supplemental documentation in [55].

parameter according to its uncertainty individually. The BDT itself is not retrained in each new "universe" (i.e. the data distribution remains fixed). In cases where the up-shifted and down-shifted variations produce an effect on the cross section in the same direction, the total contribution to the systematic uncertainty is defined to be the magnitude of the larger error in both directions. Systematics errors associated with underlying simulation models, which impact the number of estimated background events and the efficiency of the selection, are evaluated by varying a set of parameters in the GENIE simulation package relevant [91] to the ν_e CC interaction channel and its backgrounds. Additional systematic errors are assigned to the external background, the integrated flux, the total POT, and the number of argon targets. Each systematic error source is described in detail below and a summary of each parameter's uncertainty and its impact on the total cross section uncertainty is given in Table 4.2.

GENIE Systematic Uncertainties. To account for systematic errors associated with uncertainties related to the modeling of neutrino interactions in simulation, the following GENIE parameters are varied. Details about each parameter can be found in [91] and the uncertainties on each parameter are listed in Table 4.2.

- **Qema** — Axial mass for CC quasi-elastic
- **NcelAxial** — Axial mass for NC elastic
- **CcresAxial** — Axial mass for CC resonance neutrino production
- **CcresVector** — Vector mass for CC resonance neutrino production
- **NcresAxial** — Axial mass for NC resonance neutrino production
- **NcresVector** — Vector mass for NC resonance neutrino production
- **CohMA** — Axial mass for CC and NC coherent pion production
- **CohR0** — Nuclear size parameter controlling pion absorption in Rein-Sehgal model
- **NonResRvbarbp1pi** — $\nu + n$ and $\overline{\nu} + p$ (1 π) type interactions
- **NonResRvbarbp2pi** — $\nu + n$ and $\overline{\nu} + p$ (2 π) type interactions
- **NonResRvp1pi** — $\nu + p$ and $\overline{\nu} + n$ (1 π) type interactions
- **NonResRvp2pi** — $\nu + p$ and $\overline{\nu} + n$ (2 π) type interactions

- **FormZone** — Hadron formation zone
- **IntraNukePlabs** — Pion absorption probability.

External Background. A conservative 100% systematic uncertainty is assigned to the outside background. This is also consistent with the errors on the external background fit extrapolated to the signal region. We further note that the magnitude of this uncertainty is still sub-dominant to the statistical uncertainty of the analysis.

POT and Flux. The uncertainty on the combined number of electron neutrinos and antineutrinos in antineutrino mode is 6.6% [55]. There is an additional 1% uncertainty assigned to the POT collected by ArgoNeuT [102].

Fiducial Volume/Number of Argon Targets. There exists an uncertainty on the number of argon targets due to the uncertainty on the fiducial volume defined for this analysis [80]. The uncertainty in the y and z dimensions comes from the 1 mm uncertainty on the locations where wires intersect. The x uncertainty stems from the electron drift time uncertainty and is $\sim$1 cm. This yields a 2% uncertainty on the number of argon targets, as reported in [102].

4.8 Cross Section(s)

As there is no ability to sign-select the electrons reconstructed in ArgoNeuT, we present a flux-integrated cross section for combined ν_e and $\overline{\nu}_e$ CC interactions in ArgoNeuT. The flux-integrated total cross section is given by

$$\langle\sigma\rangle = \frac{N}{\epsilon N_{\mathrm{Ar}} \int \Phi dE} \tag{4.1}$$

where N is the number of signal events after background subtraction, ϵ is the efficiency of reconstruction and selection, N_{Ar} is the number of target nuclei in the detector fiducial volume, and $\int \Phi dE$ is the integrated neutrino flux.

Similarly, a differential cross section in terms of a particular kinematic variable u is given by

$$\frac{d\sigma(u_i)}{du} = \frac{N_i}{\Delta u_i \epsilon_i N_{\mathrm{Ar}} \int \Phi dE}. \tag{4.2}$$

Uncertainty Source	**Parameter Variation (%)**	**Fractional Cross Section Uncertainty (%)**
Qema	$^{+25}_{-15}$	$^{+2.6}_{-4.1}$
NcelAxial	±25	$^{+0.7}_{-0.5}$
CcresAxial	±20	$^{+3.3}_{-3.2}$
CcresVector	±10	$^{+1.4}_{-1.6}$
NcresAxial	±20	$^{+0.6}_{-0.3}$
NcresVector	±10	±0.1
CohMA	±50	±0.1
CohR0	±10	±0.1
NonResRvbarbp1pi	±50	$^{+2.2}_{-2.0}$
NonResRvbarbp2pi	±50	$^{+0.2}_{-0.1}$
NonResRvp1pi	±50	±0.4
NonResRvp2pi	±50	±0.7
FormZone	±50	$^{+2.9}_{-17.2}$
IntraNukePlabs	±20	$^{+3.2}_{-3.0}$
Background Scale Factor	±100	±10.7
POT	—	±1.0
Flux	—	±6.6
Number of Argon Targets	—	±2.0
Total Systematic Uncertainty	—	$^{+14.4}_{-22.4}$

Table 4.2: A summary of the impact each systematic uncertainty has on the final cross section. Uncertainties on the POT, flux, and number of argon targets play no role in the selection and are only applied at the stage of calculating the cross section.

We note that the bin efficiency is defined as $\epsilon_i = u_{i,\text{selected,reco}}/u_{i,\text{total,true}}$. That is, the numerator of efficiency is defined using reconstructed kinematic variables while the denominator of the efficiency is defined using true kinematic variables. This takes into account smearing between bins without a formal unfolding.

The total protons on target (POT) recorded in antineutrino mode during ArgoNeuT's six month run 1.25×10^{20} POT. The integrated neutrino flux is given by:

$$\begin{aligned}\int \Phi dE &= \int \Phi_{\overline{\nu}_e} dE + \int \Phi_{\nu_e} dE && (4.3)\\ &= 4.09 \times 10^{10}\ \text{cm}^{-2} + 1.07 \times 10^{10}\ \text{cm}^{-2} && (4.4)\\ &= 5.16 \times 10^{10}\ \text{cm}^{-2} && (4.5)\end{aligned}$$

The number of target nuclei (N_{Ar}) in the fiducial volume ($V = 41\ \text{cm} \times 32\ \text{cm} \times 64\ \text{cm} = 83,968\ \text{cm}^3$) is

$$\begin{aligned}N_{\text{Ar}} &= \frac{Vd}{M_{\text{Ar}}} N_{\text{A}} && (4.6)\\ &= 83,968\ \text{cm}^3 \times 0.0014 \frac{\text{kg}}{\text{cm}^3} \div 0.039948 \frac{\text{kg}}{\text{mol}} \times 6.02 \times 10^{23} && (4.7)\\ &= 1.77 \times 10^{27}\ \text{Ar nuclei} && (4.8)\end{aligned}$$

Combining these yields

$$\langle \sigma_{\overline{\nu}_e + \nu_e} \rangle = \frac{N}{\epsilon} \cdot 1.0949 \times 10^{-38}\ \text{cm}^2/\text{Ar} \qquad (4.9)$$

for a flux-averaged cross section on argon. The efficiency of the selection is 10.5% (11.2 ν_e selected from a predicted 106.5 ν_e interactions in the fiducial volume). The purity of the sample is 78.9%; 2.99 background events are expected. There are 13 events in data with BDT score > 0.9. Thus we extract a flux averaged $\overline{\nu}_e + \nu_e$ cross section of

$$\langle \sigma_{\overline{\nu}_e + \nu_e} \rangle = \left(1.04 \pm 0.38^{+0.15}_{-0.23}\right) \times 10^{-36}\ \text{cm}^2/\text{Ar} \qquad (4.10)$$

which can be compared to the cross section extracted from simulation: $1.17 \times 10^{-36}\ \text{cm}^2/\text{Ar}$.

After substitution, the flux-averaged differential cross section is defined as

$$\frac{d\sigma(u_i)}{du} = \frac{N_i}{\Delta u_i \epsilon_i} \cdot 1.0949 \times 10^{-38}\ \text{cm}^2/\text{Ar}. \qquad (4.11)$$

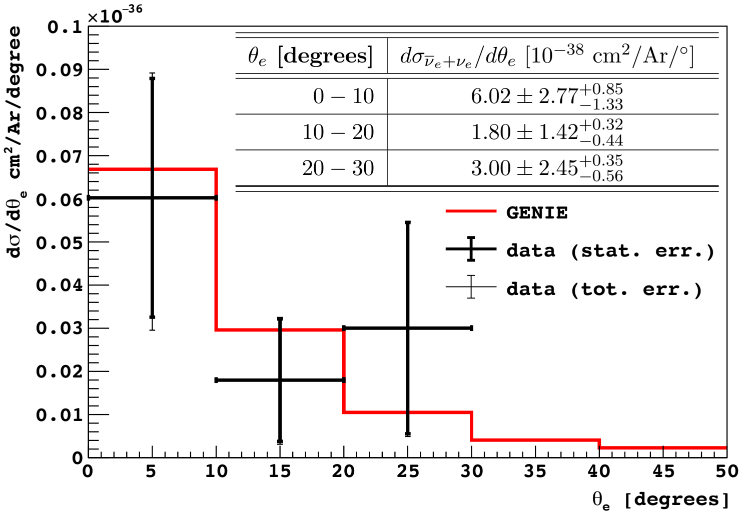

θ_e [degrees]	$d\sigma_{\overline{\nu}_e+\nu_e}/d\theta_e$ $[10^{-38}\ \mathrm{cm}^2/\mathrm{Ar}/^\circ]$
$0-10$	$6.02 \pm 2.77^{+0.85}_{-1.33}$
$10-20$	$1.80 \pm 1.42^{+0.32}_{-0.44}$
$20-30$	$3.00 \pm 2.45^{+0.35}_{-0.56}$

Figure 4.31: The ArgoNeuT $\nu_e + \overline{\nu}_e$ CC differential cross section for electron/positron angle with respect to the neutrino beam compared to the GENIE prediction.

The differential cross section in terms of electron angle with respect to the NuMI beam is shown in Figure 4.31, again as a combination of ν_e and $\overline{\nu}_e$ defined in this way:

$$\frac{d\sigma(\theta_{e,i})}{d\theta_e} = \frac{N_i - B_i}{\epsilon_i \Delta\theta_{e,i} N_{\mathrm{Ar}}(\Phi_{\nu_e} + \Phi_{\overline{\nu}_e})}. \tag{4.12}$$

Importantly, the interpretation of these results, for example in comparisons to model predictions and event generators, *requires* the consideration of both the detailed ν_e and $\overline{\nu}_e$ fluxes simultaneously [55].

4.9 Summary

As demonstration of the selection technique presented here, we have extracted a total cross section of $\langle\sigma_{\overline{\nu}_e+\nu_e}\rangle = (1.04 \pm 0.38^{+0.15}_{-0.23}) \times 10^{-36}\ \mathrm{cm}^2/\mathrm{Ar}$, consistent with the GENIE total cross section. A differential cross section in terms of electron angle with respect to the NuMI beam was also measured. The selection achieves $10.5^{+0.6}_{-0.5}\%$ efficiency (for events originating inside the fiducial volume) with $78.9^{+8.1}_{-11.8}\%$ purity, where the spread in both numbers is due to systematic variations dominated by GENIE variations. The results are statistics limited, and further limited by the reconstruction efficiency in ArgoNeuT. However, we emphasize that the novelty of this analysis is not the cross sections extracted, though they represent the first measurement of electron neutrino scattering on argon, but the demonstration of the first fully-automated reconstruction and selection of inclusive ν_e CC events from GeV-scale neutrino interactions, one that builds upon traditional classification methods that cannot provide sufficient efficiency and background rejection at higher energies.

This analysis expands on first order electron/photon classification techniques to develop inclusive ν_e CC selection strategies for complex event topologies; it employs the full topology of candidate electrons to classify each interaction based on longitudinal and transverse charge distribution. In a detector where a containment requirement is feasible, one could build upon this work by developing an electron likelihood method for LArTPCs modeled on the method developed by the NOνA Experiment, defining templates for electron showers and other particle depositions in LArTPCs as a function of energy [103]. Our approach is novel in its use of charge and position information across the full extent of electromagnetic showers produced in a LArTPC rather than relying strictly on vertex separation and dE/dx, which is often obscured in GeV-scale interactions by hadronic activity. Despite limitations in size and statistics, ArgoNeuT has successfully adapted these strategies for use in LArTPCs, toward indentifying inclusive ν_e interactions for GeV-scale experiments like DUNE. Further development of calorimetry-based techniques for ν_e classification is necessary to provide a valuable cross check for the nascent machine learning-based image classification methods being applied to the task [75, 76].

ArgoNeuT is the only experiment that will be able to report neutrino beam data measurements at the GeV scale for the foreseeable future (MicroBooNE's off-axis NuMI energy spectrum is more comparable to the 100s of MeV scale seen from the BNB, without even noting that the MicroBooNE result is not published), making this analysis unique among imminent ProtoDUNE (also unpublished, and studying single electrons from a test beam which are much easier to reconstruct) and MicroBooNE results. While ArgoNeuT is statistics limited, the exercise of extracting ν_e signal from CC and NC backgrounds in a LArTPC and at the GeV scale has never been done before and this result presents valuable insight toward doing this efficiently in future detectors.

CHAPTER 5

The MicroBooNE Low Energy Excess Search And Cross Section Opportunities with Wire-Cell

MicroBooNE is a school bus-sized LArTPC that has been taking data since 2015. Its primary goals are to investigate the MiniBooNE low energy excess (LEE) and pursue a wide-ranging cross section program and novel beyond-the-Standard-Model searches. MicroBooNE has also led the way in next-generation LArTPC calibration and reconstruction. This chapter introduces the MicroBooNE detector and its high level physics goals, focusing on analyses that use the Wire-Cell reconstruction toolkit.

5.1 The MicroBooNE Detector

MicroBooNE is the first of three planned detectors that make up the Short Baseline Neutrino (SBN) Program at Fermilab. It sits in the Booster Neutrino Beam (BNB) at Fermilab at a baseline of 470 m [104]. MicroBooNE also observes an off-axis flux from the NuMI beam line, with average neutrino energies peaked in the hundreds-of-MeV range (this off-axis NuMI flux peaks at lower energies than the GeV-scale on-axis flux). Neutrinos from NuMI serve not only as a validation tool for the blinded capstone LEE analysis underway in MicroBooNE, but also provide many additional interesting analysis opportunities, several of which are discussed in this chapter.

The MicroBooNE detector is a 2.6 m (w, drift direction) $\times$ 2.3 m (h) $\times$ 10.4 m (l, beam direction) LArTPC with an active mass of 85 t. The 170 t detector cryostat is shown being lowered into the surface-level detector hall in Figure 5.1. Operated with a drift field of 273 V/cm, the maximum drift time in MicorBooNE is 2.2 ms. The anode plane is instrumented with three wire planes, each

Figure 5.1: The MicroBooNE detector being lowered into the detector hall at Fermilab. Courtesy of Fermilab.

with wires spaced at 3 mm and rotated at 60 degrees from the other two planes. Across all three planes there are a total of 8,256 readout channels.

MicroBooNE has a photon detection system consisting of 32 8″ photomultiplier tubes (PMTs), each placed behind a wavelength-shifting plate, and four scintillator light guides to record prompt scintillation light that aids in identifying beam-related actively among cosmic backgrounds. The PMTs and light guides are mounted behind the anode wire planes. A diagram of the MicroBooNE photon detection system inside the TPC is shown in Figure 5.2.

The detector is also outfitted with a cosmic ray tagger (CRT) external to the cryostat to tag cosmic backgrounds prevalent in surface detectors with ms-scale readout windows [105]. MicroBooNE observes cosmic rays at a rate of about 5 Hz, which corresponds to about 24 cosmic-related backgrounds per 4.8 ms readout window. The CRT is made of plastic scintillator paddles that provide position and timing information for cosmic muons that pass through the detector.

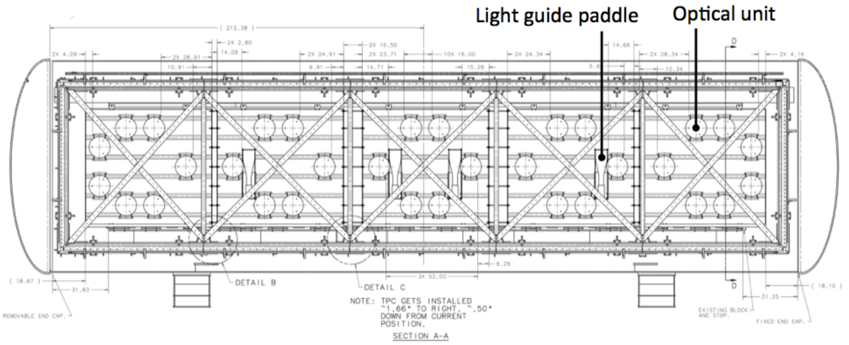

Figure 5.2: Diagram of the MicroBooNE photon detector system in the TPC. The light collection system consists of 32 8″ PMTs, each behind a wavelength-shifting plate (labeled "optical unit" in the diagram) and four scintillator light guides. Image from Ref. [104].

5.2 Physics in MicroBooNE

MicroBooNE's primary goal is to shed light on the anomalous low energy electron-like excess observed initially by LSND and then MiniBooNE (with 4.8σ significance, see Section 1.4.1 for details). While MiniBooNE has some ability to differentiate between electrons and photons, the primary background in the MiniBooNE result remains neutral pions (which decay to a pair of gammas with a branching ratio of 99%). LArTPCs are ideal for electron/gamma separation because they provide high-resolution calorimetry and topological information that can be used to separate electrons, which originate from the neutrino interaction vertex and have dE/dx equivalent to one minimum ionizing particle (1.7 MeV/cm), while photons produced from π^0 decays typically begin some distance away from the neutrino vertex, and have dE/dx near their vertex equivalent to two minimum ionizing particles. MicroBooNE seeks to resolve whether the excess observed in MiniBooNE is electron-like (eLEE) or photon-like (gLEE). The observed MiniBooNE excess, unfolded into true neutrino energy, is shown in Figure 5.3 for the electron-like and photon-like hypothesis. While the electron-like excess exhibits strong energy dependence, the photon hypothesis (interpreted as an increase in the NC resonant Δ production, here) is a uniform scaling of the photon production rate across all neutrino energies.

The ICARUS and SBND detectors, in combination with MicroBooNE, will be able to further elucidate the mystery. Should the MiniBooNE excess be explained by a eV-scale sterile neutrino oscillation, SBND will measure the unoscillated BNB flux, sitting at a shorter baseline than Micro-

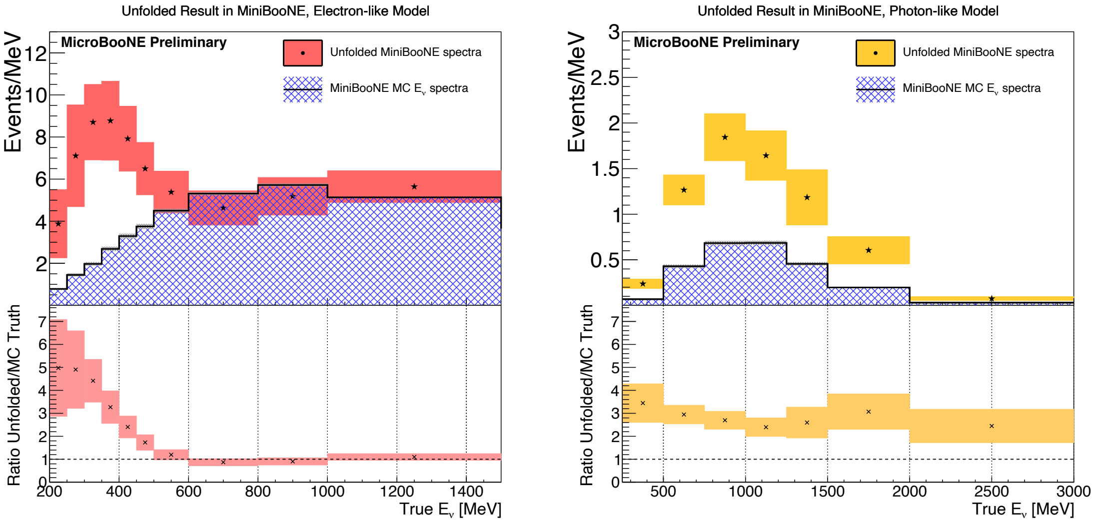

Figure 5.3: The MiniBooNE low energy excess as a function of true neutrino energy, unfolded under the (left) electron (from intrinsic ν_e) and (right) photon (from NC resonant Δ production) hypotheses. While the electron-like hypothesis shows strong energy dependence, the photon hypothesis can be thought of as a uniform scaling of the photon-like signal by a factor of $\sim$3. Figure from Ref. [106].

BooNE and ICARUS, reducing beam-related uncertainties in the MicroBooNE observations.

In addition to the LEE searches, MicroBooNE has also begun reporting [99, 107–110] and continues to pursue high statistics neutrino-argon cross section measurements and other data-driven model constraints [111, 112].

Several reconstruction paradigms are being pursued in parallel within the MicroBooNE collaboration, with three primary toolkits, each pursuing an LEE result in addition to being applied to other physics analyses. Having multiple analysis tracks working in parallel allows for coverage of a wide range of final state topologies and also makes it possible to check for consistency across analyses in the process of unblinding the LEE region for the first result. The three reconstruction paradigms are know as Pandora [113], Deep Learning [75, 114–116], and Wire-Cell [117–119]. Each approach has unique advantages, but the remainder of this chapter will focus on the Wire-Cell toolkit.

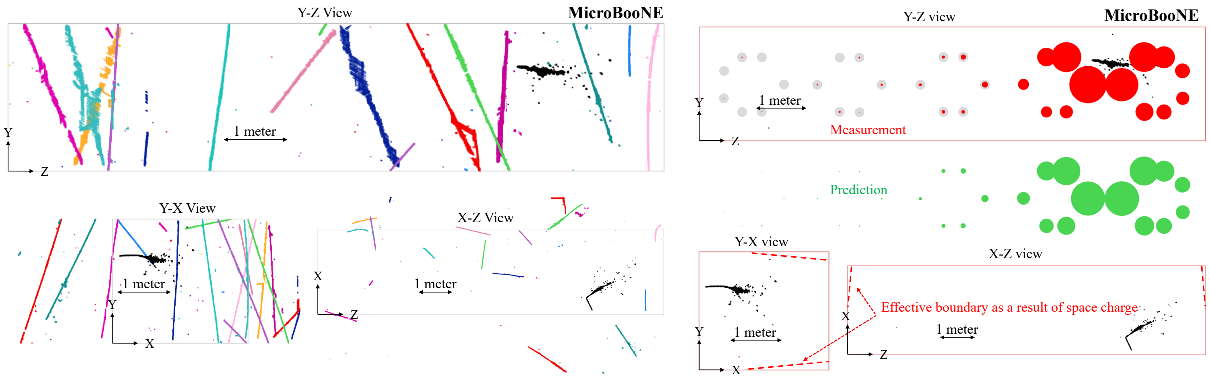

Figure 5.4: A ν_e charged current interaction candidate in MicroBooNE, reconstructed and identified with Wire-Cell. Here, the y coordinate increases going up in the vertical direction and the z coordinate increases moving downstream along the beam direction. (left) Reconstructed clusters in a single event. Most of the clusters are from through-going cosmic muons. The electron neutrino candidate is visible in black on each view. (right) The result of TPC light and charge matching, showing the measured (red) and expected (green) PMT signals for a beam-related candidate like the cluster shown in black. The effective detector boundaries (due to space charge effects) are also shown. Figure from Ref. [117].

5.3 Wire-Cell Reconstruction and Generic Neutrino Selection

After noise removal [120] and signal processing [121, 122], the Wire-Cell reconstruction algorithm takes two-dimensional charge information from the three wire planes in MicroBooNE and uses a custom tomographic three-dimensional image reconstruction algorithm to reconstruct the event in slices of 2 μs. Additional algorithms were developed to handle regions where detector defects, including nonfunctional channels (representing about 10% of the readout wires in MicroBooNE, corresponding to 30% of the detector volume), impact reconstruction performance. These algorithms reduce the unusable detector volume to 3% of the total detector active volume. The reconstructed 3D "blobs" of detected ionization charge are clustered based on proximity, with gap removal tools to handle the uninstrumented 3% of volume, into clusters that represent either cosmic ray activity or beam-related activity (neutrino interactions). Reconstructed clusters are shown in Figure 5.4, where each cluster is drawn in a different color. The neutrino activity (a candidate electron neutrino) is shown in black.

To isolate the neutrino cluster from the cosmic backgrounds, a many-to-many charge-light matching algorithm identifies the PMT signal in time with the beam spill that corresponds with the beam-related activity in the event. Figure 5.4 shows the observed and predicted PMT signal for

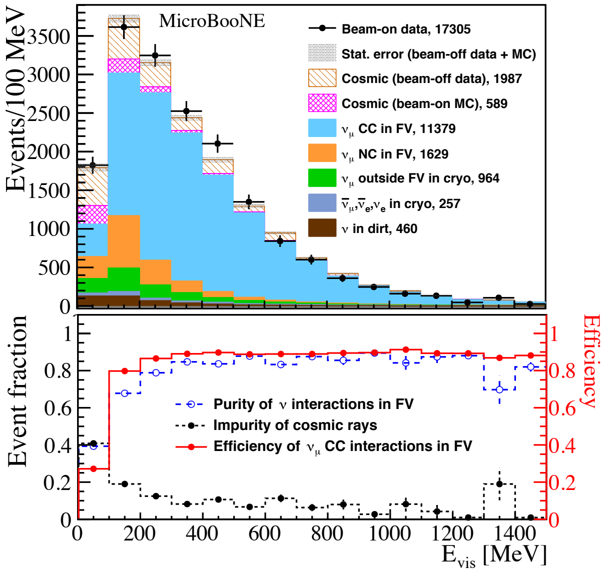

Figure 5.5: The Wire-Cell generic neutrino selection visible energy distribution and efficiency as a function of visible energy for 5×10^{19} POT of BNB data. Figure from Ref. [117].

the candidate electron neutrino event (shown in black). The high level of agreement between the observed and predicted PMT signal is visibly apparent. Additional cosmic background rejection occurs after charge-light matching to further reduce several prominent background categories. Through-going muons that coincide with beam activity are rejected based on the fact that they cross two TPC boundaries (taking into account the effective boundary due to build up of space charge around the edges of the detector; the fiducial volume boundary is 3 cm inside this effective boundary). Stopping muons (cosmic muons that enter the detector and come to a stop inside the detector volume) coincident with the beam signal are rejected based on direction. Their direction is defined using the characteristic increase of dQ/dx (the Bragg peak) as the muon comes to a stop. Finally, events in which the observed PMT response disagrees with the predicted light signal for the cluster of activity selected in the light-charge matching, are also rejected. This "generic" (i.e. flavor agnostic) neutrino selection has efficiency of 80.4% and achieves cosmic rejection at the 10^{-6} level, yielding a neutrino-to-cosmic ratio of 5.2. The distribution of selected neutrino events as a function of visible energy is shown in Figure 5.5. The simulation is scaled to match the 5×10^{19} POT of unblinded BNB data shown overlaid. An example candidate ν_e charged current interaction is shown in Figure 5.6 before and after cosmic rejection for the generic neutrino selection.

Having achieved a high efficiency and purity generic neutrino selection, the Wire-Cell toolkit

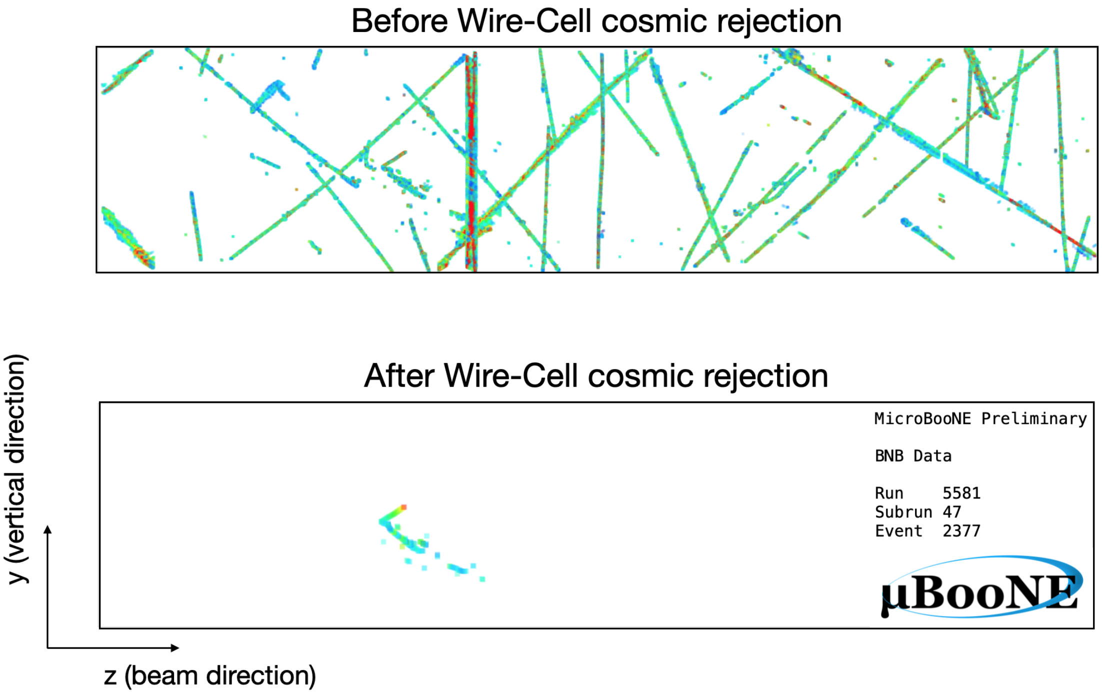

Figure 5.6: An example event display for a candidate charged current ν_e interaction before and after Wire-Cell cosmic rejection.

then focuses on neutrino flavor identification and energy reconstruction. This requires further particle-level pattern reconstruction. The components of Wire-Cell's pattern recognition tools are illustrated in Figure 5.7. Vertices between particles are found using an algorithm that searches for kinks in the 3D cluster. With particle-level sub-clusters defined, particle identification is done using dQ/dx and topological information (primarily for track/shower separation), and particle direction is subsequently defined. Using the collection of reconstructed particles and directions, a neutrino interaction vertex is defined based on particle flow information in combination with deep learning tools. Higher-level electromagnetic shower reconstruction is then performed, often requiring reclustering of multiple sub-clusters, including reconstruction of neutral pions from pairs of photon electromagnetic showers.

Finally, neutrino energy is reconstructed. Particle energies are reconstructed using a combination of range- and dQ/dx-based techniques depending on whether the particle is track-like or shower-like and whether it stops inside the detector. Data-driven charge scaling is also applied, primarily to electromagnetic showers, to better calibrate the reconstructed energy. An additional 8.6 MeV binding energy is added for every proton reconstructed in an interaction, and muon,

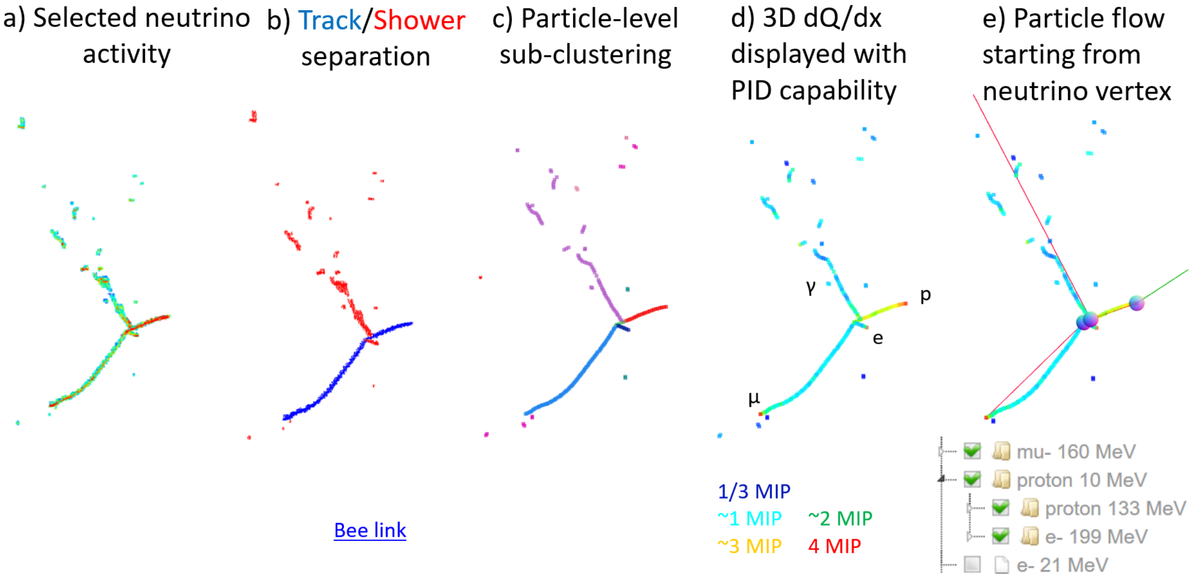

Figure 5.7: Wire-Cell pattern recognition output at several stages in the process. (a) The candidate neutrino activity is selected using the generic neutrino selection. Color represents reconstructed charge. (b) Track (blue) -shower (red) separation. (c) Particle-level clustering. Each particle cluster is shown in a different color. (d) Three-dimensional dQ/dx measurement. The approximate dQ/dx in terms of minimum ionizing particles (MIPs) as a function of color is indicated in the key. (e) Particle flow is determined, starting at the neutrino vertex. This interaction contains a a muon, proton, and gamma extending from the neutrino vertex. (The gamma is labeled as an electron as a proxy for all EM showers. Detailed electron/gamma separation has not occurred at this point.) Courtesy of Ref. [123].

charged pion, and electron masses are included as necessary. The neutrino energy reconstruction achieves 10-15% resolution for ν_e CC events across all BNB energies. A more detailed discussion and thorough validation of the Wire-Cell neutrino energy reconstruction can be found in Ref. [123].

5.4 The Wire-Cell ν_e Selection and Low Energy Excess Search

The Wire-Cell eLEE search aims to efficiently select a highly pure sample of low-energy charged current inclusive electron neutrino interactions in MicroBooNE. In addition, a series of background channel selections are defined to act as constraints. After Wire-Cell generic neutrino selection, the ν_μ CC and ν_e CC selection efficiencies are approximately 80% and 90%, respectively, with signal-to-background ratios of 2:1 and 1:190. Inclusive BDT-based ν_μ and ν_e selections were defined, in addition to CC and NC π^0 selections to constrain these photon backgrounds.

The ν_μ and ν_e selections were developed in stages. The collection of variables used as input for the finalized BDT-based selections were developed first as cut-based taggers with designs motivated by both physics and reconstruction performance. For example, electromagnetic (EM) shower gap and vertex dQ/dx are defined to separate electrons from gamma backgrounds. Common reconstruction failures identified via hand scans of hundreds of events are also removed with dedicated taggers. After preliminary selections were developed combining a variety of case-specific taggers, each dependent on a number of variables, the complete collection of variables from all the taggers was used as input to train BDTs for classifying ν_μ and ν_e CC interactions. The evolution of the ν_e selection, from cut-based taggers through to the final BDT implementation, is shown in Figure 5.8. The BDTs were validated independently by several collaborators. The rejection matrix for each of the taggers in the ν_e selection is shown in Figure 5.9, which also indicates the fraction of events simultaneously rejected by each unique pair of taggers, to illustrate the correlation between taggers. The ν_μ and ν_e CC inclusive selections achieve 83% and 93% efficiency, respectively, and 42% and 64% purity.

To maximize the eLEE sensitivity, a seven-channel fit is done. The LEE search channel is fully contained ν_e CC events. Three more channels, partially contained ν_e CC, fully contained ν_μ CC, and partially contained ν_μ CC, are used to constrain the signal prediction via, for example, neutrino flux, cross section, or detector systematics. The final three channels, fully contained CC π^0,

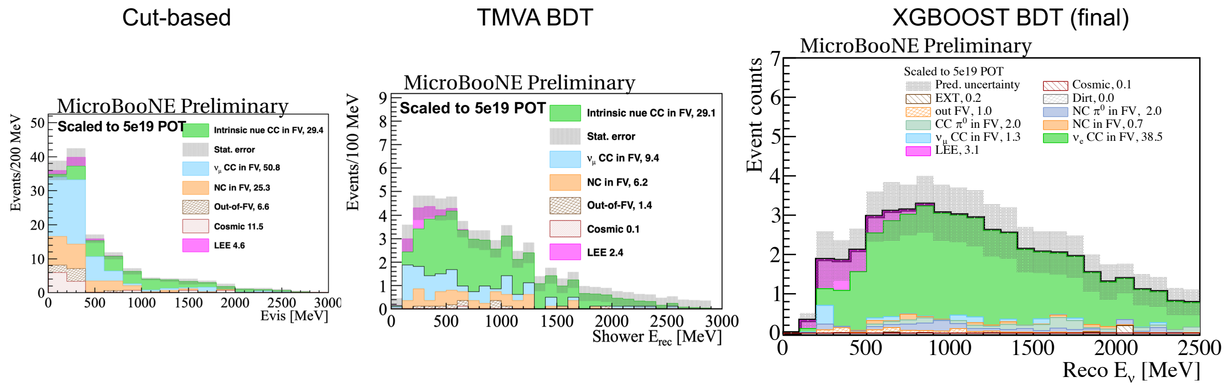

Poor purity
32% nueCC eff
4.6 LEE

63% nueCC purity
32% nueCC eff
2.4 LEE

83% nueCC purity
42% nueCC eff
3.1 LEE

Figure 5.8: Evolution of the Wire-Cell ν_e selection, from (left) low statistics hand-scan and cut-based tools to (right) high staticistics machine learning-trained classifiers that yield high purity ν_e CC selections. Courtesy of Ref. [123].

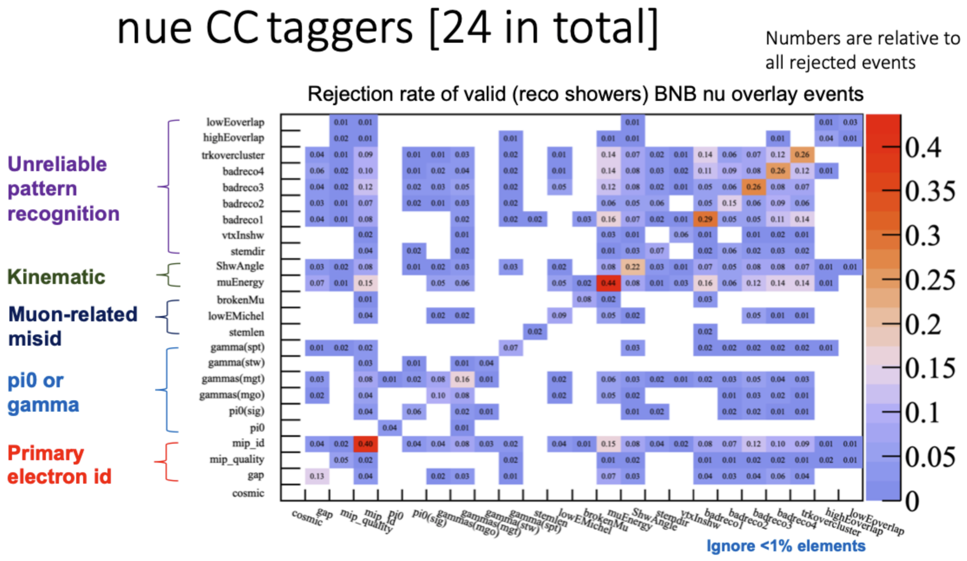

Figure 5.9: Rejection matrix of the various ν_e taggers developed and included in the BDT-based ν_e selection. Each tagger is designed to identify a common signal or background feature that can be grouped roughly into five different types: 1) electron identification including vertex dQ/dx and gap information, 2) photon background classification, 3) muon misidentification, (e.g. low-energy ν_e interactions can often resemble low-energy muons), 4) background rejection via kinematic information, and 5) poor/unreliable pattern recognition. The off-diagonal terms indicate the fraction of events rejected by both taggers to illustrate correlations between taggers.

partially contained CC π^0, and NC π^0 serve to improve π^0 background estimates (remember that is the most prominent background in the MiniBooNE LEE). The channel definitions are exclusive (i.e. CC π^0's are removed for the ν_μ and ν_e CC channels) to make them statistically independent. The distributions of events in each channel are shown in Figure 5.10. Systematic uncertainties take into account uncertainties in neutrino flux, cross sections, detector response, and simulation statistics. Total systematic uncertainties are indicated by the red band in the bottom panel of each plot. In all plots, simulation is scaled to 5×10^{19} POT, corresponding to the amount of open BNB data. No data is overlaid on the ν_e channels because there are very few of these signal events in the open data. Validation of the ν_e selection performance on a large sample of signal events is done using a separate, unblinded data stream from NuMI, discussed in the next section.

Towards finalizing the first Wire-Cell eLEE search in MicroBooNE, a series of side bands around the signal region are defined, to test and validate the analysis on samples of currently blinded events that surround the signal region. Side bands are defined along two axes: an energy axis and a ν_e ID axis (for Wire-Cell ν_e BDT score is used). A far side band, with reconstructed neutrino energy above 800 MeV or ν_e BDT score below 0, was recently approved for unblinding in Wire-Cell. Pending approval of the far side band results, the LEE analysis will be fully frozen and a near side band, defined to include events with reconstructed neutrino energy between 600 and 800 MeV and ν_e BDT score above 0, or with ν_e BDT score between 0 and 7 and reconstructed neutrino energy less than 800 MeV, will be unblinded. The signal box for the Wire-Cell LEE search is defined to include all events with a reconstructed neutrino energy below 600 MeV and a ν_e BDT score above 7. This unblinding procedure (with adjustments as necessary to the definitions of each side band) are the same across all LEE analyses working in parallel, and each requires independent approval to open its side bands. Thorough crosschecks for consistency across the parallel LEE analyses will also be performed and reported. An example ν_e candidate selected by Wire-Cell is shown in Figure 5.11.

5.5 Validation with NuMI Data

To complement the formal unblinding of BNB data in stages, independent validation of the Wire-Cell selections can be done using the NuMI data stream. NuMI's flux has higher intrinsic ν_e rates

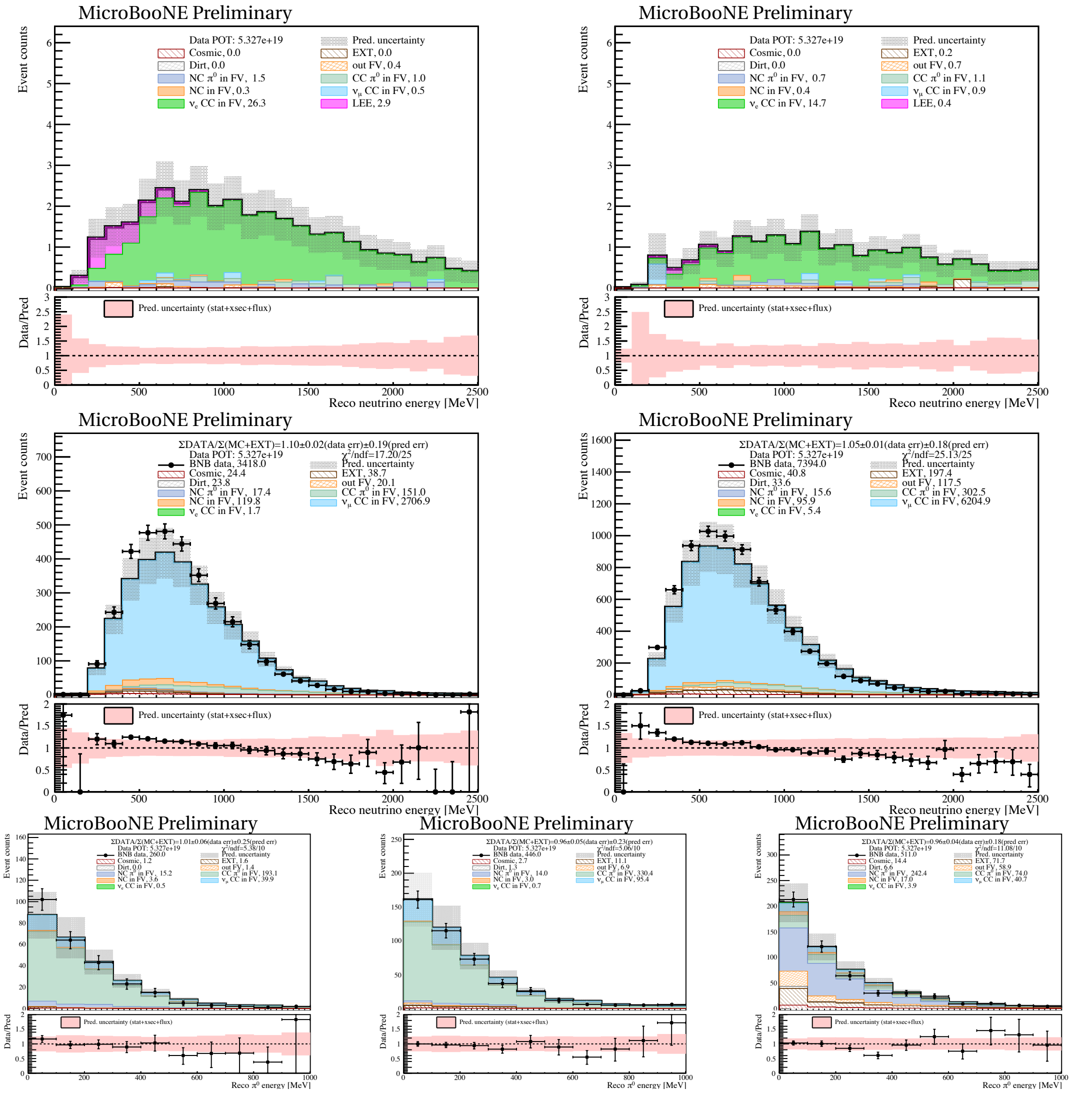

Figure 5.10: The seven-channel selection for the Wire-Cell low energy excess search with open BNB data overlaid. (top left) Fully contained ν_e CC, (top, right) partially contained ν_e CC, (middle left) fully contained ν_μ CC, (middle right) partially contained ν_μ CC, (bottom left) fully contained CC π^0, (bottom middle) partially contained CC π^0, (bottom left) and NC π^0. MC statistics and systematic (including flux and cross section) uncertainties are shown in the red band on the bottom panel.

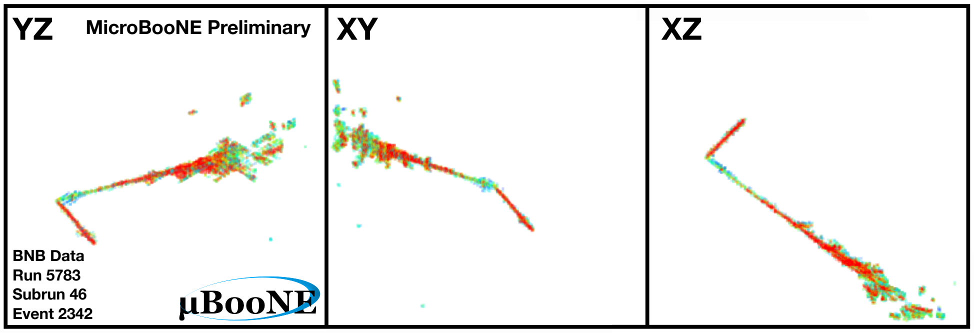

Figure 5.11: An example ν_e candidate selected by Wire-Cell.

than BNB. In addition, there is ten times the amount of open data available (just under 7×10^{20} POT of NuMI data has been processed with Wire-Cell reconstruction). In particular, agreement between data and simulation for high ν_e BDT scores is much easier to evaluate with the large number (on the order of hundreds) of ν_e interactions available. The ν_e BDT score distribution for NuMI data and simulation are shown in Figure 5.12. The ν_e selection requires a score greater than 7. At high BDT scores there is good agreement between data and simulation. The NuMI distributions for all seven channels defined in the Wire-Cell LEE analysis are shown in Figure 5.13.

A hand scan of the NuMI data events in the ν_e channels between 400 MeV and 800 MeV was performed to investigate the region where a slight excess of ν_e CC candidate events is observed in data. None of the selected events had unexpected features or failures of reconstruction. Independent validation of the NuMI results was done outside of the Wire-Cell framework to confirm that no new analysis framework-related bugs were introduced in porting the framework over to NuMI. Additional validation of the data processing workflow and careful investigation of the results are ongoing.

5.6 Cross Section Opportunities with Wire-Cell

Given Wire-Cell's high resolution (in the realm of neutrino physics) energy reconstruction capabilities and incredibly efficient particle and neutrino flavor identification tools, it can also be used for making cross section measurements. A general framework for cross section analyses, including unfolding using the Weiner-SVD method and systematics evalutation, has been built on top of Wire-Cell reconstruction. Already, a BNB ν_μ CC inclusive cross section result is in preparation for

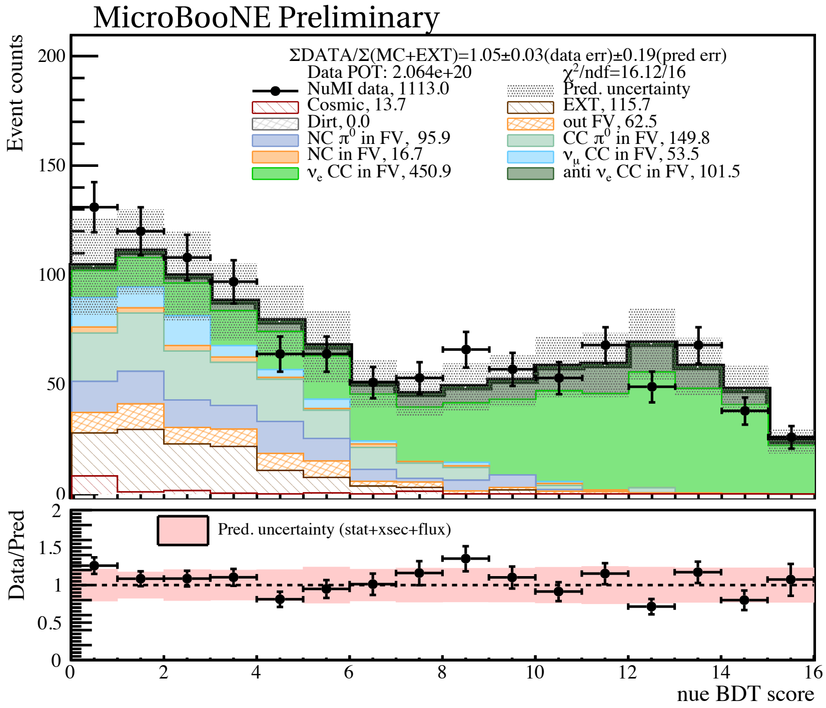

Figure 5.12: Wire-Cell ν_e BDT score for NuMI data (both fully and partially contained events are included). The increased ν_e statistics provide validation of the BDT training for high BDT scores with good data/MC agreement. This is the blinded signal region for BNB data.

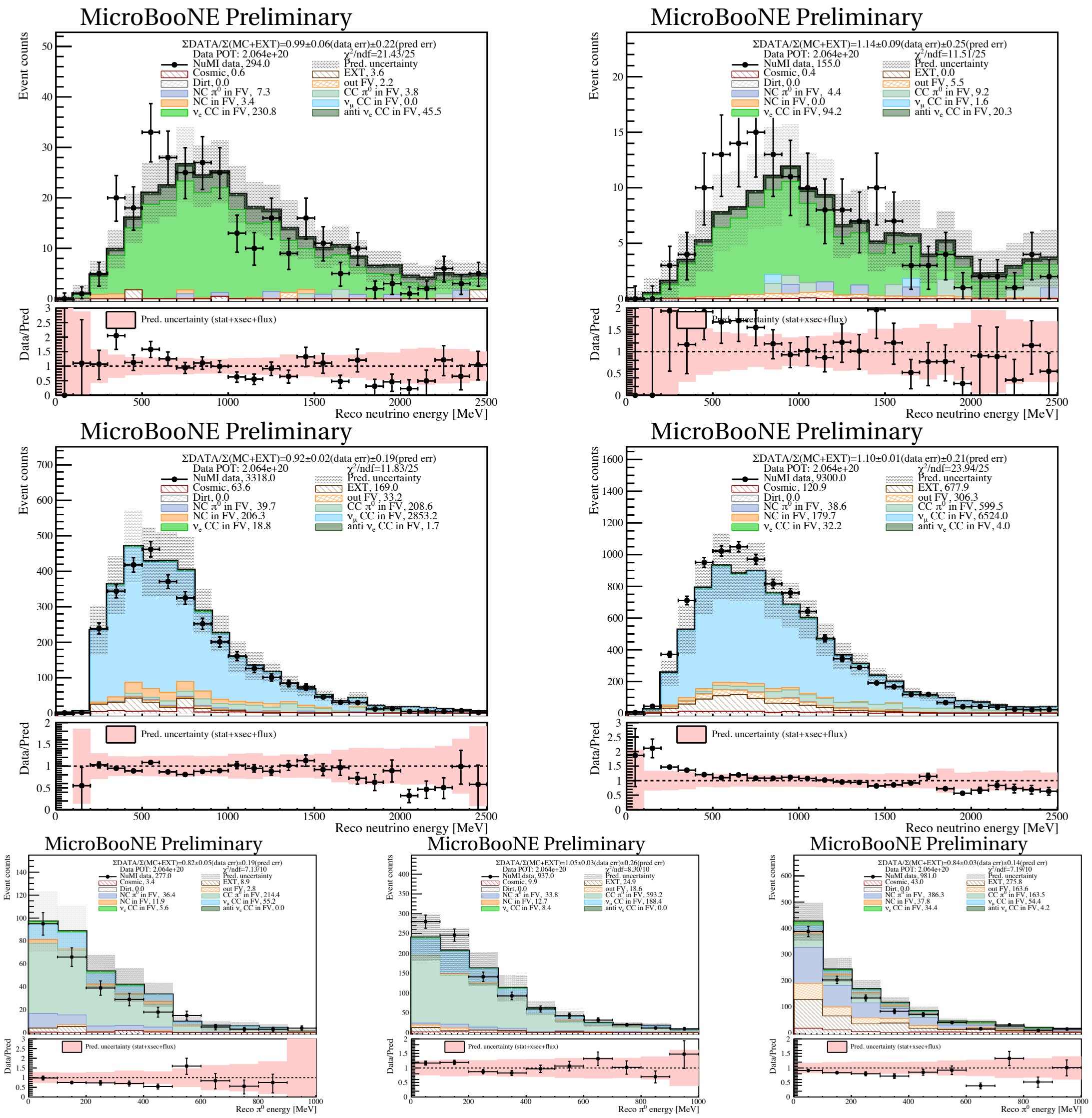

Figure 5.13: The seven-channel selection for the Wire-Cell applied to NuMI data. (top left) Fully contained ν_e CC, (top, right) partially contained ν_e CC, (middle left) fully contained ν_μ CC, (middle right) partially contained ν_μ CC, (bottom left) fully contained CC π^0, (bottom middle) partially contained CC π^0, (bottom left) and NC π^0. MC statistics, flux, and cross section uncertainties are shown in the red band on the bottom panel.

publication to lead the way on what will be a robust cross section program within a single reconstruction framework. Novel cross section measurements are also possible. In particular, the MicroBooNE detector observes monoenergetic 236 MeV muon neutrinos produced by kaon decays at rest (KDAR) in the NuMI beam dump. Chapter 8 discusses these special neutrinos in depth. The KDAR neutrino flux in MicroBooNE can be isolated from background using both direction (the neutrino should come from the direction of the NuMI beam dump) and timing information. Measuring this known-energy signal can both help to constrain neutrino-nucleus interactions models and also be used as an energy calibration tool for evaluating the detector response in MicroBooNE.

CHAPTER 6

Photon Detection for The Short Baseline Near Detector[1]

This chapter summarizes five years of hardware tests during the development of a final strategy for SBND photon detection (PD), culminating in the imminent installation of the PD system and the start of data taking in SBND later in 2021. The design has been through several iterations, responding both to collaboration testing and validation but also the results and research and development needs of the larger community.

6.1 The SBND Detector and Physics in SBND

SBND is the final of three LArTPCs that together form the Short Baseline Neutrino Program (SBN) [86, 96]. SBND, as the near detector, will join ICARUS [124] and MicroBooNE [104] to complete the suite of detectors that was designed to 1) search for short baseline oscillations that would be evidence for sterile neutrinos, 2) measure neutrino-argon interactions, and 3) perform a slew of other beyond the Standard Model physics searches. The SBN Program is illustrated in Figure 6.1 with each of the detector baselines indicated. The three detectors sit on axis in the BNB source, and also observe off-axis flux from the NuMI beam line.

SBND sits a mere 110 m from the BNB target and, once operational, will collect beam neutrino interactions at an unprecedented rate. It is a single phase LArTPC with an active mass of 112 t. The 5 m (l) $\times$ 4 m (w) $\times$ 4 m (h) TPC has a central cathode plane to be held at -100 kV with two

---

[1] It would be remiss if I didn't highlight the contributions of several Spitz group undergraduates in this work over the years. Claire Savard performed the analysis that yielded the earliest observations of single-photoelectron signals with the Mu2e front end board (Section 6.4). Polina Abratenko performed tests to demonstrate that noise on a TPC from the photon detector electronics was low to negligible (Section 6.7). Daniel Mishins developed the laptop-based DAQ system that has been used for the cryocooler tests (which he performed, Section 6.8), in early ICEBERG runs, and for QA/QC test of the X-TDBs for SBND.

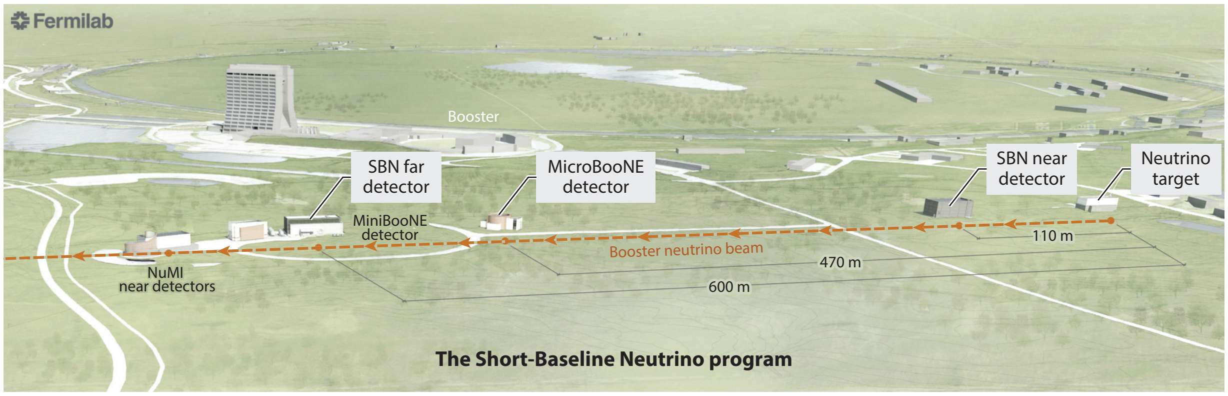

Figure 6.1: The SBN Program in the Booster Neutrino Beam. Image for Ref. [86].

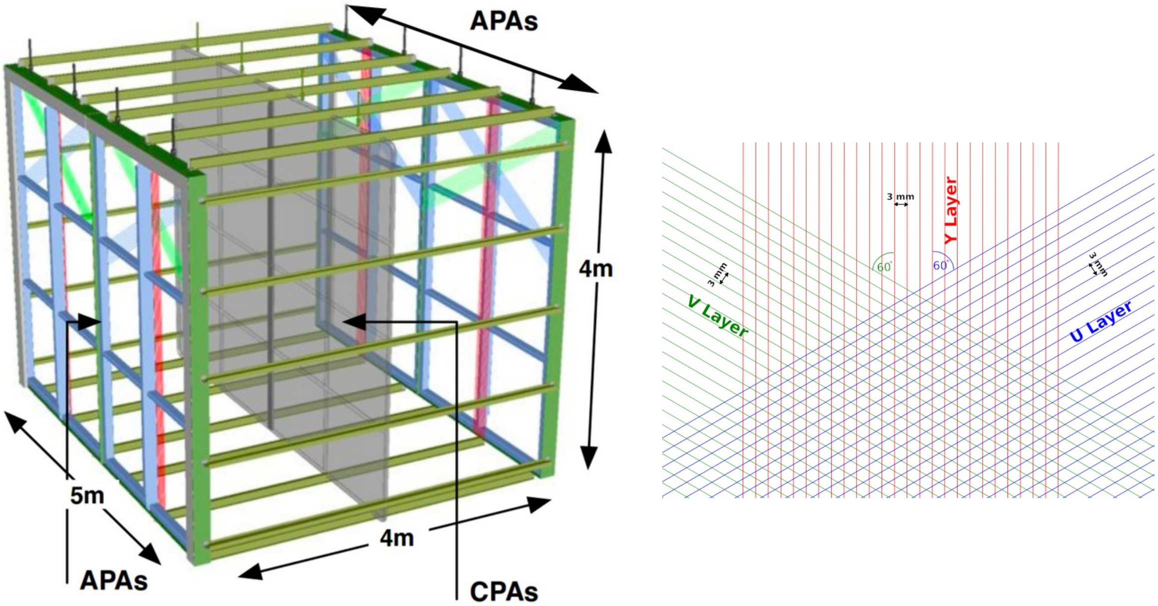

Figure 6.2: (left) The SBND detector and (right) the orientation of each of the three wire planes on both anode planes. Images from Ref. [125].

fully instrumented anode planes on either side held at ground. This yields a drift field of 500 V/cm and maximum drift distance of 2 m. A schematic of SBND is shown in Figure 6.2. The anode planes are each instrumented with three wire planes. There are 1664 wires on the vertical planes and 1984 wires on the planes oriented at $\pm 60^\circ$. The wires are all separated by 3 mm. SBND is a surface detector, so like MicroBooNE it will contend with a high rate of cosmic interactions. The detector is surrounded almost entirely by a solid scintillator cosmic-ray muon tracker (CRT) that can be used to tag these backgrounds. Recent advances have been made in cosmic background removal for SBND using neural networks [126]. Finally, the TPC is also outfitted with a photon detection system to collect prompt scintillation photons produced by particles traversing the liquid argon. Particularly for a surface detector, the photon detection system provides useful timing and position information for distinguishing beam-related interactions from backgrounds. The development and testing of the photon detection system is the focus of the remainder of this chapter.

6.2 Overview of the SBND Photon Detector System

The photon detector system in SBND is designed to bridge new and old light collection paradigms in LArTPCs. The detector is outfitted with both PMTs, like MicroBooNE, but will also employ X-ARAPUCA light collectors with SiPMs. The redundancy of the photon detector system enables both cross comparison and R&D opportunities inside a fully operational large-scale TPC. The photon detector system represents its own subsystem, and will not be discussed in detail here. The X-ARAPUCA system has evolved over time from a combination of light bars and ARAPUCAs to the final designs consisting of solely X-ARAPUCAs. Design concepts and testing of the X-ARAPUCA light collectors are discussed in more detail in Chapter 7. The transition to a fully X-ARAPUCA-based system (in combination with PMTs) was motivated in part by parallel work by DUNE. The SBND photon detector system is shown in Figure 6.3. There are 6 PDS boxes per APA frame (with two frames per anode plane). Each PDS box houses five 8″ Hamamatsu PMTs with 1 ns timing resolution and 8 X-ARAPUCAs, each with four readout channels. Ninety-six of the 120 PMTs are coated in TPB and the remaining 24 (the center PMTs in each box) are left uncoated. Among the X-ARAPUCAs, half are sensitive to visible light and the other half are sensitive to

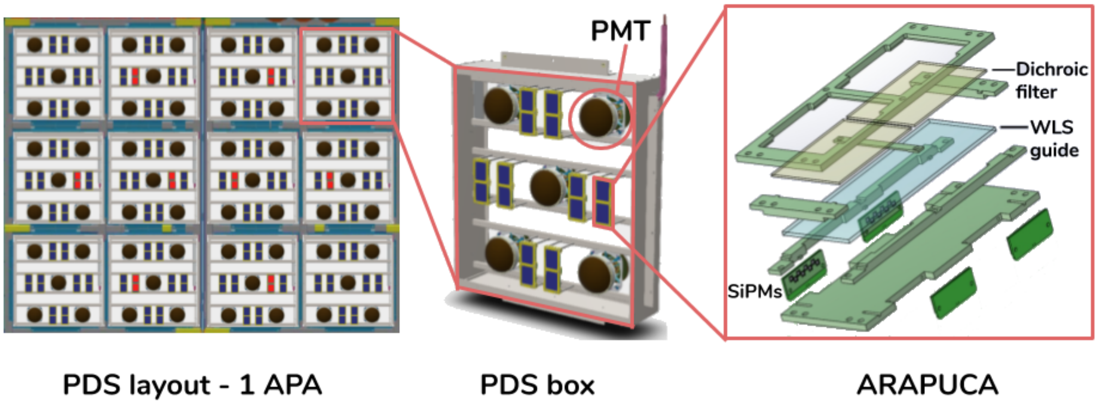

Figure 6.3: The SBND photon detector system uses both traditional PMTs and new X-ARAPUCAs. Courtesy of T. Brooks.

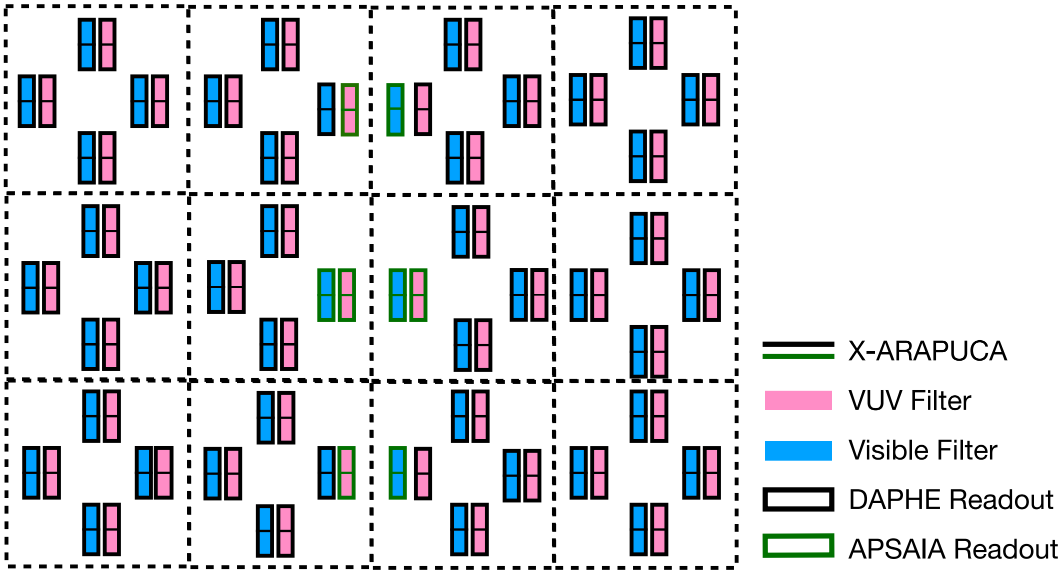

Figure 6.4: The X-ARAPUCA layout on one SBND anode plane. Courtesy of J. Mousseau.

VUV light. Eight of the 96 X-ARAPUCAs on each anode plane are being read out with APSAIA readout electronics (beyond the scope of this work). The remaining majority are read out with Mu2e readout electronics. The layout of the different X-ARAPUCA configurations is illustrated in Figure 6.4. The remainder of this chapter details the testing and design of the Mu2e-based readout system and the X-ARAPUCA SiPM carrier boards (X-TDBs).

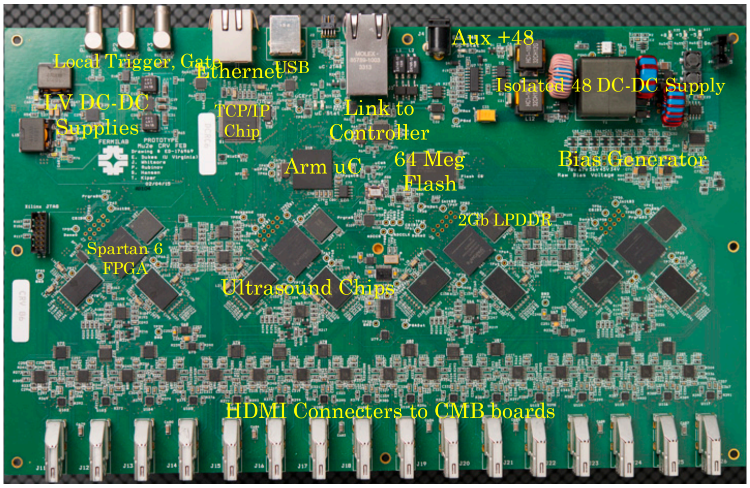

Figure 6.5: The Mu2e front end board. Courtesy of S. Hansen.

6.3 A Cost-Effective Solution for Photon Detector Readout Electronics

Motivated by their cost effectiveness, the University of Michigan group began studies in 2016 to determine the viability of existing Mu2e prototype front end boards (FEBs) for the SBND photon detection system. These boards were designed to be used in the Mu2e veto system and were appealing for their core ultrasound chip technology. These commercially available ultrasound chips have 8-channel 12-bit analog-to-digital converters (ADCs). Each readout board can accommodate 64 readout channels in groups of four per cable. The Mu2e FEBs can transfer data at 10 MB/s. A rough estimate based on observed MicroBooNE rates suggests that the readout must be able to handle 22 MB/s of data. The planned 12 FEBs for reading out all 768 photon detector channels will be sufficient for handling this data rate, which can be further adjusted by altering the length of the PDS readout window or introducing zero suppression to the data stream.

6.4 Preliminary Tests with the Mu2e Front End Boards

Initial tests were done with hardware on hand to illustrate that the Mu2e prototype boards could achieve single-photoelectron resolution using an array of SiPMs on a carrier board. An existing ProtoDUNE SiPM carrier board, which housed 12 6 mm × 6 mm SiPMs grouped into four channels, with the SiPMs connected in parallel within each channel, was used. Light was provided by an LED flasher pulsed in time with the FEB trigger. The LED and SiPMs were placed inside a

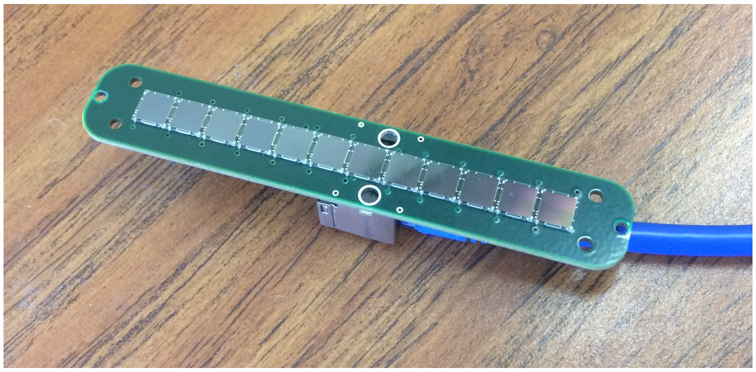

Figure 6.6: The ProtoDUNE SiPM carrier board used in initial tests with the Mu2e FEB. The SiPMs are ganged in parallel in group of three (see Figure 6.7).

dark box and the SiPMs were cooled with liquid nitrogen. The carrier board is shown in Figure 6.6 and the circuit configuration is shown in Figure 6.7. A Cat6 cable connects to the board and each twisted pair carries one channel of data. A Cat6 to HDMI converter board (also borrowed from Mu2e) was used to connect the output to the FEB for reading out data.

Example average waveforms on each channel are shown in Figure 6.8[2] along with a comparison of data taken with the LEDs on, powered using 2.68 V, and off. The SiPMs were biased with 28.5 V. The long fall time of the pulse is related to the increased capacitance of the system that results from connecting the SiPMs in parallel. Shielded cables were found to reduce the amount of noise in the system, as expected. The noise (or "pedestal") data piles up in the first peak above zero, with some indication of dark rate pulses in the tail up to higher values. When the LED is on and flashing a distinct set of peaks is visible, each representing a number of photoelectrons (PE) above zero. The first peak represents noise or no light, the second 1 PE, the third 2 PE, etc. To better mimic a realistic detector setup, a much longer $\sim$50 m Cat6 cable was tested and a significant reflection was observed, shown in some example waveforms in Figure 6.9.

As noted previously, the default ProtoDUNE board configuration ganged SiPMs together in parallel within each readout channel. This has a disadvantage of tripling the capacitance of the source and naturally leads to a longer pulse length and a smaller pulse height. An alternative scenario was tested with the SiPMs ganged in series to reduce the capacitance of the system by a factor of three. In this configuration, the same overvoltage can be applied to the SiPMs by tripling

---

[2] Note: throughout this chapter and the next chapter, when waveforms are shown in units of ticks, it can be assumed that 1 tick = 12.55 ns.

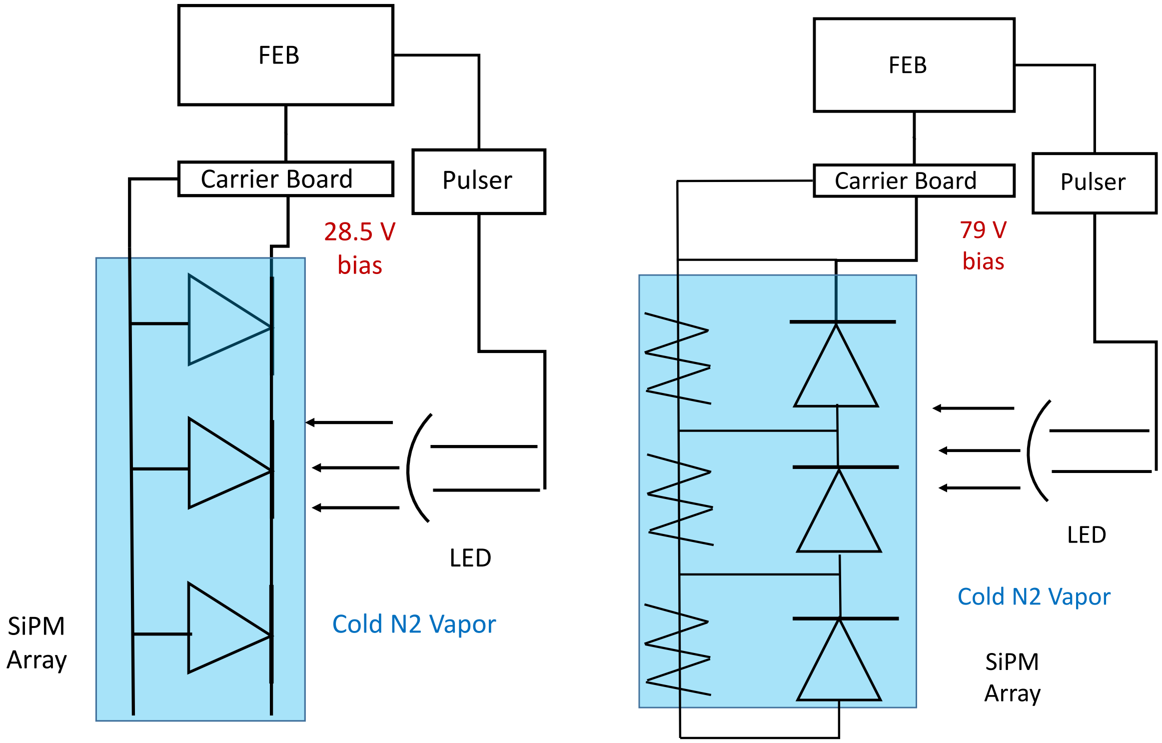

Figure 6.7: ProtoDUNE carrier board circuit configurations with SiPMs wired (left) in parallel and (right) in series.

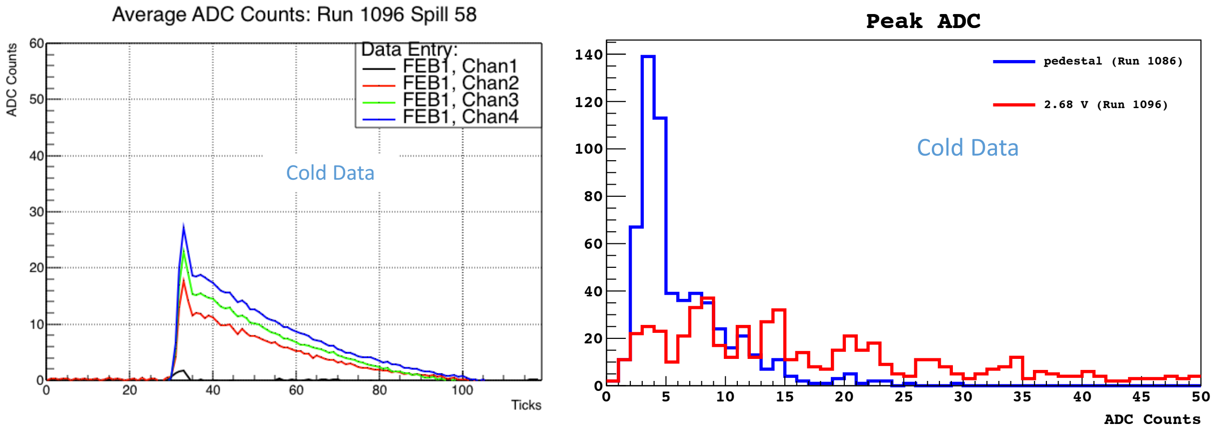

Figure 6.8: (left) Average waveforms collected and read out by the ProtoDUNE carrier board with SiPM connected in parallel and the Mu2e FEB. The low pulse amplitude and long tail are a factor of the increased capacitance that results from connecting the SiPMs in this configuration. (right) Evidence of single photoelectron resolution above noise ("pedestal"). With the LED powered at 2.68 V, the first peak in data above zero is noise, matching data taken with the LED off, and the second peak represents one PE, the third 2 PE, etc.

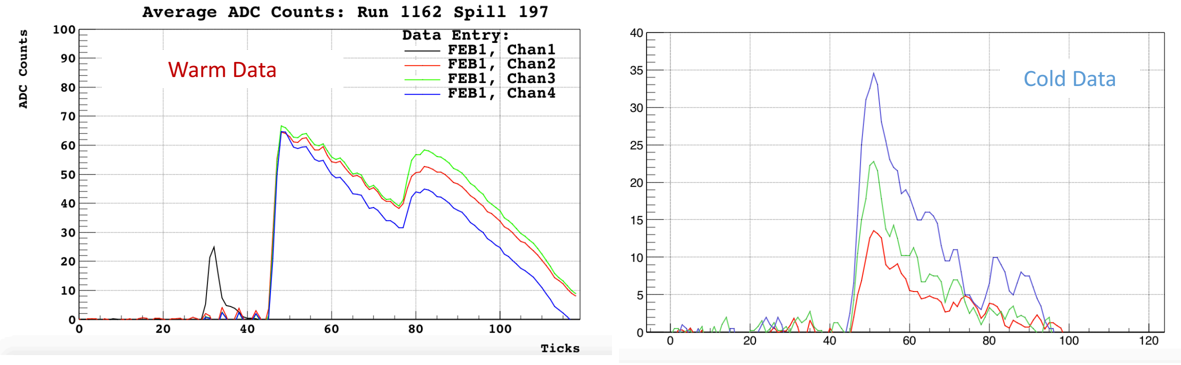

Figure 6.9: (left) Average waveform from warm data taken with the ProtoDUNE carrier board SiPMs wired in parallel. (right) Average waveform from cold data taken with the ProtoDUNE carrier board SiPMs wired in series. Though recorded at different temperatures, the shapes of the waveforms are representative of signals at any temperature. (See Figure 6.10, for example.)

the bias voltage (79 V is used here). 500 kΩ resistors were used as voltage dividers. The wiring is shown in Figure 6.7 and a side-by-side comparison of pulse shape with the long Cat6 cable is shown in Figure 6.9. In addition to significantly reducing the pulse length, the reflection has also almost entirely disappeared. Evidence of single PE signals was also observed, as shown in Figure 6.10.

6.5 Custom Carrier Board, First Iteration: The TDB

Based on the outcome of the initial SiPM readout tests with the Mu2e boards, a custom carrier board was designed for the SBND light bars (the first iteration of the SBND PD system included scintillator light bars in place of X-ARAPUCAs. The final iteration of the SiPM carrier board will be discussed in the next section). This design ganged arrays of four 3 mm × 3 mm Sensl SiPMs in parallel and then wired three arrays together in series to form one readout channel. A picture of this carrier board (the “tongue depressor board”, or TDB) is shown in Figure 6.11 along with the schematic for one channel of 12 SiPMs.

The dark rate expected for the SiPMs in a warm environment is 3-4 MHz. To verify this and measure the dark rate in cold, for a large sample of readout windows, the number of samples (ticks) that exceeded 10 ADC (the empirically measured approximate 1 PE threshold) was converted to frequency and reduced by a factor of 1.5 to roughly correct for cases where there are two consecutive samples above 10 ADC, presumably from the same pulse:

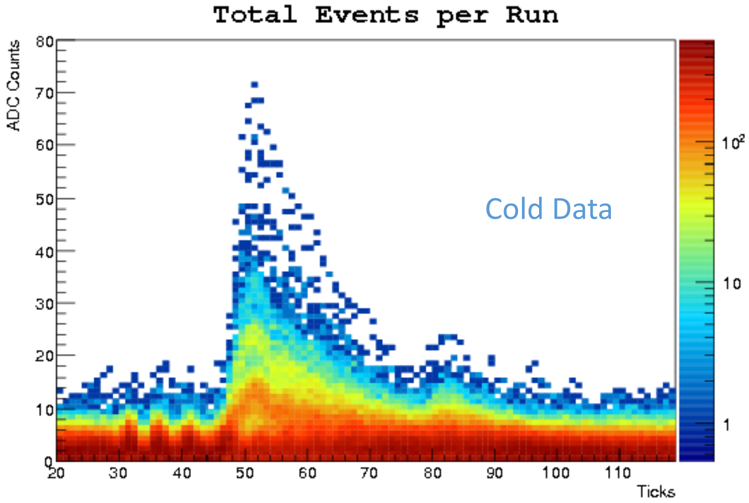

Figure 6.10: Evidence of single photoelectrons observed using the Mu2e readout electronics and ProtoDUNE carrier board with SiPMs wired in series.

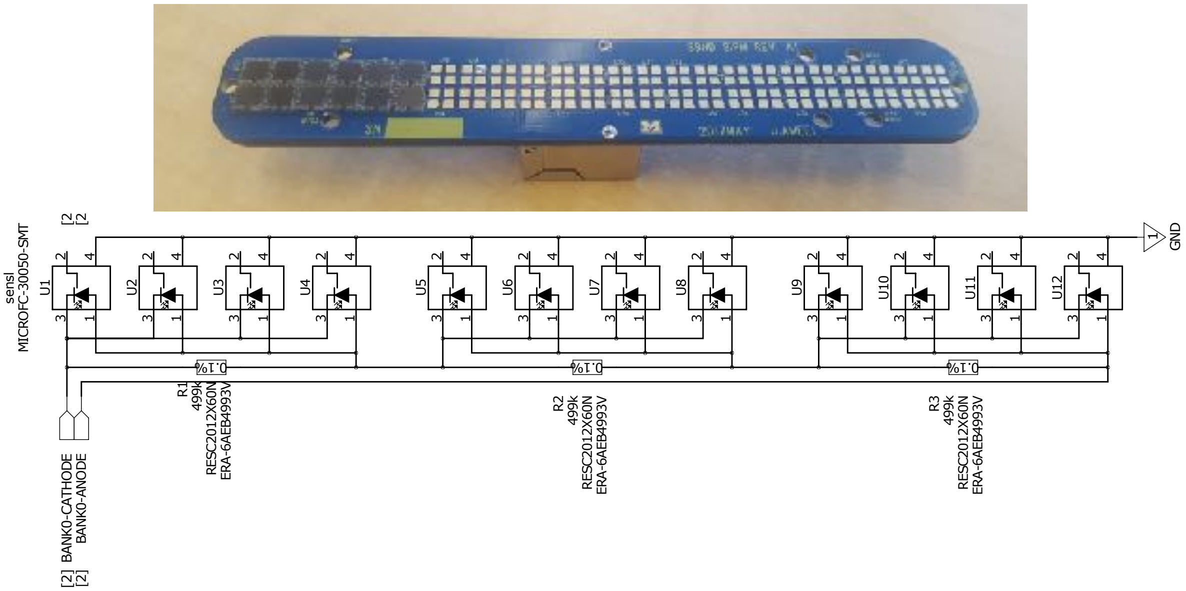

Figure 6.11: The SBND SiPM carrier board prototype (the TDB). The design gangs arrays of four 3 mm × 3 mm Sensl SiPMs in parallel and then wires three arrays together in series to form one readout channel. The are four readout channels per TDB. The bottom schematic shows one channel of 12 SiPMs.

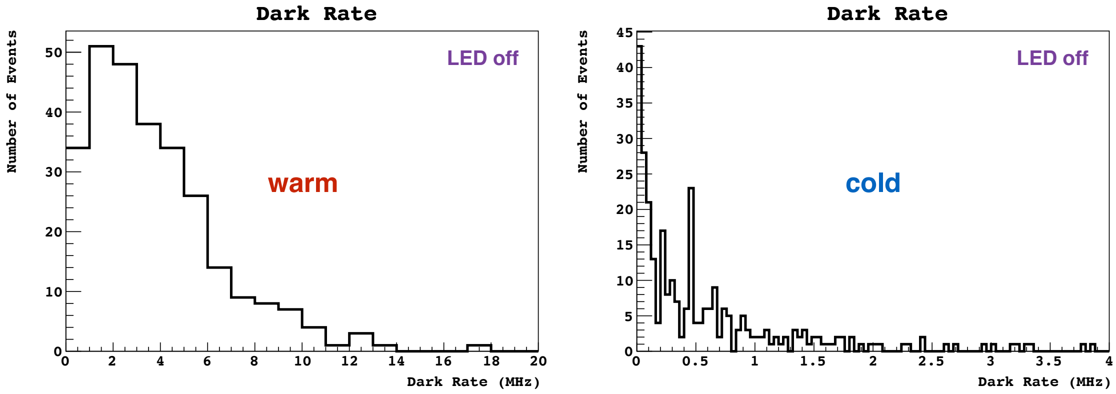

Figure 6.12: The dark rate observed by the TDB in (left) warm and (right) cryogenic temperatures. The warm rate is in the expected range of 3-4 MHz and the cold dark rate is much lower.

$$\text{dark rate} = \frac{\#\ \text{samples} > 10\ \text{ADC}}{12.55\ \text{ns} \times \#\ \text{samples}} \div 1.5. \tag{6.1}$$

The results are shown in Figure 6.12. As expected, the dark rate in a warm environment peaks around 3-4 MHz. The dark rate at cryogenic (LN2) temperatures is significantly lower.

The TDBs were tested in a cold environment with long Cat6 cables to check for single PE resolution. The results are shown in Figure 6.13 for 25 m of cable and in Figure 6.14 for 50 m of cable. 75 V was supplied to the TDB to bias the SiPMs. A reflection is visible in the data taken with the shorter cable, but in both cases individual photon peaks are clearly visible above noise (the first peak above zero, shown in blue with data taken while the LED was off in Figure 6.14).

At this point, a decision was made to replace all the light bars in SBND, for which the TDB was designed, with X-ARAPUCAs, based on several factors including convincing evidence that the X-ARAPUCA design concept significantly increases efficiency for light detection systems, and X-ARAPUCAs in SBND will provide ample R&D opportunities for DUNE. As a result, the TDB underwent one more major redesign to become the X-TDB.

6.6 Final Carrier Board Design: The X-TDB

The X-TDB design adheres to the same principles as the TDB design, but only combines two arrays of four SiPMs ganged in parallel into a single channel, and each X-TDB only houses one channel. There are four X-TDBs per X-ARAPUCA. A fabricated X-TDB and a rendering of an X-ARAPUCA

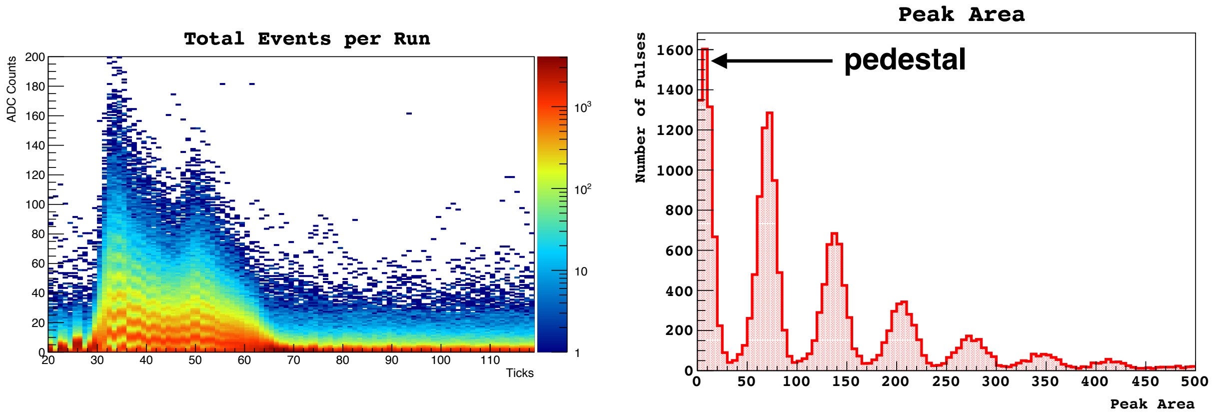

Figure 6.13: Data collected at cyrogenic (LN2) temperatures with the custom TDB and Mu2e readout electronics and 25 m of Cat6a cable. The SiPMs were biased with 75 V. (left) A heat map of many waveforms overlayed on top of one another, with individual PE steps clearly visible. (right) Distribution of peak area measured by integrating over the five samples surrounding the peak in each window, measured in ADC. The first peak above zero represents noise and each subsequent peak represents a 1PE, 2PE, etc. signal.

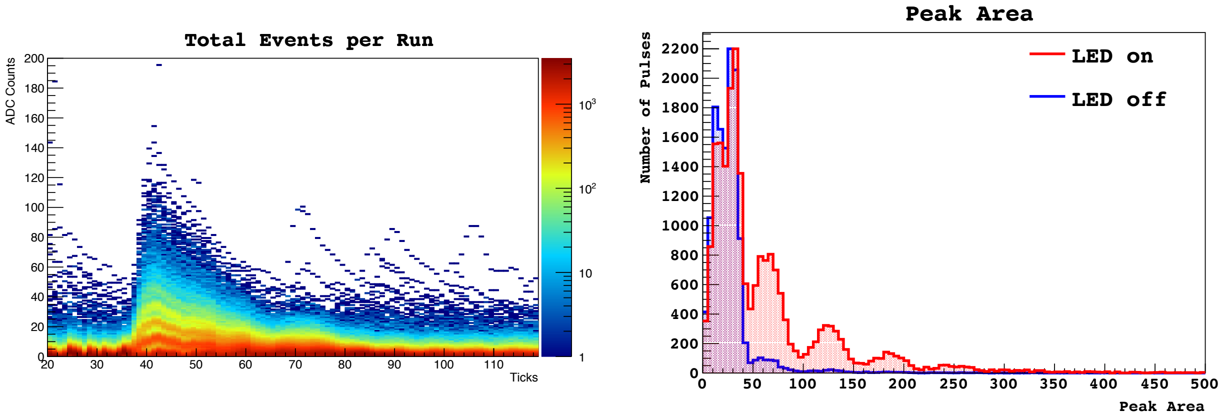

Figure 6.14: Data collected at cyrogenic (LN2) temperatures with the custom TDB and Mu2e readout electronics and 50 m of Cat6a cable. The SiPMs were biased with 75 V. (left) A heat map of many waveforms overlayed on top of one another, with individual PE steps clearly visible. (right) Distribution of peak area measured by integrating over the five samples surrounding the peak in each window, measured in ADC. The first peak above zero represents noise and each subsequent peak represents a 1PE, 2PE, etc. signal. Data taken with the LEDs off is shown in blue to confirm the location of the noise peak.

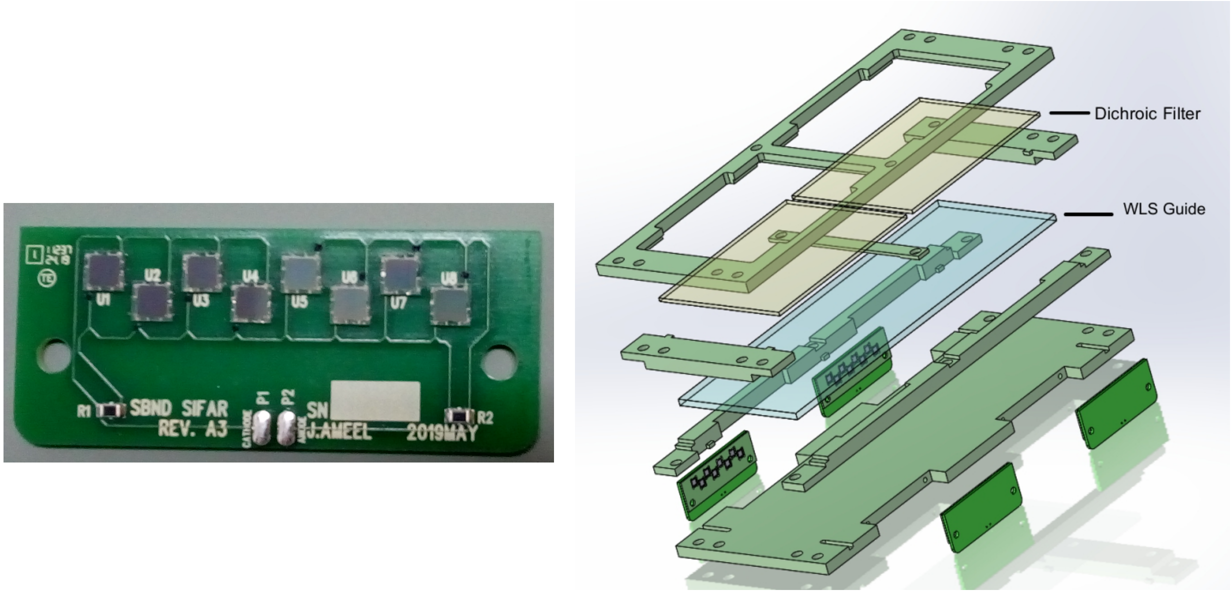

Figure 6.15: (left)The SBND SiPM carrier board final design (the X-TDB). The design gangs arrays of four 3 mm × 3 mm Sensl SiPMs in parallel and then wires two arrays together in series to form one readout channel. (right) A rendering of the X-ARAPUCA design for SBND. There around four X-TDBs per X-ARAPUCA, each containing one channel made of 8 SiPMs ganged in groups of four.

are shown in Figure 6.15. Each board holds eight 3 mm × 3 mm Sensl Series A SiPMs.

The remaining sections of this chapter describe a variety of tests performed using the X-TDBs, culminating in the final quality assurance tests currently being performed on the batch of fabricated X-TDBs intended for installation in SBND later this year.

6.7 Noise Tests at DZero

Tests of PD electronics interference with a TPC system were done at the D0 Assembly Building (DAB) at Fermilab. Room 209 houses a Faraday cage that contains a TPC with two wire planes. The TPC has a cold interface board mounted on top of the wire planes that connects to a warm interface board (WIB) mounted on the exterior of the shielded room. Data acquisition tools for measuring noise levels in the TPC were available. These tests were performed using the original TDB, but as the SiPM ganging strategy remains unchanged in the X-TDBs, the results remain relevant. Cabling and grounding schemes are also unchanged. A diagram of the setup and grounding connections in the setup at DAB is shown in Figure 6.16. The TDB, populated with SiPMs, was

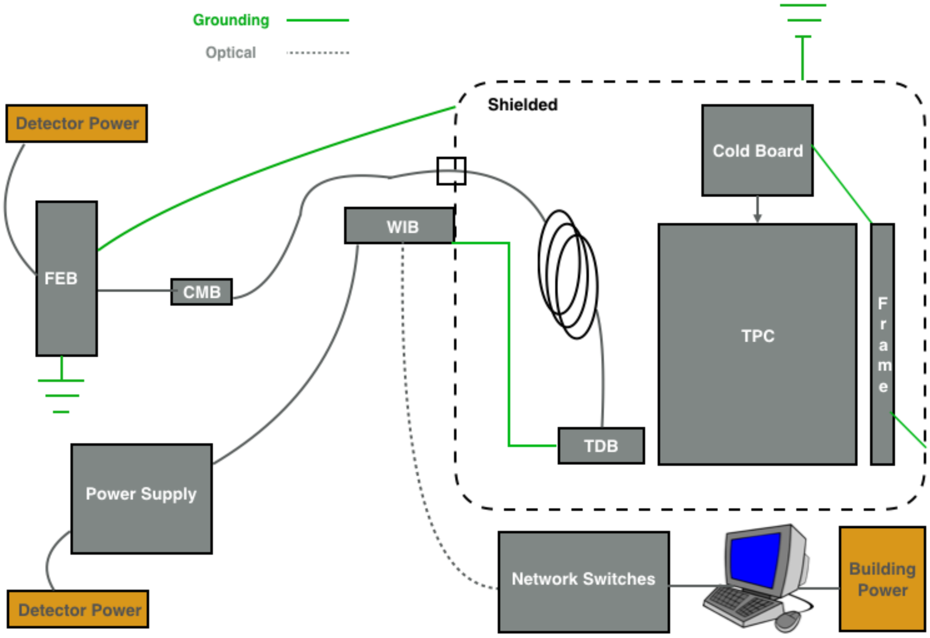

Figure 6.16: The setup of PD/TPC noise interference tests at the D0 Assembly Building at Fermilab. Courtesy of P. Abratenko.

placed face down on the ground next to the TPC and held down with G10 tape such that the SiPMs were in a reasonably light-tight environment. The Cat5 cable from the TDB was fed up along the side of the TPC to mimic the cable configuration intended for SBND and then connected to a Cat5-Cat5 feedthrough on the wall of the shielded room. Outside the cage the Cat5 cable was stripped so one channel could be soldered to a custom Mu2e board that converts four stripped twisted pair (Cat5) channels to HDMI to connect to the Mu2e FEB. The noise levels observed in the TPC with the photon detector system powered fully off and on are shown in Figure 6.17. When the PD system is powered on, the FEB biases the SiPMs on the TDB with $V_b = 80$ V. No increase in noise levels on the TPC was observed with nominal cable and grounding configurations for the light detection system.

In addition to testing reasonable detector grounding and cabling configurations (results shown in Figure 6.17), we aimed to maximize noise injection into the TPC from the PD cabling and electronics using worst case, completely unrealistic scenarios including wrapping PD Cat5 cable several times around the TPC. PD-induced noise levels on the TPC remained negligible. The results remained consistent across several runs of data.

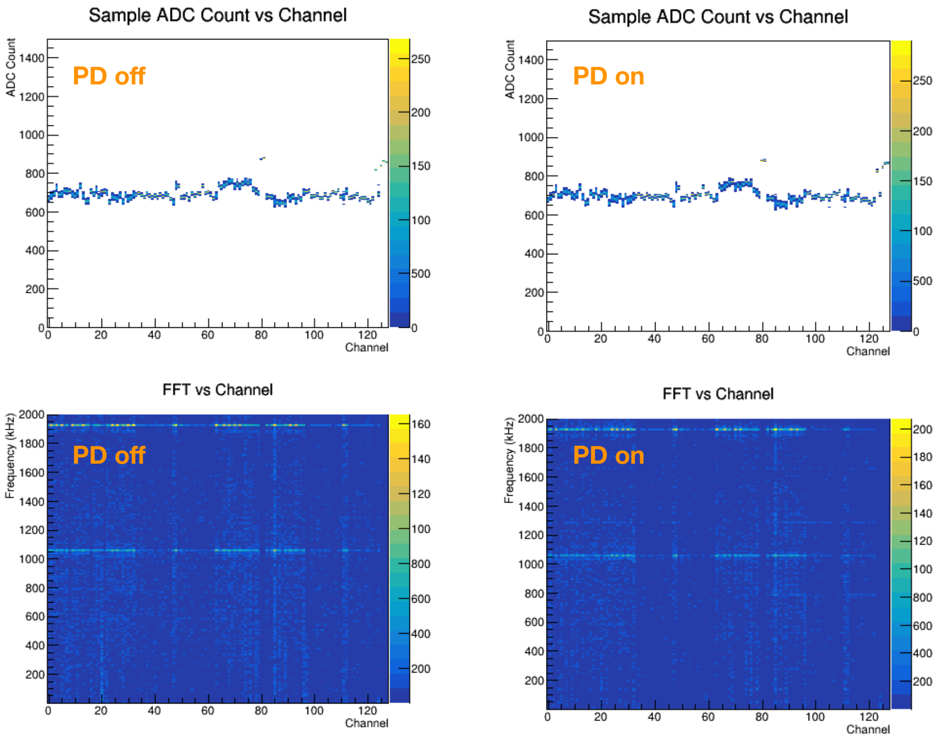

Figure 6.17: Noise observed by the TPC at the D0 Assembly Building with the PD electronics off and powered on. (top) The distribution of ADC counts per sample for a run of data taking. (bottom) the fast Fourier transform of data taken on each TPC readout channel. Courtesy of P. Abratenko.

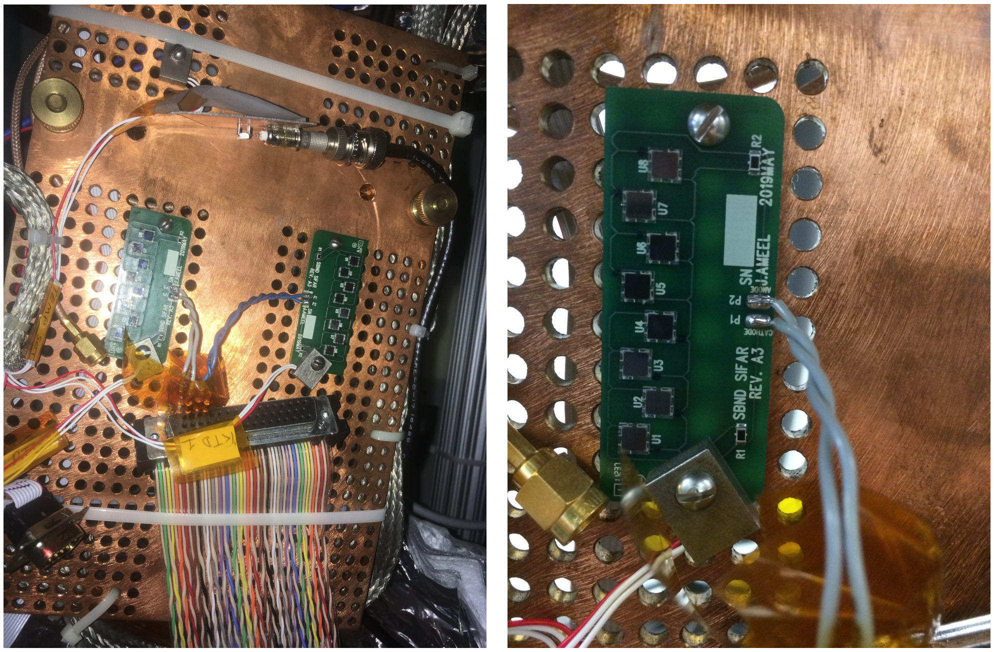

Figure 6.18: The interior of the Wilson Hall Fourteenth Floor cryocooler. The X-TDBs are bolted to a copper plate for cooling and thermal paste is applied between the X-TDB back face and copper plate to insure maximum conductivity. An RTD is bolted to the face of the X-TDB to measure the temperature of the board (see close up in right image), providing an accurate estimate of the temperature of the SiPMs themselves within 10s of K.

6.8 Cryocooler Tests

Cold grounding and noise tests were performed in a cryocooler on the fourteenth floor of Wilson Hall at Fermilab. The aim of the tests was to demonstrate single photoelectron resolution using the X-TDBs at cryogenic temperatures with cable lengths similar to those required in SBND. The setup was designed to be as close to representative of the full SBND design as possible.

The cryocooler flange contains two 50-pin D-sub connectors (SBND plans to use 32-pin D-sub connectors) used to transfer power and signal from warm to cold and vice versa. A 50-wire ribbon cable was attached to the flange on the interior the cryocooler. Short twisted pair wires were slotted into neighboring clamp connectors on this cable and soldered to the X-TDB anode and cathode pads. The X-TDBs were bolted to a copper plate to aid cooling. An RTD was bolted to the front face of the X-TDB to measure the temperature of the board, which is expected to be representative of the temperature of the SiPMs within 10s of K. The setup of the interior of the cryocooler is shown in Figure 6.18.

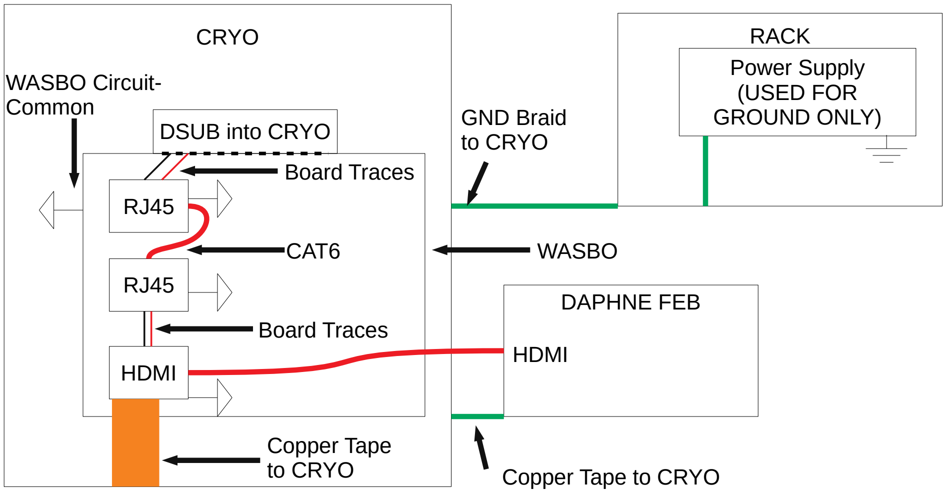

Figure 6.19: Schematic of the most effective warm-side grounding scheme for X-TDB tests in the cryocooler on the fourteenth floor of Wilson Hall at Fermilab. Courtesy of D. Mishins and J. Mousseau.

On the warm side, a breakout board with HDMI output connects to the exterior D-sub connector. Additional RJ45 connector pairs on this board allow for the installation of arbitrary Cat6 cable lengths to better mimic the length of Cat6 cable required in SBND. The HDMI output connects to the Mu2e FEB. A laptop was used for data acquisition. The empirically best grounding configuration for warm-side components is illustrated in Figure 6.19.

The results for a short length of Cat6 cable are shown in Figure 6.20, and for 50 ft of Cat6 cable in Figure 6.21. Example single photoelectron signals are shown alongside the distribution of maximum ADC in each readout window. Single photoelectron signals are resolved in both configurations.

6.9 X-TDB Quality Assurance Tests in Stella

The X-TDBs for SBND are now fabricated and quality assurance testing is underway at Fermilab's Proton Assembly Building (PAB). The Stella test stand is a small cryostat with a foam lid that was outfitted with an LN2 filling line and N2 gas line for batch testing X-TDBs in a cryogenic environment. Five resistive temperature devices (RTDs) are place on the vessel walls to monitor fill level. A custom X-TDB carrier board was designed to hold 100 X-TDBs, read out in groups

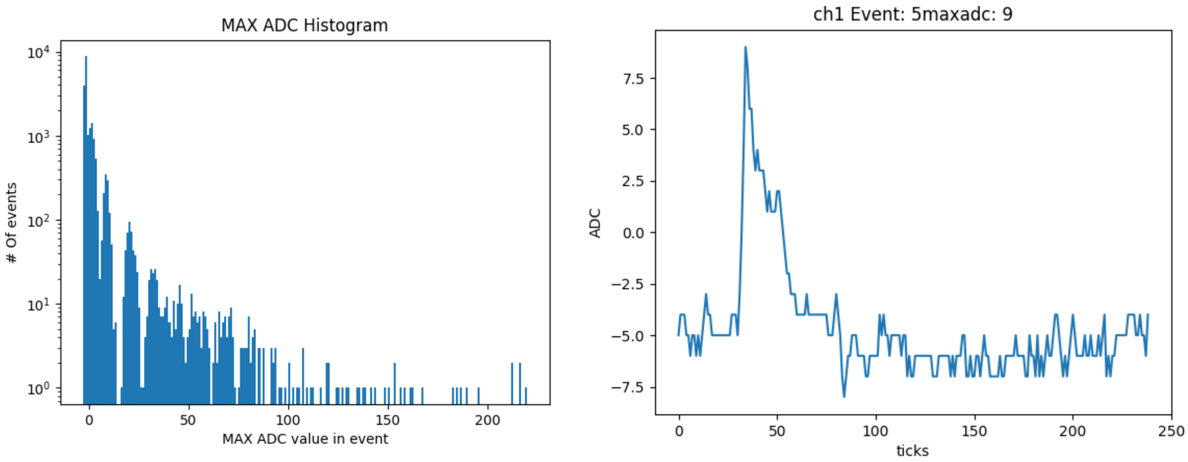

Figure 6.20: (left) Distribution of peak ADC per readout window observed with 1 ft of Cat6 cable in the Wilson Hall 14th floor cryocooler. Single photoelectron signals are clearly visible above noise (the first peak above zero). (right) An example single photoelectron signal.

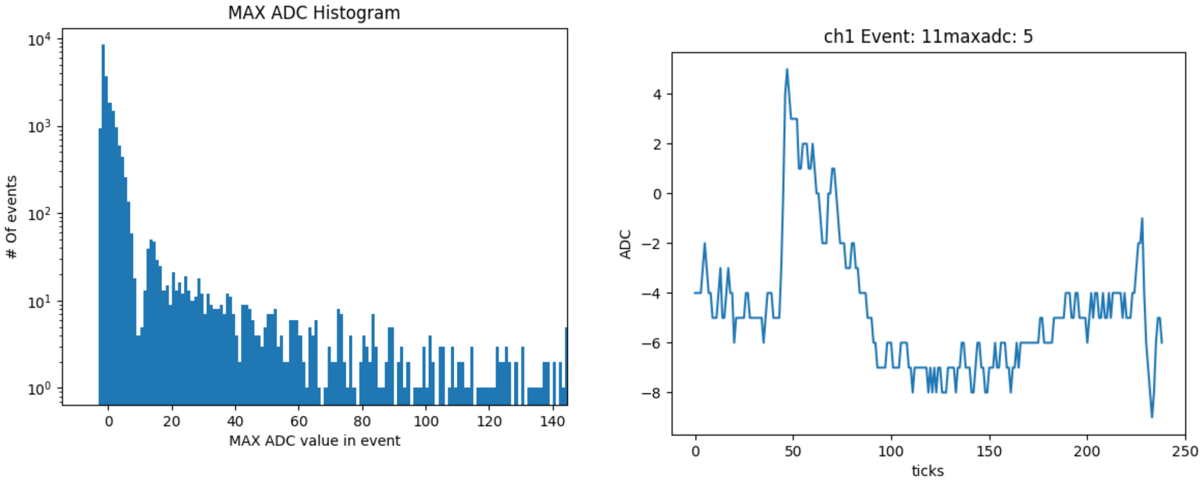

Figure 6.21: (left) Distribution of peak ADC per readout window observed with 50 ft of Cat6 cable in the Wilson Hall 14th floor cryocooler. Single photoelectron signals are clearly visible above noise (the first peak above zero). (right) An example single photoelectron signal.

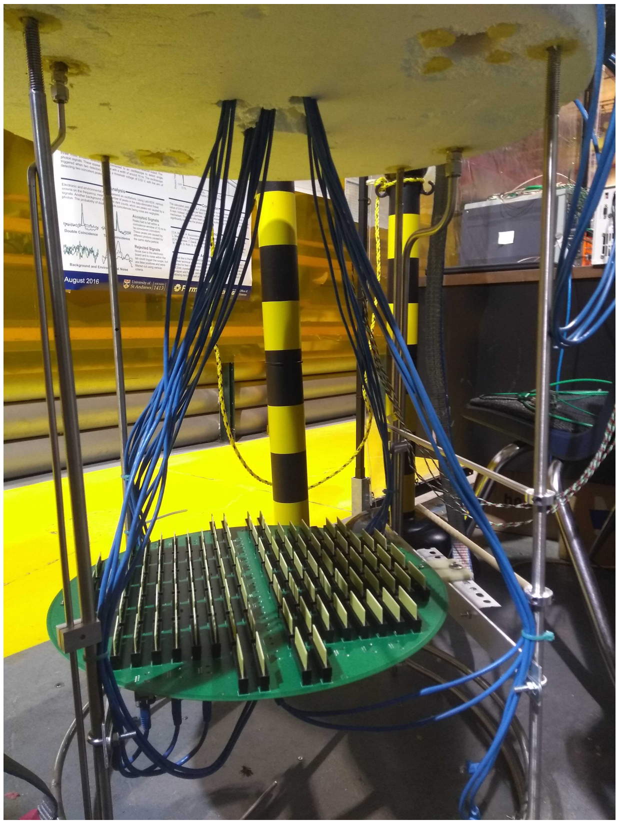

Figure 6.22: The Stella cryostat lid with the DBB SiPM carrier board suspended from it. The DBB holds 100 SiPMs read out in groups of four using 25 Cat6 cables, which can be seen coming from the bottom side of the DBB and fed through the lid of the cryostat.

of four on 25 Cat6 cables that feed through holes in the top of the cryostat. A configurable array of 11 purple/UV LEDs is installed to illuminate the boards. While in operation, the cryostat is covered completely with black cloth to achieve a light tight environment while the SiPMs are powered. The X-TDB carrier board, known as the DBB, is suspended from the lid of the vessel. A picture of the Stella lid and DBB are shown in Figure 6.22. The Cat6 cables connect on the warm side to a custom RJ45-to-HDMI converter board (I2DBB) which connects to the FEB. The FEB provides 50 V bias to the SiPMs and collects data using the python-based DCA3 data acquisition system, developed by D. Mishins and collaborators. (This portable interactive DAQ tool will also be used for PD checkout tests during SBND installation.) The warm-side electronics are shown in Figure 6.23. A Tektronix pulse generator provides an in-time trigger and power to a custom PCB board for biasing the LEDs. A detailed diagram of power distribution and grounding is shown in Figure 6.24.

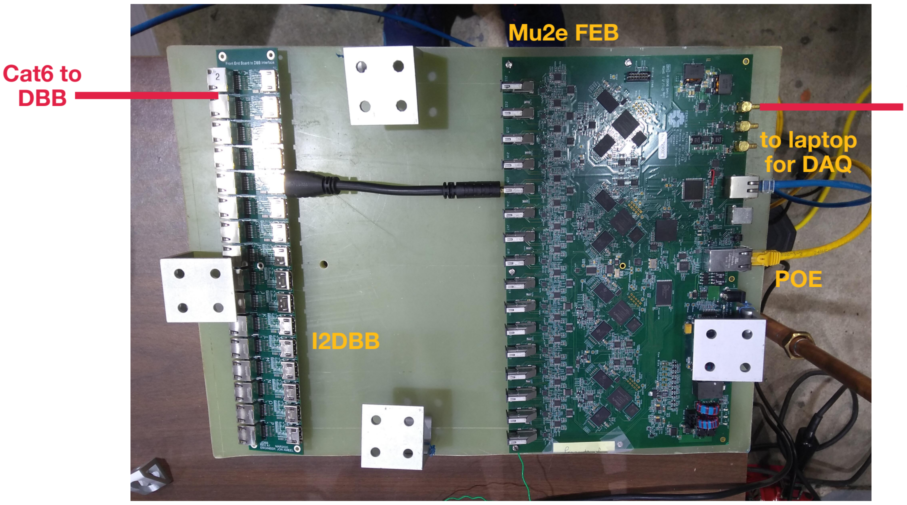

Figure 6.23: The Stella warm-side electronics.

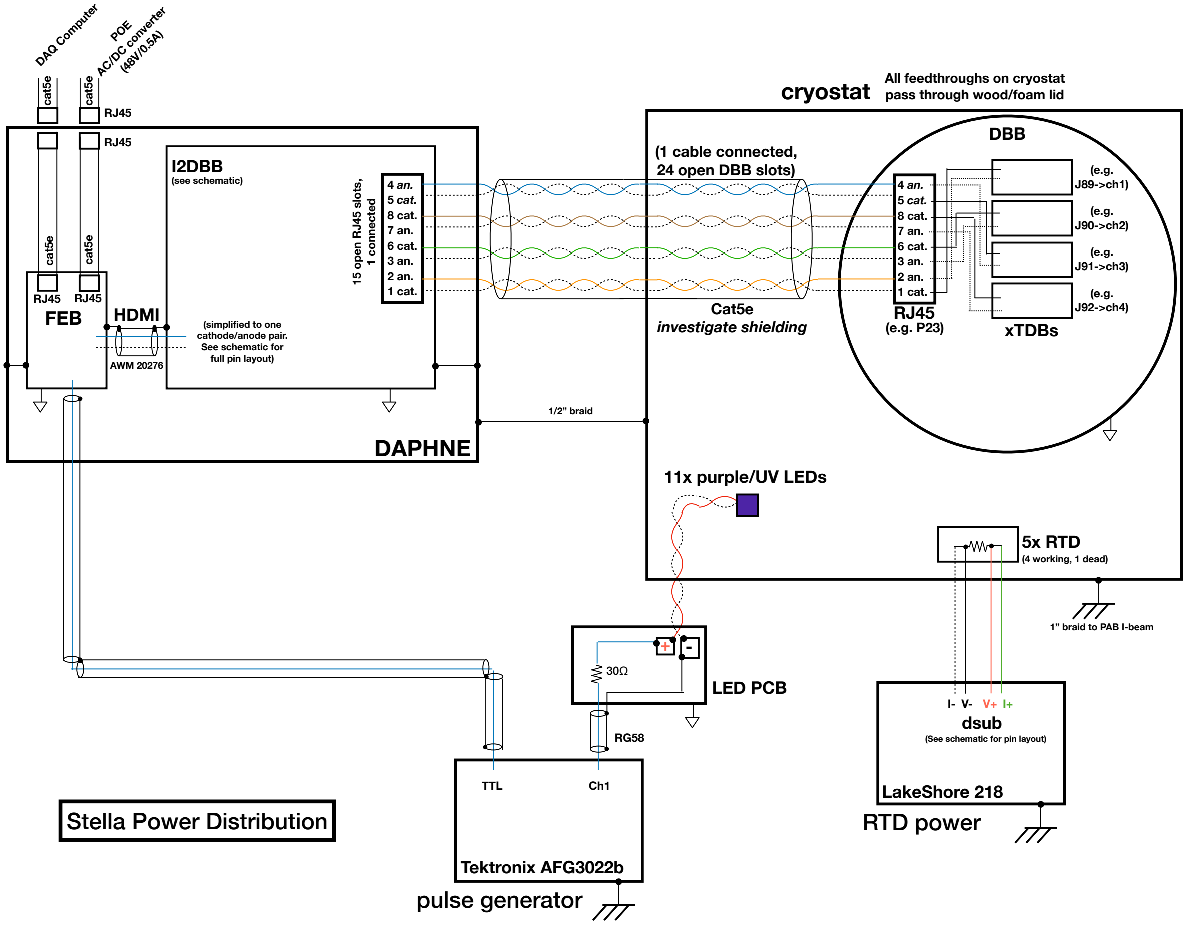

Figure 6.24: Power distribution and grounding for the Stella test stand.

Steps to mitigate noise were taken, including careful grounding and use of shielded cables, but the noise levels of the system are not expected to reach the levels required in SBND. A simple yes/no check for light signals on each SiPM will indicate viability of each X-TDB. The process of filling, taking data, and emptying the cryostat for each batch of 100 X-TDBs takes approximately one week. To test the 768 X-TDBs required for SBND with 10% additional spares will take nine fills. A small batch of control X-TDBs will remain in place through the full run of tests. The Stella test stand is on schedule to begin its first batch of testing imminently and should finish tests on the time scale of about three months, barring any unanticipated changes in schedule.

CHAPTER 7

Progress Toward Finalizing the Design of the DUNE Far Detector Single Phase Photon Detection System

7.1 The Deep Underground Neutrino Experiment

To this point, we have discussed past, present, and imminent LArTPC neutrino detectors, all on site at Fermilab in Batavia, IL, with baselines on the order of kilometers. These detectors, ArgoNeuT, MicroBooNE, and SBND have each innovated and led to deeper understanding of the detector technology, in addition to yielding a collection of physics measurements for neutrino interactions on argon targets, with more in the pipeline as MicroBooNE finishes its data taking and SBND and ICARUS start processing their initial high intensity data sets. These experiments have generated a wealth of new knowledge, but they also serve a second purpose, each building on top of the previous, contributing to research and development for LArTPC and related technology for future detectors. All this R&D culminates (at least for the foreseeable future) with DUNE, the Deep Underground Neutrino Experiment.

DUNE is a massive neutrino detector that will be located 1.5 km underground at the Sanford Underground Research Facility (SURF) in South Dakota, an overwhelming 1300 km from the high-intensity neutrino beam (1.5 MW with the possibility of upgrades to multi-MW) originating at Fermilab. The modular 40-kt (fiducial) far detector is paired with a precision near detector at Fermilab that is designed to characterize the flux of the neutrino beam at a mere 574 m from the source. With innovative, moveable components, the near detector is comprised of multiple detector technologies that work together to generate a more complete picture of the energy spectrum of the neutrinos that make their way underground on a 1300 km trip to South Dakota from

Illinois. The near detector is a critical tool for minimizing systematic errors in neutrino energy reconstruction for DUNE physics. The international collaboration has over a thousand members from more than 30 countries and nearly 200 different institutions. DUNE's far detector (FD) is so massive that it is split up into four individual 10-kt detectors that will each collect charge and optical information from interactions, but use slight variations in detector technology. Both single- and dual-phase modules are being prototyped. This chapter will describe efforts toward finalizing the photon detector system for the single-phase (SP) FD module [70], and will aim to provide a complete picture of the nominal detector setup as currently planned, in addition to summarizing future full system tests of the design.

Each of DUNE's FD modules will reside in a cryostat with dimensions 15.1 m (w) $\times$ 14.0 m (h) $\times$ 62.0 m (l) capable of holding about 17 kt of liquid argon. The deployment is staged and the module designs are flexible to respond to advances in technology throughout the several-year commissioning of the full DUNE detector. Nominally, the first module to be deployed will be a single-phase TPC, the same configuration used in both ArgoNeuT and MicroBooNE, in which the entire detector is surrounded by liquid argon, and the drift is horizontal across the detector. These detectors require relatively high signal-to-noise ratios, as there is no opportunity to amplify the ionization signal before it reaches the anode plane. Additional efforts are underway to test and better understand the unique challenges and added advantages of large-scale dual phase detectors, in which the top layer of the cryostat, and as a result some of the detector components, operate in gaseous argon. In this detector configuration, which has traditionally been used by dark matter experiments, ionized electrons drift vertically toward the top of the detector. The transition from liquid to gas provides an opportunity for the electron signal to be amplified by LEMs (large electron multipliers) before it reaches the the anode. Schematics of each type of detector are shown in Figure 7.1. Under current plans, two of DUNE's first three FD modules will be single-phase and one will be dual-phase, with installation order depending in part on results from prototype tests. The fourth module will employ a more advanced design that is yet to be finalized.

The design of the SP LArTPC is shown in Figure 7.2. Ionized electrons drift horizontally, toward the anode planes in each of the four drift volumes, over which an electric field of 500 V/cm is applied. This corresponds to a cathode high voltage of 180 kV and the maximum drift length for each volume is 3.5 m. Each anode plane contains a grid of 6.5 m (h) $\times$ 2.3 m (w) anode

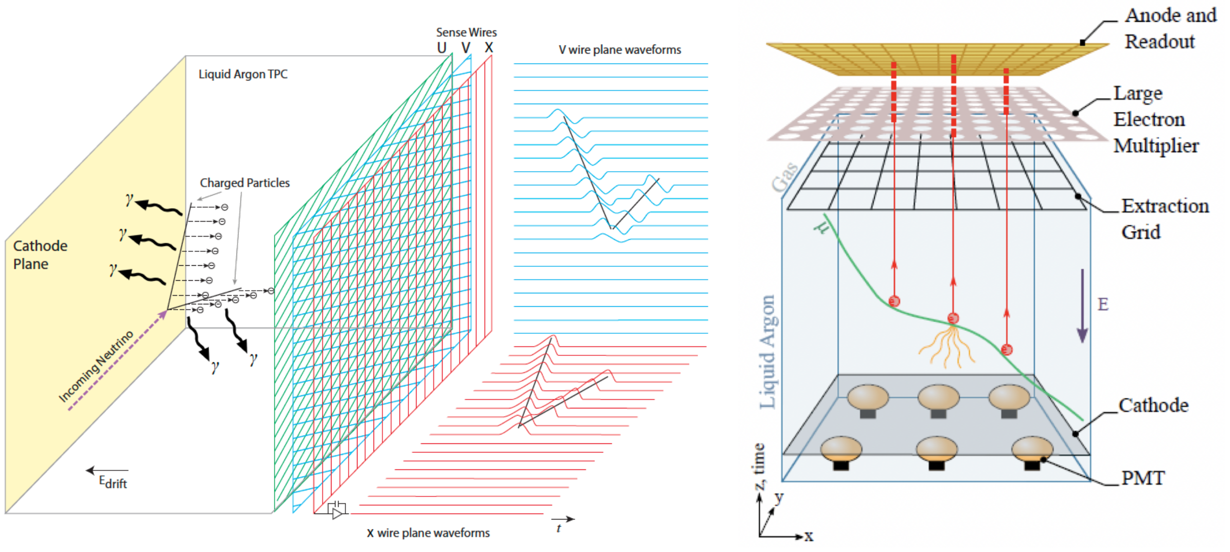

Figure 7.1: (left) Illustration of a single phase TPC, in which ionization electrons drift horizontally across the detector to be collected on the anode. While not shown, light detectors provide t_0 timing information for the interactions from the prompt scintillation photons. (right) Illustration of a dual phase TPC, where ionization electrons drift vertically toward the top of the detector. In the gaseous argon layer a LEM magnifies the ionization signal. Again, light detectors (PMTs here) are used to collect optical information that can be used to tag the start of the event t_0. Images from Ref. [127].

plane assemblies (APAs). There are 50 APAs per anode plane and 150 APAs total. The photon detectors, discussed in more detail below, slot into the inactive space between the wire planes to eliminate any impact on the detector fiducial volume.

Briefly, DUNE's near detector stands on its own as a tool for studying physics processes that can be best probed using high-intensity neutrino sources. However, for DUNE it will provide crucial information about the distribution of neutrino flavors and energies that travel to the far detector. Like the far detector, the near detector is not one but a collective of detectors that work in concert to form a holistic picture of beam composition. Sitting 574 m downstream of the beam, there are three main components: 1) ArgonCube, a LArTPC, 2) the MPD (multi-purpose detector), a high pressure gaseous argon TPC encased by a 0.5 T electromagnetic calorimeter, and 3) SAND, the System for on-Axis Neutrino Detection. An illustration of the near detector complex is shown in Figure 7.3. Notably, the first two components are designed such that they can be moved off axis up to 33 m perpendicular from their on-axis locations.

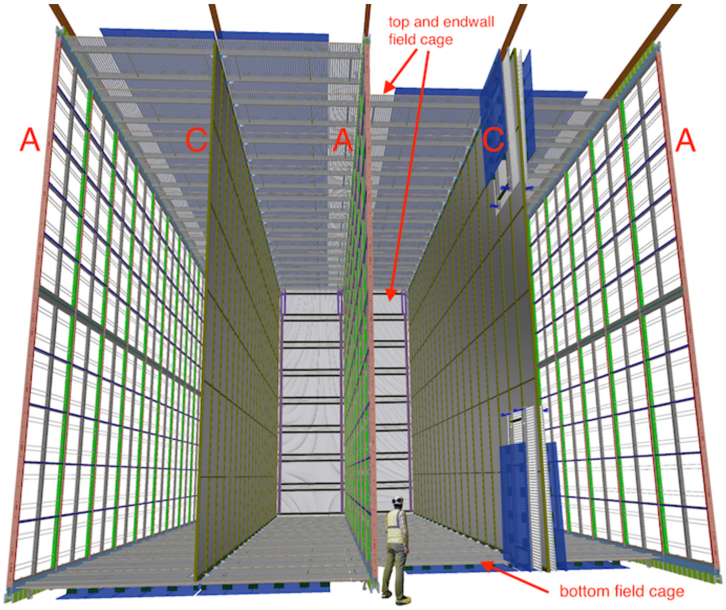

Figure 7.2: The DUNE single-phase far detector module, which contains four drift regions of 3.5 m each to reduce maximum drift time. Light detectors on the exterior anode planes are designed to collect light only from one direction, while the light detectors on the inner anode plane collect light from both directions. Image from Ref. [127].

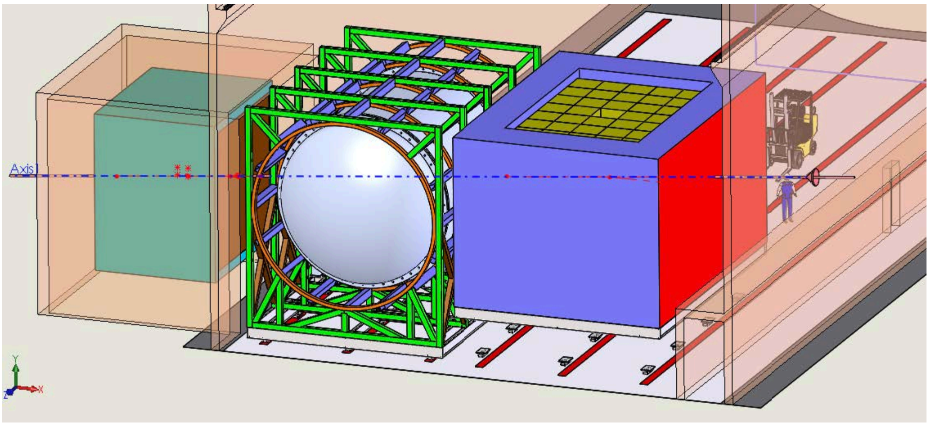

Figure 7.3: The DUNE near detector complex. From left to right, the on-axis beam monitor (SAND), the MPD, and ArgonCube. The MPD and ArgonCube can move up to 33 m off axis. Image from Ref. [127].

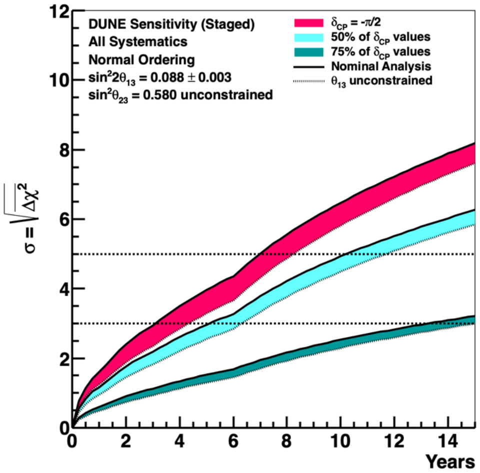

	Expected Events (3.5 years staged per mode)	
	ν mode	$\bar{\nu}$ mode
ν_e Signal NO (IO)	1092 (497)	76 (36)
$\bar{\nu}_e$ Signal NO (IO)	18 (31)	224 (470)
Total Signal NO (IO)	1110 (528)	300 (506)
Beam $\nu_e + \bar{\nu}_e$ CC background	190	117
neutral current (NC) background	81	38
$\nu_\tau + \bar{\nu}_\tau$ CC background	32	20
$\nu_\mu + \bar{\nu}_\mu$ CC background	14	5
Total background	317	180

Figure 7.4: (left) DUNE's sensitivity for measuring δ_{CP} as a function of time. The sensitivities assume a staged rollout of the detector over the course of 3 years and a beam intensity upgrade after 6 years. (right) The expected ν_e appearance and relevant background rates for a seven year period assuming $\delta_{CP} = 0$, with exposure split evenly between neutrino and antineutrino modes. Figures from Ref. [49].

7.2 DUNE Physics Goals

DUNE was designed explicitly to answer a number of open physics questions, though its reach will certainly extend beyond these capstone goals. First and foremost, DUNE is a neutrino oscillation experiment. Its goal is to measure, with precision, the CP-violating phase, δ_{CP}. More specifically, it aims to achieve greater than 3σ sensitivity to at least 75% of possible values. DUNE's long baseline is optimal for probing this parameter. In addition, DUNE will be capable of measuring the mass ordering of the neutrinos and the mixing angle θ_{23}. To achieve this, DUNE's far detector must have accumulated exposure of 120 kt $\cdot$ MW $\cdot$ year by approximately 2035. In fact, these physics goals are what drive the design goals of the entire detector. DUNE's sensitivities for measuring δ_{CP} are shown in Figure 7.4 along with the ν_e appearance rates assuming $\delta_{CP} = 0$ for seven years of running, with time split evenly between neutrino and antineutrino modes. Note that the sensitivities are calculated based on a nominal deployment plan that has two FD modules running in a 1.2 MW beam to begin (20 kt fiducial volume), a third FD module added after one year (30 kt fiducial volume), a fourth FD module after 3 years (40 kt fiducial volume), and beam power upgrade to 2.4 MW after 6 years.

DUNE is also designed to be capable of proton decay searches via several decay modes, and able to detect core-collapse supernova ν_e flux. The photon detection system is particularly useful for these searches, which do not coincide in time with beam-related activity. Finally, a wealth of additional BSM physics searches are possible in DUNE, but beyond the scope of this chapter.

7.3 Photon Detection in DUNE

The photon detection system is critical for several of DUNE's physics goals in addition to providing valuable cross checks to charge readout. The prompt scintillation photons produced when charged particles pass through liquid argon can be detected, and indicate a start time (t_0), for events once properly matched with charge collected on the anode planes. In particular, the timing information in combination with known drift velocities gives a handle for measuring position in the drift direction to complete the high resolution two-dimension image provided by the wire plane readout. For nucleon decay physics, the PD system-provided t_0 is needed for determining containment of candidate events. The optical information can also be used as a complementary trigger mechanism for supernova burst events, when beam timing information is irrelevant. For example, the PD system system as designed yields $\sim$1 mm position resolution for 10 MeV supernova burst events. The PD system is capable of calorimetric energy reconstruction for all events, which can be used as a crosscheck or in combination with charge information to improve energy resolution and quantify necessary drift corrections for ionization electrons. Michel electrons, which are a valuable calibration sample for antineutrino flux, can be tagged using the PD system. In short, the PD system greatly enhances the physics capabilities of the DUNE FD, working independently and in cooperation with charge and beam timing information.

7.4 Design of the Photon Detector System

Simply put, the PD system must collect VUV scintillation light of 127 nm produced by ionizing particles traversing the TPC. In DUNE, the PD system was designed to have no impact on the detector fiducial volume; the PD modules are placed in the inactive space between the wire planes in the APAs. The system is designed to maximize VUV photon collection efficiency while minimizing the number of silicon photosensors, a necessary tradeoff for making the system cost-effective. DUNE was designed with a baseline system of components, but is also actively studying alternatives prior to making a final decision on all PD components. The baseline system is composed of four main components: 1) a light collection system, 2) photosensors for converting incident photons to electrical signals, 3) “cold electronics” that actively gang signals prior to transmitting them outside of the cryostat, and 4) “warm electronics” for digitizing electric signals. The key to an effective PD system in DUNE is threefold: it must have 1) efficient conversion of VUV photons to captured photons, 2) a high fraction of captured photons incident on photosensors, and 3) efficient photosensors for converting photons into electric signals.

In the DUNE FD, each SP module will have 1500 photon detector (PD) modules (10 per APA). Five hundred of the PD modules will be mounted on central APA frames and are required to collect light from both sides. The remaining 1000 PD modules will be mounted on APA frames near the vessel wall and only have to collect light incident from one direction. See Figure 7.2 for reference. Specifications for the PD system are dictated by the physics goals in DUNE. A partial list of the system requirements are shown in Figure 7.5. For example, the minimum light yield is driven by supernova and nucleon decay physics, interactions in which very little light (relative to say, beam neutrinos events) is produced. Others, like the clean area specifications during installation, have been validated experimentally during prototype tests. A schematic of an APA frame is shown in Figure 7.6, with two of the ten slots for APAs indicated. As currently designed, the nominal components for each part of the SP PD system are outlined in Figure 7.7. They are each discussed in more detail below.

7.4.1 Light Collection

The DUNE experiment plans to use X-ARAPUCAs to maximize the VUV sensitive area of the detector. X-ARAPUCAs are based on the original concept of the ARAPUCA, a light trap that captures wavelength-shifted light inside highly reflective boxes. SiPMs housed in these boxes collect the light that is captured and convert it to electrical signals. The X-ARAPUCA expands upon this technique by making use of total internal reflection to capture wavelength-shifted photons and further improve detection efficiency. Lab tests have shown that the X-ARAPUCA is more efficient than the S-ARAPUCA model. Though the relative efficiency between the two models is not yet known precisely, tests done at UNICAMP using an S-ARAPUCA and X-ARAPUCA of the same size indicate that the X-ARAPUCA is around 15%-40% more efficient. ICEBERG, discussed in

Label	Description	Specification (Goal)	Rationale	Validation
SP-FD-3	Light yield	$>$ 20 PE/MeV (avg), $>$ 0.5 PE/MeV (min)	Gives PDS energy resolution comparable to that of the TPC for 5-7 MeV SN νs, and allows tagging of $>$ 99 % of nucleon decay backgrounds with light at all points in detector.	Supernova and nucleon decay events in the FD with full simulation and reconstruction.
SP-FD-4	Time resolution	$<$ 1 µs ($<$ 100 ns)	Enables 1 mm position resolution for 10 MeV SNB candidate events for instantaneous rate $< 1\,\mathrm{m}^{-3}\mathrm{ms}^{-1}$.	
SP-FD-15	LAr nitrogen contamination	$<$ 25 ppm	Maintain 0.5 PE/MeV PDS sensitivity required for triggering proton decay near cathode.	In situ measurement
SP-PDS-1	Clean assembly area	Class 100,000 clean assembly area	Demonstrated as satisfactory in ProtoDUNE-SP, and is the DUNE assembly area standard.	ProtoDUNE-SP and in Fermilab materials test stand
SP-PDS-2	Spatial localization in y-z plane	$<$ 2.5 m	Enables accurate matching of PD and TPC signals.	SNB neutrino and NDK simulation in the FD
SP-PDS-3	Environmental light exposure	No exposure to sunlight. All other unfiltered sources: $<$ 30 minutes integrated across all exposures	Shown to prevent damage to WLS coatings due to UV.	Studies in ProtoDUNE-SP, and at IU

Figure 7.5: A partial list of specifications for the DUNE SP photon detection system. The specifications are driven by physics goals for the DUNE experiment. From Table 5.1 in Ref. [70].

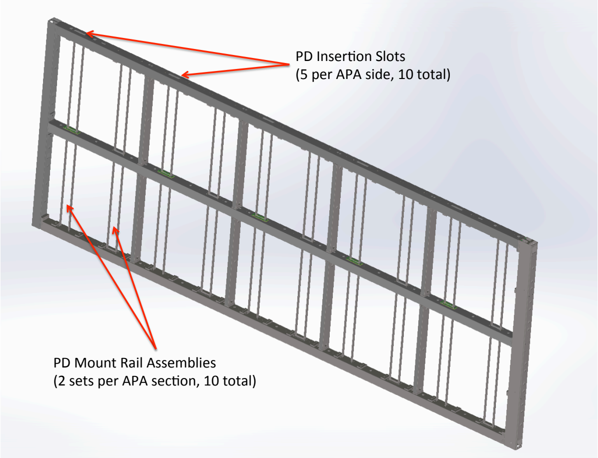

Figure 7.6: An APA frame for the DUNE SP FD module. The 10 PD modules are inserted into the 10 spots as indicated between the innermost wire planes such that they have no impact on the total fiducial volume of the detector. Image from Ref. [70].

Component	Description	Quantity
Light collector	X-ARAPUCA	10 modules per APA; 1500 total (1000 single-sided; 500 double-sided)
Photosensor	Hamamatsu MPPC 6 mm×6 mm	192 SiPM per module; 288,000 total
SiPM signal summing	6 passive × 8 active	4 circuits per module; 6000 total
Readout electronics	Based on commercial ultrasound chip	4 channels/module; 6000 total
Calibration and monitoring	Pulsed UV via cathode-mounted diffusers	45 diffusers/CPA side; 180 diffusers for 4 CPA sides

Figure 7.7: The DUNE single phase far detector PD system baseline configuration. Table from Ref. [70].

detail below, is an ideal testing environment for direct comparisons between the two models. S-ARAPUCAs were tested in a number of environments including ProtoDUNE-SP to demonstrate their viability for DUNE. The X-ARAPUCA design has been tested in small cryostats and will be further studied in subsequent large-scale ProtoDUNE runs. The X-ARAPUCA concept is illustrated in Figure 7.8. The top plate is a dichroic filter coated on the outside with a wavelength shifter (PTP in this case) that emits light a wavelength below the dichroic filter threshold so the photons can enter the box. A second wavelength shifter that emits light with wavelength greater than the filter's cutoff is mounted inside the box. Having passed through this second wavelength shifter, photons are now trapped inside the highly reflective ($> 98\%$) box interior until coming into contact with SiPMs mounted inside the X-ARAPUCAs that collect the light. As such, X-ARAPUCAs dramatically increase the active area of the photosensors in the detector.

7.4.2 Photosensors

The photosensors used in DUNE must hold up mechanically and electrically in cryogenic environments for many years. Silicon photomultipliers (SiPMs) have high photon conversion efficiency, operate at low voltage, and are physically small, unlike traditionally used PMTs. The baseline device intended for DUNE is the 6 mm by 6 mm Hamamatsu MPPC. There will be 192 MPPCs per PD module, with 48 MPPCs ganged together for every four readout channels. In this configuration, that means there are 288,000 MPPCs per SP module. Under consideration is also an alternative Hamamatsu model and a device that was designed by the company FBK in collabora-

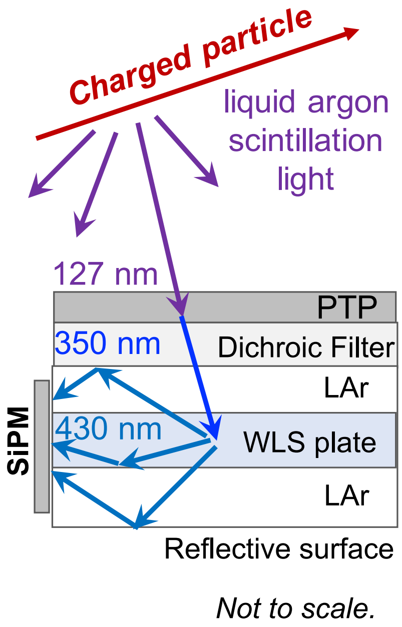

Figure 7.8: The X-ARAPUCA design (single-sided). The top plate is a dichroic filter coated on the outside with a wavelength shifter (PTP in this case) that emits light a wavelength below the dichroic filter threshold so the photons can enter the box. A second wavelength shifter (WLS plate) that emits light greater than the filter's cutoff is mounted inside the box. Having passed through this section wavelength shifter, photons are now trapped inside the highly reflective ($> 98\%$) box interior until coming into contact with SiPMs mounted inside the X-ARAPUCAs and collect the light. Image from Ref. [70].

	Hamamatsu (Baseline)	Hamamatsu-2	FBK
Series part #	S13360	S14160	NUV-HD-LF
V_{br} (typical)	50 V to 52 V	36 V to 38 V	31 V to 33 V
V_{op} (typical)	V_{br}+3 V	V_{br}+2.5 V	V_{br}+3 V
Temperature dependence of V_{br}	54 mV/K	35 mV/K	25 mV/K
Gain at V_{op}(typical)	1.7×10^6	2.5×10^6	0.75×10^6
Pixel size	50 μm	50 μm	25 μm
Size	6 mm x 6 mm	6 mm x 6 mm	4 mm x 4 mm
Wavelength	320 to 900 nm	280 to 900 nm	280 to 700 nm

Figure 7.9: Some of the specifications of the three candidate SiPM options for the DUNE FD PD system. Table from Ref. [70].

tion with DarkSide for use in liquid argon. Some of the specifications for each of the three devices are shown in Figure 7.9.

7.4.3 Cold Electronics

There are four readout channels per PD module, or one per X-ARAPUCA supercell. In each readout channel, 48 SiPMs are ganged together into a single differential output. A cold amplifier is used to adjust the MPPC output level prior to transmitting the signal out of the cryostat to the warm readout electronics. The active ganging circuits were developed at Fermilab and have demonstrated operation and single photoelectron resolution at liquid argon temperatures repeatedly.

7.4.4 Warm Electronics

The warm digitizer to be used in DUNE is known as DAPHNE (Detector Electronics for Acquiring PHotons from NEutrinos). The front end electronics are adapted from a cost-effective waveform digitization system that was originally developed by the Mu2e experiment and relies on commercial ultrasound chips (12-bit, 80 MS/s). These Mu2e boards were employed (out of the box) for the photon detection system in SBND, discussed in Chapter 6. Several features from the Mu2e electronics are in the process of being updated and tested for DAPHNE, including but not limited to, reducing the number of available readout channels from 64 to 40, upgrading the FPGAs from Xilinx Spartan-6 to Xilinx Spartan-7 or Artix-7, and replacing the 12-bit TI AFE5807 ultrasound chip with the pinout-compatible 14-bit TI AFE5808 ultrasound chip to increase the dynamic range of the readout. These ultrasound-based front-end electronics have replaced the custom-designed Signal SiPM Processor (SSPs) that was used in early development of the DUNE PD system. While the SSPs provide incredibly high resolution for observing single photoelectrons, both cost and reduced engineering support for the SSP make DAPHNE the appropriate baseline design. Early bench tests, described in detail below, indicated that the Mu2e front end boards achieved sufficient and comparable resolution when compared to single photoelectron data taken in similar configurations with the SSP.

7.5 DUNE Photon Detection Research and Development

A number of environments exist for testing prototype components for the DUNE SP FD module. They range from small-scale, easily adaptable test stands to full-size prototype detectors. The following sections outline the goals and results of the various DUNE research and development work pertaining to the photon detection system, with specific focus on the bench top warm-readout tests performed at Fermilab and the design, installation, and first results of the ICEBERG test stand located at the Fermilab Proton Assembly Building. Testing of the photon detection system for DUNE is still ongoing. These results provide a snapshot of the state at this point in time.

7.5.1 Initial Warm Readout Tests

To determine the viability of the Mu2e readout electronics for use in DUNE, initial readout tests were performed using a 72-MPPC (Hamamatsu 6×6 mm^2) active ganging board in combination with a balun to convert the differential signal to a single-ended signal that the Mu2e FEB would accept. The SiPMs were biased with $V_b = 47.2$ V. The MPPC board was operated at cryogenic temperatures suspended inside a dewar of liquid nitrogen. A blue/UV LED was flashed in time with the trigger on the warm readout board, which was connected to a laptop set up for data acquisition. A schematic of the setup and the components is shown in Figure 7.10. These cold tests demonstrated single-photon sensitivity with signal-to-noise levels comparable to similar setups tests previously with the SSPs.

A trigger was used to take data in time with the LED flasher. Each flash was recorded over

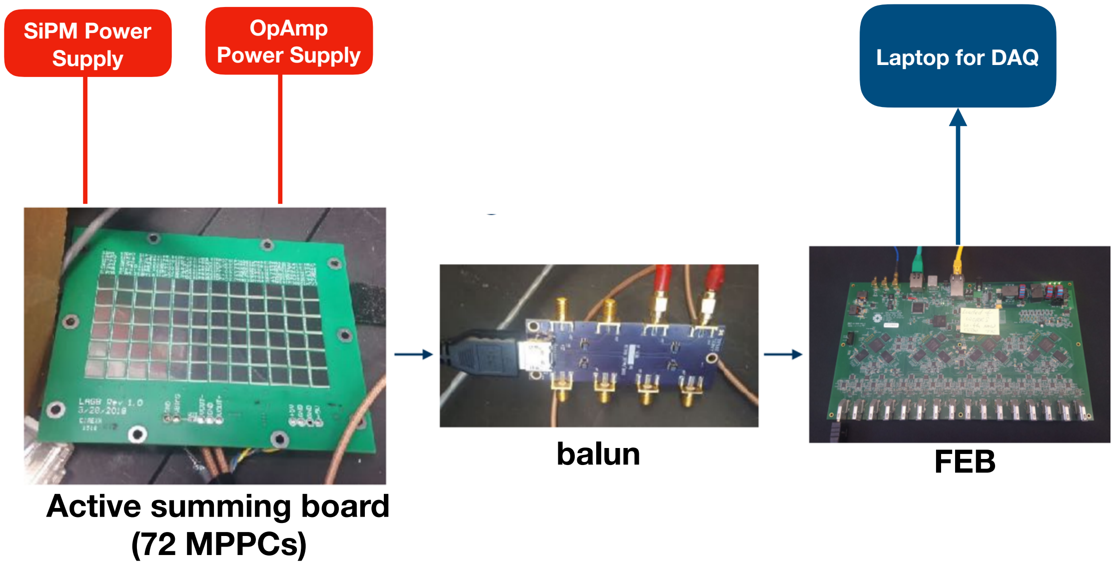

Figure 7.10: An schematic of data readout for early tests pairing the Mu2e prototype front end board with actively ganged SiPMs. The balun was a custom design created specifically for these tests to converted the active ganging board's differential signals to a single-ended signal compatible with the Mu2e front end board.

a ~ 3 μs window with samples taken every 12.55 ns. Figure 7.11 shows the average pulse shape. Pulses had a rise time of ~ 125 ns, a fall time of ~ 350 ns, and a recovery time of of order 2 μs, noting that the maximum readout window for the Mu2e FEB used in these tests was ~ 3 μs and the full pulse recovery is not quite captured within that window. Figure 7.12 shows the distribution of maximum ADC recorded in each readout window. The first peak above zero corresponds to electronics noise and the second peak is the single photo electron signal. The S/N was measured to be 4, calculated using the ratio of the single photon peak (20, after subtracting the noise peak) to the spread in the noise ($\sigma_{\text{noise}} = 5$ ADC). This is comparable to the value found when using the SSP (S/N = 5, shown in Figure 7.13).

Having demonstrated the end-to-end capabilities of the Mu2e front end boards, they were then integrated into the ICEBERG TPC at Fermilab for further testing in parallel with new efforts to update and redesign parts of the board to better suit the needs of DUNE, while taking advantage of the low-cost commercial ultrasound ADC capabilities demonstrated with the prototype Mu2e front end boards.

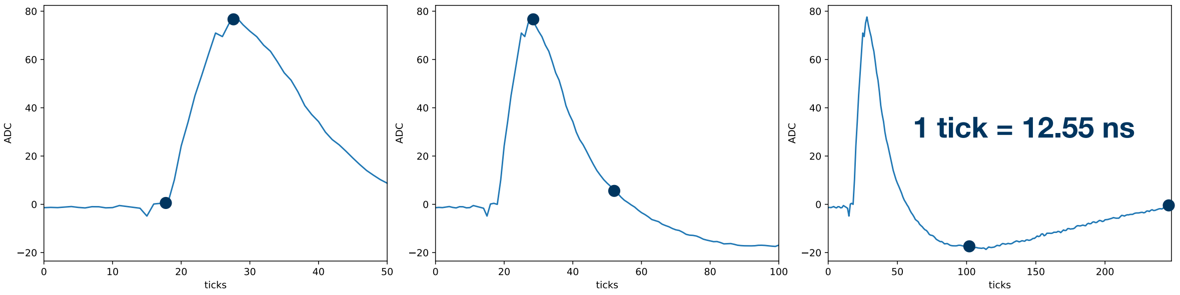

Figure 7.11: Average signal shape in tests with the Mu2e front end electronics and a 72-MPPC active ganging board. Pulses had a rise time of ∼125 ns, a fall time of ∼350 ns, and a recovery time of order 2 μs, noting that the maximum readout window for the prototype board used in these tests was ∼3 μs and the full pulse recovery is not quite captured within that window.

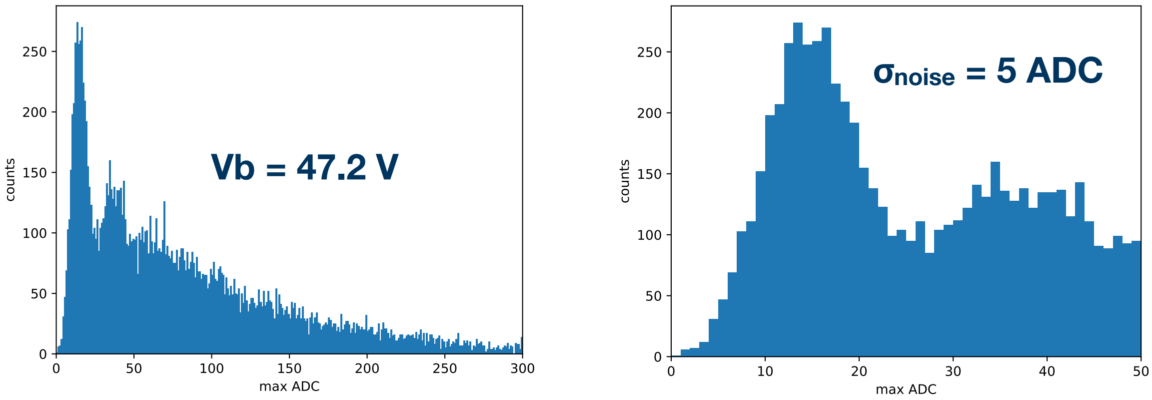

Figure 7.12: Maximum ADC recorded in each readout window in tests with the Mu2e front end electronics and a 72-MPPC active ganging board. The first peak above zero corresponds to electronics noise and the second peak is the single photoelectron signal. The signal-to-noise ratio was measured to be 4.

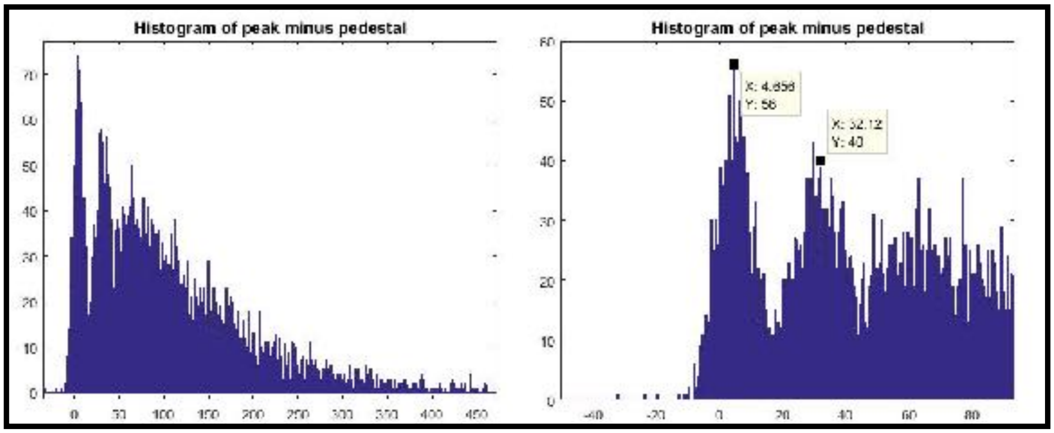

Figure 7.13: Maximum ADC recorded in each readout window in tests with the SSP and a 72-MPPC active ganging board. The SSP achieves S/N = 5 for this configuration. Provided by G. Cancelo and D. Totani.

7.5.2 ICEBERG Test Stand

The ICEBERG (Integrated Cryostat and Electronics Built for Experimental Research Goals) test stand is a reduced-size (94.7 cm $\times$ 79.9 cm) version of the FD APA designed for DUNE. The cryostat, built new for this purpose holds about 3500 liters of liquid argon. The ICEBERG APA has 2180 readout channels and two drift chambers each with a maximum drift distance of 30 cm. The anode plane sits at the center of the field cage with cathode planes on either side. The APA has two slots for $\sim$half-size photon detector modules, oriented horizontally, such that one sits directly above the other. The ARAPUCA modules are outfitted on one end with active ganging electronics for an array of 48 SiPMs spaced along the sides of the modules to make one readout channel. The SiPMs are biased at $V_b = 48$ V. A rendering of the ICEBERG TPC with its field cage and a PD module are shown in Figure 7.14.

The cryostat is outfitted with four external scintillator paddles, with two overlapping each on the top and bottom of the cryostat, directly above each other on one side of the central anode plane. Cosmic rays that pass through both pairs of paddles, such that a coincident signal is seen across all four paddles, indicates a cosmic trigger. A drawing of the cosmic paddle configuration in shown in Figure 7.15. In this configuration, the two photon detector modules should see approximately equal quantities of light from cosmics traversing the detector. That said, an effort to properly simulate photon detection in ICEBERG is underway. In addition, ICEBERG's capacity for rapid turnaround provides an opportunity to simply swap prototype photon detectors to eliminate any systematic differences between slots (relevant for cases where the goal is to compare two alternative components).

During the initial data-taking runs with photon detectors in ICEBERG, the Mu2e FEB-based DAQ was not integrated with the `artdaq` system used by the TPC electronics. Instead, the trigger signal was forked at the NIM logic boards on the DAQ electronics rack and then routed to the electrically isolated detector eletronics rack housing the PD system readout electronics using a LuxLink optical fiber transmitter/receiver pair. The Mu2e front end board could also be triggered internally to take noise data. One data channel was read out from each PD module. A schematic of the photon detector system in ICEBERG is shown in Figure 7.16. The power distribution and grounding for the system is shown in Figure 7.17.

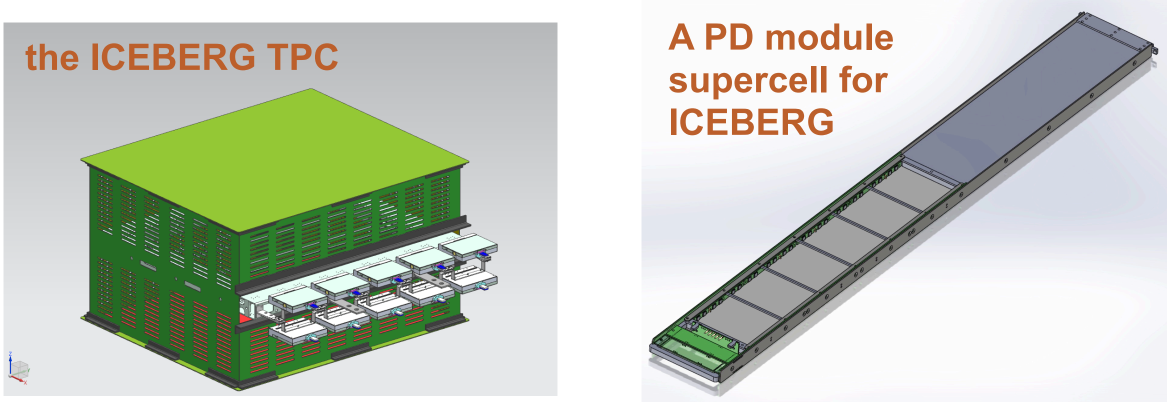

Figure 7.14: (left) The ICEBERG TPC and field cage. The TPC has two 30 cm drift chambers with an anode plane at the center of the field cage. (right) A PD module for ICEBERG. These modules are approximately half the length of full scale DUNE modules.

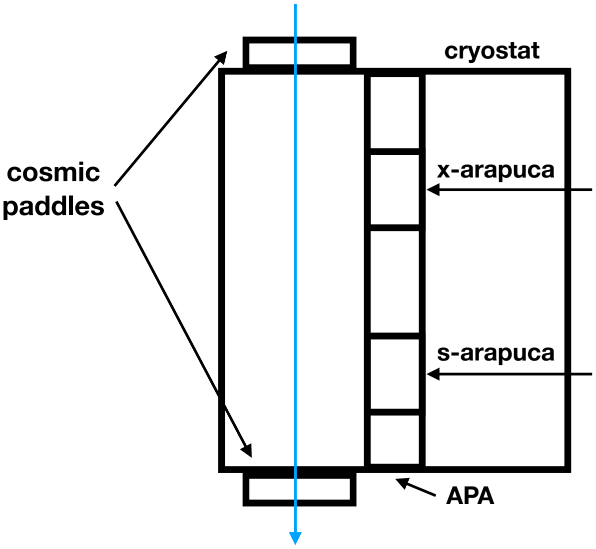

Figure 7.15: A depiction of the placement of the scintillator paddles in ICEBERG.

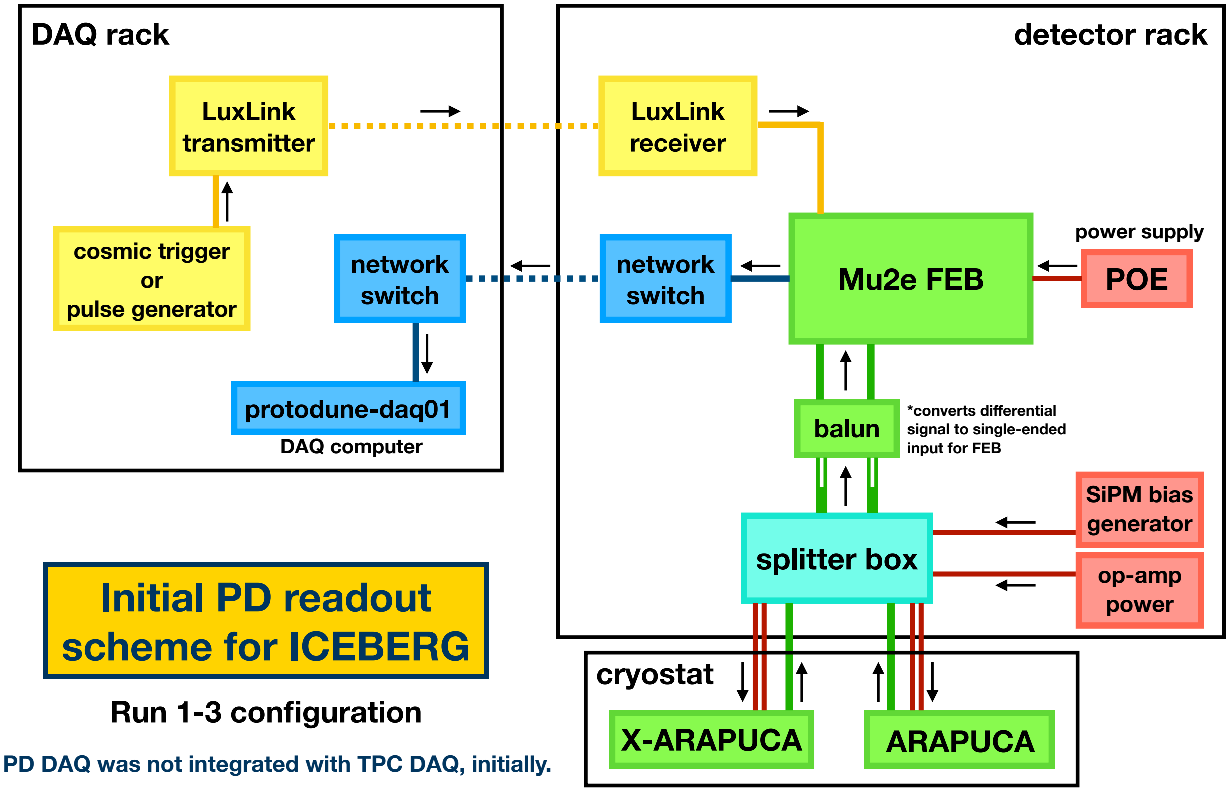

Figure 7.16: The ICEBERG photon detection system as designed for initial running in 2018. Notably, the Mu2e front end electronics could not be integrated directly into the TPC DAQ at this stage, so a separate trigger system was devised to transmit the scintillator paddle signals to the PD electronics.

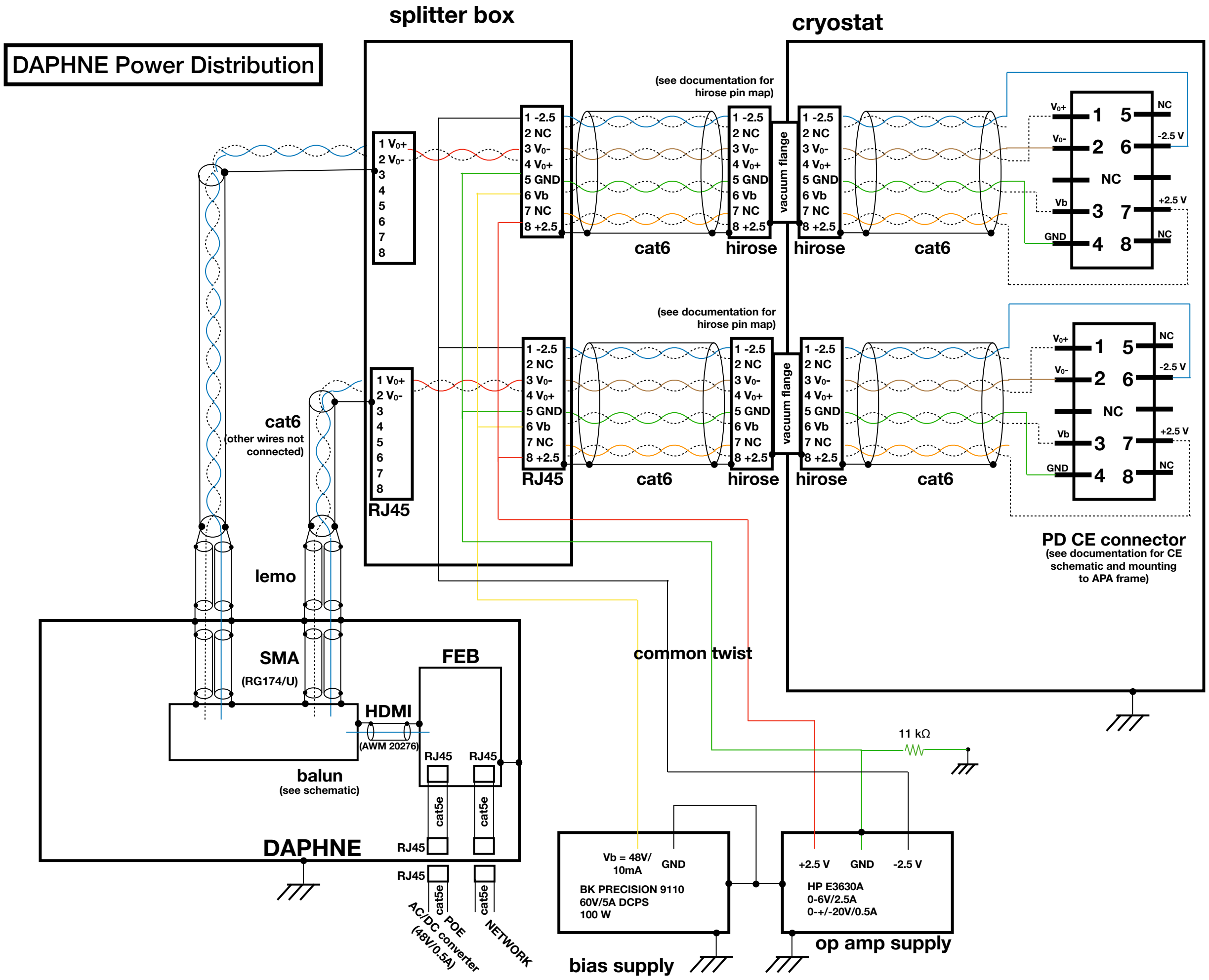

Figure 7.17: The power distribution and grounding for the ICEBERG PD system during initial runs with the Mu2e front end electronics in 2018.

The photon detector system in ICEBERG allows direct comparisons between the ProtoDUNE SSP and the Mu2e-based DAPHNE readout electronics, and the original ARAPUCA design and updated X-ARAPUCA designs. It also provides a flexible space to test future designs of photosensor active ganging boards. ICEBERG was initially instrumented with one S-ARAPUCA and one X-ARAPUCA to enable direct measurement of relative efficiency in an environment similar to that of DUNE (though on a significantly smaller scale).

The photon detector system in ICEBERG received operation readiness approval on March 1, 2018, and recorded first light on March 11 (the first cosmic signals seen by any part of the detector!). Initially, data could not be read out simultaneously from the S-ARAPUCA and X-ARAPUCA due to problem with one of the channels on the balun used. This problem was solved for subsequent runs by switching to an alternate channel on the balun. Examples of the first waveforms collected in ICEBERG are shown in Figure 7.18. As noted earlier, these waveforms from the S-ARAPUCA and X-ARAPUCA taken during the first run were not collected simultaneously and cannot be directly compared. Subsequent runs showed consistent simultaneous signal observations between photon detectors, but noise issues prevented a precise comparison between the modules. However, preliminary investigations simply comparing pulse height between the two for the same event show some indication of higher light yield in the X-ARAPUCA, consistent with earlier comparisons by UNICAMP. Figure 7.18 shows the result. The data fall along a line with a slope slightly greater than 1, a hint favoring the X-ARAPUCAs (as expected) before future higher precision comparisons are made.

Notably, a number of noise sources were visible to the photon detection system in these early runs. The primary goal during the initial checkout tests were to demonstrate end-to-end capabilities of the readout chain, with the exception of fully integrated DAQ, and characterize the noise of the system. To check that the photon detector system did not inject noise into the TPC, the photon detector was powered on in several phases with TPC noise runs taken at each stage to verify that TPC noise levels remained unchanged. No crosstalk was observed between the photon detection system and TPC electronics during these tests.

The original power supply used for biasing the SiPMs, a Keithley 2400, was found to be producing a mid-frequency chirping noise at regular intervals that interfered with a significant fraction of data. The Keithley was replaced by a BK Precision 9110 60V/5A power supply, completely

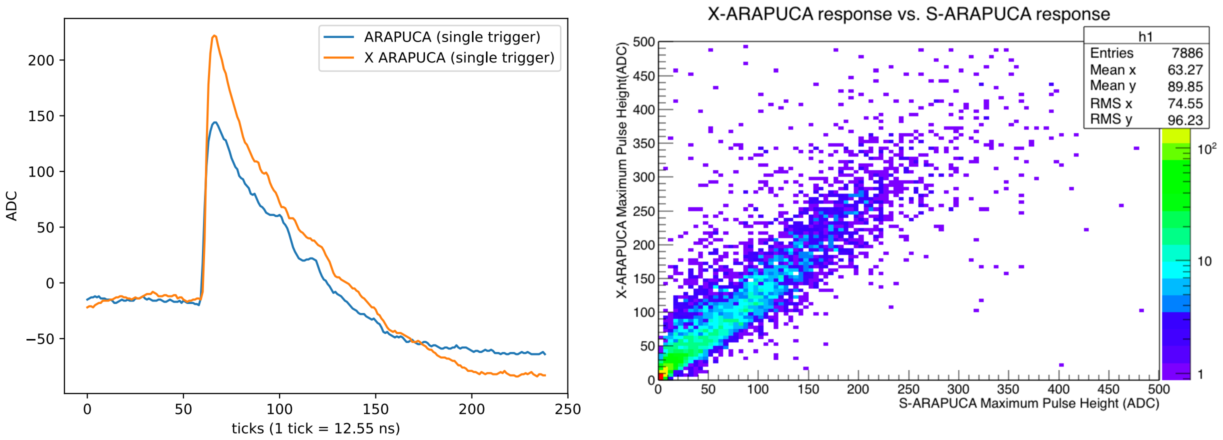

Figure 7.18: (left) Examples of the first waveforms collected by the photon detection system in ICEBERG. Note that these pulses should not be directly compared as they were not collected simultaneously. This problem was solved for future runs. (right) Data from Run 2 in ICEBERG comparing pulse height observed on the X- and S-ARAPUCAs for the same event. The data trend has a slope slightly greater than 1, hinting at agreement with early tests by UNICAMP that found the X-ARAPUCA to be more efficient than the S-ARAPUCA.

eliminating the chirping noise. Average FFTs for a sample of data collected using both power supplies are shown in Figure 7.19. The sharp peak around 3.5 MHz in the left plot represents the Keithley-generated chirping noise.

With the initial proof of concept achieved and better understanding of noise features both inherent to the system and from the lab environment itself (the ICEBERG cryostat was electrically isolated from the building ground to significantly reduce environmental noise), the next round of PD tests in ICEBERG will use new prototype DAPHNE boards (as opposed to the retrofitted Mu2e front end electronics) that will be capable of integrating with the TPC DAQ. Future tests in ICEBERG will not only be able to make precision comparisons between prototype photon detector components, but also take advantage of the calorimetric and topological information provided by the TPC. The rapid turn around capabilities at the smaller scales in ICEBERG complement the large-scale long term tests of the ProtoDUNEs at CERN, creating a flexible and powerful suite of R&D detectors for fully optimizing the DUNE single phase photon detection system.

7.5.3 ProtoDUNE-SP

ProtoDUNE is a large-scale, fully-instrumented prototype detector for DUNE that operated in the presence of a single-particle beam in 2018. The ProtoDUNE PD system included three pro-

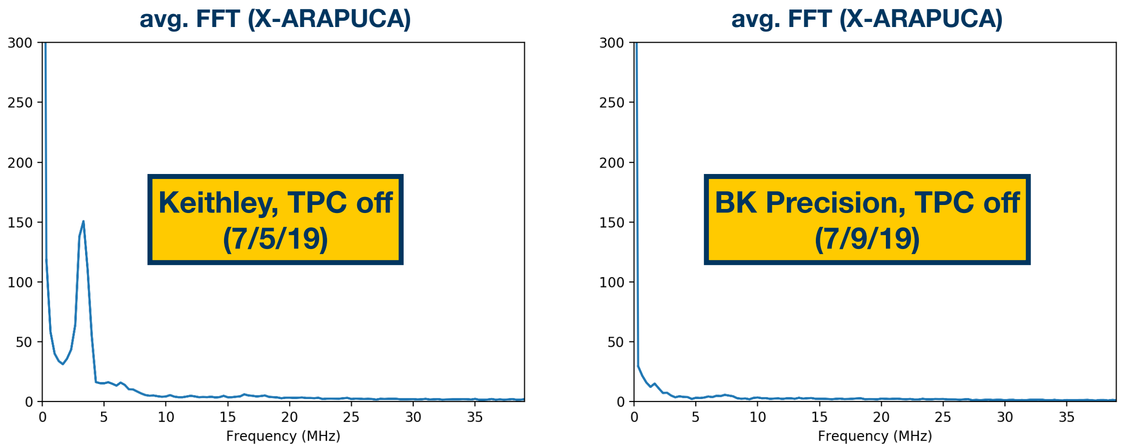

Figure 7.19: (left) Average FFT for PD data taken using the Keithley 2400 to supply $V_b = 48$ V to the SiPMs. The sharp peak around 3.5 MHz in the left plot represent the Keithley-generated chirping noise. (right) Average FFT for PD data taken using the BK Precision 9110 60V/5A to supply $V_b = 48$ V to the SiPMs. The power supply generated noise has been eliminated.

totype photon collectors: 29 double-shift light guides, 29 dip-coated light guides, and 2 standard ARAPUCA arrays. ProtoDUNE was successful on a number of fronts: it confirmed the superior detection efficiency of the ARAPUCA over light guides, it demonstrated the timing capabilities of the PD system, and the data was used to calibrate the ARAPUCA light yield using both a UV-light calibration system and tagged cosmic rays [128]. There are plans to test the X-ARAPUCA design in a future run of ProtoDUNE. During the first ProtoDUNE run, ProtoDUNE's PD digitizers were not the Mu2e electronics currently intended for use in DUNE, but the alternative Signal SiPM Processor (SSP). The layout of the different photon detectors and detector response for a 7 GeV electron are shown in Figure 7.20. The S-ARAPUCA is clearly superior to both types of light guides.

7.5.4 ProtoDUNE-SP-2

ProtoDUNE-2, a second test run in the ProtoDUNE detector, will be used for large-scale end-to-end testing of the final pre-production PD system, representing the culmination of the research and development described throughout this chapter. The ProtoDUNE-2 system will be re-outfitted to include: full size X-ARAPUCAs, 48-channel active ganging cold-side electronics, and readout using the optimized ultrasound ADC-based electronics (DAPHNE) including full integration of the TPC and PD DAQ systems.

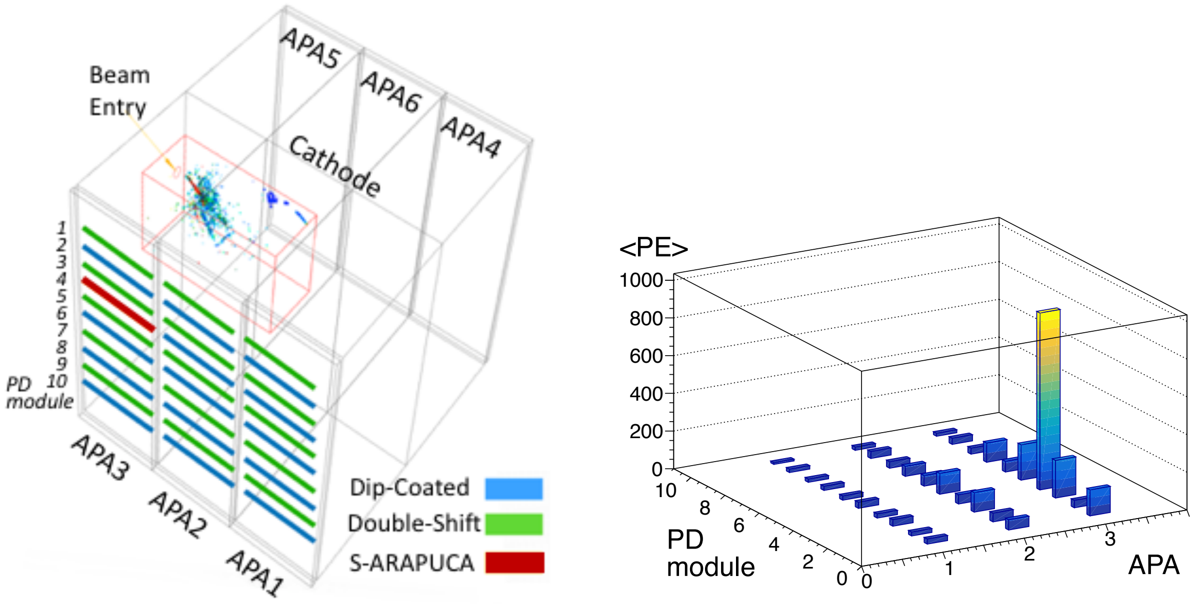

Figure 7.20: (left) A schematic illustrating the layout of the photon collector modules in ProtoDUNE-SP shown with an event display. (right) PD response in photoelectrons to a 7 GeV electron. The S-ARAPUCA is clearly superior to the light guides.

7.5.5 SBND

While not officially part of the DUNE experiment, SBND will provide a large-scale operational testing environment for X-ARAPUCAs, similar to those designed for DUNE, and demonstration of DAQ integration with the prototype Mu2e warm readout electronics. SBND is planning to begin taking data in 2021. Assembly and installation of the X-ARAPUCA modules will provide valuable insight for DUNE's future plans, and PD data collected using the X-ARAPUCAs will help to further characterize the performance of the detection technology. The SBND photon detection system is discussed in more detail in Chapter 6.

7.6 Outlook

The DUNE PD system is critical for achieving both the nucleon decay- and supernova-related physics goals in DUNE. In addition, it will provide valuable crosschecks to charge readout, supplemental calibration methods, and improved time and energy resolution. Extensive testing and validation of the component for the PD system are underway and the system is well on its way toward achieving the specifications driven by the physics goals of the experiment.

CHAPTER 8

First Measurement of Monoenergetic Muon Neutrino Charged Current Interactions[1]

Oscillation experiments, which are used to measure the parameters that govern neutrino mixing, rely on our ability to correctly reconstruct neutrino energies. Unfortunately, a number of factors make this task extremely difficult. Final state interactions and short range correlations between nucleons have been studied, but predictions are extremely model dependent and neutrino generators use a wide range of strategies for including these effects in their calculations. Detector limitations also contribute to worsening reconstructed energy resolution. Detectors are often insensitive to certain types of final state particles. For example, the MiniBooNE experiment is a mineral oil Cherenkov detector that cannot see neutrons or protons because both fall below the Cherenkov threshold, and time projection chambers like MicroBooNE are insensitive to neutral final state particles. Detector and model limitations both contribute to yield typical energy resolutions of $\Delta E/E \sim 25\%$. A simulated example of energy resolution for three neutrino energies interacting with ^{12}C is shown in Figure 8.1.

8.1 Neutrinos from Kaon Decay at Rest

A charged kaon decays to a muon and a muon neutrino ($K^+ \to \mu^+\nu_\mu$) 63.6% of the time [42]. In the case that the kaon is at rest when it decays, the muon neutrino is monoenergetic at 236 MeV.

---

[1] The work presented in this chapter was published in the following paper: *Phys. Rev. Lett.* **120** 141802 (2018) [129], which was selected as an Editors' Suggestion and featured in *Physics*. R. S. Fitzpatrick is a corresponding author along with J. Jordan, J. Grange, and J. Spitz. The text in this chapter comes largely from a technical note produced by those listed, focused on the contributions of RSF.

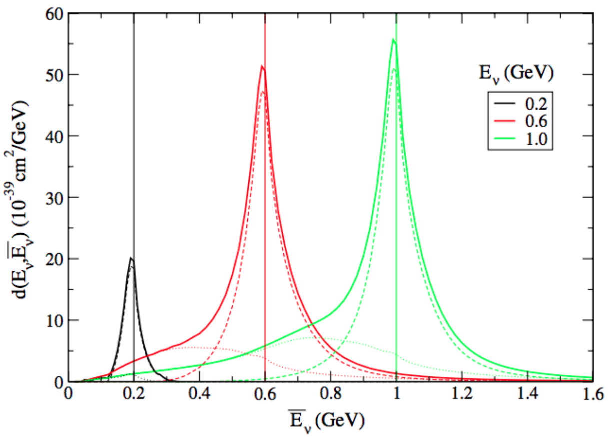

Figure 8.1: Simulated neutrino energy resolutions at 200 MeV, 600 MeV and 1 GeV for a ^{12}C target, as in the MiniBooNE detector at Fermilab. Figure 1 in [130].

This neutrino has been identified as an important source for a number of unique physics measurements, including as a source for a high-Δm^2 oscillation search [131, 132] and as a standard candle for studying the neutrino-nucleus interaction, energy reconstruction, and cross sections in the hundreds of MeV energy region [133]. There are other ideas for how to use this neutrino as well, including as a source to make a precision Δ_s measurement [133] and as a possible signature of dark matter annihilation in the sun [134]. Despite the importance of the KDAR (kaon decay-at-rest) neutrino, it has never been isolated and identified.

Other than the monoenergetic neutrino from charged pion decay-at-rest (29.8 MeV, well below the CC interaction threshold), the KDAR neutrino is the only relevant case in accelerator-based neutrino physics where the neutrino's energy is known. In particular, the KDAR neutrino represents the first known-energy, weak-interaction-only probe of the nucleus. The measurement reported here, in terms of a variable historically reserved for electron scattering probes of the nucleus, $\omega = E_\nu - E_\mu$ ($E_\nu = 236$ MeV), is unprecedented.

Uncertainties associated with the neutrino interaction and energy reconstruction currently dominate [135, 136], and are expected to continue to dominate [137], the systematics in both short and long baseline neutrino oscillation experiments. Unfortunately, there is no silver bullet experiment that can solve all of the issues associated with the neutrino interaction and energy reconstruction across all relevant energies and nuclear targets. A worldwide program of cross section measurements on multiple targets and at multiple energies is underway [90, 135, 138–141]. KDAR neutrino interaction measurements have their place among these, specifically targeting the long baseline low energy region, where the second and third oscillation maxima, depending on energy and baseline, dominate. Notably, there is no resonant pion production at 236 MeV, which simplifies the treatment of the interaction. However, these low energies are challenging to deal with from a theoretical perspective, because the impulse approximation, in which it is assumed that the incoming neutrino strikes a single nucleon, breaks down. That is, these energy transfers are right at the transition between neutrino scattering off of nucleons ($\nu_\mu n \rightarrow \mu^- p$) and neutrino scattering off of nuclei (e.g. $\nu_\mu {}^{12}\mathrm{C} \rightarrow \mu^- X$, where X is an excited nucleus or proton) and are therefore difficult to model.

Historically, our knowledge of what is inside of the nucleus has come largely from electron scattering experiments. Electrons of known energy ($\Delta E/E \sim 10^{-4}$ is typical) are shot at a nuclear target and the energies and scattering angles of the outgoing electrons are measured. The recoiling target nuclei/nucleons are sometimes studied as well. The energy transferred to the nucleus can immediately be inferred using the variable $\omega = E_e - E_e'$, or energy transfer, in order to discern the structure and behavior of the nucleons (and quarks, at high energy transfer). Such a measurement has never been done with neutrinos, unfortunately, as the neutrino energy has always been an unknown. KDAR provides the tool, for the first time with neutrinos, to study nuclear structure and the axial-vector component of the interaction using electron scattering variables such as ω. The dearth of knowledge of the neutrino-nucleus interaction at these energies is apparent in Figure 8.2, which shows a number of leading model predictions for the differential cross section in terms of energy transfer (ω) for 300 MeV ν_μ CC scattering. The disagreement between the models, in terms of both shape and normalization, is striking.

8.2 The MiniBooNE Experiment

The MiniBooNE detector uses 445 tons (fiducial volume) of mineral oil and 1280 photomultiplier tubes (PMTs), with an additional 240 PMTs instrumenting a veto region, to identify neutrino events originating from the Booster Neutrino Beamline (BNB) and Neutrinos at the Main Injector (NuMI) neutrino sources. The experiment has reported numerous oscillation and cross section measurements and new physics searches since data taking began in 2002 [87]. For this analysis,

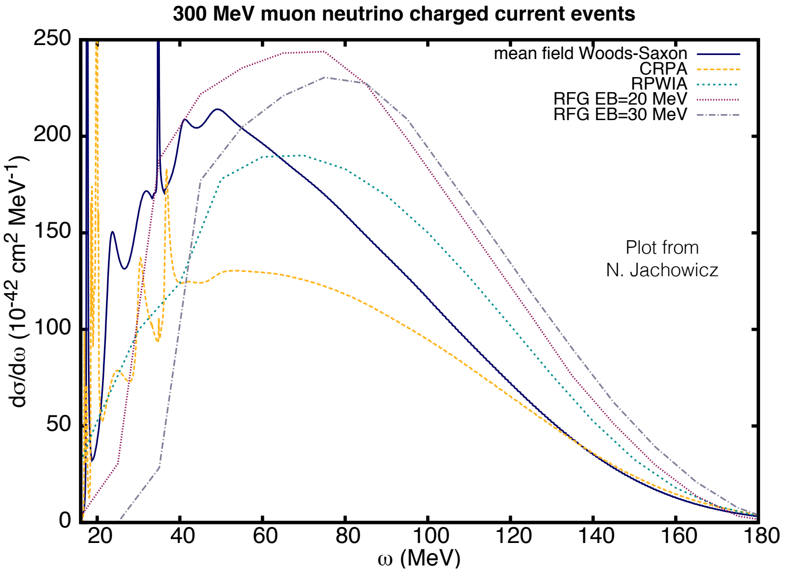

Figure 8.2: The differential cross section in terms of energy transfer ($\omega = E_\nu - E_\mu$) for 300 MeV ν_μ CC scattering on carbon. Predictions from various models are shown. Note that the x-axis cuts off at $\omega \sim 18$ MeV due to the effect of binding energy. This plot is adapted from Ref. [142].

we consider the charge and time data of PMT hits collected during the NuMI beam spill.

8.3 The NuMI Beamline and KDAR Neutrinos in MiniBooNE

The Neutrinos as the Main Injector (NuMI) beamline provides an intense source of KDAR neutrinos that can be observed by the MiniBooNE detector, which is 86 m from the NuMI absorber, where the majority of KDAR neutrinos are produced. The 2.0-interaction-length NuMI target allows approximately 14% of the energy associated with the primary NuMI protons (120 GeV) to pass through. A significant fraction of these protons reach the beam absorber where they interact to produce charged kaons, the majority of which come to rest and then decay at rest. The energy distribution of primary and secondary protons (originally 120 GeV) that reach the dump is shown in Figure 8.3.

A schematic of the NuMI beamline with respect to MiniBooNE is shown in Figure 8.4. The various contributions to the NuMI neutrino-mode neutrino flux at MiniBooNE, in terms of neutrino creation position, are shown in the inset. MiniBooNE sees significant contributions from neutrinos

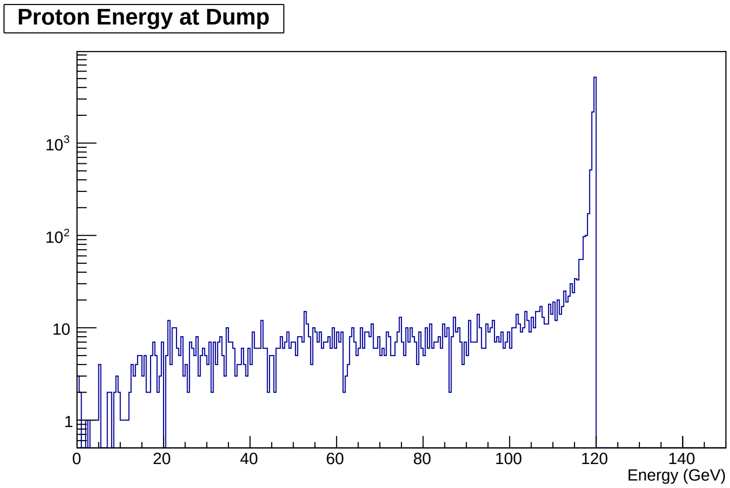

Figure 8.3: Energy distribution of protons reaching the beam dump from the target in a toy NuMI beam simulation.

created at the target/decay pipe, the horns, shielding around the beamline, the air in the beamline, and, most importantly for this analysis, the absorber. The NuMI beamline coordinate (z) creation positions of muon neutrinos, muon antineutrinos, and KDAR muon neutrinos that reach MiniBooNE in NuMI antineutrino-mode (the configuration used for this analysis) according to the FLUGG simulation (discussed later), are shown in Figure 8.5. The location of the beam dump is easily seen at $z \sim 72000$ cm. About 84% of KDAR neutrinos that reach MiniBooNE are predicted to originate at the NuMI dump ($z > 72000$ cm in Figure 8.5).

8.4 Expected KDAR Event Rate in MiniBooNE

The KDAR event rate at MiniBooNE is expected to be similar in both NuMI's low-energy neutrino and antineutrino modes, since KDAR production from the absorber is not dependent on the polarization of the horns. However, the background ν_μ and $\overline{\nu}_\mu$ event rate is predicted to be about 30% lower in the antineutrino mode. We use data taken in this configuration from 2009–2011, corresponding to 2.62×10^{20} protons on the NuMI target. A timeline overview of the NuMI beamline configuration is given in Figure 8.6.

The total cross section of KDAR 236 MeV ν_μ CC interactions on carbon is around 1.3×10^{-39} cm^2/neutron according to NuWro and the theoretical prediction in Ref. [143]. The Martini *et al.* RPA model predicts a KDAR ν_μ QE cross section of 1.3×10^{-39} cm^2/neutron and an additional np-nh cross

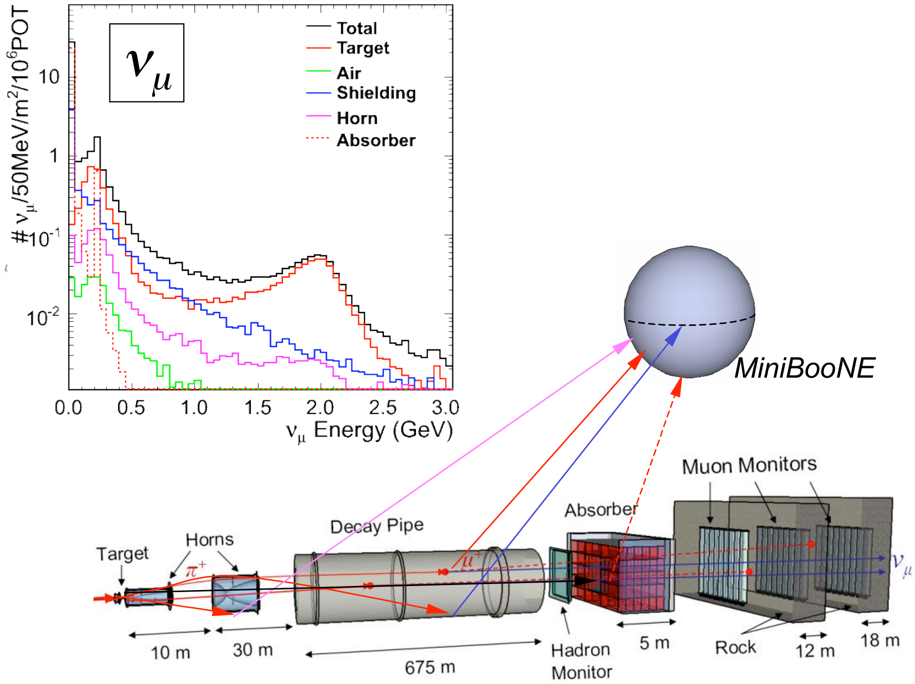

Figure 8.4: A schematic (not to scale) of the NuMI beamline with respect to MiniBooNE. The neutrino-mode flux, and the various neutrino creation position contributions to the flux, are shown on the top left. The KDAR ν_μ contribution can be seen as the dotted red line (corresponding to neutrinos from the absorber) with the clear spike in the E_ν =200-250 MeV bin.

section of 2.0×10^{-40} cm^2/neutron [130, 144, 145]. Based on the various predictions for the total cross section at this energy, we assign a 25% uncertainty to the KDAR ν_μ CC cross section with a central value of 1.3×10^{-39} cm^2/neutron.

An estimate of the KDAR event rate at MiniBooNE, along with some relevant assumptions, is shown in Table 8.1. This table assumes all KDAR neutrinos interact at the center of MiniBooNE, 86.3 m away from the NuMI dump, and that KDAR neutrinos from the dump represent 84% of the total KDAR neutrinos that interact in MiniBooNE, the others coming from the NuMI target station, decay pipe, and shielding, well upstream of the dump. No uncertainty is assigned to this number as it is negligible compared to both the uncertainty on the number of KDAR neutrinos produced at the dump per proton on target and the neutrino interaction cross section. A number of software-based predictions for the KDAR neutrino production rate at the NuMI dump are shown in Table 8.2. As can be seen, the predictions for the KDAR neutrino production rate per POT at the

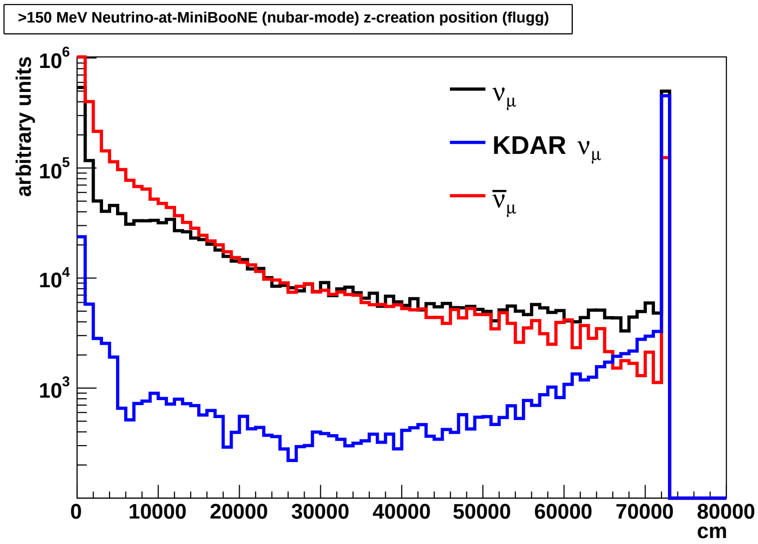

Figure 8.5: The creation position of ν_μ that reach MiniBooNE in NuMI antineutrino-mode, according to the FLUGG simulation. 84% of KDAR neutrinos originate at the NuMI dump ($z > 72000$ cm).

NuMI dump vary significantly. The low-end and high-end predictions differ by almost a factor of two, from 0.061 ν_μ/POT (FLUKA05) to 0.115 ν_μ/POT [MARS2014 (simplified geometry)].

We take the mean and standard deviation of the five values in Table 8.2 as the central value and uncertainty on the ν_μ/POT expected, 0.084 ± 0.023 KDAR ν_μ/POT at the dump. This is rather naive and simple but, once again, this derived rate prediction is not used for any part of this analysis; it is useful only as a sanity check and developing a feel for what is expected in the detector with the analysis exposure considered.

Before efficiency corrections, we expect 3500 ± 1300 KDAR ν_μ CC events in MiniBooNE's fiducial volume (500 cm radius) with the analysis exposure of 2.62×10^{20} POT. The large total uncertainty comes mainly from both the neutrino cross section uncertainty and the at-dump kaon production uncertainty.

8.5 KDAR Analysis

The high-level goal of the KDAR selection is to isolate the signal 236 MeV KDAR neutrinos originating from the NuMI beam dump (absorber) from decay-in-flight backgrounds originating throughout the NuMI horns and decay pipe. A schematic of the MiniBooNE, NuMI, and the

Assumption	Value	Uncertainty
KDAR ν_μ flux at MiniBooNE	0.90 $\nu_\mu/\text{m}^2/10^6$ POT	± 0.24
Fiducial radius cut (mass)	500 cm (442.4 tons @ 0.845 g/cm^3)	-
σ / neutron	1.3×10^{-43} m^2	$\pm 25\%$
POT	2.62×10^{20}	-
KDAR ν_μ CC events @ 236 MeV	3500	1300

Table 8.1: An estimate for the number of KDAR ν_μ CC events in the MiniBooNE KDAR analysis, along with relevant assumptions.

Model	KDAR ν_μ/POT (dump-only)
FLUKA05 (ν-mode [146])	0.061
FLUGG software (NuMI run 1, $\overline{\nu}$-mode)	0.062
GEANT4.9.6P04 (QGSP_BERT, simplified geometry)	0.085
GEANT4.9.6P04 (QGSP_FTFP, simplified geometry)	0.098
MARS2014 (simplified geometry)	0.115

Table 8.2: A number of software-based predictions for the KDAR neutrino production rate at the NuMI dump. Please note: "POT" refers to proton-on-target, not proton-on-dump. The numbers shown in the table are referring to the number of KDAR neutrinos produced at the dump for every proton on target. Note that KDAR ν_μ/POT is largely independent of horn polarization; neutrino- and antineutrino-mode have similar yields.

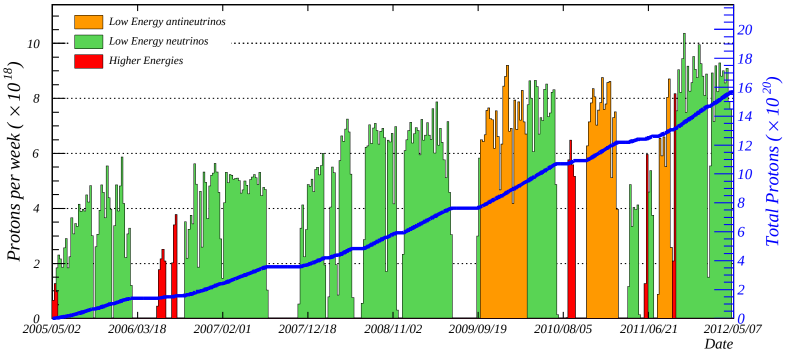

Figure 8.6: Overview of the NuMI beamline configuration from inception through mid 2012. This analysis uses the two earliest low-energy antineutrino configuration runs marked in orange. The figure is from [58].

different signal and background sources is shown in Figure 8.7. First a strategy for reconstructing low energy muons in MiniBooNE is explored, as this signal sits below the traditional MiniBooNE analysis energy threshold (Section 8.5.1). Next, a set of selection cuts is designed to isolate signal-like events, including a discussion of the signal models available from Nuance (Section 8.5.2). It will become clear that a more generic signal model is preferable to the Nuance distributions, though these models are still used to generate the folding matrices used in the analysis. The folding matrices and selection efficiencies are then described (Section 8.5.3). And finally, given the still strong background contributions, a time dependent statistical framework was designed to extract KDAR shape and rate information from the data after the selection cuts by taking advantage of the changing ratio between signal and background during the beam window (Section 8.6). This section includes a discussion of the more generic signal model used. Finally, results and validation are described in Section 8.7.

8.5.1 Reconstructing Low-Energy Muons

Although the signal muon energy range considered for this measurement is lower than past MiniBooNE cross section analyses featuring $\nu_\mu/\overline{\nu}_\mu$ [147–153], the energy and timing distributions of MiniBooNE's vast calibration sample of 0–53 MeV electrons from muon decay provide a strong benchmark for understanding the detector's response to low energy muons in terms of both scintillation and Cherenkov light. Further, a scintillator "calibration cube" in the MiniBooNE volume

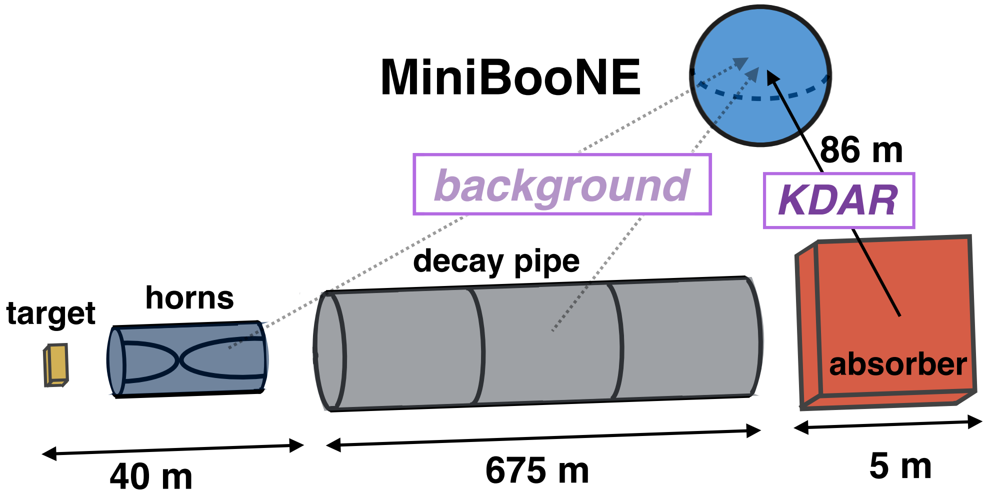

Figure 8.7: The NuMI beamline and the various sources of neutrinos that reach MiniBooNE (dashed lines). The signal KDAR neutrinos (solid line) originate mainly from the absorber.

at 31 cm depth, used to form a very pure sample of tagged 95 ± 4 MeV cosmic ray muons, shows excellent agreement between data and Monte Carlo simulations in terms of timing, Cherenkov angle, and energy reconstruction [87]. The energy resolution for 95 MeV muons is measured to be 12%; a detailed detector simulation agrees and predicts that the muon energy resolution in low energy ν_μ CC events drops gradually to about 25% for 50 MeV muons. The detection efficiency for KDAR ν_μ CC events is $>$ 50% for events containing muons with energy $>$ 50 MeV.

We note again that, according to NuWro's prediction for muon kinematics, approximately 14% of muons created in 236 MeV ν_μ CC events are expected to be produced with energy less than 39 MeV, the Cherenkov threshold for muons in MiniBooNE mineral oil. Given that the energy range of this analysis is lower than previous ν_μ CC analyses, which have all featured a **TankHits** $>$ 200 requirement, we have explored in some detail the various available techniques and variables for reconstructing such events.

The figure of merit for this analysis is muon kinetic energy in KDAR events. A number of reconstruction algorithms have been studied for extracting this quantity with as high resolution as possible. The relationships between true muon kinetic energy and various first-subevent reconstructed quantities for simulated background (true ν_μ CCQE events of all energies passing cuts) in NuMI antineutrino-mode are shown in Figure 8.8 (requiring $T_\mu > 50$ MeV). All reconstructed quantities shown produce a strong correlation with muon kinetic energy, although the correlation tends to breaks down, as expected, for muons produced near or below Cherenkov threshold. The variables tested are:

- **TankQTot**, the integrated PMT charge of the event.
- **TankHits**, the total number of PMT hits.
- **TankHits*myStFull_fqlt05 (also referred to as $\mathtt{PMThits}_{\mathtt{5ns}}$)**[2], the total number of PMT hits times the fraction of light in the first 5 ns.
- **TankHits*myStFull_fqlt10**, the total number of PMT hits times the fraction of light in the first 10 ns.
- **myStFull_energy**, the total energy of the event according to the Stancu Full Fitter.
- **myStFull_energy_mu**, the total energy of the muon according to the Stancu Full Fitter.
- **myStFlux_Ecer_mu**, the total energy of the muon according to the Stancu Fitter and in consideration of early (Cherenkov) light.

Figure 8.9 shows the energy resolution of each variable, evaluated using a simple linear fit to the simulated data (requiring $T_\mu > 50$ MeV). As can be seen, **myStFlux_Ecer_mu** performs the best; a Gaussian fit to this distribution in Figure 8.9 provides a 1σ resolution of about 11% (the fit is poor). The "fqlt" variables, **TankHits*myStFull_fqlt05** and **TankHits*myStFull_fqlt10**, perform strongly as well–a Gaussian fit to the **TankHits*myStFull_fqlt05** distribution provides a 1σ resolution of about 12% (the fit is poor).

KDAR-induced muons are expected to populate a "signal region" defined as 0–120 **TankHits*fqlt05** and representing T_μ in the range 0–115 MeV. Because of the kinematics of 236 MeV ν_μ CC events, no signal is expected at higher energies. The "background-only region" is defined as **TankHits*fqlt05** > 120.

8.5.2 KDAR Sample Selection

The following selection criteria are applied for isolating a KDAR-like ν_μ CC sample:

---

[2] This variable, which is ultimately employed for this analysis, is also referred to in shorthand as **TankHits*fqlt05** and ultimately, for clarity in the final publication as $\mathtt{PMThits}_{\mathtt{5ns}}$. They are used somewhat interchangeably throughout this chapter.

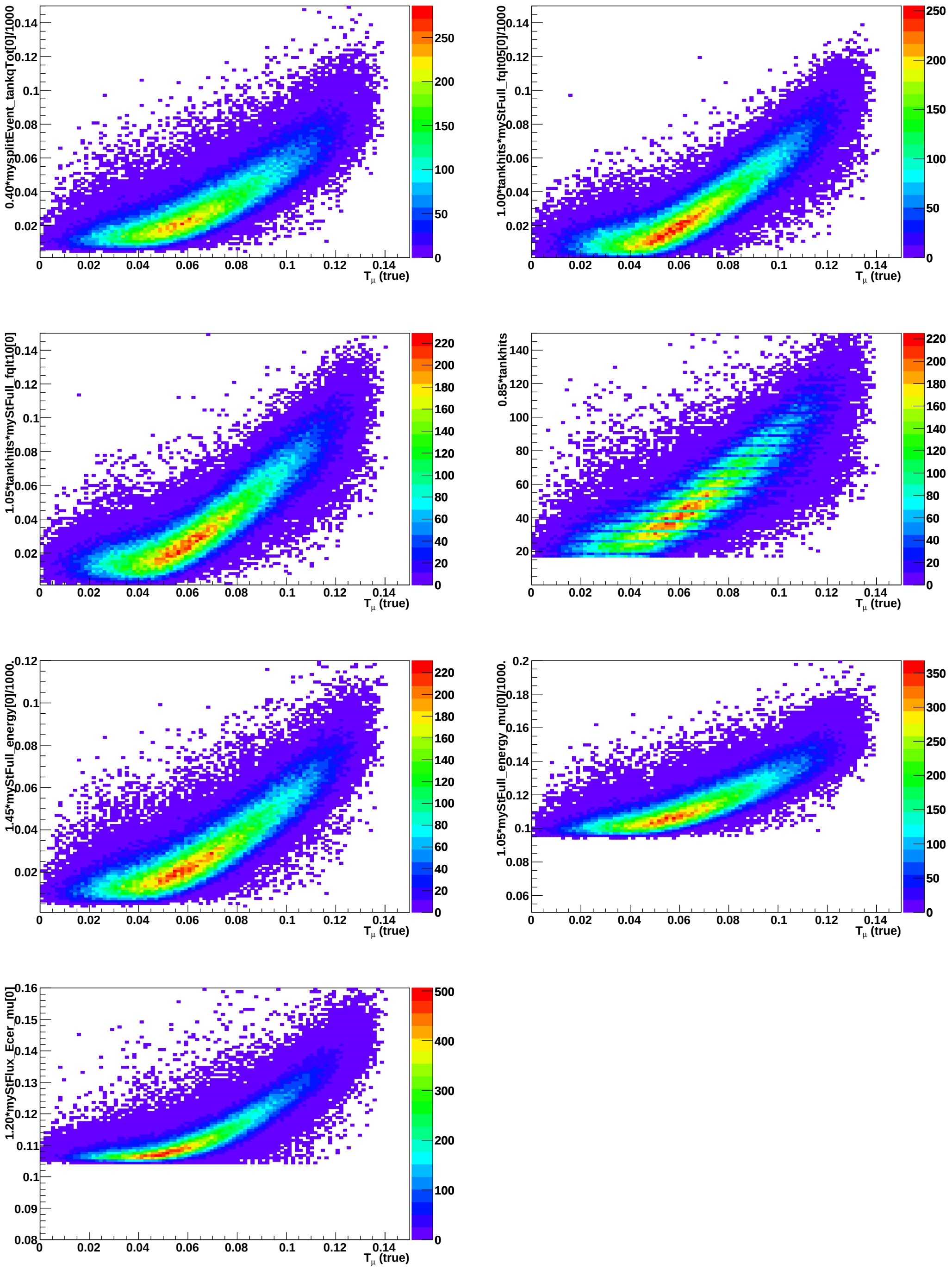

Figure 8.8: The relationship between true energy and reconstructed energy for events (simulated background; true ν_μ CCQE with $E_\nu < 300$ MeV) passing cuts in NuMI antineutrino-mode. Note that, in some cases, a multiplicative factor has been added to the underlying reconstructed quantity for visualization purposes.

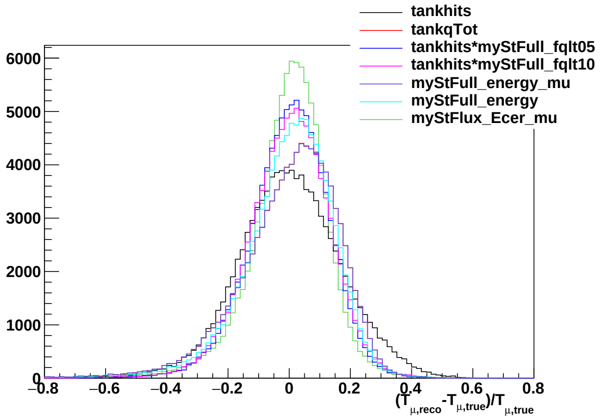

Figure 8.9: The muon energy resolution capabilities of various reconstructed quantities. This plot is in consideration of NuMI antineutrino-mode ν_μ CC from $E_\nu < 300$ MeV and $T_\mu > 50$ MeV.

1. **Two subevents and $<$ 6 veto tube hits in each SE:** Enforcing observation of the primary muon and its decay electron along with requiring containment of both particles. This cut also serves to reject incoming charged particles (e.g. cosmics).

2. **Muon subevent in beam time window:** Average PMT hit time between 2.5 and 11.7 μs from the opening of the NuMI beam trigger window. This cut removes non-beam events from consideration.

3. **2nd SE TankHits $<$ 200 and $>$ 20:** The upper bound enforces that the 2nd SE is consistent with a Michel. The lower bound is due to an observed increased strength in the low **TankHits** region of the 2nd SE of events with low energy in the first SE. This shape is present in the simulation but its origin is not clear and so out of caution we choose to discard these events.

4. **Reconstructed vertex radius $<$ 500 cm from tank center:** Avoids interactions close to the detector wall which are reconstructed less accurately. We use the *TransRFull* reconstruction. See Section 8.5.1.

5. **1st SE TankHits $>$ 20:** Ignores the lowest-energy events which likely contain contributions from unsimulated and poorly-simulated nuclear processes. This cut is explicitly included in the usual OneTrack reconstruction package used by the bulk of previous MiniBooNE analyses.

6. **1st SE PMT hit time RMS $<$ 50 ns:** PMT hit times in the 1st SE should be well-grouped together in time if they are associated with the same particle activity. This cut is also explicitly included in the usual OneTrack reconstruction package used by the bulk of previous MiniBooNE analyses.

7. **Michel distance $<$ 150 cm:** Requiring the distance between the reconstructed event vertex and the Michel decay to be less than 150 cm significantly removes coincident background events. This cut is discussed in more detail below.

8.5.2.1 Nuance and κ

The fundamental difficulty with this analysis is that the background in the KDAR signal region is poorly known and difficult to constrain, both in terms of shape and normalization. This issue mainly arises due to uncertainty in the cross section and kinematics of ν_μ CC events at low energies, although significant uncertainties in the neutrino and antineutrino flux (which are at the $\sim$20% level) are present. Although one can develop a "side-band contraint" at some level, looking at events just outside the signal region (e.g. 150-300 **TankHits**) in terms of shape and normalization, this constraint will only be relevant on one side of the expected signal region (0-100 **TankHits**). Identifying a sideband on either side of the signal region might alleviate this issue, allowing the background in the signal region to be inferred. Of course, this is not possible for the case of extracting KDAR as the expected signal is at the lower extreme of the distribution. In general, any chosen side-band (e.g. 150-300 **TankHits**) cannot successfully constrain the shape and normalization of the background in the KDAR signal region. Even if it could at some level, it is very hard to assign a reasonable uncertainty estimate to this prediction. Relying on a cross section and kinematic model/generator for predicting the background in this region not considered acceptable and an alternative analysis strategy has therefore been pursued. Examples of Nuance-generated signal models are shown in Figure 8.10, with shape variations driven by scaling a Nuance parameter κ, which has the effect of scaling the magnitude of the Pauli blocking effect (see Ref. [154] for more details). A more generic signal model is adopted for the signal and background shape measurements. The only use of the Nuance-generated models is in defining the folding matrix and efficiencies for the analysis, discussed in the next section.

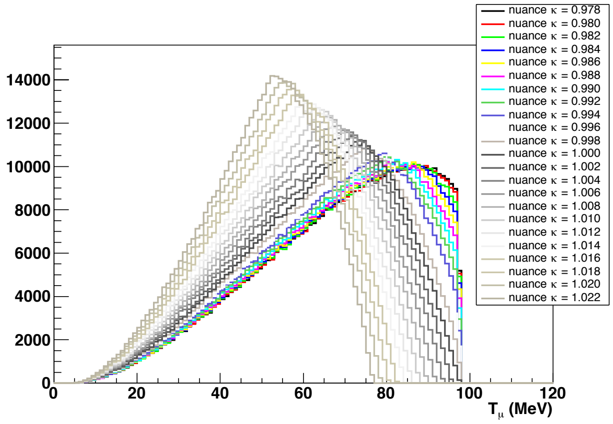

Figure 8.10: Nuance-generated 236 MeV ν_μ CC T_μ distributions for various κ values. Increasing κ results in a softer muon kinetic energy spectrum.

8.5.3 Folding Matrix and Efficiency

While the analysis presented here does not rely on a generator or model to provide a background prediction, it does rely on determinations of both the detection efficiency and folding matrix (used to transform true muon kinetic energy into a detector observable), which are *weakly* dependent on the Nuance event generator and choice of generator parameters, including κ.

The after-all-cuts detection efficiency for simulated antineutrino mode ν_μ CCQE events ($\kappa = 0.978$) in terms of T_μ is shown in Figure 8.11. Also, the "folding-matrix", representing the relationship between true T_μ and `PMThits`$_{\texttt{5ns}}$, is shown. This folding matrix is created after all analysis cuts, and requires each true event to be ν_μ CCQE and have an interaction vertex with radius < 500 cm. Ultimately, while the Nuance event generator (and choice of κ) is not used to make a signal-region background prediction for this analysis (e.g. for background subtraction), the detection efficiency and folding matrix are used to transform from reconstructed `PMThits`$_{\texttt{5ns}}$ to efficiency-corrected T_μ. The choice of κ in the Nuance signal model is therefore relevant for creating these distributions. Fortunately, the choice of κ has a negligible impact on both the efficiency and folding matrix, as shown later. For reference, the efficiency and folding matrix distributions are shown for the case of $\kappa = 1.022$ in Figure 8.11 on the bottom, to be compared to the case of $\kappa = 0.978$ on the top.

8.6 Analysis Procedure

Finally, we describe the procedure for extracting the time-dependent KDAR signal from the sample defined in the previous section. The section will begin with an overview of the procedure and glossary of terms.

8.6.1 Summary of the Analysis Strategy

The next section describes the analysis in full detail. Here, we offer a basic summary of the analysis strategy.

As has been discussed, forming a reliable background prediction with reasonable error bars in the KDAR signal region is very difficult. In the absence of timing information, any such prediction

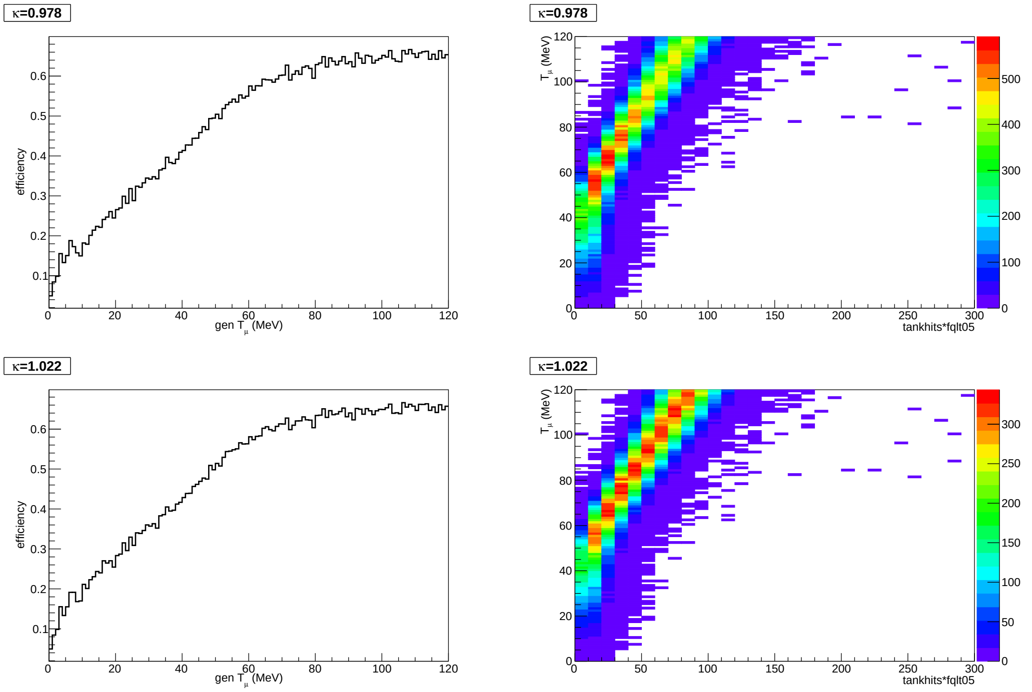

Figure 8.11: (Left, top) The muon neutrino CCQE reconstruction efficiency as a function of T_μ, given the full analysis cuts discussed and $\kappa = 0.978$. (Right, top) The "folding matrix", representing the relationship between true T_μ and **TankHits*fqlt05**. This folding matrix is created after all analysis cuts, and requires each true event to be ν_μ CCQE and with a true interaction vertex with radius < 500 cm. The bottom plots are analogous to the top ones, but with $\kappa = 1.022$.

would be highly dependent on the chosen neutrino event generator and input parameters. In order to overcome these issues, we employ an alternative strategy, which takes advantage of the unique beam timing characteristics of KDAR events, recalling that signal KDAR ν_μ CC events are expected to come from the beam dump while background pion/muon decay-in-flight $\nu_\mu/\overline{\nu}_\mu$ CC events are expected to come from the target station and decay pipe. The main points to remember are:

- A KDAR signal is expected in the 0-120 **TankHits*fqlt05** region, corresponding to muon kinetic energies in the range ~0-115 MeV (see Figure 8.8, top right). No KDAR signal is expected for >120 **TankHits*fqlt05**.
- The shape (in **TankHits*fqlt05**) of both the background and KDAR signal are expected to be constant for all times.
- The KDAR signal and background normalizations change as a function of time. But, they do

not change in the same way. In particular, the ratio of signal-to-background is suppressed at early times (2500-3100 ns) and enhanced at late times (11100-11700 ns). Further, no signal is expected at times 2500-2700 ns.

The analysis proceeds in five steps:

1. The data sample is broken up into 7 time slices: 3 early-time bins (2500-2700 ns, 2700-2900 ns, and 2900-3100 ns), 1 "*normal-time*" bin (3100-11100 ns), and 3 late-time bins (11100-11300 ns, 11300-11500 ns, and 11500-11700 ns).

2. A background template and signal template (both in **TankHits*fqlt05**) are formed using events in *normal-time*. The background template is made equal to the *normal-time* data distribution in the region where no signal is expected (>120 **TankHits*fqlt05**). Concurrently, a candidate signal template is created using a generic three-parameter beta distribution (two parameters control the shape, one parameter controls the normalization), drawn from a large number of possible signal shapes and normalizations within reasonable physical limits. In the signal region (<120 **TankHits*fqlt05**), the background template is chosen such that the candidate signal distribution plus the background distribution is equal to the *normal-time* data distribution. For all values of **TankHits*fqlt05**, the sum of the signal template plus the background template is equal to the *normal-time* data distribution.

3. In each of the 3 early and 3 late time bins, the normalization of each background template is adjusted so that it is consistent with the number of events observed in each time bin's non-signal region (>120 **TankHits*fqlt05**).

4. Given background templates in each of the 3 early and 3 late time bins, the candidate KDAR signal shape (from *normal-time*) is tested in each time bin (except for the first time bin, where there is no signal expected). The signal shape is held constant for all early and late time bins; the normalization is allowed to float.

5. Finally, a χ^2 is formed from a comparison between the signal+background templates and data in the 3 early and 3 late time bins. This procedure is repeated many 1000s of times for various candidate signal shapes and normalizations.

8.6.2 Notation and Definition of Terms

Throughout this section, the following index notation will be used:

- i — time bin [e.g. 2500-2700 ns, 3100-11100 ns (*normal-time*)].
- j — energy variable bin (e.g. **TankHits*fqlt05**). The bin width for the default analysis using **TankHits*fqlt05** is 10.
- k — a particular test signal normalization in *non-normal-time*.
- N — *normal-time* region. A particular case of index i.
- M — energy variable bin (j) above which no signal is expected. M is defined for each energy variable as follows: **TankHits** $\rightarrow M = 150$; **myStFull_energy_mu** $\rightarrow M = 185$; **myStFlux_ecer_mu** $\rightarrow M = 120$; **TankHits*fqlt05** $\rightarrow M = 120$; **TankHits*fqlt10** $\rightarrow M = 120$. As an example, no KDAR events are expected to produce **TankHits*fqlt05** > 120.
- d — MiniBooNE data, usually presented $d_{i,j}$, representing data inside an energy variable bin j and time bin i.

The time bins are defined such that there are three signal-suppressed bins ($2500 - 2700$ ns, $2700 - 2900$ ns, and $2900 - 3100$ ns), one high-statistics *normal-time* bin in which the signal to background ratio is expected to be constant over time ($3100-11100$ ns), and three signal-enhanced bins ($11100 - 11300$ ns, $11300 - 11500$ ns, and $11500 - 11700$ ns).

We also adopt the following notation for commonly used terms:

- NT — *normal-time*
- NNT — *non-normal-time* (signal-enhanced and signal-suppressed regions)

The χ^2 minimization for this analysis is performed using the **TankHits*fqlt05** variable.

In the absence of a reliable background prediction, we employ a template-based analysis which tests the consistency of various candidate KDAR signal T_μ distributions with data. We consider a broad and well-defined set of possible T_μ signal shapes and determine how well each matches the data. This procedure can be thought of as the reverse of the usual differential cross section measurement extraction. Instead of starting from a detector observable and turning it into a measure of T_μ, for example, we start with a candidate "true" T_μ distribution and map (or "fold") it into a detector observable distribution in `PMThits`$_{\texttt{5ns}}$. The candidate true T_μ signal shapes are based on a beta distribution. This carefully chosen function, with only two parameters characterizing its shape, is meant to cover all physical and continuous shapes that the true KDAR-induced T_μ distribution can take, noting that we are not sensitive to few-MeV-scale resonance features (e.g. as predicted by continuous random phase approximation calculations [155]). The shape of the signal model (T_μ spectrum) is defined by two parameters, a and b, according to the beta distribution: $x^{a-1}(1-x)^{b-1}/B(a,b)$, where $B(a,b) = \Gamma(a)\Gamma(b)/\Gamma(a+b)$ and $x = T_\mu/T_\mu^{\max}$. After correcting for detector efficiency, each candidate T_μ distribution is folded into the corresponding `PMThits`$_{\texttt{5ns}}$ distribution and compared to data as a function of time. The normalizations of signal and background are expected to change at early and late times, but the shapes of each stay nearly constant.

8.6.3 Test Statistic

We leverage a vast set of signal templates (described in Section 8.6.4) and the high-statistics NT region ($d_{N,j}$) to define a data-driven background spectrum for a given signal model shape S_j (normalized to 1), and signal normalization η. The background B_j is then defined as:

$$B_j \equiv d_{N,j} - \eta S_j. \tag{8.1}$$

The inferred background is an estimate of the background with relatively small uncertainties because of the high statistics in the NT region. We expect the background and signal shapes to remain constant for all time bins, so we can use this background prediction to compare the data from NNT regions to the signal model. Thus, the model prediction in each NNT region, $T_{i,j,k}$, is given by:

$$T_{i,j,k} \equiv \alpha_i B_j + \beta_{i,k} S_j, \tag{8.2}$$

where $\beta_{i,k}$ is the signal normalization in the ith time bin, and the background normalization α_i is defined by

$$\alpha_i \equiv \frac{d_{i,j>M}}{d_{N,j>M}} \tag{8.3}$$

and is independent of NT signal normalization η. The notation $d_{i,j>M}$ ($d_{i,j<M}$) implies a sum over all bin contents for $j > M$ ($j < M$). This takes advantage of the fact that S_j is only defined for $j < M$ (i.e., signal is only expected in the signal-region). Events above M energy units must be background events.

Furthermore, we impose the following requirements:

- $T_{i,j,k} \geq 0$
- $B_j \geq 0$,

to address the fact that it is nonsensical for any model (signal, background, or total) to include a bin with less than zero events.

It has also been shown that no signal events are expected in the first time bin. This bin then represents the expected shape of the background distribution. We include this information in our test statistic by defining a pull term

$$f_{\text{pull}} \equiv \frac{\left(\frac{d_{0,j<M}}{d_{0,\text{all}}} - \frac{B_{j<M}}{B_{\text{all}}}\right)^2}{\left(\sigma\left[\frac{d_{0,j<M}}{d_{0,\text{all}}}\right]\right)^2}, \tag{8.4}$$

where

$$\sigma\left[\frac{d_{0,j<M}}{d_{0,\text{all}}}\right] = \frac{d_{0,j<M}}{d_{0,\text{all}}}\sqrt{\frac{1}{d_{0,j<M}} + \frac{1}{d_{0,\text{all}}}}. \tag{8.5}$$

The pull term penalizes candidate models that produce background templates whose shape is inconsistent with the first time bin. The standard minimization procedure is calculated in the region $j < M$. Including the pull term provides us with a secondary test to the validity of the background template by comparing the number of background events observed in the $j < M$ region to the total number of events observed at all energies and ensures that the background model is consistent. The effect of the pull term is not dramatic, but it helps to reduce the spread in signal normalization, disfavoring those too large or small.

In the remaining NNT bins, after the first early time one, we marginalize over signal normalization $\beta_{i,k}$ in each time bin independently.

For a particular time bin $i \neq N$, we construct χ^2_i for a Poisson-distributed variable by comparing our model with data[3]:

$$\chi^2_{i,k} = 2\sum_j \begin{cases} T_{i,j,k} - d_{i,j} + d_{i,j}\ln(d_{i,j}/T_{i,j}) & d_{i,j} > 0 \\ T_{i,j,k} & d_{i,j} = 0, \end{cases} \tag{8.6}$$

and then marginalize over $\{\beta_{i,k}\}$ to produce

$$\chi^2_i = \min(\chi^2_{i,k}). \tag{8.7}$$

Finally, the total χ^2 for a particular point in phase space is given by

$$\chi^2 = \sum_i \chi^2_i + f_{\text{pull}}. \tag{8.8}$$

The $\pm 1\sigma$ bands can be found in the traditional way using $\chi^2_{\text{min}} + Q$, where Q is determined by the number of parameters being fitted. For three parameters $\{a, b, \eta\}$, $Q = 3.53$.

As the maximum energy (endpoint) of the T_μ spectrum is somewhat unknown, although constrained due to kinematics and binding energy, we extend our phase space to include T_μ^{max}, the endpoint of muon kinetic energy. The test statistic outlined above is calculated for $T_\mu^{\text{max}} \in [95, 115]$ MeV. This range of endpoints is chosen based on the extrema of model predictions and in consideration of binding energy, noting that 236 MeV (KDAR neutrino energy) - 106 MeV (muon mass) - 30 MeV (roughly the binding energy of carbon)= 100 MeV. The best fit endpoint is used for subsequent calculations (e.g. goodness of fit and error calculations). Including endpoint as a parameter in four-parameter space $\{a, b, \eta, T_\mu^{\text{max}}\}$, $Q = 4.72$.

8.6.4 Signal Model

The goal of this analysis is to extract the muon kinetic energy distribution in KDAR events. To this end, we use a well-defined set of possible T_μ signal shapes based on a "beta distribution." This carefully-chosen function, with only two parameters characterizing its shape, is meant to cover all of the possible and reasonable continuous shapes that the T_μ distribution can take on.

---

[3] Note: while the terms $d_{i,j}$ and $d_{i,j}\ln d_{i,j}$ remain constant for a particular χ^2_i, we include them in the calculation because the resulting χ^2 is always positive, simplifying interpretation.

The shape of the signal model (T_μ spectrum) is defined by two parameters, a and b, according to the beta distribution:

$$\frac{x^{a-1}(1-x)^{b-1}}{B(a,b)} \tag{8.9}$$

where $B(a,b) = \Gamma(a)\Gamma(b)/\Gamma(a+b)$. The distribution is nominally defined for $x \in [0,1]$, but we extend it to take values on $[0, T_\mu^{\max}]$.

We select a set of physically allowed and reasonable test models with the parameter sets $a \in [2.0, 8.0]$, $b \in [0.1, 6.0]$, requiring $b \le a$. As shown in Figure 8.12, relaxing these requirements and allowing templates with $a < 2.0$ or $a < b$, results in unphysical models. Ultimately, the requirement $b \le a$ is automatically satisfied by the allowed region result shown in Section 8.7 — so this restriction ends up being unimportant. The full set of signal model shapes is displayed in Figure 8.13. The single-parameter Nuance models based on κ are overlaid in black for reference. The beta distributions tested adequately cover the range of κ models and significantly extend the possible candidate T_μ distribution shapes. For each signal shape determined by the set $\{a, b\}$, we also marginalize over the endpoint $T_\mu^{\max} \in [95, 115]$ (MeV).

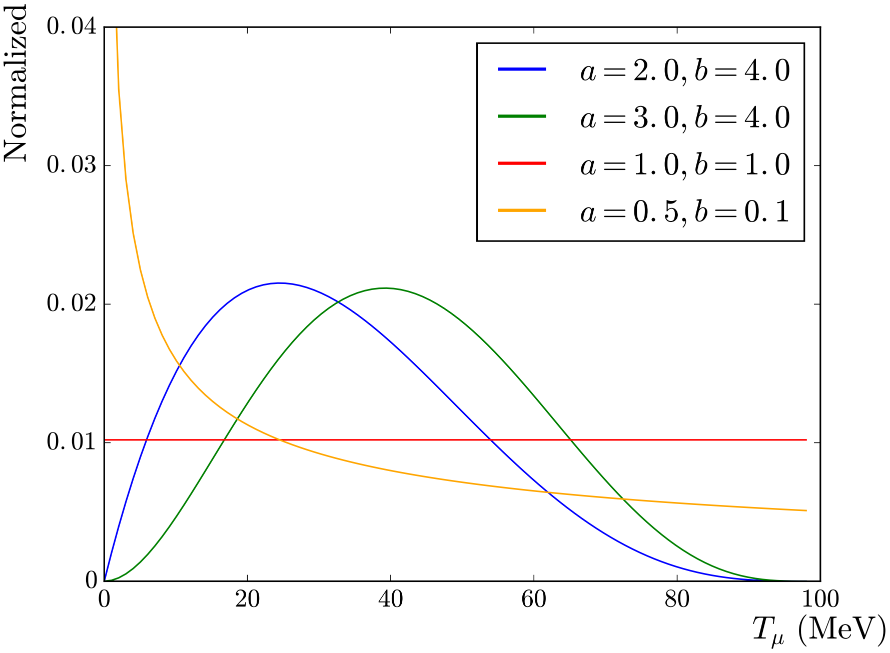

Figure 8.12: Signal models with combinations of a and b which are not allowed in the KDAR analysis.

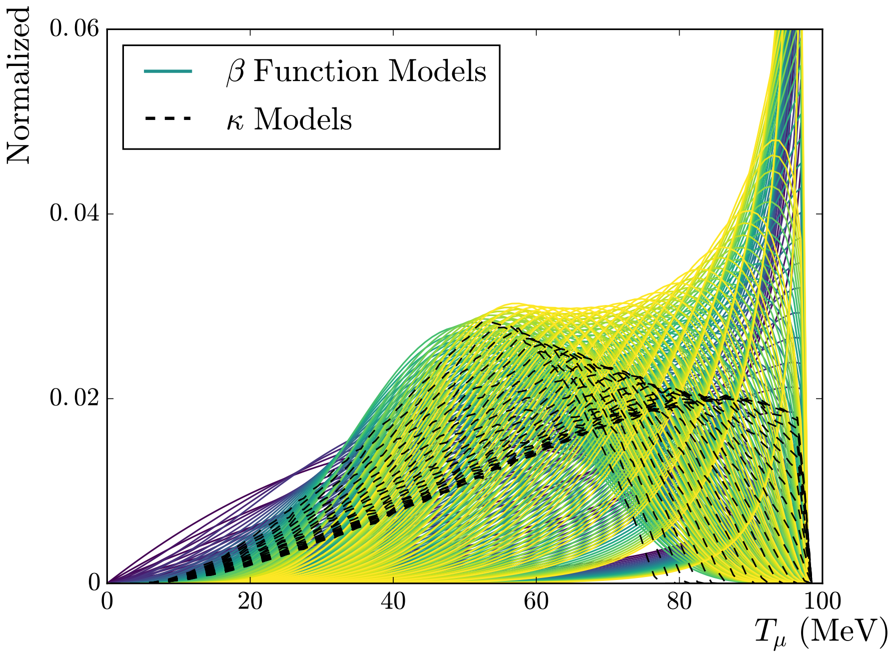

Figure 8.13: The set of T_μ template shapes defined by the beta distribution and compared to data in this analysis. In black, the models parameterized by Nuance (varying κ) are shown. The beta models cover the range of shapes defined by the κ models, and extend our range of test values. Note that 98 MeV is used as the KDAR muon kinetic energy endpoint in this example to match Nuance. In the full analysis, we consider all endpoints in the range $T_\mu^{\max} \in [95, 115]$ (MeV).

As we are interested in extracting the KDAR muon kinetic energy distribution, our signal models are derived from true T_μ. However, we need to correct for detector efficiency and fold the signal model T_μ distribution into our detector observable (**TankHits*fqlt05**) in order to compare to data and form a χ^2. We can think of this procedure as the exact reversal of the usual differential cross section measurement extraction. Instead of starting from a detector observable and turning it into a true measure of muon kinetic energy, we start with a true muon kinetic energy distribution and turn it into a detector observable distribution (in **TankHits*fqlt05**).

Starting with our true muon kinetic energy distribution, $T_{\mu,true,i}$ (i represents a bin of width 1 MeV), we first efficiency correct this distribution:

$$T_{\mu,observed,i} = \epsilon_i \times T_{\mu,true,i} \tag{8.10}$$

The after-all-cuts efficiency distribution (ϵ_i) is defined explicitly as:

$$\epsilon_i = \frac{\text{MC events passing all cuts}}{\text{MC true } \nu_\mu \text{ CCQE events with true event vertex inside of 500 cm fiducial volume}} \tag{8.11}$$

The distribution of ϵ_i in terms of true T_μ is shown on the top of Figure 8.11. Note that $\kappa = 0.978$ is used to form this efficiency distribution. We choose this κ value simply because it is most consistent with the data. Later, we show that this choice does not affect the final result significantly.

Next, we turn our $T_{\mu,observed,i}$ into our detector observable distribution S_j (j represents a bin of width 10, in terms of **TankHits*fqlt05**) by "folding." This procedure simply involves distributing the weight of each $T_{\mu,observed,i}$ bin amongst the corresponding S_j (**TankHits*fqlt05**) bins according to the folding matrix shown on the top of Figure 8.11. This matrix is formed after all analysis cuts, and requires each MC event to be a true ν_μ CCQE with a true interaction vertex inside the fiducial volume (radius $<$ 500 cm). Once again, we note that $\kappa = 0.978$ is used to form this folding distribution. Later, we show that this choice does not affect the final result significantly.

Figure 8.14 shows the evolution from $T_{\mu,true,i}$ (top), to $T_{\mu,observed,i}$ (middle), and finally to S_j (in **TankHits*fqlt05**) (bottom) for an arbitrary example input $T_{\mu,true,i}$ distribution with $a = 2.20$, $b = 1.10$, and T_μ endpoint $= 100$ MeV.

For a particular time bin (i), excluding the NT bin, the signal region data are distributed into 12 `PMThits`$_{\texttt{5ns}}$ bins (j) from 0–120. A χ^2_i for a Poisson-distributed variable is then formed by comparing the data ($d_{i,j}$) and a prediction ($P_{i,j,\alpha}$) based on the signal model ($T_{j,\alpha}$) with signal normalization α plus the background ($B_{i,j}$) such that $P_{i,j,\alpha} = T_{j,\alpha} + B_{i,j}$:

$$\chi^2_{i,\alpha} = 2\sum_j \begin{cases} P_{i,j,\alpha} - d_{i,j} + d_{i,j}\ln(d_{i,j}/P_{i,j,\alpha}) & d_{i,j} > 0 \\ P_{i,j,\alpha} & d_{i,j} = 0\ . \end{cases}$$

We then marginalize over the signal normalizations in each time bin to produce $\chi^2_i = \min\limits_{\alpha}(\chi^2_{i,\alpha})$.

No KDAR signal events from the absorber are expected in the first 200 ns time bin. This time period, therefore, contains the expected `PMThits`$_{\texttt{5ns}}$ shape of the background distribution in the signal region. In the first time bin, the measured ratio of data events in the 0–120 `PMThits`$_{\texttt{5ns}}$ signal region (28) to total number of events (118) is compared to the equivalent ratio for the current candidate model's background prediction to form an uncertainty weighted pull term (f_{pull}). This pull term penalizes candidate models that produce background templates inconsistent with the

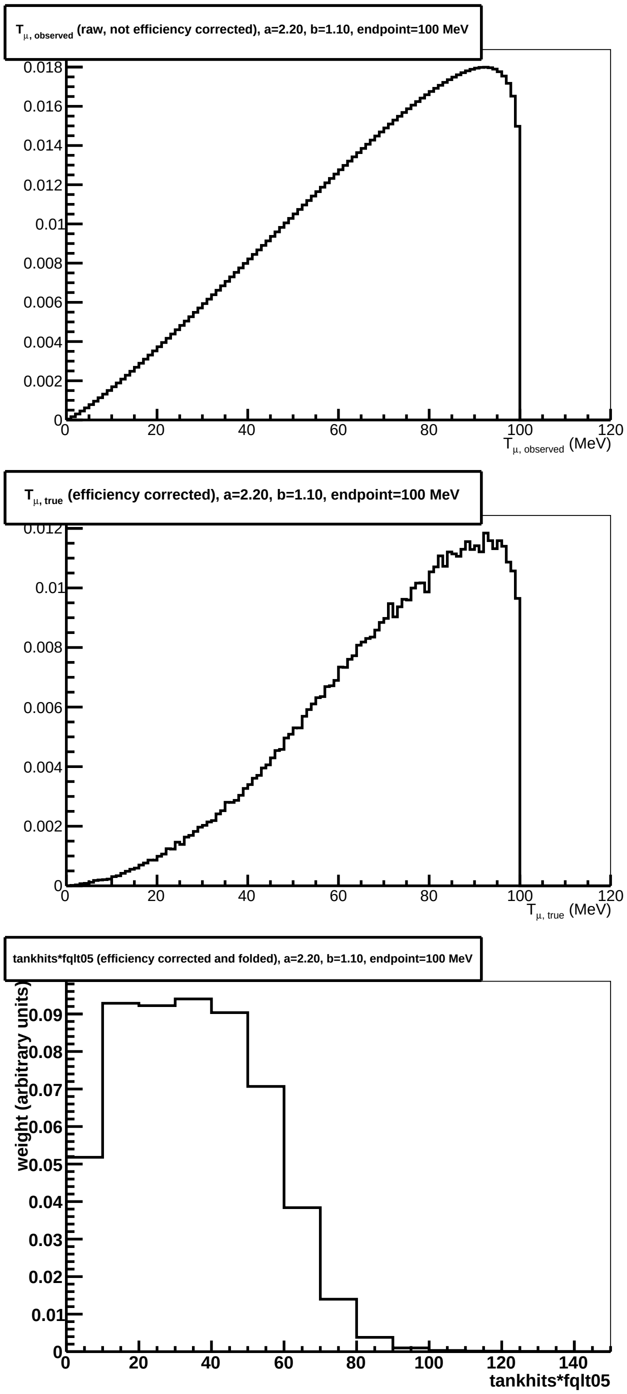

Figure 8.14: The evolution from $T_{\mu,true,i}$ (top), to $T_{\mu,observed,i}$ (middle), and finally to **TankHits*fqlt05** (bottom) for an arbitrary example input $T_{\mu,true,i}$ distribution with $a = 2.20$, $b = 1.10$, and T_μ endpoint $= 100$ MeV. The $\kappa = 0.978$-derived efficiency and folding distributions from Figure 8.11 are used.

first time bin. Finally, the total χ^2 for a particular model shape and normalization is given by $\chi^2 = \sum_i \chi_i^2 + f_{\text{pull}}$.

We test a set of physically allowed and reasonable models with the parameter sets $a \in [2.0, 8.0]$, $b \in [0.0, 6.0]$. Models with $0.0 < a < 2.0$ are considered unphysical and inconsistent with all predictions since they are initially concave down or do not go to zero at $T_\mu = 0$ MeV. We also test a range of muon kinetic energy "effective end points," $T_\mu^{\max} = 95$–115 MeV. Although the separation energy in ^{12}C is 17 MeV, corresponding to a T_μ end point of 112 MeV, we consider this range of effective end points for capturing the characteristic behavior of the distribution near threshold, limited by the coarse sensitivity of a two-parameter model.

8.7 Results

The best fit model parameters found are $a = 2.0$, $b = 0.88$, with a signal normalization of 3700 ± 1250 events ($\chi^2_{\text{min}} = 72.6$ with 64 degrees of freedom). The NT data and best fit signal and background distributions are shown in Fig. 8.15 and the corresponding results for each early- and late-time bin are shown in Fig. 8.16. The extracted T_μ and $\omega = 236\ \text{MeV} - m_\mu - T_\mu$ distributions with 1σ ($\chi^2_{\text{min}} + 2.3$) shape-only allowed bands are shown in Fig. 8.17. The result is shown with $T_\mu^{\max} = 95$ MeV, representing the best fit effective end point, noting that $T_\mu^{\max}$ values up to the physical limit of 112 MeV are not strongly disfavored. A simulation with events distributed according to the best fit shape and data normalizations in each time bin confirms that the size of the 1σ allowed region is reasonable, with 61% (65%) of best fit values falling in the 2 (3) parameter shape-only (rate+shape) contour. In the case that the end point is included as an additional shape parameter, we find that 66% of best fit values fall in the three parameter shape+end point contour. The contours and best fit points are shown in Figure 8.18.

In order to determine the significance of the KDAR ν_μ observation, we compare the best-fit result ($\chi^2_{\text{min}} = 72.6$) to a zero-parameter, background-only hypothesis ($\chi^2_{\text{null}} = 113.8$). Simulated data, created by distributing events according to the background-only hypothesis and the data normalization in each time bin, are used to study the significance of this result. We find that the probability of obtaining a $\Delta\chi^2 = \chi^2_{\text{null}} - \chi^2_{\text{min}} > 41.2$ is about 1.1×10^{-4}, corresponding to 3.9σ (two sided).

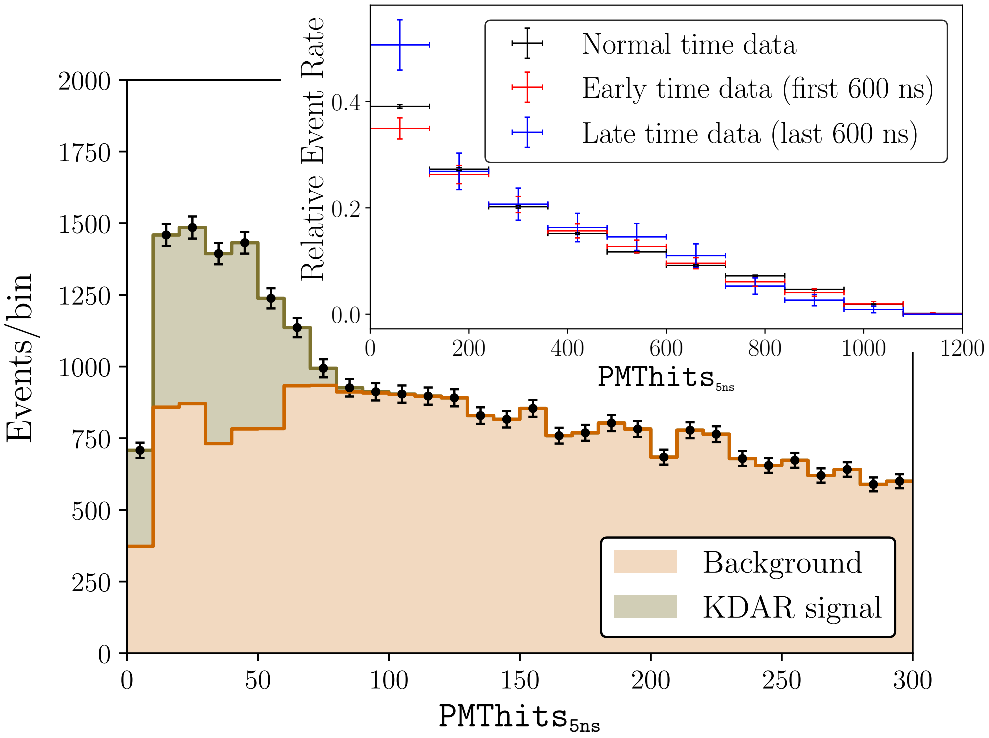

Figure 8.15: The normal time data distribution (black points with error bars) with the best-fit signal template (green) stacked on the inferred background (orange). The inset shows the relative event rate for early time, late time, and normal time after normalizing the three distributions in the background-only region (`PMThits`$_{5ns}$>120). A deficit (excess) of KDAR-like events at early (late) times can be seen.

8.7.1 Verification of Results

In the following sections, we present tests intended to verify the results reported in Figures 8.15 and 8.16. We begin by measuring the goodness of fit of our result and confirming our allowed regions using fake data studies. We then test other energy variables for extracting T_μ to confirm that they produce similar results. Finally, we test the effect of additional cuts and the dependence on the Nuance-derived folding matrix and efficiency distributions in our result. A summary of those results is presented in Table 8.3 at the end of this section.

8.7.1.1 Goodness of fit

In consideration of the fact that there are low statistics in our data sample, we would like to assess the veracity of the one-sigma regions in Figures 8.18 defined by the Poisson χ^2 statistic. Therefore, we perform a fake data study using the best fit results. The fake data in the NNT regions are generated by randomly distributing events according to the shape of the best fit spectra for $j < M$ (where signal is expected). The number of random draws is determined by the number of data events observed in each NNT region. The *normal-time* region is left unchanged, recalling that it is not used in the calculation of χ^2; it is only used for determining background shape and normalization.

We then perform the χ^2 minimization on the generated fake-dataset and tally the best fit result. This process is repeated many thousands of times. If our results are valid, $\sim 68\%$ of fake data best fits should fall within our $\chi^2_{\mathrm{min}} + Q$ region. The χ^2 minimization was performed holding the signal endpoint fixed at 95 MeV (the best fit endpoint). Thus, there are three fitted parameters (a, b, η) and $Q = 3.53$. To improve computational efficiency, we reduced the number of test $\beta_{i,k}$ to $k_{\mathrm{max}} = 7$. The contours generated in this case are shown in Figure 8.19. The step size in a and b was also increased by a factor of 2. The change in k_{max} alters the shape of the best fit regions. In particular, we observe a rough periodicity along the normalization axis as k_{max} decreases. However, it is apparent from Figure 8.19 (left) that the allowed space in a and b remains nearly identical. It is most important that the shape-related parameter space be robust to changes in the value of k_{max} because our final result is presented for shape only. Fake data studies will be a valid test of our minimization method so long as k_{max} is consistent between our fake data tests and the result produced from data.

The results for 5000 fake datasets are shown in Figure 8.20. 3267/5000 (65.3%) tests fall inside $\chi^2_{\mathrm{min}} + 3.53$, displayed in Figure 8.19. The goodness of fit can be inferred from this study by comparing the best-fit χ^2 of data to the distribution of best-fit χ^2 for fake data. The result is shown in Figure 8.22. Our result sits comfortably in the peak of the distribution, indicating a reasonable fit. Also shown is the χ^2 distribution for 64 degrees of freedom [6 NNT bins × 12 energy bins $-$ (5β + a + b + normalization) = 64]. The fake data shows excellent agreement with the χ^2 distribution.

The fake data results for normalization held fixed is shown in Figure 8.21. 135/201 (67.2%) of tests fall inside $\chi^2_{\mathrm{min}} + 2.3$, verifying that the shape-only contour we plan to present is a valid 1σ contour.

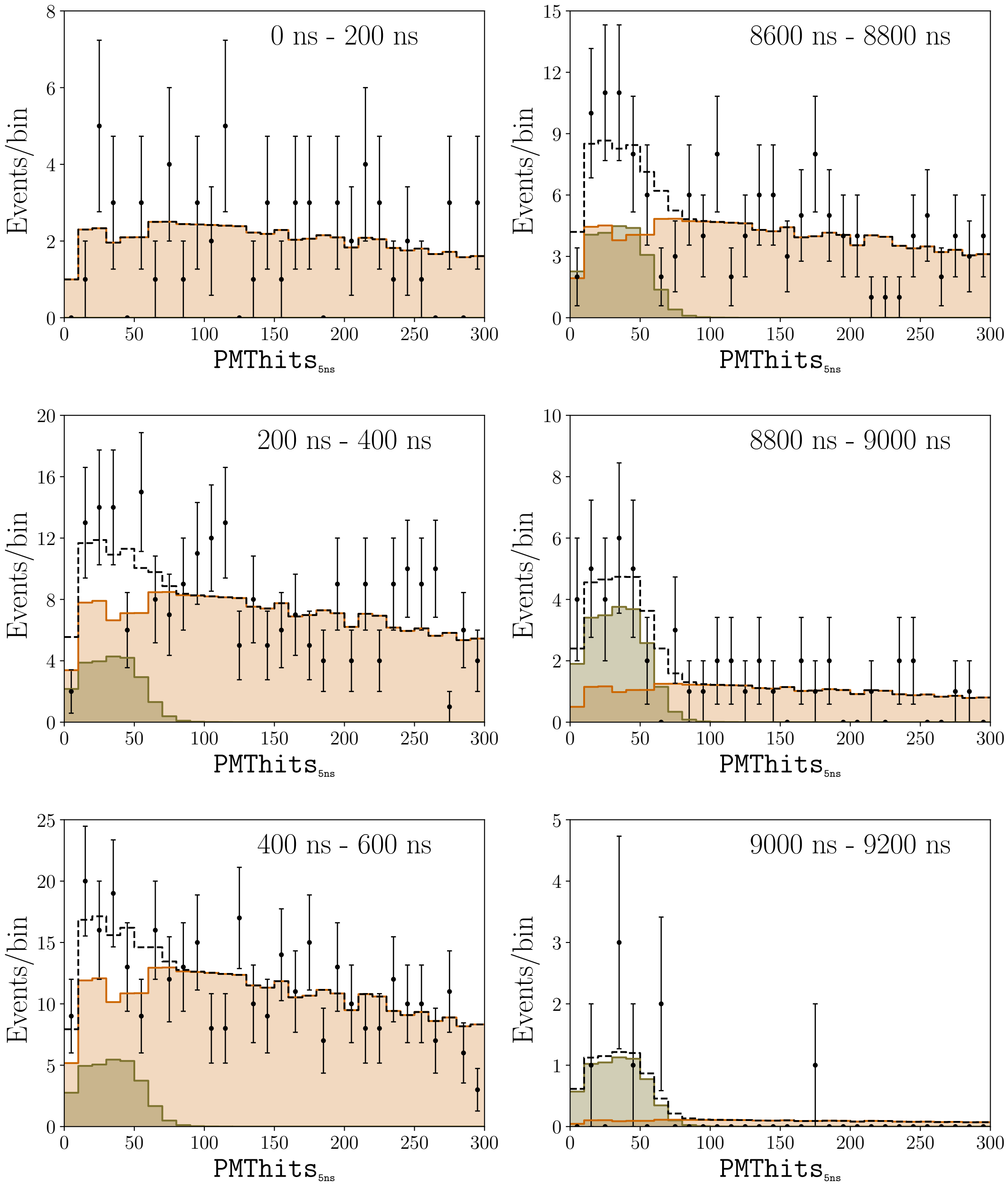

Figure 8.16: (left) The three early-time, background-enhanced bins. (right) The three late-time, signal-enhanced bins. The data (black solid line with stat-only error bar), best-fit signal (green), best-fit background (orange), and total signal+background (black dotted-line) distributions are shown.

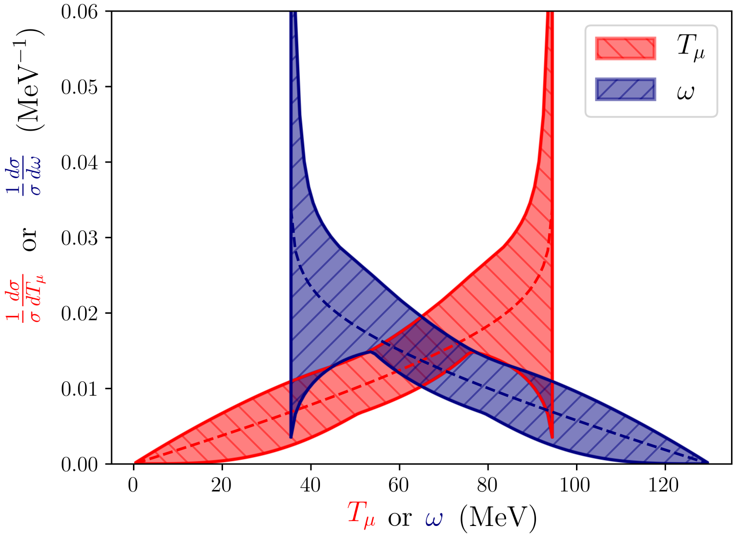

Figure 8.17: The best fit T_μ (red-dashed) and ω (blue-dashed) spectra with shape-only 1σ error bands, given a fixed end point of $T_\mu^{\max} = 95$ MeV. The distributions are fully correlated.

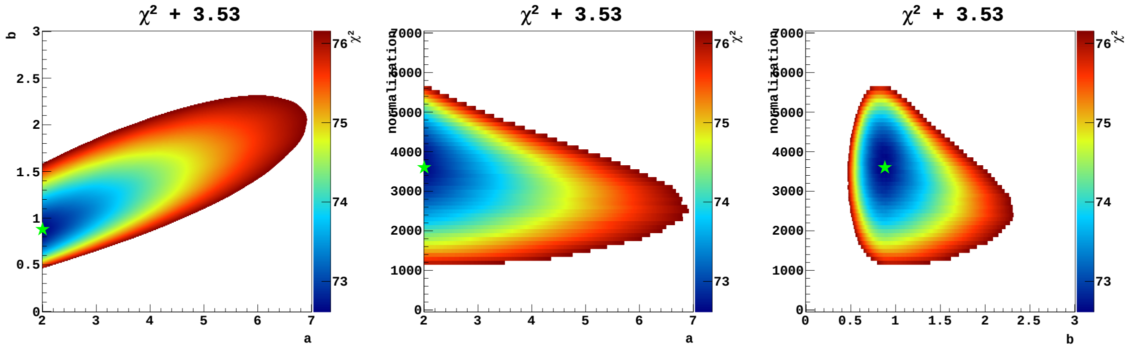

Figure 8.18: **TankHits*fqlt05** with $k_{\max} = 25$. The best fit parameters are $a = 2$, $b = 0.88$, normalization = 3600 and $\chi^2_{\min} = 72.6$.

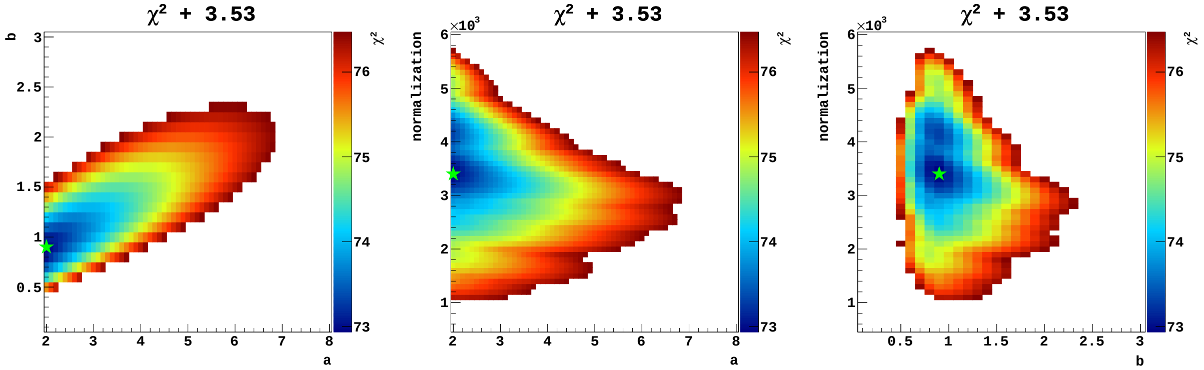

Figure 8.19: The result used in our fake data study, generated with $k_{\max} = 7$. Additionally, the step size in a and b is increased by a factor of two. All of these modifications are done to make feasible running several thousand fake data tests.

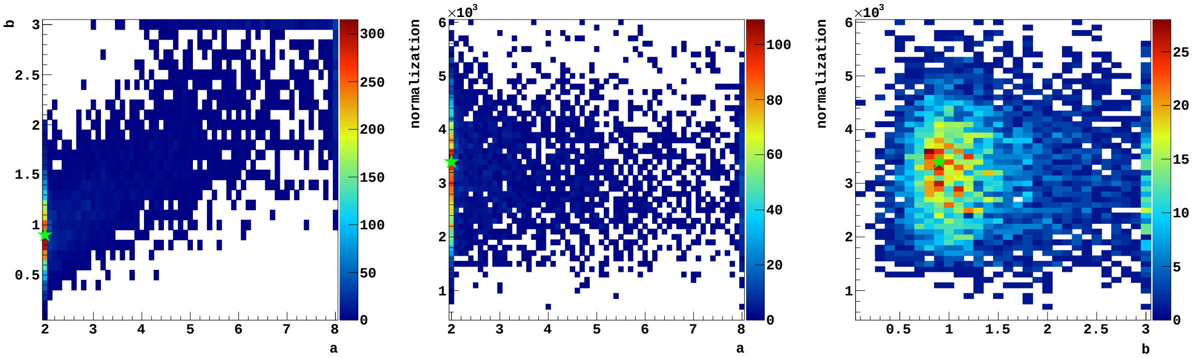

Figure 8.20: Best fit results for 5000 fake datasets generated from the best fit model. 3267/5000 (65.3%) fall in $\chi^2_{\text{min}} + 3.53$. $k_{\text{max}} = 7$.

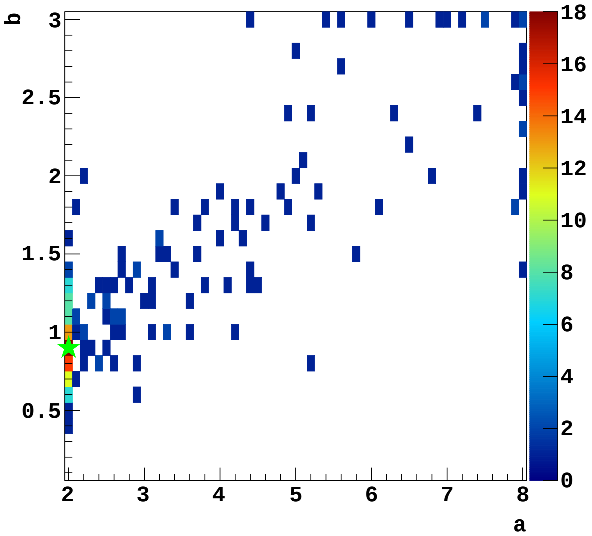

Figure 8.21: The fake data distribution with normalization held fixed at 3400 (the best fit for $k_{\text{max}} = 7$). 135/201 (67.2%) tests fall in $\chi^2_{\text{min}} + 2.3$.

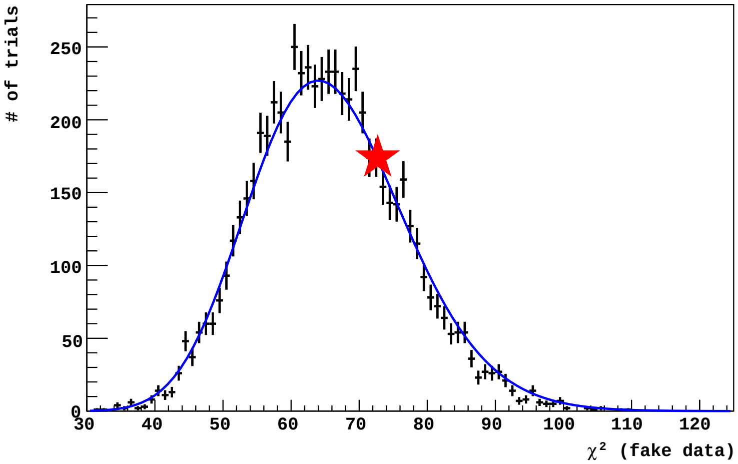

Figure 8.22: The distribution of best fit χ^2 for 5000 fake data tests. The best fit χ^2 for real data indicated by the red star. The χ^2 distribution for 64 degrees of freedom is shown in blue. The number of degrees of freedom is given by the number of bins being fitted (6 NNT bins × 12 energy bins = 72) less the number of parameters used in the fit ($5\ \beta + a + b +$ normalization $= 8$). The expected distribution is normalized to the number of fake data results reported.

8.7.1.2 Alternative energy variables

It is important to show that our result is not dependent, or only weakly dependent, on the choice of detector observable used to infer muon kinetic energy. The same procedure as described above is performed using the **myStFull_energy_mu** and **myStFlux_ecer_mu** variables to confirm that the allowed regions do not depend dramatically on choice of energy variable. The results are shown in Appendix D.1. The differences between these results in $T_\mu^{\max}$ and b compared to the results for **TankHits*fqlt05** are not unexpected given the high degeneracy in $T_\mu^{\max}$ vs b space.

8.7.1.3 Choice of folding matrix

The χ^2 minimization is performed using signal templates that are transformed from T_μ spectra to **TankHits*fqlt05** spectra using folding matrix and efficiency distributions that rely on the Nuance-specific parameter $\kappa = 0.978$. This is due to the fact that the detector MC has been produced using the Nuance neutrino event generator. Here, we verify that the choice of κ in Nuance, and use of Nuance in general, has a negligible influence on the results. We run the same fitting procedure as described above on the best fit T_μ endpoint (95 MeV) after employing $\kappa = 1.022$ in creating the folding matrix and efficiency (see Figure 8.11), representing the opposite extreme value as compared to our default $\kappa = 0.978$ (discussed in Section 8.5.2.1). The results with altered κ, which are highly consistent with the default analysis, are shown in Appendix D.2.

8.7.1.4 Neutrino energy cut in signal region

The analysis procedure minimization is also performed after applying the following cut:

`tHits_1SE > 160 && tHits_1SE*myStFull_fqlt05[0] < 120,` (8.12)

which removes events from the signal region that have total neutrino energy greater than that expected for KDAR. The Results are shown in Appendix D.3. Notably, the allowed regions are similar in shape, but the inclusion of a neutrino energy cut yields smaller allowed regions. The best fit parameters for this case are $a = 2$, $b = 0.95$, $\eta = 4100$ and $T_\mu^{\max} = 95$ MeV.

8.7.1.5 Kaon/pion decay-in-flight background

We expect an $\sim$8% background contribution from dump kaon and pion decay-in-flight that cannot be mitigated using beam timing. Here, we verify that the contribution of the decay-in-flight background to the results of this analysis is negligible. Appendix D.4 shows the resulting phase space when the decay-in-flight background is included in the definition of the signal model. Note that the best fit normalization (3700) includes the 8% background contribution. The result is consistent with the standard result that excludes the decay-in-flight contribution.

8.7.1.6 Choice of $T_\mu^{\max}$

In the subsequent sections, we report results for a fixed T_μ endpoint at 95 MeV. This value was chosen after performing the minimization process over a range of endpoints from 95-115 MeV, inclusive. To illustrate the effect that the choice of endpoint has on the shape that is extracted, we provide Appendix D.5. Figures D.13 - D.14 show the allowed phase space with a fixed normalization of 4000 (the global, all-endpoint best fit) and fixed $T_\mu^{\max}$. In Figures D.15-D.16, the normalization is fixed according to the best fit for that particular $T_\mu^{\max}$, varying from 4000-4300 depending on endpoint.

8.7.1.7 Summary of result verification

As with most physics measurements, a number of alternative techniques are possible for extracting results. In this section, we have confirmed that the size and shape of our default allowed regions in terms of the shape and normalization of KDAR muon kinetic energy make sense, and that our goodness of fit is reasonable, based on fake data studies. Further, we have studied a number of alternative methods for extracting the result. Ultimately, we have found that these methods yield very similar results as compared to the default one. Further, any possible incorporation of these alternative techniques into the default result, perhaps in the form of a systematic uncertainty, is rejected given the completely dominant statistical error bars in the final spectrum. Table 8.3 shows a summary of the best fit results among the default and alternative techniques.

energy variable	other adjustments	χ^2_{min}	T_μ^{max} (MeV)	a	b	norm.
TankHits*fqlt05	[default]	72.74	95	2	0.9	4000
myStFull_energy_mu		73.53	115	2	1.65	4100
myStFlux_ecer_mu		81.31	115	2.3	1.4	3500
TankHits*fqlt05	$\kappa = 1.022$ folding&eff.	72.84	95	2	0.9	4000
TankHits*fqlt05	neutrino energy cut	74.73	95	2	0.95	4100
TankHits*fqlt05	decay-in-flight bkgd. incl.	72.88	95	2	0.9	3700

Table 8.3: A summary of the tests described in Section 8.7.1.

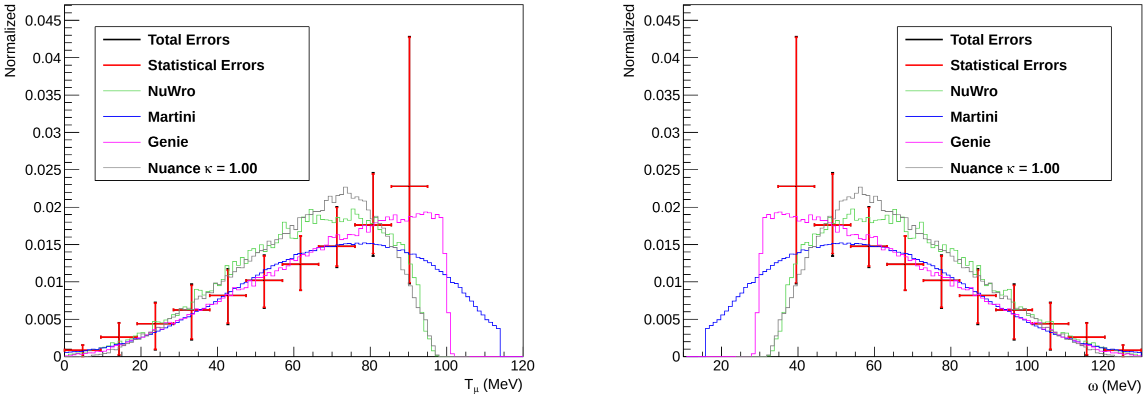

Figure 8.23: Best fit T_μ spectrum (left) and ω spectrum (right), given a fixed endpoint of $T_\mu^{\text{max}} =$ 95 MeV, with different model predictions overlaid.

8.8 Future of KDAR Neutrinos

The error on the MiniBooNE result is dominated by statistics and cannot rule out any current models. However, this measurement will be further constrained by a measurement from MicroBooNE, which can also detect KDAR neutrinos from the NuMI beam dump, and by the JSNS^2 experiment in Japan. The expected charged current muon neutrino event rates for all current and upcoming KDAR experiments are listed in Table 8.4 and the MicroBooNE and JSNS^2 experiments are described in detail below.

8.8.1 KDAR at MicroBooNE

The MicroBooNE experiment is a liquid argon time projection chamber (LArTPC) located in the BNB beam line at Fermilab and capable of detecting off-axis neutrinos from the NuMI beam. It also sits 720 m from the NuMI beam dump, which provides a source of KDAR neutrinos that can be observed by the detector [139]. Unlike MiniBooNE, MicroBooNE can reconstruct incoming neutrino direction using charged hadrons produced at the interaction vertex. The incident angle for KDAR neutrinos from the NuMI beam dump should be be $110°$.

As MicroBooNE is further from the NuMI absorber, it occupies a smaller solid angle of the KDAR neutrino flux, which reduces the rate in the detector. Furthermore, since the MiniBooNE data was recorded in 2009-2011, the target for the NuMI beam has been lengthened from 2.0 interaction lengths to 2.6 interaction lengths. The increase in target length means that fewer primary protons will pass through the target and decay pipe and make it to the absorber. Thus, the intrinsic flux of KDAR neutrinos is also reduced and MicroBooNE expects to detect fewer charged current KDAR neutrino events. In three years of running, the detector expects to record $\sim$2300 charged current KDAR neutrino events [139]. With the added benefit of being able to reconstruct angles with better resolution than MiniBooNE, MicroBooNE is still in a position to make a significant contribution the physics of 100s of MeV neutrinos while also probing a nuclear target (^{40}Ar) different from that of MiniBooNE (^{12}C).

8.8.2 KDAR at JSNS^2

Perhaps the most ideal experiment for studying the KDAR neutrino is the J-PARC Sterile Neutrino Search at the J-PARC Spallation Neutron Source (JSNS^2). The primary physics goal of JSNS^2 is a search for $\Delta m^2 \sim 1$ eV^2 oscillations that would indicate the presence of a heavy sterile neutrino. It is a Gd-doped liquid scintillator detector that began taking data in 2020. Spallation neutron sources like the J-PARC Materials and Life Sciences Facility (MLF) are the best locations for studying KDAR neutrinos because the decay-in-flight background is minimal and the beams are extremely intense. The beam at the J-PARC MLF has high enough energy for kaons to be produced at sufficient rates, and the detector sits 24 m from the decay-at-rest source. In 3 years of running, the detector will record anywhere between 30,000 and 60,000 charged current KDAR neutrino interactions [156]. Furthermore, the beam's short pulse time allows for strict timing cuts that can significantly reduce background ν_μs. All this to say that the JSNS^2 experiment is the best suited in the world to probe physics using the KDAR neutrino.

Experiment	Exposure (POT)	Distance from source (m)	236 MeV ν_μ events
MiniBooNE	2.62×10^{20} (1 year)	86 m	3500 ± 1500
MicroBooNE	1.2×10^{21} (2 years)	102 m	~ 2300
JSNS^2	1.125×10^{23} (3 years)	24 m	30-60k

Table 8.4: A summary of experiments that can detect KDAR neutrinos and the event rates expected.

CHAPTER 9

Concluding Remarks

Neutrino cross sections are critical for the success of oscillation experiments. Precise understanding of the rate at which neutrinos interact in a detector, in combination with detailed knowledge of the unoscillated neutrino flux (the primary role of near detectors) make it possible to extract neutrino oscillation parameters that are challenging to measure such as δ_{CP} and neutrino mass ordering from the subtle changes they cause in the observed oscillation spectrum for $\nu_\mu \to \nu_e$ appearance searches (like DUNE). The future of long baseline accelerator neutrino experiments is heavily dependent on liquid argon time projection chamber technology. LArTPCs capture digitized high resolution images of interactions inside the detector that provide both topological and calorimetric information that can be used to identify the charged particles produced as a result of neutrino interactions and from them infer the flavor and energy of the initial neutrino.

While the neutrino physics community has pursued a broad neutrino cross section effort over the past several decades, probing a wide range of interaction mechanisms and neutrino energies, the story remains incomplete. In particular, neutrino-argon cross section measurements are in their nascency. ArgoNeuT provided the world's first ν_μ-argon cross sections after its six-month run at Fermilab in a GeV-scale neutrino beam. This thesis presents an analysis of ArgoNeuT data that culminates in the world's first ν_e-argon cross section measurement, published more than a decade after ArgoNeuT's data was collected.

The ArgoNeuT ν_e cross section result, albeit limited in statistics, is uniquely relevant to future DUNE measurements that will need to efficiently reconstruct ν_e signals at the GeV scale, where deep inelastic scattering contributions are more prominent, yielding complex event topologies that can be difficult to reconstruct. The ArgoNeuT result identifies and provides strategies for overcoming the challenges unique to automated reconstruction of GeV-scale neutrinos. Currently, ArgoNeuT's dataset, in combination with the ν_e cross section measurement, are being used to validate deep learning tools being designed for reconstruction in DUNE with an actual neutrino beam data sample, a critical but previously unavailable resource for DUNE.

Following up on ArgoNeuT's first ν-argon cross sections, the SBN Program at Fermilab (SBND, MicroBooNE, and ICARUS) are now producing high statistics total and differential cross sections that build on the foundation laid by ArgoNeuT. These detectors sit in a neutrino beam of lower energy (peaked at hundreds of MeV) than ArgoNeuT, but still observe a substantial tail of higher energy neutrino flux. The Wire-Cell reconstruction toolkit developed in MicroBooNE has demonstrated unprecedented efficiency for selecting neutrino interactions from among cosmic backgrounds on surface-based detectors, and is well on its way to finalizing a blinded low-energy excess analysis with high sensitivity. The tools developed for the Wire-Cell low energy excess analysis can also be employed as part of a robust cross section program in MicroBooNE to select large high purity samples of many different final state interaction topologies.

For each of these experiments, one of the biggest challenges is reconstructing neutrino energy. Current reconstruction tools only achieve roughly 20% resolution, impacted by a number of factors including detector thresholds, un-detectable particles (like neutral particles in LArTPCs), and complicated final states. Coupled with large uncertainties in beam composition, resulting from uncertainties on nuclear models for hadron production when creating neutrino beams, reconstruction limitations make knowing the exact energy of any given neutrino nearly impossible. Yet oscillation probabilities at a fixed baseline are directly dependent on neutrino energies. Fortunately, there exist unique neutrino sources that eliminate this uncertainty entirely and can be used to better constrain existing neutrino-nucleus scattering models. Muon neutrinos from pion and kaon decay at rest, a process that occurs in neutrino beam dumps at high rates, are monoenergetic. The 236 MeV muon neutrino from kaon decay at rest in the NuMI beam dump generates a large enough isotropic flux to be observed by several detectors at Fermilab. This work presents the first measurement of this signal using data from the MiniBooNE experiment; and MicroBooNE has the ability to repeat the measurement with an argon target. Known energy neutrinos are invaluable probes of neutrino-nucleus interactions and can be used to constrain the currently wide-ranging nuclear model predictions. For experimentalists, they can be used to better calibrate detector energy reconstruction.

Timing information also has a role to play in improving the neutrino cross section landscape. As LArTPCs grow in size, long electron drift times both increase the uncertainty in position along the detector drift direction, and require a longer a readout window that inevitably contain more background interactions. Prompt scintillation light produced by neutrino-argon interactions in time with the neutrino beam can aid in isolating neutrino signals from backgrounds. Photon detector systems can also provide secondary cross checks for energy calibration in a detector. Design, construction, and analysis of data in full scale experiments like SBND not only enhance the detector's own physics program but provide valuable understanding of new technologies that can be adopted and improved upon for future detectors like DUNE, which is still in the design phase.

Neutrino cross section measurements made across a range of energies and with a variety of target nuclei provide widespread benefits. They constrain theory-based neutrino-nucleus interaction models, improving our understanding of the complex processes that occur when a neutrino interacts with a composite particle. They also improve oscillation experiments, which rely on knowledge of neutrino interaction rates to measure how often a particular flavor of neutrino oscillates into another. Automated flavor identification and energy reconstruction are also critical for future experiments as efficiency and purity thresholds for extracting new knowledge about the neutrino continue to increase. In particular, the LArTPC-based neutrino program at Fermilab has been a staged effort, building on learning from previous detectors while designing larger, optimized experiments. ArgoNeuT led the way in the neutrino-argon cross section program. Now MicroBooNE, ICARUS, and SBND will build on its foundation with significantly larger data samples are more mature reconstruction tools. In the next decades, DUNE will capitalize on this wealth of knowledge, including both cross section measurements and understanding of detector response, to shed light on many of the remaining open questions in neutrino physics.

APPENDIX A

An Overview of the Standard Model of Particle Physics Focusing on Neutrinos and the Electroweak Sector

The Standard Model is an $SU(3) \otimes SU(2)_L \otimes U(1)_Y$ gauge theory. The particles and interactions in the Standard Model are described by Lagrangians and their corresponding field equations. For example, the Lagrangian for a free fermion is known as the Dirac Lagrangian:

$$\mathcal{L} = \bar{\psi}(i\gamma^{\mu}\partial_{\mu} - m)\psi \tag{A.1}$$

where ψ is the field describing a fermion of mass m and γ_{μ} are the Dirac matrices. The Lagrangian is invariant under the global gauge transformation:

$$\psi \longrightarrow e^{i\alpha}\psi, \tag{A.2}$$

where α is a real number. A local gauge transformation can also be defined:

$$\psi \longrightarrow e^{i\alpha(x)}\psi, \tag{A.3}$$

where α is a function of the four-position x^{μ}. The Dirac Lagrangian is not invariant under the local gauge transformation:

$$\mathcal{L} \longrightarrow \mathcal{L} - (\partial_{\mu}\alpha)\bar{\psi}\gamma^{\mu}\psi, \tag{A.4}$$

but must be in order to accurately reflect reality, as physics should not change if your reference point changes. To demand invariance under a local gauge transformation, an additional term must be added to the Lagrangian to cancel the additional term that arises in Eq. A.4 from the local gauge transformation. Suppose

$$\mathcal{L} = \bar{\psi}(i\gamma^\mu \partial_\mu - m)\psi - e\bar{\psi}\gamma^\mu \psi A_\mu \tag{A.5}$$

where A_μ is a new gauge field (or gauge boson) that transforms under local gauge transformations as

$$A_\mu \longrightarrow A_\mu - \frac{1}{e}\partial_\mu \alpha(x) \tag{A.6}$$

With the added gauge field term, the Lagrangian is invariant under local gauge transformations, as desired. Now, since we've introduced a new field to the Lagrangian, we must define a kinetic energy term for the field. The relevant Lagrangian in this case is the Proca Lagrangian, which describes a spin-1 field with mass m_A:

$$\mathcal{L} = -\frac{1}{4}F^{\mu\nu}F_{\mu\nu} + \frac{1}{2}m_A^2 A^\nu A_\nu. \tag{A.7}$$

Now note that the first term, $F^{\mu\nu} \equiv \partial^\mu A^\nu - \partial^\nu A^\mu$, is invariant under local gauge transformations (Eq. A.3), but $A^\nu A_\nu$ is not, indicating that the gauge field must be massless ($m_A = 0$) in order to satisfy the demand for invariance under local gauge transformations. We have now constructed the complete Lagrangian for quantum electrodynamics (QED) and A_μ is the photon (γ) field required by local gauge invariance.

$$\mathcal{L} = \bar{\psi}(i\gamma^\mu \partial_\mu - m)\psi - \frac{1}{4}F^{\mu\nu}F_{\mu\nu} - e\bar{\psi}\gamma^\mu \psi A_\mu. \tag{A.8}$$

The last term ($-e\bar{\psi}\gamma^\mu \psi A_\mu$) describes the coupling of the fermion fields (ψ and $\bar{\psi}$) to the gauge field (A_μ). To simplify the expression, we define a covariant derivative:

$$D_\mu \equiv \partial_\mu + ieA_\mu \tag{A.9}$$

And the Lagrangian can be rewritten:

$$\begin{aligned}\mathcal{L} &= \bar{\psi}(i\gamma^\mu D_\mu - m)\psi - \frac{1}{4}F^{\mu\nu}F_{\mu\nu} \\ &= \bar{\psi}(i\not{D} - m)\psi - \frac{1}{4}F^{\mu\nu}F_{\mu\nu}\end{aligned} \tag{A.10}$$

where we have further simplified the terms by using $\not{D} = \gamma^\mu D_\mu$.

The $SU(3)$ invariance in the Standard Model describes the quantum chromodynamics (QCD) sector. In this sector, strong interactions are governed by eight massless gauge bosons known as gluons. Color is a conserved quantity in QCD analogous to charge in QED. Neutrinos are not charged under QCD and do not couple to gluons. As such, it does not serve us in this context to dive any deeper into the world of QCD.

Finally (and most relevant for the neutrino), the extended $SU(2)_L \otimes U(1)_Y$ symmetry governs electroweak theory, which unifies electromagnetic and weak interactions. The imposed invariance introduces four gauge fields: the photon, two charged weak bosons ($W^\pm$) and a neutral weak boson (Z^0). As we showed with QED, imposing local gauge invariance requires that these mediators be massless. This is true in the case of the photon (and gluon, in QCD) but breaks down for the W and Z bosons, which possess mass. In order to generate mass terms in the Lagrangian for the W, Z bosons we must introduce a new process known as the Higgs mechanism.

A.1 Spontaneous Symmetry Breaking and the Higgs Mechanism

The mechanism by which a massless gauge boson acquires mass is known as spontaneous symmetry breaking. Consider a complex scalar field that couples to the electromagnetic field:

$$\mathcal{L} = |D_\mu \phi|^2 - V(\phi) - \frac{1}{4}(F_{\mu\nu})^2 \tag{A.11}$$

with $D_\mu = \partial_\mu + ieA_\mu$, as before. The Lagrangian is invariant under the local $U(1)$ transformation

$$\phi(x) \longrightarrow e^{i\alpha(x)}\phi(x), \;\; A_\mu(x) \longrightarrow A_\mu(x) - \frac{1}{e}\partial_\mu \alpha(x). \tag{A.12}$$

We can define a potential $V(\phi)$ of the form

$$V(\phi) = -\mu^2\phi^*\phi + \frac{\lambda}{2}(\phi^*\phi)^2 \tag{A.13}$$

with $\mu^2 > 0$. We can now show that such a potential with cause the field ϕ to acquire a vacuum expectation value (VEV) and the $U(1)$ global symmetry will be spontaneously broken. The minimum (vacuum state) of this potential occurs at

$$\langle\phi\rangle = \phi_0 = \left(\frac{\mu^2}{\lambda}\right)^{1/2} \tag{A.14}$$

If we expand the Lagrangian A.11 around the vacuum state A.14 and rewrite the complex field as

$$\phi(x) = \phi_0 + \frac{1}{\sqrt{2}}\big[\phi_1(x) + i\phi_2(x)\big], \tag{A.15}$$

then the potential then becomes

$$V(\phi) = -\frac{1}{2\lambda}\mu^4 + \frac{1}{2}\cdot 2\mu^2\phi_1^2 + \mathcal{O}(\phi_i^3) \tag{A.16}$$

and the kinetic term in the Lagrangian becomes

$$|D_\mu\phi|^2 = \frac{1}{2}(\partial_\mu\phi_1)^2 + \frac{1}{2}(\partial_\mu\phi_2)^2 + \sqrt{2}e\phi_0\cdot A_\mu\partial^\mu\phi_2 + e^2\phi_0^2A_\mu A^\mu + \cdots \tag{A.17}$$

where cubic and quartic terms in the fields A_μ, ϕ_1, and ϕ_2 are omitted. We see now that the Lagrangian describes a massive scalar field ϕ_1 with mass $\sqrt{2}\mu$ and a massless scalar field ϕ_2. It is a general result, known as Goldstone's theorem, that massless particles (bosons) arise when a continuous symmetry is spontaneously broken. The massless field ϕ_2 is known as a Goldstone boson. Goldstone's theorem has wide-ranging applications in physics: for example, pions can be approximated as Goldstone bosons in the QCD sector.

Finally, let's examine the last term in the expanded kinetic term (A.17):

$$\mathcal{L} \supset \frac{1}{2}m_A^2A_\mu A^\mu \tag{A.18}$$

where the mass $m_A^2 = 2e^2\phi_0^2$ is a direct result of the non-zero vacuum expectation value of ϕ.

In this setup, the massless Goldstone boson can be eliminated by adding a term to the gauge transformation:

$$A_\mu(x) \longrightarrow A_\mu(x) - \frac{1}{\sqrt{2}e\phi_0}\partial_\mu\phi_2, \tag{A.19}$$

such that the Lagrangian becomes

$$\mathcal{L} = -\frac{1}{4}F^{\mu\nu}F_{\mu\nu} + \frac{1}{2}(\partial_\mu\phi_1)^2 + e^2\phi_0^2 A_\mu A^\mu - V(\phi). \tag{A.20}$$

The mechanism by which as massless gauge boson (A_μ in this case) attains mass via spontaneous symmetry breaking is known as the Higgs mechanism. Having explored the case for the abelian scalar field (ϕ), we can now proceed to develop a description of electroweak interactions, based on the $SU(2)_L \otimes U(1)_Y$ gauge invariance.

A.2 The Electroweak Sector

The leptons can be written as singlet and doublet representations of the $SU(2)$ group:

$$e_R,\ \mu_R,\ \tau_R,\ \begin{pmatrix} \nu_e \\ e \end{pmatrix}_L,\ \begin{pmatrix} \nu_\mu \\ \mu \end{pmatrix}_L,\ \begin{pmatrix} \nu_\tau \\ \tau \end{pmatrix}_L, \tag{A.21}$$

noting that right-handed neutrinos have not yet been observed, so only the left handed components are doublets.

The Lagrangian under $SU(2)_L \otimes U(1)_Y$ invariance (simplified to include only the first generation of leptons) is given by

$$\mathcal{L}_0 = \bar{l}_L i\not{D} l_L + \bar{l}_R i\not{D} l_R - \frac{1}{4}\vec{F}^{\mu\nu}\cdot\vec{F}_{\mu\nu} - \frac{1}{4}G^{\mu\nu}G_{\mu\nu} \tag{A.22}$$

where

$$
\begin{aligned}
l_L &= \begin{pmatrix} \nu_e \\ \\ e \end{pmatrix}_L , \quad l_R = e_R, \\
D_\mu &= \partial_\mu - ig\vec{T} \cdot \vec{A}_\mu - ig' Y B_\mu \\
\vec{F}_{\mu\nu} &= \partial_\mu \vec{A}_\nu - \partial_\nu \vec{A}_\mu + g(\vec{A}_\mu \times \vec{A}_\nu), \\
G_{\mu\nu} &= \partial_\mu B_\nu - \partial_\nu B_\mu .
\end{aligned}
\tag{A.23}
$$

$\vec{T}$ is the isospin operator ($\vec{T} = \vec{\sigma}/2$), Y is the hypercharge operator, and g and g' are $SU(2)_L$ and $U(1)_Y$ gauge coupling constants. There are four massless gauge boson present: three $SU(2)_L$ bosons, $\vec{A}_\mu \equiv (A^1_\mu, A^2_\mu, A^3_\mu)$ and one $U(1)_Y$ boson, B_μ.

The local gauge transformations for lepton scalars and doublets and gauge bosons in Eq. A.22 under which the Lagrangian is invariant are

$$
\begin{aligned}
l_{L,R} &\to U l_{L,R} \\
\vec{T} \cdot \vec{A}_\mu &\to U\big[\vec{T} \cdot \vec{A}_\mu - \frac{i}{g} U^{-1}(\partial_\mu U)\big] U^{-1} \\
B_\mu &\to B_\mu + \partial_\mu \Lambda(x)
\end{aligned}
\tag{A.24}
$$

where

$$
U = \exp\{ig\vec{T} \cdot \vec{\Lambda}(x) + ig' Y \Lambda(x)\}
\tag{A.25}
$$

with gauge functions $\Lambda(x)$ and $\vec{\Lambda}(x)$.

We can define what will become the three massive weak mediators ($W^+_\mu, W^-_\mu, Z^0_\mu$) and one massless mediator (the photon, A_μ) as linear combinations of the massless bosons $\vec{A}_\mu$ and B_μ:

$$
\begin{aligned}
W^\pm_\mu &= \frac{1}{\sqrt{2}}(A^1_\mu \mp iA^2_\mu) \\
Z^0_\mu &= \frac{1}{\sqrt{g^2 + g'^2}}(gA^3_\mu - g' B_\mu) \\
A_\mu &= \frac{1}{\sqrt{g^2 + g'^2}}(g' A^3_\mu + g B_\mu).
\end{aligned}
\tag{A.26}
$$

Extracting the mass terms for each boson is now just a matter of rearranging the Lagrangian, cleverly defining terms, and imposing spontaneous symmetry breaking.

First, the covariant derivative can be written (first in terms of A^i_μ and B_μ and then in terms of $W^+_\mu, W^-_\mu, Z^0_\mu$ and A_μ) as

$$\begin{aligned} D_\mu &= \partial_\mu - igT^a A^a_\mu - ig'YB_\mu \\ &= \partial_\mu - i\frac{g}{\sqrt{2}}(W^+_\mu T^+ + W^-_\mu T^-) - i\frac{1}{\sqrt{g^2+g'^2}} Z^0_\mu (g^2 T^3 - g'^2 Y) \\ &- i\frac{gg'}{\sqrt{g^2+g'^2}} A_\mu (T^3 + \frac{Y}{2}) \end{aligned} \tag{A.27}$$

where

$$T^\pm = (T^1 \pm iT^2) = \frac{1}{2}(\sigma^1 \pm i\sigma^2) = \sigma^\pm. \tag{A.28}$$

and σ^i are the Pauli matrices.

We can directly equate the coefficient of the electromagnetic interaction with the electron charge:

$$e = \frac{gg'}{\sqrt{g^2+g'^2}}. \tag{A.29}$$

We can further clarify the physical implications of each term in the Lagrangian by defining the weak mixing angle θ_W to be the angle for changing basis from (A^3, B) to (Z^0, A):

$$\begin{pmatrix} Z^0 \\ A \end{pmatrix} = \begin{pmatrix} \cos\theta_W & -\sin\theta_W \\ \sin\theta_W & \cos\theta_W \end{pmatrix} \begin{pmatrix} A^3 \\ B \end{pmatrix} \tag{A.30}$$

or

$$\cos\theta_W = \frac{g}{\sqrt{g^2+g'^2}}, \ \sin\theta_W = \frac{g'}{\sqrt{g^2+g'^2}}. \tag{A.31}$$

It is now quite simple to write the electric charge as $e = g\sin\theta_W = g'\cos\theta_W$, and the covariant derivative can be written as

$$D_\mu = \partial_\mu - i\frac{g}{\sqrt{2}}(W^+_\mu T^+ + W^-_\mu T^-) - i\frac{g}{\cos\theta_W} Z^0_\mu (T^3 - \sin^2\theta_W Q) - ieA_\mu Q. \tag{A.32}$$

This fully describes the coupling between $W^\pm$, Z^0 and the fermions once inserted into the Lagrangian (Eq. A.22).

The electroweak interaction Lagrangian can now be written out succinctly as

$$\mathcal{L} = g(W_\mu^+ J_W^{\mu+} + W_\mu^- J_W^{\mu-}) + \frac{g}{\cos\theta_W} Z_\mu^0 J_Z^\mu + eA_\mu J_{\text{EM}}^\mu \tag{A.33}$$

with

$$\begin{aligned}
J_W^{\mu+} &= \frac{1}{\sqrt{2}}\bar{\nu}_L\gamma^\mu e_L + \bar{u}_L\gamma^\mu d_L \\
J_W^{\mu-} &= \frac{1}{\sqrt{2}}\bar{e}_L\gamma^\mu \nu_L + \bar{d}_L\gamma^\mu u_L \\
J_Z^\mu &= \sum_f \bar{f}\gamma^\mu(T^3 - \sin^2\theta_W Q)f \\
&= \bar{\nu}_L\gamma^\mu\big(\tfrac{1}{2}\big)\nu_L + \bar{e}_L\gamma^\mu\big(-\tfrac{1}{2} + \sin^2\theta_W\big)e_L + \bar{e}_R\gamma^\mu(\sin^2\theta_W)e_R \\
&\quad + \bar{u}_L\gamma^\mu\big(\tfrac{1}{2} - \tfrac{2}{3}\sin^2\theta_W\big)u_L + \bar{u}_R\gamma^\mu\big(-\tfrac{2}{3}\sin^2\theta_W\big)u_R \\
&\quad + \bar{d}_L\gamma^\mu\big(-\tfrac{1}{2} + \tfrac{1}{3}\sin^2\theta_W\big)d_L + \bar{d}_R\gamma^\mu\big(\tfrac{1}{3}\sin^2\theta_W\big)d_R \\
J_{\text{EM}}^\mu &= \bar{e}\gamma^\mu(-1)e + \bar{u}\gamma^\mu\big(+\tfrac{2}{3}\big)u + \bar{d}\gamma^\mu\big(-\tfrac{1}{3}\big)d.
\end{aligned} \tag{A.34}$$

The charged current interactions between leptons and quarks are described by the first term ($W^\pm$ boson will only couple to left-handed helicity states of quarks and leptons), the the neutral current interactions by the second term, and the photon (A_μ) interactions by the final term. Having written down terms for each of the fermion-gauge couplings, only the mass terms remain to be studied. For now, we ignore neutrino mass, as it does not arise naturally via the Higgs mechanism.

To induce spontaneous symmetry breaking, we must add a Higgs sector in the Lagrangian, which introduces a new complex scalar field doublet:

$$\mathcal{L}_\phi = |D_\mu\phi|^2 + \mu^2\phi^\dagger\phi - \lambda(\phi^\dagger\phi)^2 \tag{A.35}$$

with $\mu^2 < 0$, $\lambda > 0$ and

$$\phi = \begin{pmatrix} \phi^+ \\ \phi^0 \end{pmatrix} = \begin{pmatrix} \phi_1 + i\phi_2 \\ \phi_3 + i\phi_4 \end{pmatrix} \tag{A.36}$$

The vacuum expectation value (VEV) is determined by the stationary point in the Lagrangian

$$\phi^\dagger\phi = \frac{1}{2}(\phi_1^2 + \phi_2^2 + \phi_3^2 + \phi_4^2) = \frac{1}{2}v^2 = -\frac{\mu^2}{2\lambda} \tag{A.37}$$

Now, we know that the photon must remain massless, which implies that there must be a non-zero vacuum expectation value for only the neutral scalar field (ϕ^0). Thus we can write the VEV of the field as

$$\langle\phi\rangle = \frac{1}{\sqrt{2}}\begin{pmatrix} 0 \\ v \end{pmatrix} \tag{A.38}$$

As in our example, we will expand the Lagrangian around the VEV with a Higgs field ϕ:

$$\phi = \frac{1}{\sqrt{2}}\begin{pmatrix} 0 \\ v + H \end{pmatrix} \tag{A.39}$$

where H is a real scalar field that is assumed to be neutral. Plugging this into the Lagrangian (Eq. A.35), it becomes

$$\begin{aligned} \mathcal{L} = \frac{1}{2}(\partial^\mu H)(\partial_\mu H) - \frac{1}{2}(2\lambda v^2)H^2 + \frac{1}{2}\left(\frac{gv}{2}\right)^2 W^{\mu +}W_\mu^{+\dagger} \\ + \frac{1}{2}\left(\frac{gv}{2}\right)^2 W^{\mu -}W_\mu^{-\dagger} + \frac{1}{2}\left(\frac{v\sqrt{g^2+g'^2}}{2}\right)^2 Z^{0\mu}Z_\mu^0 + \cdots \end{aligned} \tag{A.40}$$

where we have expanded the term with the covariant derivative in terms of the electroweak fields as in Eq. A.27.

It is now easy for us to read off the masses of the fields in this equations:

$$m_H = \sqrt{2\lambda}v,\ m_W = \frac{gv}{2},\ m_Z = \frac{\sqrt{g^2+g'^2}}{2}v \tag{A.41}$$

We can also equate

$$\left(\frac{m_W}{m_Z}\right)^2 = \cos^2\theta_W. \tag{A.42}$$

The vacuum expectation value of the Higgs boson is measured to be $v = 246$ GeV.

Having defined the mass of the bosons, we now turn to the fermions. We assume the form of the coupling between the scalar field and the fermions takes the form of a Yukawa coupling:

$$\begin{aligned}\mathcal{L}_{\phi e} &= - f_e \overline{\begin{pmatrix} \nu_e \\ e \end{pmatrix}}_L \begin{pmatrix} \phi^+ \\ \phi \end{pmatrix} e_R + \text{h.c.} \\ &\overset{\text{ssb}}{=} - f_e v \bar{e}_L e_R + \text{h.c.}\end{aligned} \tag{A.43}$$

where in the second line we have applied spontaneous symmetry breaking using the VEV of the scalar field. The mass term is now easily read off to be

$$m_e = f_e v. \tag{A.44}$$

No mass term is generated for the neutrino in this mechanism because there is no right-handed neutrino singlet in the Standard Model. However, compelling evidence exists in the observation of neutrino oscillations that indicates neutrinos do have mass, so the Standard Model must be extended to accommodate massive neutrinos.

APPENDIX B

ArgoNeuT Selection Performance by Interaction Mode

ArgoNeuT's ν_e CC interactions span a range of topologies with varying complexity. One can ask how this selection performs according to the mode of simulated interaction: quasielastic (QE), resonant pion production (RES), or deep inelastic scattering (DIS). Here we study how the complexity of the event topology (based on interaction mode as a proxy) impacts the effectiveness of the selection that is presented in this note. To do this we examine the BDT inputs and output for a simulated sample of ν_e CC-only interactions in ArgoNeuT. The BDT output for this sample is shown in Figure B.1. The input variables are shown in Figures B.2 and B.3. While there is less separation power for DIS interactions, the BDT remains effective. In addition, we note that the DIS performance is conflated with higher reconstruction failure rates for DIS interactions in ArgoNeuT, exacerbated by the fact that our shower reconstruction only aims to reconstruct a signal shower. This is likely to be improved upon in subsequent studies of this nature. In addition, the quantity $Q_{\text{shower}}/Q_{\text{event}}$ (see top right plot in Figure B.2 and, for background, Figure 4.12) shows the most significant difference between QE and DIS interactions while simultaneously being the most powerful BDT input, something that could be further fine-tuned in subsequent work. That said, we note that this method is still highly effective for selecting QE and RES interactions, and comparable to other ν_e CC selections in progress for QE-like topologies (see Ref. [98], for example).

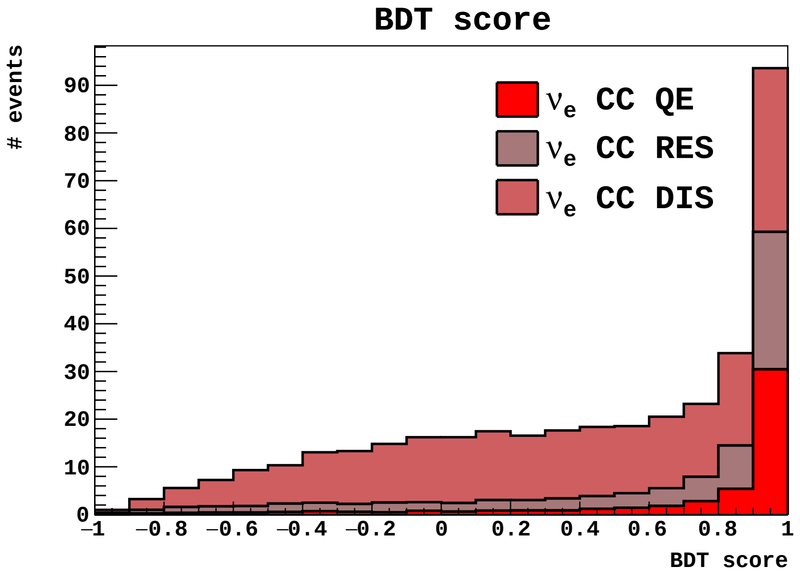

Figure B.1: BDT score for a sample of simulated ν_e CC interactions, split up by interaction mechanism: quasi-elastic, resonant, or deep inelastic scattering.

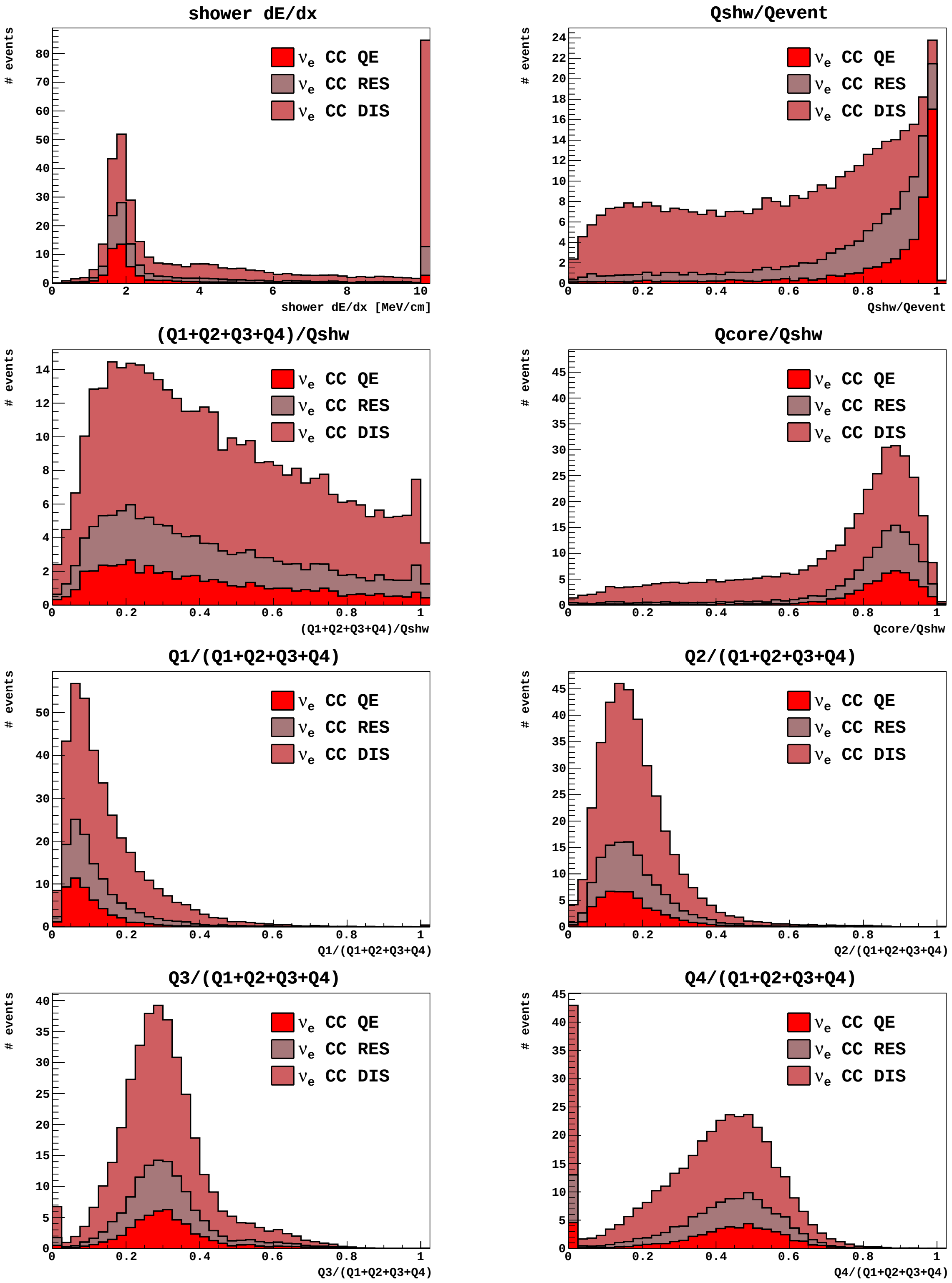

Figure B.2: BDT input variable distributions for simulated ν_e CC interactions in ArgoNeuT. The events are sorted by the interaction modes: quasi-elastic, resonant, and deep inelastic scattering.

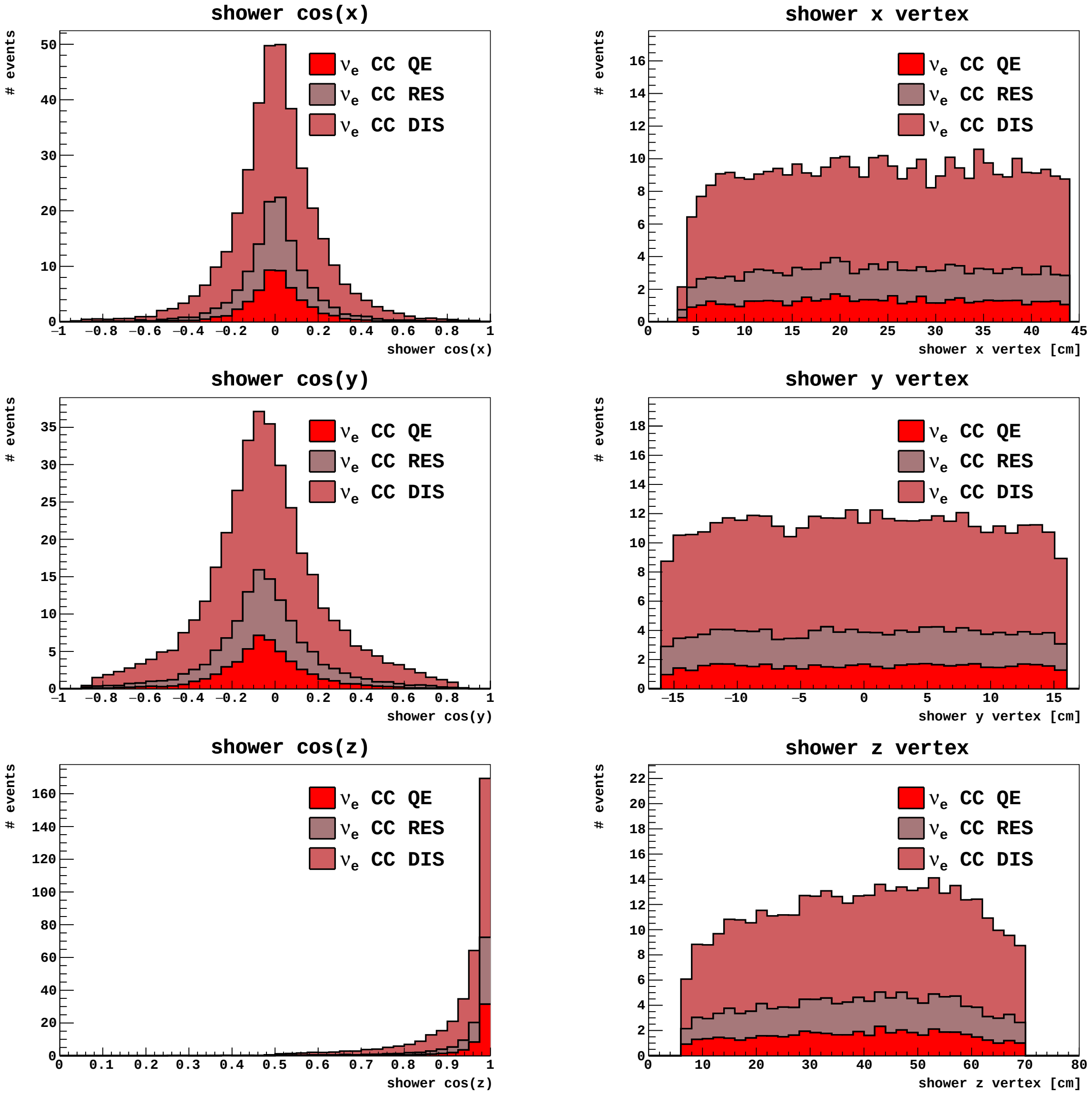

Figure B.3: BDT input variable (and shower vertex) distributions for simulated ν_e CC interactions in ArgoNeuT. The events are sorted by the interaction modes: quasi-elastic, resonant, and deep inelastic scattering.

APPENDIX C

Scan of Loosened ArgoNeuT Selection

The following images display all data events with BDT score > 0.7, including the 13 selected in the analysis presented in this note (BDT score > 0.9).

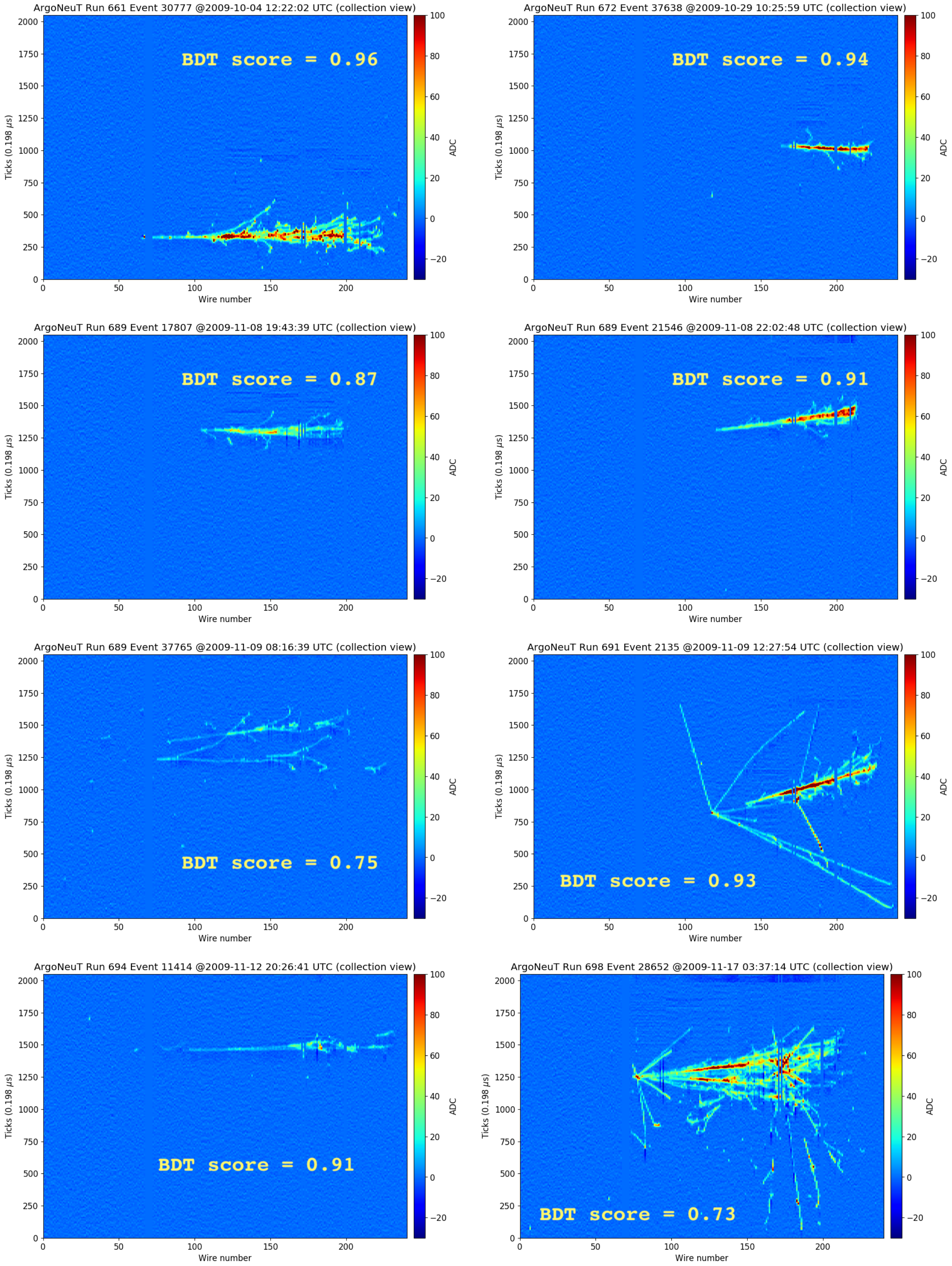

Figure C.1: Events selected from ArgoNeuT data with BDT score > 0.7. Continued in Figures C.2-C.4.

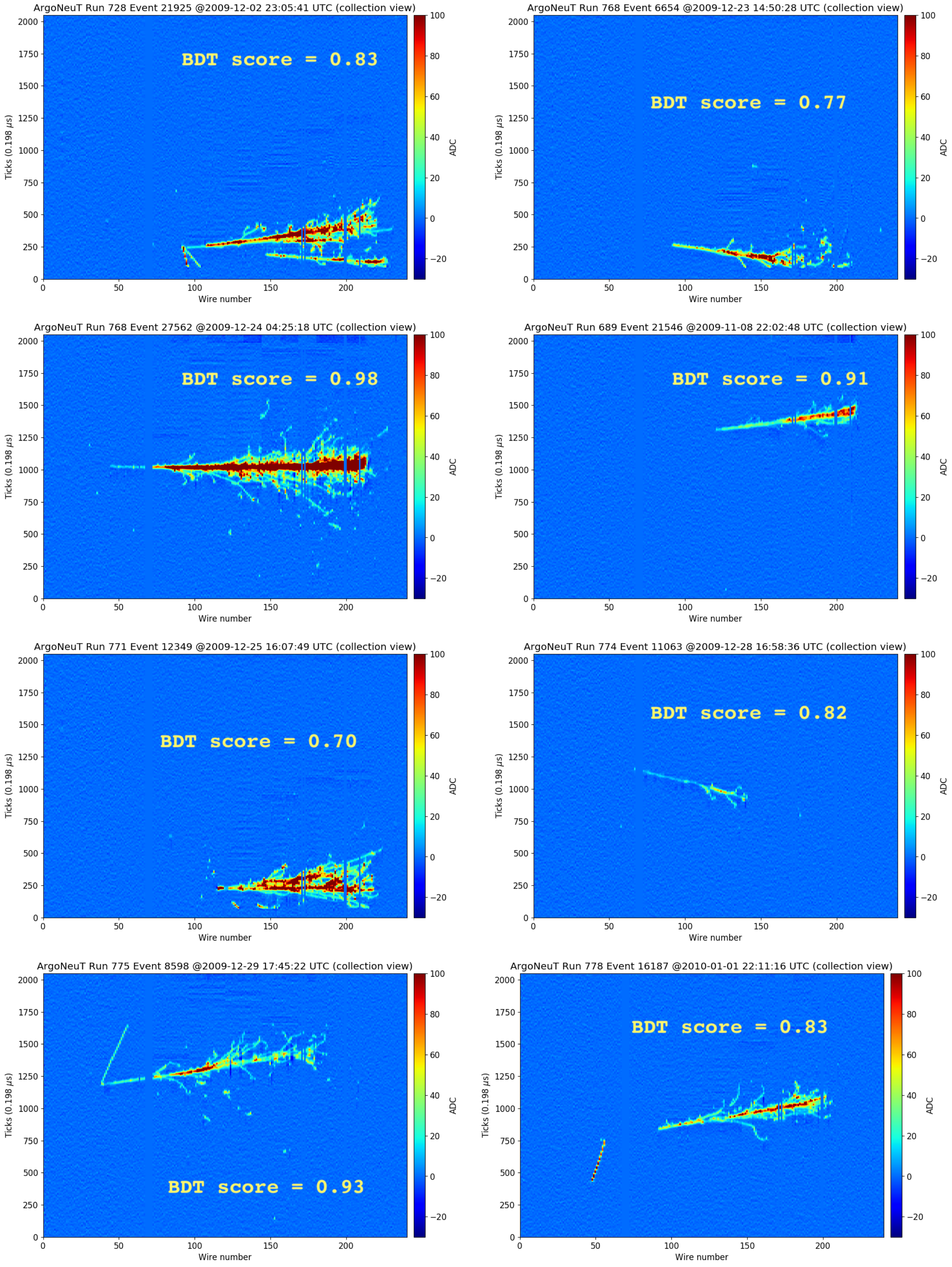

Figure C.2: Continued from Figure C.1. Events selected from ArgoNeuT data with BDT score > 0.7. Continued in Figures C.3-C.4.

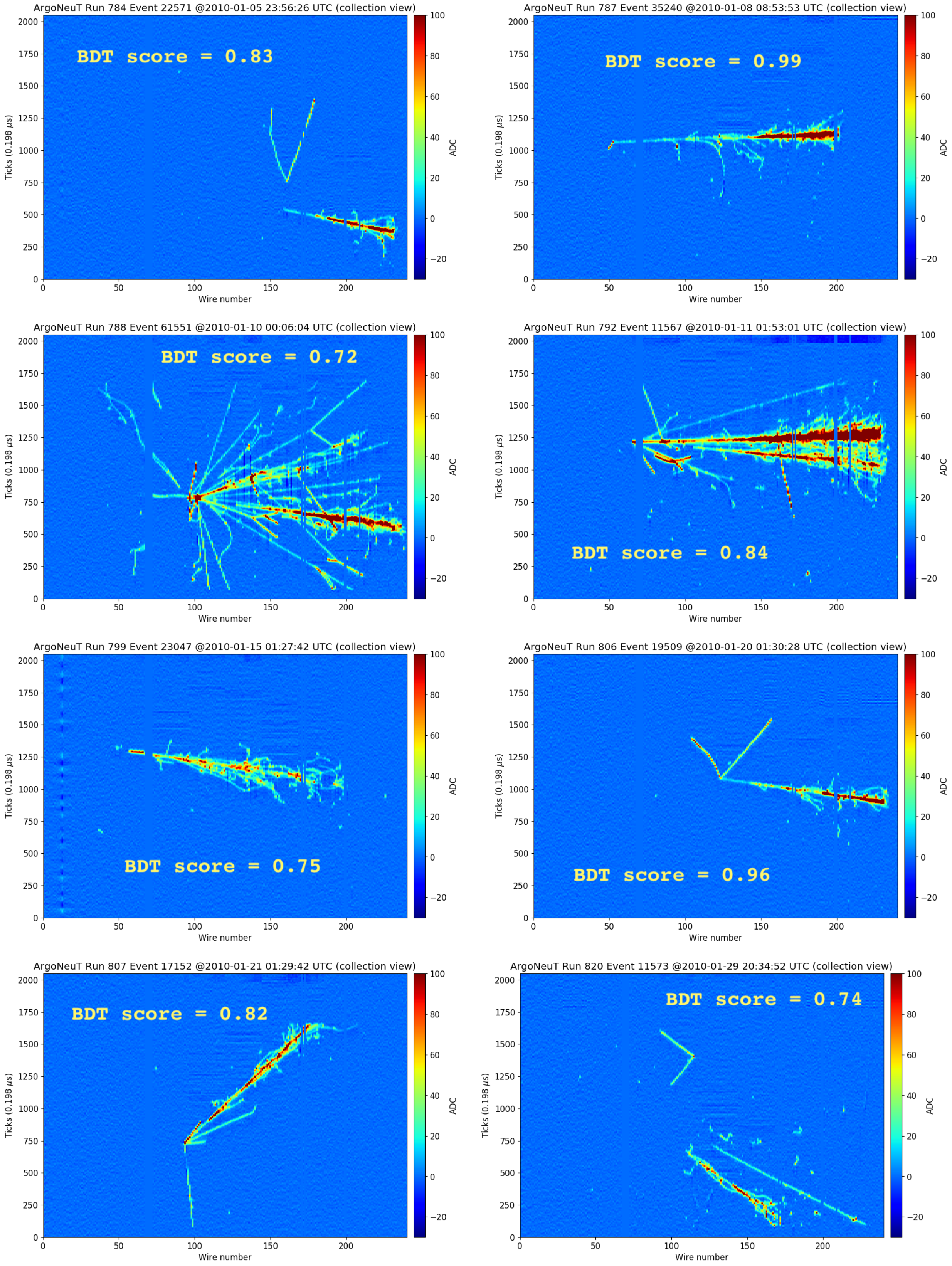

Figure C.3: Continued from Figure C.2. Events selected from ArgoNeuT data with BDT score > 0.7. Continued in Figure C.4.

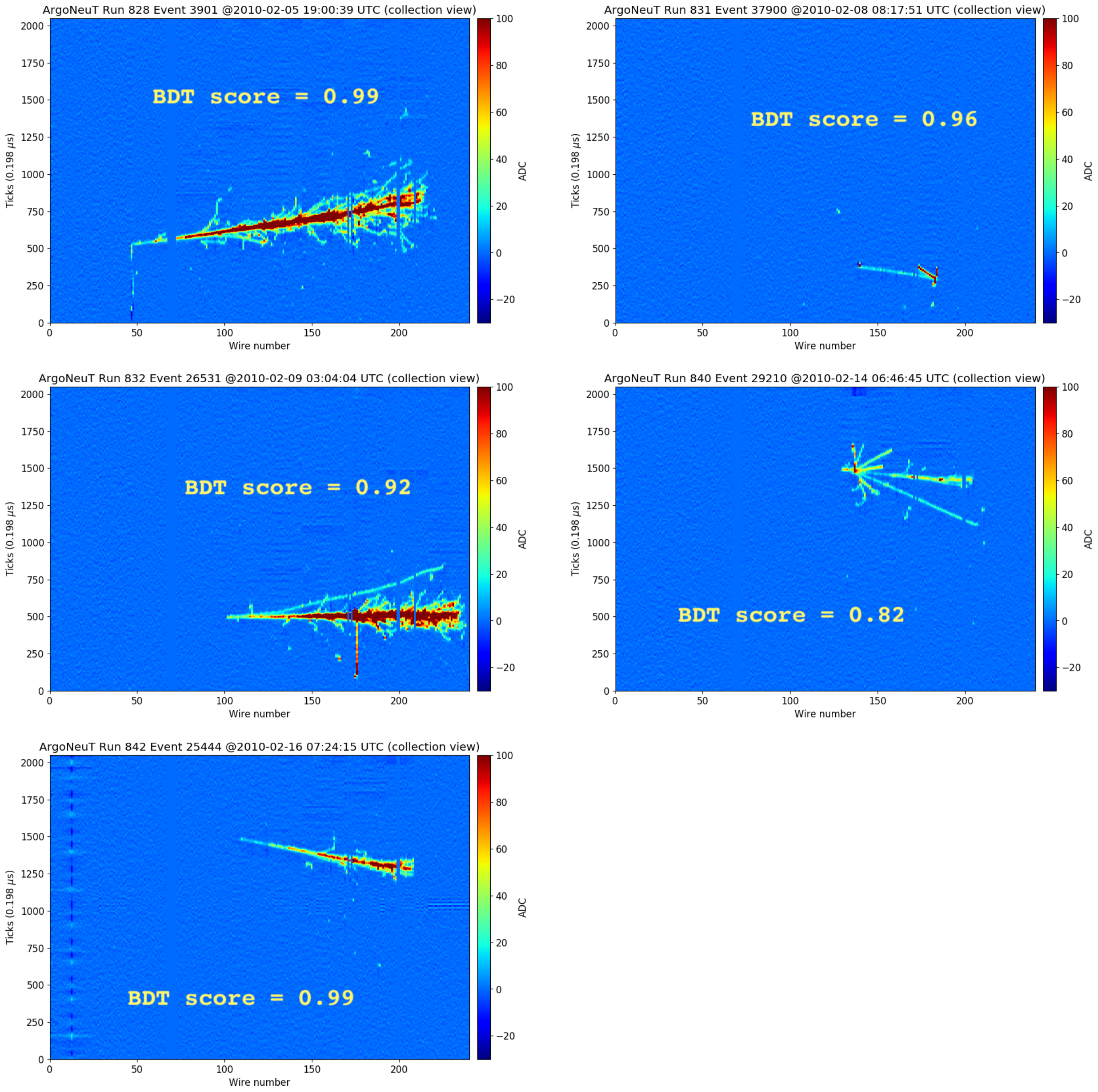

Figure C.4: Continued from Figure C.3. Events selected from ArgoNeuT data with BDT score > 0.7.

APPENDIX D

KDAR @ MiniBooNE Validation Tests

D.1 Alternative energy variables

The best fit contours for alternative energy variables for the KDAR analysis in MiniBooNE. The best fits for **myStFull_energy_mu** (Figures D.1 - D.3) and **myStFlux_ecer_mu** (Figures D.4 - D.6) yield shapes shapes consistent with **TankHits*fqlt05**.

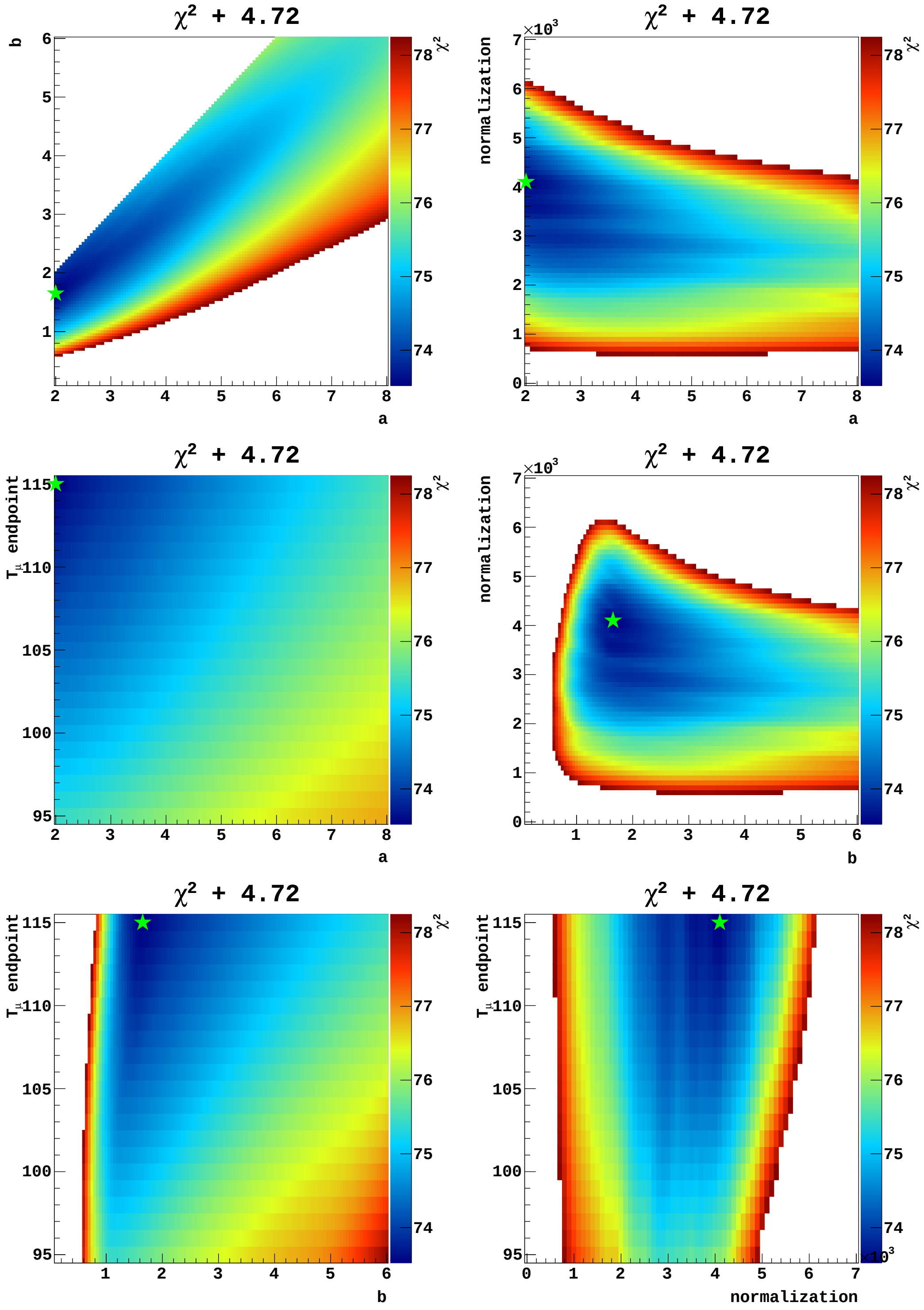

Figure D.1: $\chi^2_{\text{min}} + 4.72$. **mySTFull_energy_mu** energy variable. The best fit parameters are $a = 2$, $b = 1.65$, normalization $= 4100$ and $T_\mu^{\text{max}} = 115$ MeV.

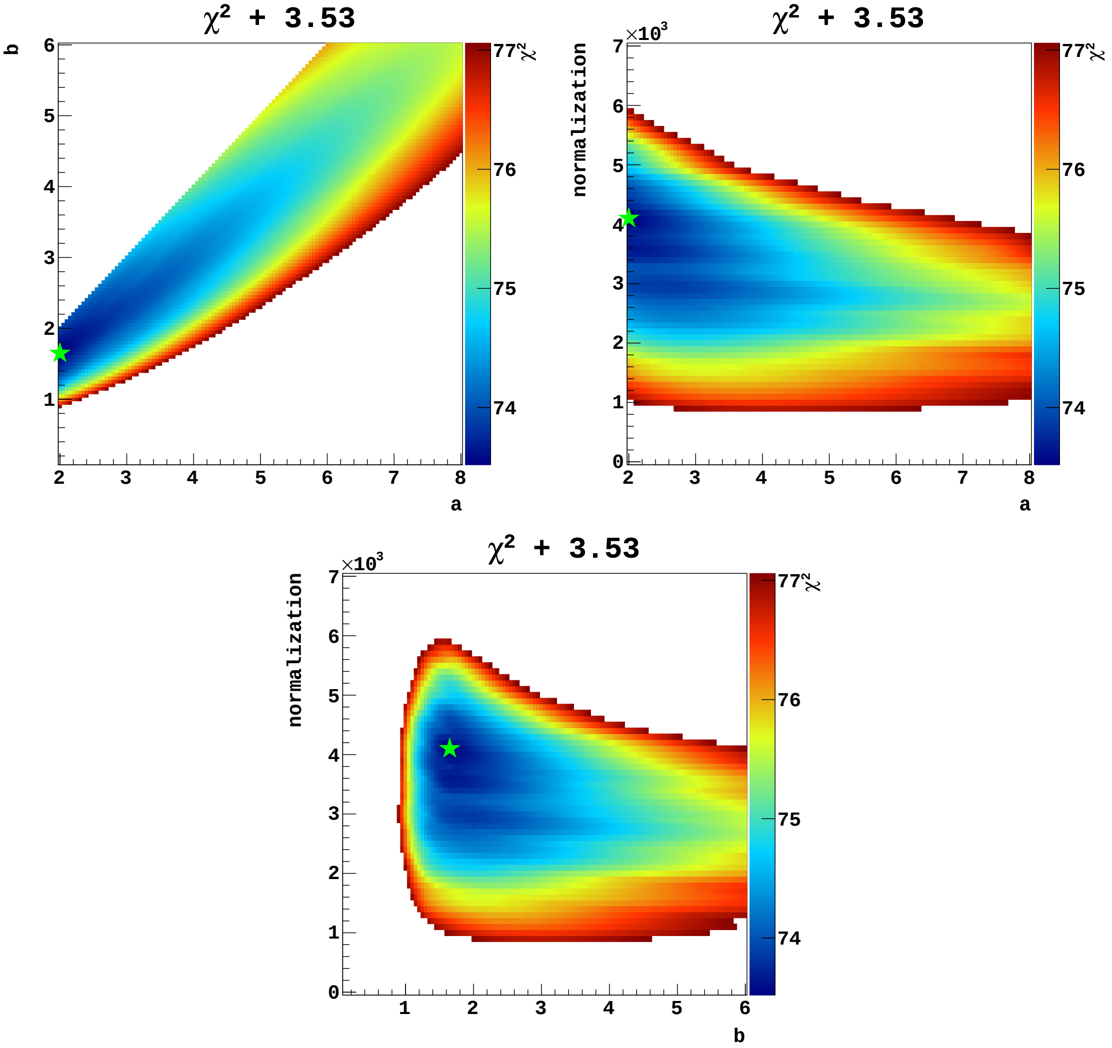

Figure D.2: $\chi^2_{\text{min}} + 3.53$ ($T_\mu^{\text{max}} = 95$ MeV). **myStFull_energy_mu** energy variable. The best fit parameters are $a = 2$, $b = 1.65$, normalization $= 4100$.

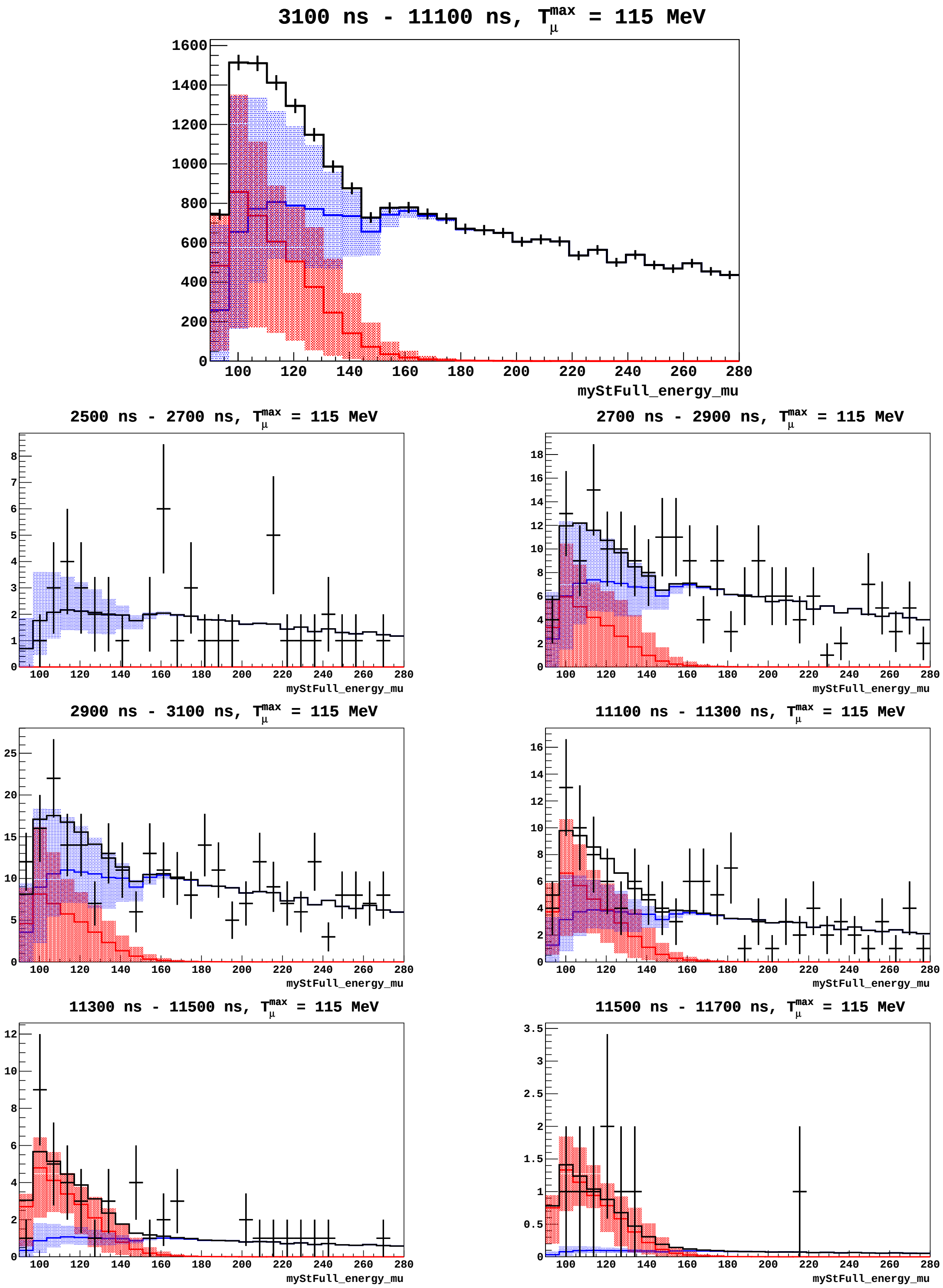

Figure D.3: (top) Best fit signal and background in high statistics NT region. (rows 2-4) Signal-suppressed (2500-3100 ns) and signal-enhanced (11100-11700 ns) regions with data (black error bars), best fit signal (red), inferred background (blue), model (black, solid line). **myStFull_energy_mu** energy variable.

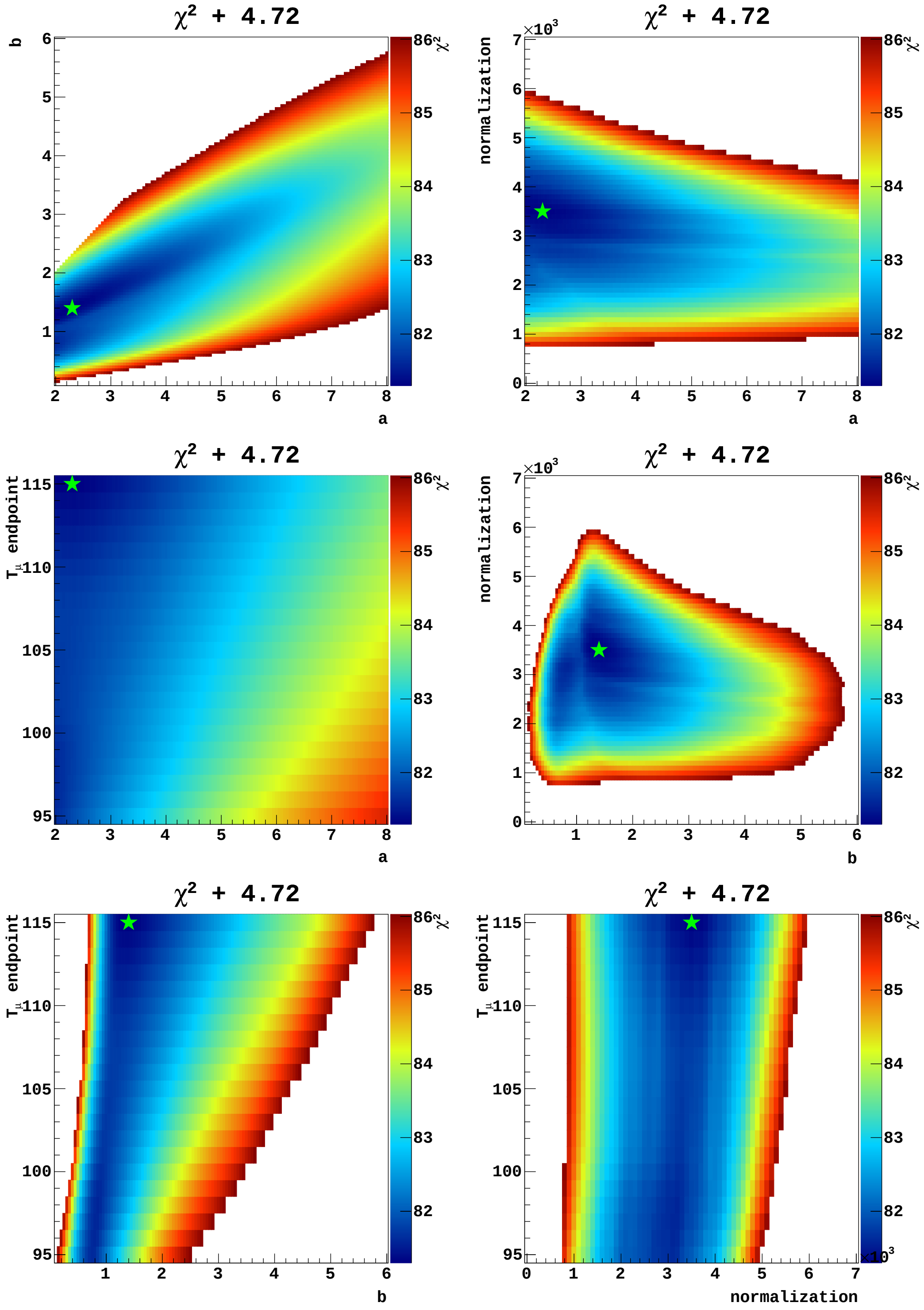

Figure D.4: $\chi^2_{\text{min}} + 4.72$. **myStFlux_ecer_mu** energy variable. The best fit parameters are $a = 2.3$, $b = 1.4$, normalization $= 3500$ and $T_\mu^{\text{max}} = 115$ MeV.

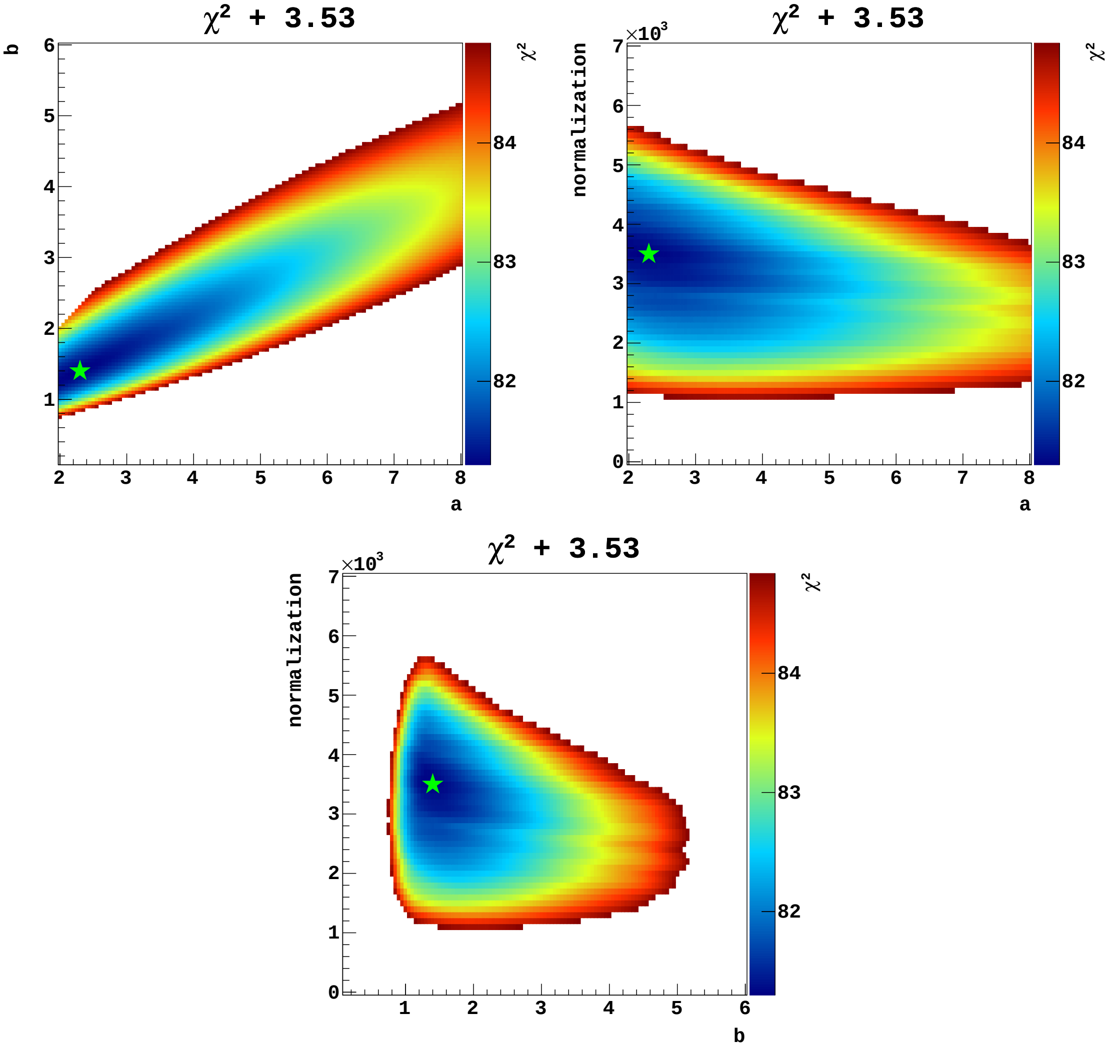

Figure D.5: $\chi^2_{\min} + 3.53$ ($T_\mu^{\max} = 95$ MeV). **myStFlux_ecer_mu** energy variable. The best fit parameters are $a = 2.3$, $b = 1.4$, normalization $= 3500$.

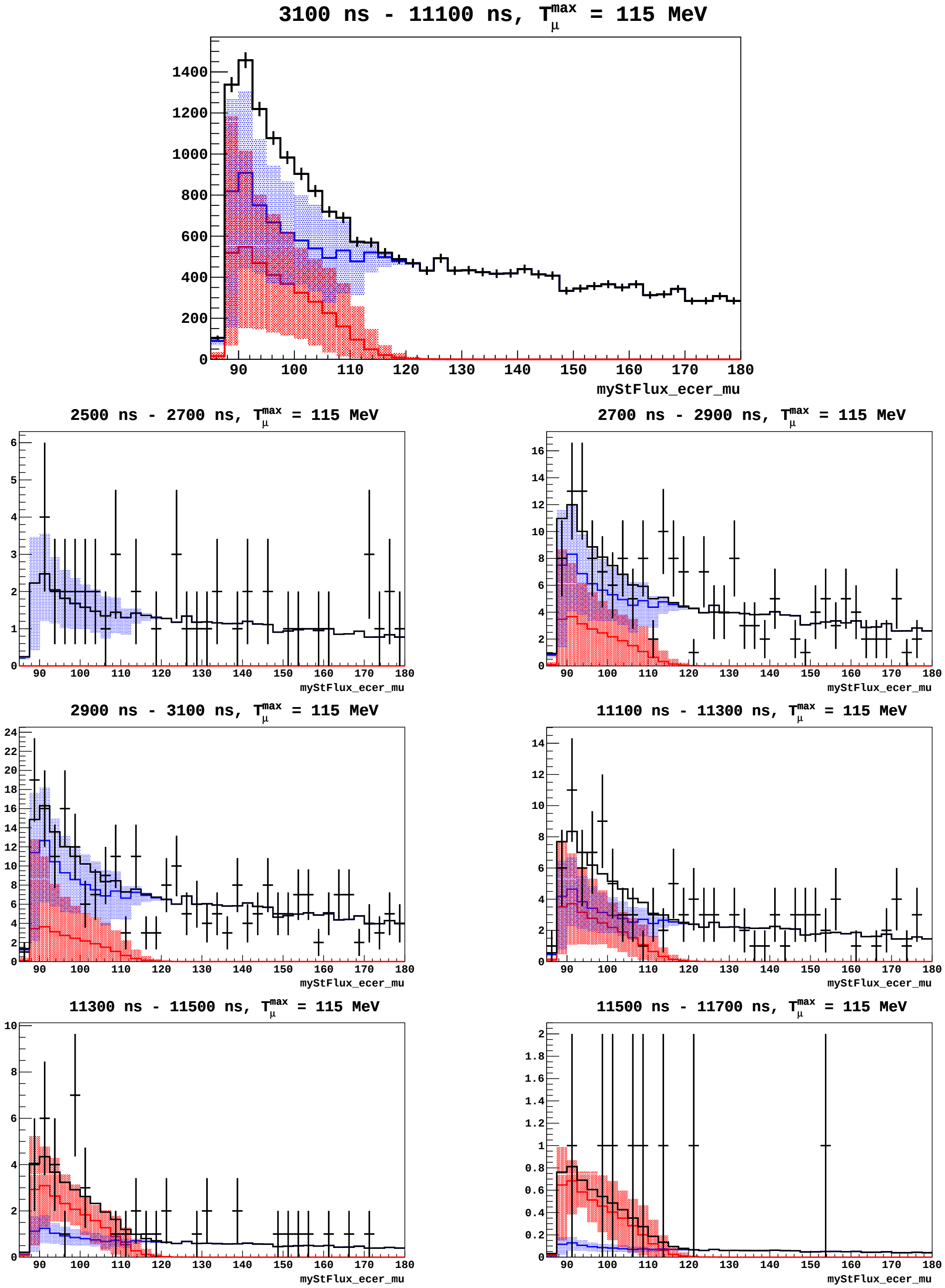

Figure D.6: (top) Best fit signal and background in high statistics NT region. (rows 2-4) Signal-suppressed (2500-3100 ns) and signal-enhanced (11100-11700 ns) regions with data (black error bars), best fit signal (red), inferred background (blue), model (black, solid line). **myStFlux_ecer_mu** energy variable.

D.2 Choice of Folding Matrix

Results of the fitting procedure using an alternative folding matrix at the opposite end of the available parameter space ($\kappa = 1.022$) are shown in Figures D.7 and D.8 on the following pages. The extracted fit is highly consistent with the result using the default folding matrix ($\kappa = 0.978$)

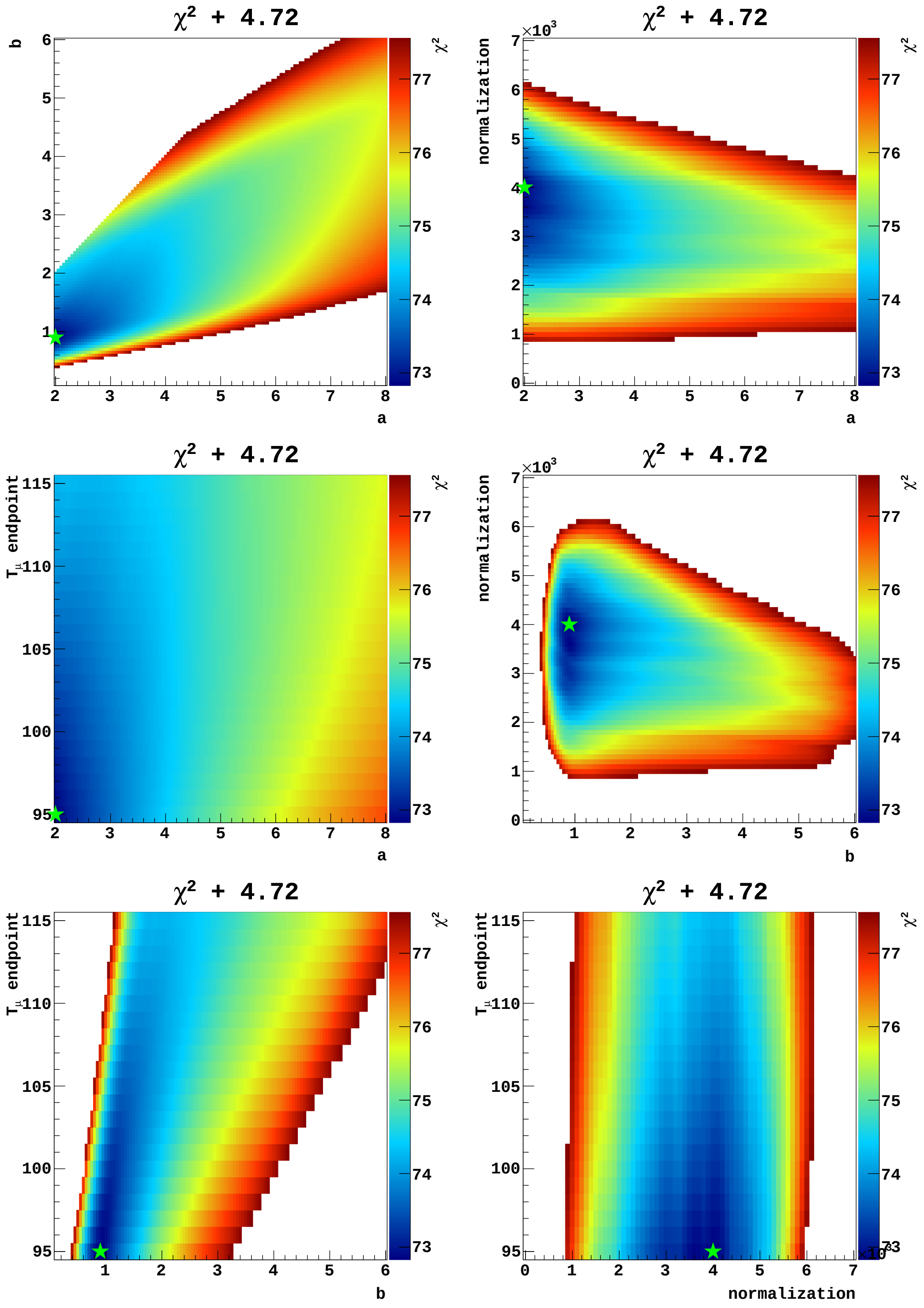

Figure D.7: χ^2_{min}+4.72. **TankHits*fqlt05** constructed using the folding matrix that depends on $\kappa = 1.022$ rather than the standard $\kappa = 0.978$. The best fit parameters are $a = 2$, $b = 0.9$, normalization $= 4000$ and $T_\mu^{\text{max}} = 95$ MeV.

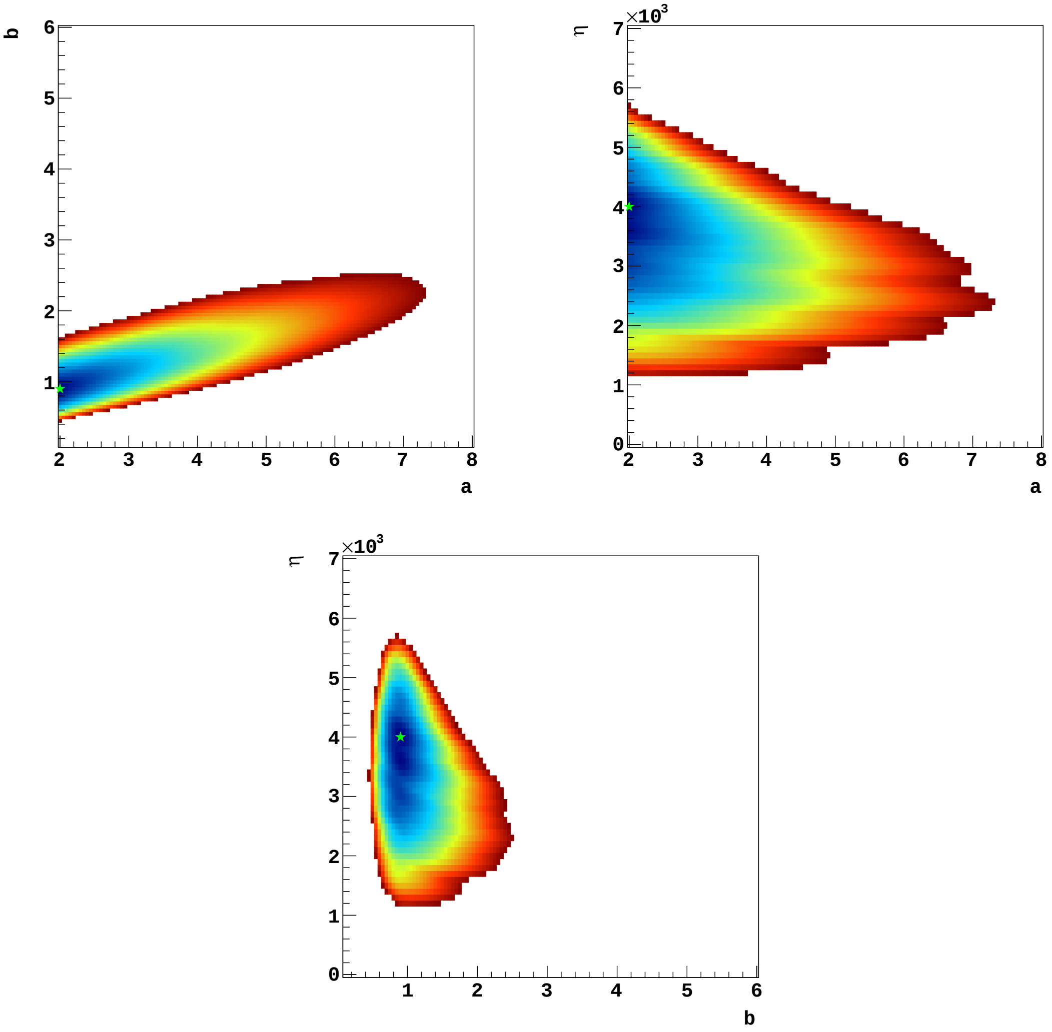

Figure D.8: $\chi^2_{\mathrm{min}} + 3.53$ ($T_\mu^{\mathrm{max}} = 95$ MeV). **TankHits*fqlt05** constructed using the folding matrix that depends on $\kappa = 1.022$ rather than the standard $\kappa = 0.978$. The best fit parameters are $a = 2$, $b = 0.9$, normalization $= 4000$.

D.3 Neutrino energy cut in signal region

The results of fitting after applying an additional neutrino energy cut:

$$\texttt{tHits\_1SE > 160 \&\& tHits\_1SE}\star\texttt{myStFull\_fqlt05[0] < 120} \tag{D.1}$$

are shown in Figures D.9 and D.10. They are comparable to the default settings.

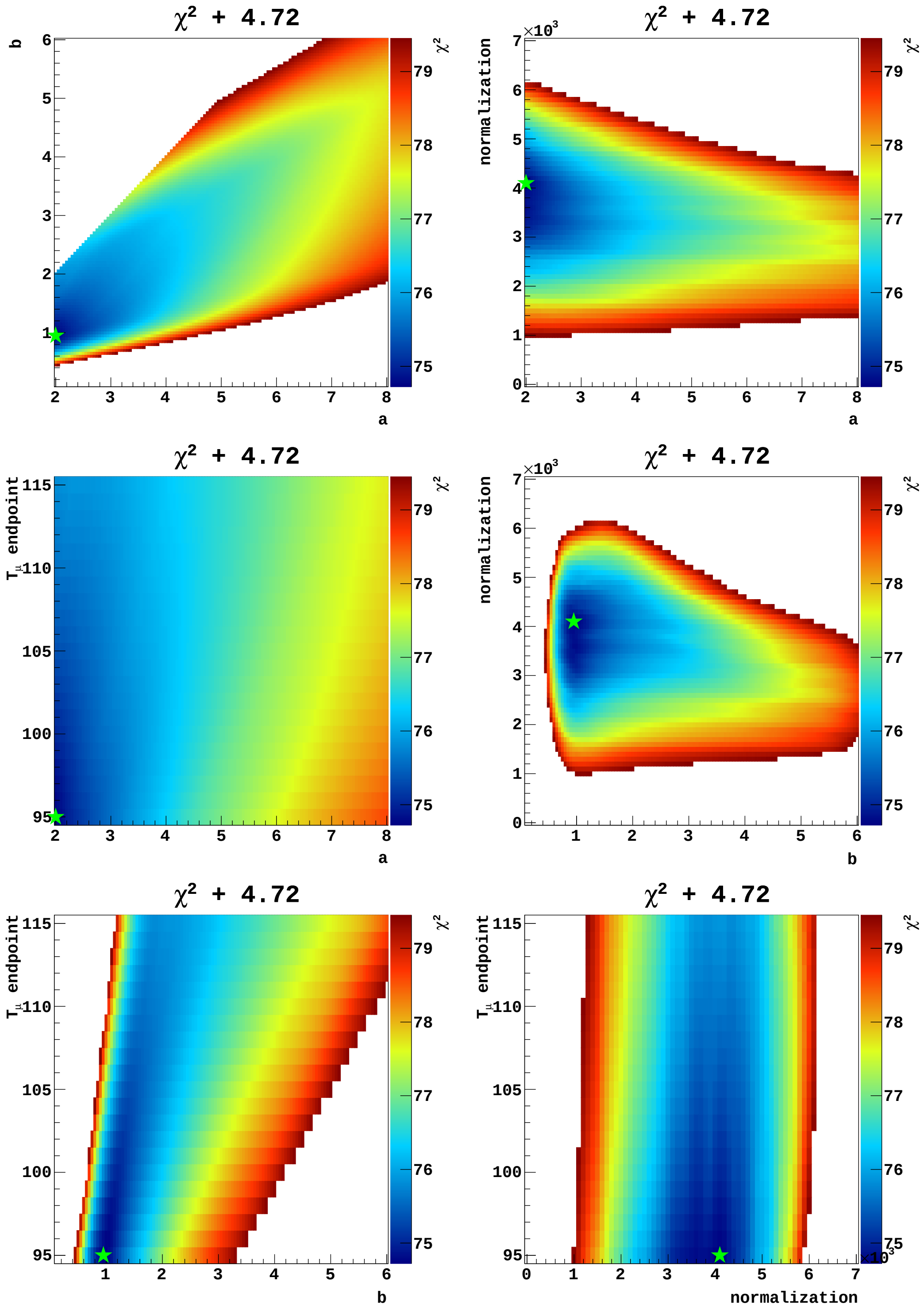

Figure D.9: $\chi^2_{\text{min}} + 4.72$. **TankHits*fqlt05** with a neutrino energy cut applied to the signal region to remove events where the reconstructed neutrino energy excited the KDAR energy. The best fit parameters are $a = 2$, $b = 0.95$, normalization $= 4100$ and $T_\mu^{\text{max}} = 95$ MeV.

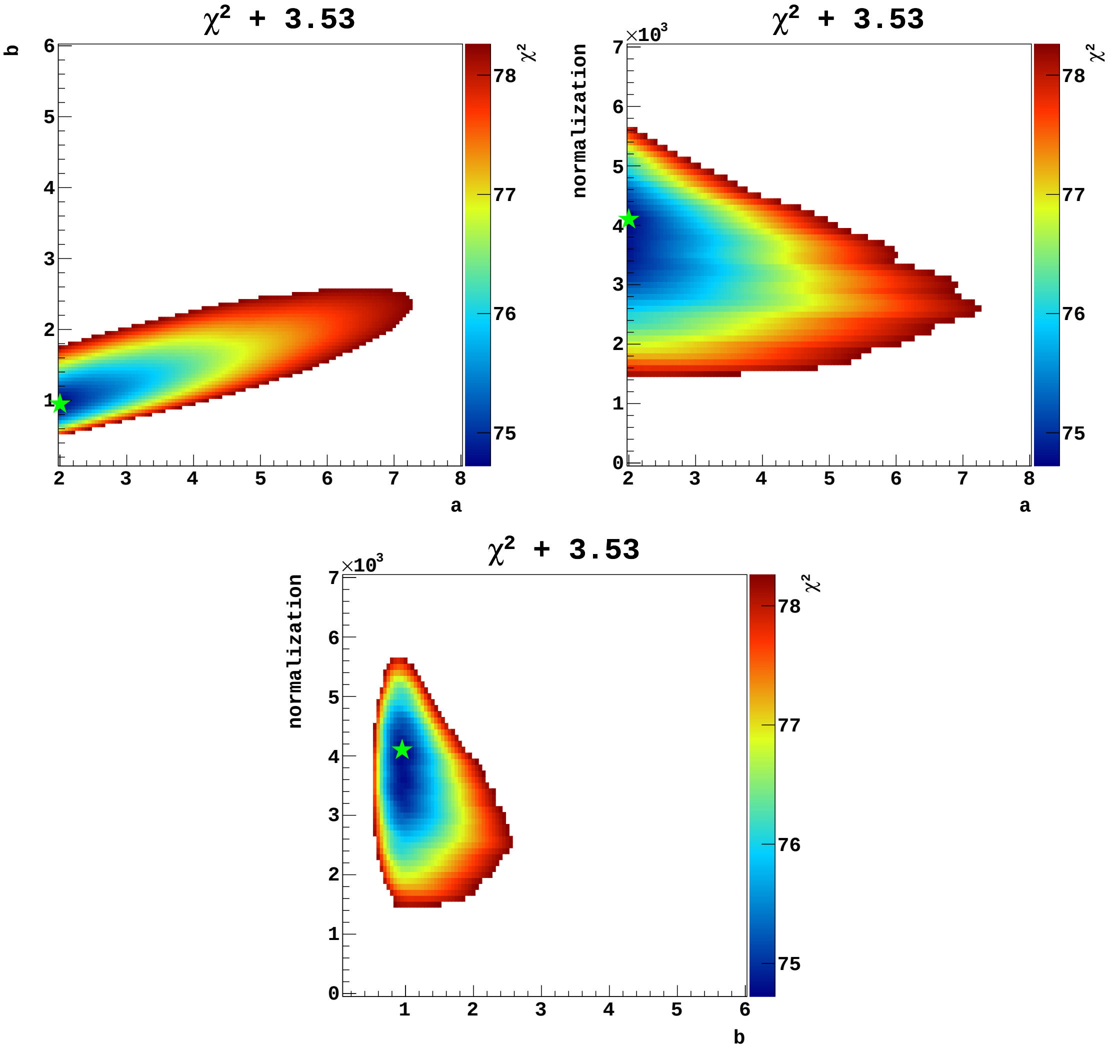

Figure D.10: $\chi^2_{\text{min}} + 3.53$ ($T_\mu^{\text{max}} = 95$ MeV). **TankHits*fqlt05** with a neutrino energy cut applied to the signal region to remove events where the reconstructed neutrino energy excited the KDAR energy. The best fit parameters are $a = 2$, $b = 0.95$, normalization $= 4100$.

D.4 Kaon/pion decay-in-flight background

Figures D.11 and D.12 demonstrate that the impact of the 8% decay-in-flight muon neutrino backgrounds in the KDAR analysis in MiniBooNE are negligible. The results included on the following pages include this background in the signal model and the new best fit normalization is comfortably within the errors of the primary result.

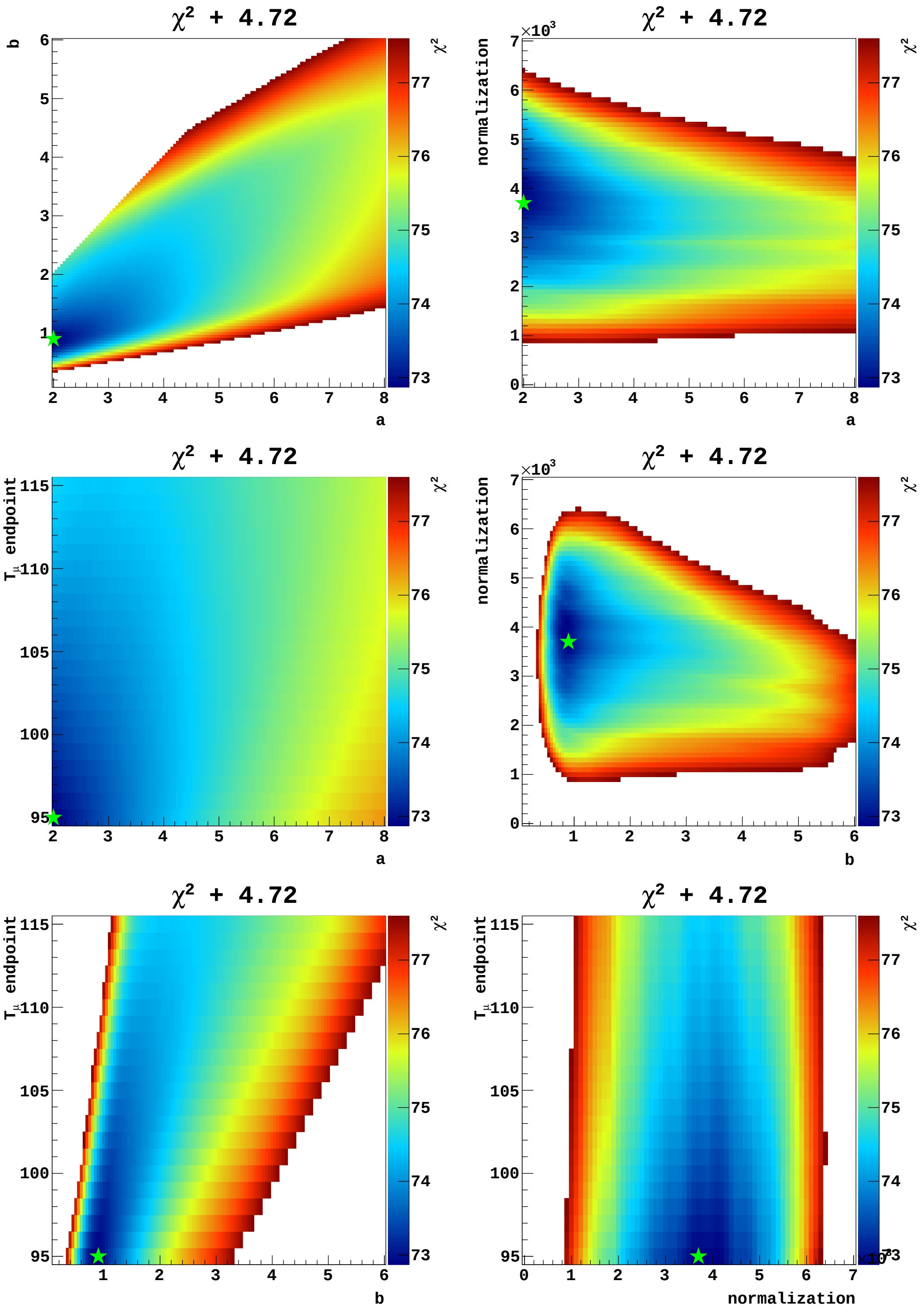

Figure D.11: $\chi^2_{\min} + 4.72$. **TankHits*fqlt05** with 8% kaon and pion decay-in-flight included in signal model. The best fit parameters are $a = 2$, $b = 0.9$, normalization = 3700 and $T_\mu^{\max} = 95$ MeV.

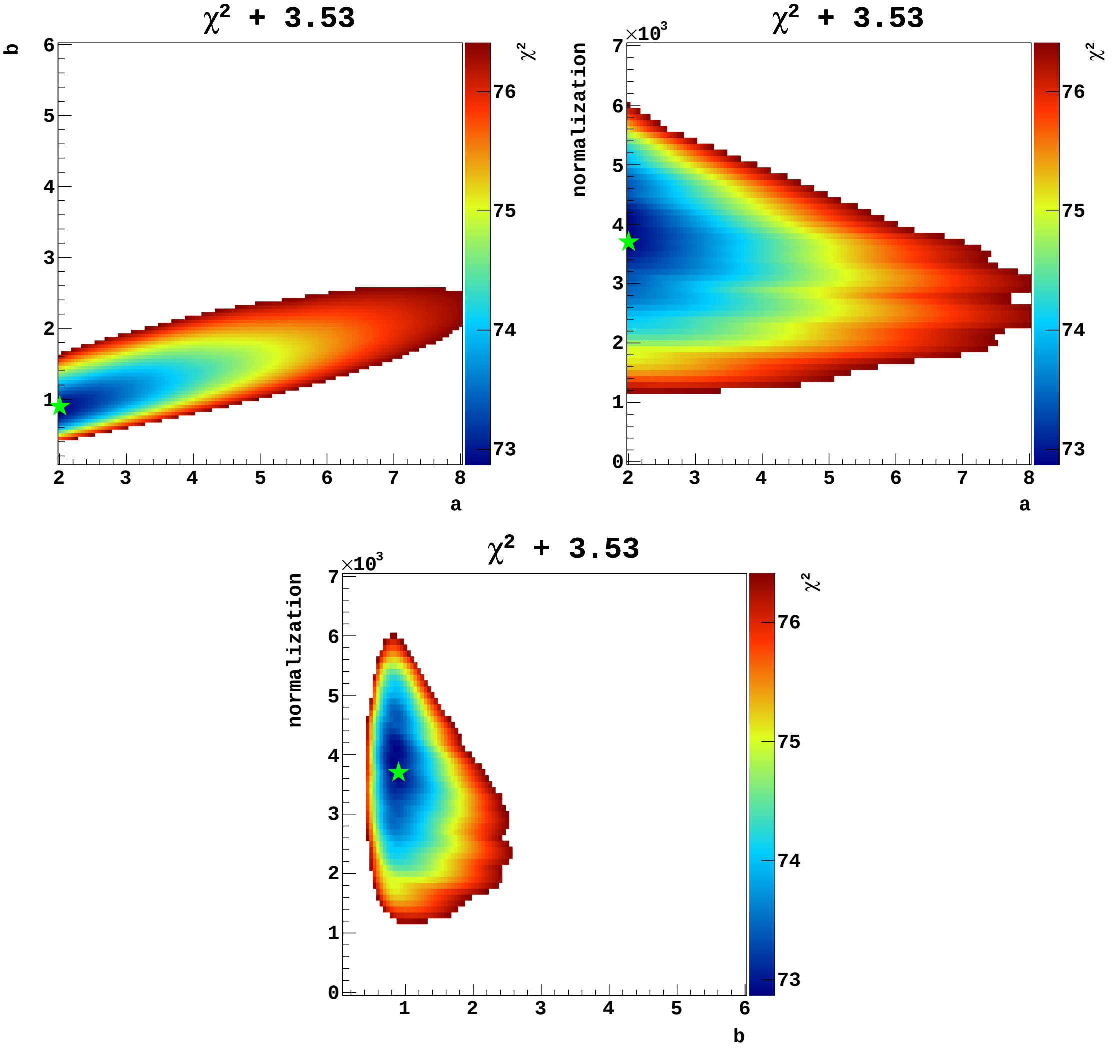

Figure D.12: $\chi^2_{\text{min}}+3.53$ ($T_\mu^{\text{max}} = 95$ MeV). **TankHits*fqlt05** with 8% kaon and pion decay-in-flight included in signal model. The best fit parameters are $a = 2$, $b = 0.9$, normalization $= 3700$.

′

D.5 Choice of $T_\mu^{\max}$

The primary result for the MiniBooNE KDAR analysis fixes the T_μ endpoint at 95 MeV. This was selected based on a χ^2 minimization over a range of endpoints from 95-115 MeV. However, Figures D.13-D.16 demonstrate that the choice of $T_\mu^{\max}$ has little impact on the allowed KDAR signal shape parameters.

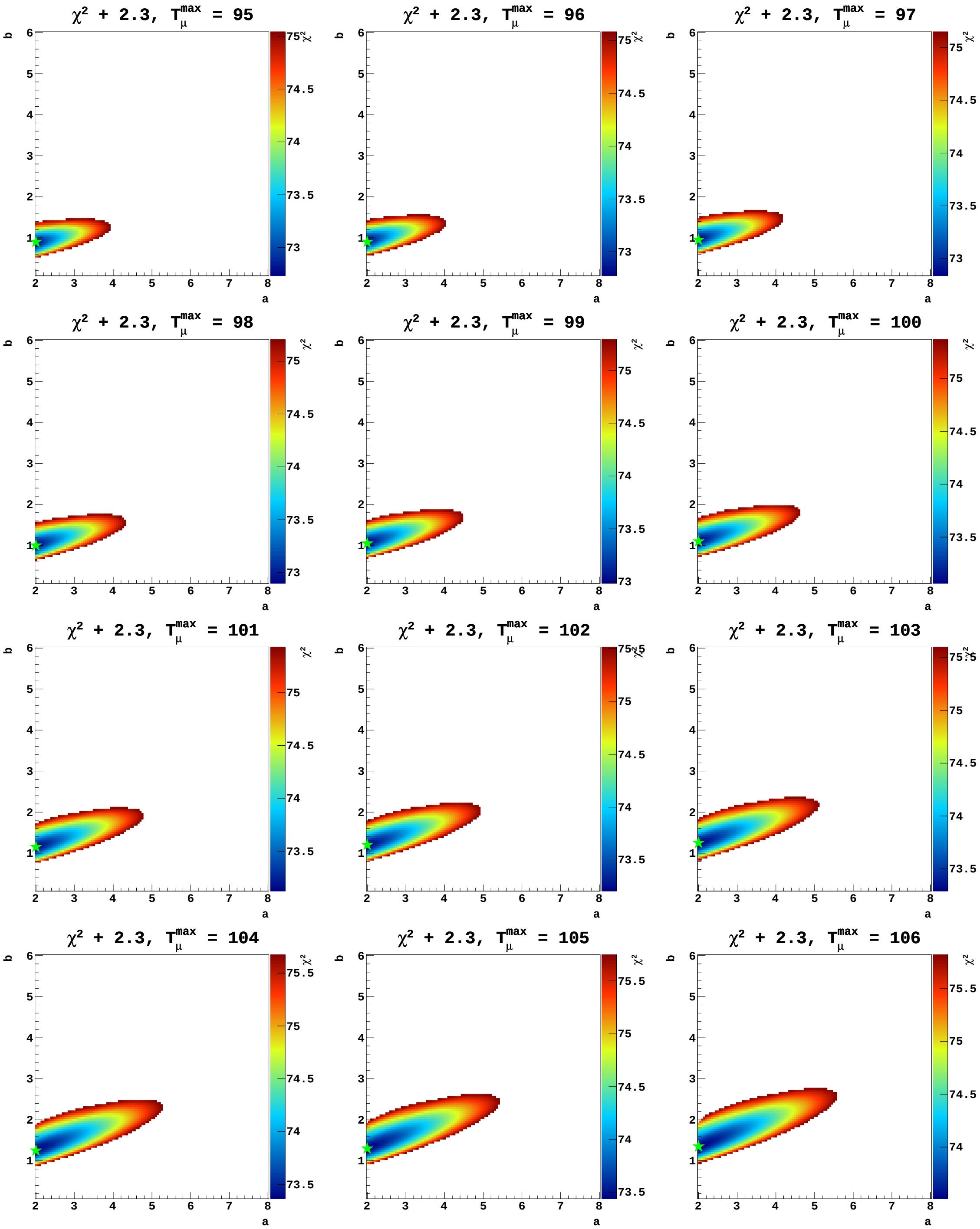

Figure D.13: The effect that choosing an endpoint has on the shape of the KDAR T_μ distribution. In general, higher $T_\mu^{\max}$ is correlated to greater values in b. Additionally, the size of the allowed region increases as $T_\mu^{\max}$ increases. Here, the normalization is fixed at 4000 (the overall best fit value) for all endpoints. The best fit value for fixed endpoint and normalization is indicated by the green star. Continued in Figure D.14.

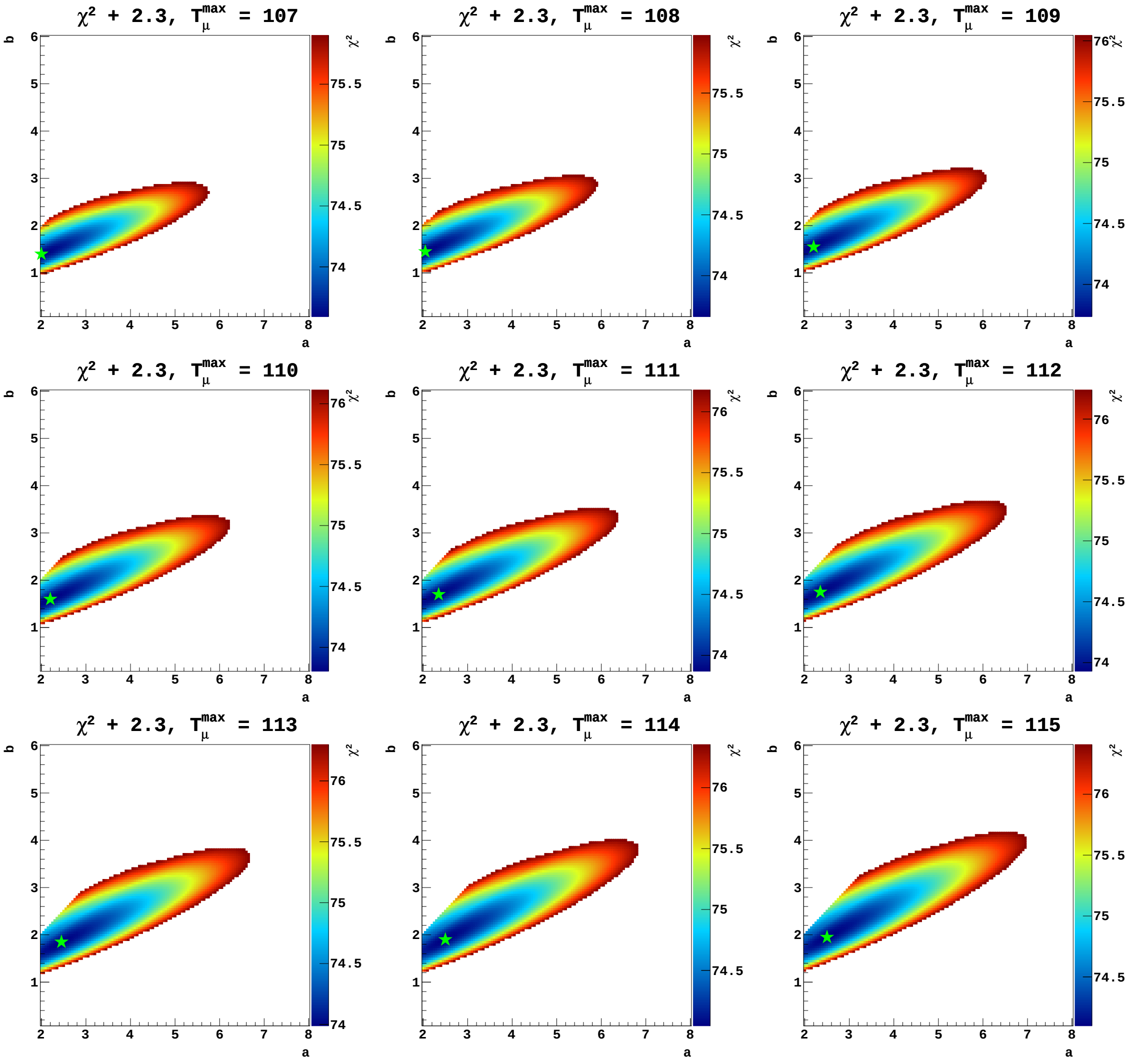

Figure D.14: Continued from Figure D.13. The effect that choosing an endpoint has on the shape of the KDAR T_μ distribution. In general, higher T_μ^{max} is correlated to greater values in b. Additionally, the size of the allowed region increases as T_μ^{max} increases. The best fit value for fixed endpoint and normalization is indicated by the green star. Here, the normalization is fixed at 4000 for all endpoints.

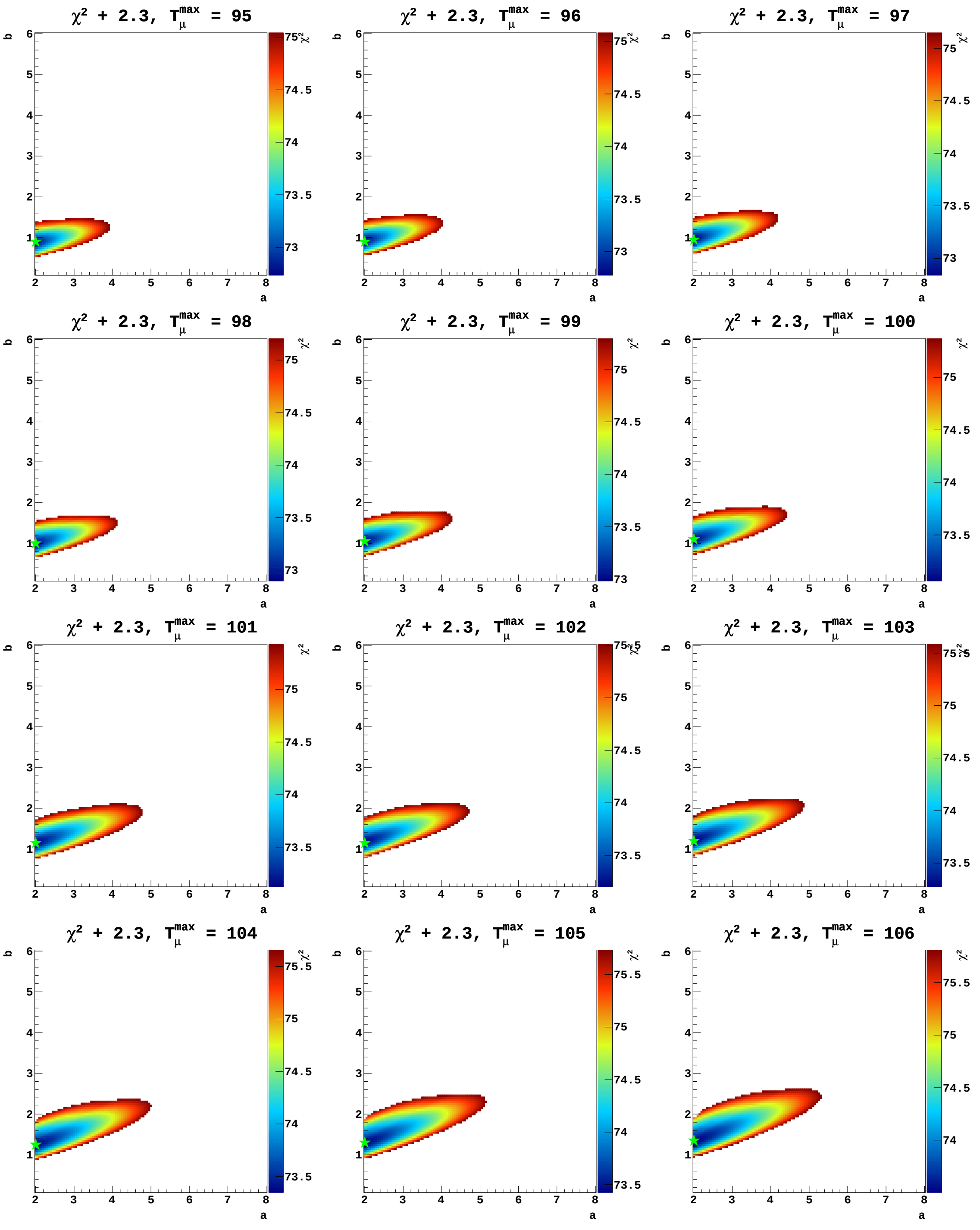

Figure D.15: The effect that choosing an endpoint has on the shape of the KDAR T_μ distribution. In general, higher T_μ^{max} is correlated to greater values in b. Additionally, the size of the allowed region increases as T_μ^{max} increases. Here, the normalization is fixed at the best fit value for a particular endpoint. It varies between 4000 and 4300 depending on the value of T_μ^{max}. The best fit value for fixed endpoint and normalization is indicated by the green star. Continued in Figure D.16.

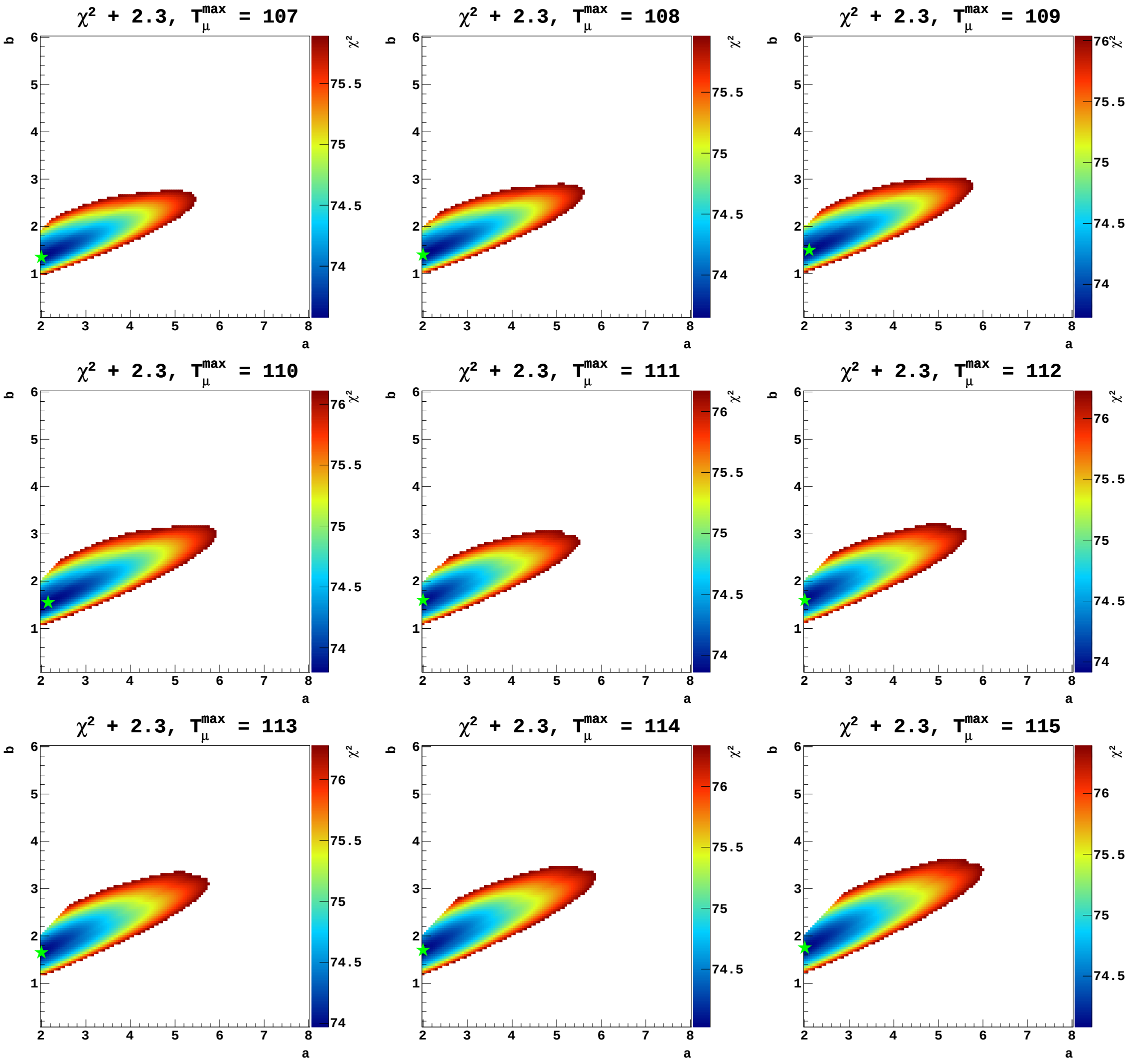

Figure D.16: Continued from Figure D.15. The effect that choosing an endpoint has on the shape of the KDAR T_μ distribution. In general, higher T_μ^{max} is correlated to greater values in b. Additionally, the size of the allowed region increases as T_μ^{max} increases. The best fit value for fixed endpoint and normalization is indicated by the green star. Here, the normalization is fixed at the best fit value for a particular endpoint. It varies between 4000 and 4300 depending on the value of T_μ^{max}.

BIBLIOGRAPHY

[1] E. Fermi, Z. Physik **88**, 161 (1934).

[2] C.L. Cowan Jr., F. Reines, F.B. Harrison, H.W. Kruse and A.D. McGuire, Science **124**, 3212 (1956).

[3] K. Riesselmann, *Neutrino invention* (2007), `symmetrymagazine.org`.

[4] G. J. Neary, Roy. Phys. Soc. (London) **71**, A175 (1940).

[5] T. Araki, S. Enomoto, K. Furuno, Y. Gando, K. Ichimura, H. Ikeda, K. Inoue, Y. Kishimoto, M. Koga, Y. Koseki, et al., Nature **436**, 499 (2005).

[6] J. A. Formaggio and G. P. Zeller, Rev. Mod. Phys. **84**, 1307 (2012).

[7] F. Reines and C. L. Cowan, Phys. Rev. **90**, 492 (1953).

[8] T. D. Lee and C. N. Yang, Phys. Rev. **104**, 254 (1956).

[9] C. S. Wu, E. Ambler, R. W. Hayward, D. D. Hoppes, and R. P. Hudson, Phys. Rev. **105**, 1413 (1957).

[10] M. Goldhaber, L. Grodzins, and A. W. Sunyar, Phys. Rev. **109**, 1015 (1958).

[11] G. Danby, J. Gaillard, K. A. Goulianos, L. Lederman, N. B. Mistry, M. Schwartz, and J. Steinberger, Phys. Rev. Lett. **9**, 36 (1962).

[12] Kodama, K. et al. [DONUT Collaboration], Phys. Lett. B **504**, 218 (2001).

[13] M. L. Perl et al., Phys. Rev. Lett. **35**, 1489 (1975).

[14] Schael, S. et al. [ALEPH, DELPHI, L3, OPAL, SLD, LEP Electroweak Working Group, SLD Electroweak Group, SLD Heavy Flavour Group], Phys. Rept. **427**, 257 (2006).

[15] R. Davis, Phys. Rev. Lett. **12**, 303 (1964).

[16] J. N. Bahcall, Phys. Rev. Lett. **12**, 300 (1964).

[17] R. Davis, D. S. Harmer, and K. C. Hoffman, Phys. Rev. Lett. **20**, 1205 (1968).

[18] J. N. Bahcall, N. A. Bahcall, and G. Shaviv, Phys. Rev. Lett. **20**, 1209 (1968).

[19] K. Hirata et al., Phys. Rev. Lett. **63**, 16 (1989).

[20] Y. Fukuda et al., Phys. Rev. Lett. **77**, 1683 (1996).

[21] J. N. Abdurashitov et al. [SAGE Collaboration], Phys. Rev. C **80**, 015807 (2009).

[22] W. Hampel et al. [GALLEX Collaboration], Phys. Lett. B **447**, 127 (1999).

[23] B. Pontecorvo, Sov. Phys. JETP **6**, 429 (1957).

[24] B. Pontecorvo, Sov. Phys. JETP **26**, 984 (1968).

[25] Z. Maki, M. Nakagawa, and S. Sakata, Progress of Theoretical Physics **28**, 870 (1962).

[26] V. Gribov and B. Pontecorvo, Physics Letters B **28**, 493 (1969).

[27] L. Wolfenstein, Phys. Rev. D **17**, 2369 (1978).

[28] L. Wolfenstein, Phys. Rev. D **20**, 2634 (1979).

[29] S. Mikheyev and A. Smirnov, Sov. J. Nucl. Phys. **42**, 913 (1985).

[30] S. Mikheyev and A. Smirnov, Zh. Eksp. Teor. Fiz. **91**, 7 (1986).

[31] Q. R. Ahmad et al. [SNO Collaboration], Phys. Rev. Lett. **89**, 011301 (2002).

[32] K. Hirata and others., Phys. Rev. Lett. **58**, 1490 (1987).

[33] R. M. Bionta et al., Phys. Rev. Lett. **58**, 1494 (1987).

[34] E. Alekseev, L. Alekseeva, I. Krivosheina, and V. Volchenko, Phys. Lett. B **205**, 209 (1988).

[35] K. Hirata et al., Physics Letters B **205**, 416 (1988).

[36] Y. Fukuda et al. [Super-Kamiokande Collaboration], Phys. Rev. Lett. **81**, 1562 (1998).

[37] Y. Fukuda et al. [Super-Kamiokande Collaboration], Phys. Rev. Lett. **93**, 101801 (2004).

[38] Y. Fukuda et al. [Super-Kamiokande Collaboration], Phys. Rev. Lett. **97**, 171801 (2006).

[39] K. Eguchi, S. Enomoto, K. Furuno, J. Goldman, H. Hanada, H. Ikeda, K. Ikeda, K. Inoue, K. Ishihara, W. Itoh, et al. (KamLAND Collaboration), Phys. Rev. Lett. **90**, 021802 (2003).

[40] T. Araki, K. Eguchi, S. Enomoto, K. Furuno, K. Ichimura, H. Ikeda, K. Inoue, K. Ishihara, T. Iwamoto, T. Kawashima, et al. (KamLAND Collaboration), Phys. Rev. Lett. **94**, 081801 (2005).

[41] S. Abe, T. Ebihara, S. Enomoto, K. Furuno, Y. Gando, K. Ichimura, H. Ikeda, K. Inoue, Y. Kibe, Y. Kishimoto, et al. (The KamLAND Collaboration), Phys. Rev. Lett. **100**, 221803 (2008).

[42] J. Beringer et al. (Particle Data Group), Phys. Rev. D **98**, 030001 (2018).

[43] M. Betti et al., Journal of Cosmology and Astroparticle Physics **2019**, 047 (2019).

[44] A. Aguilar et al. [LSND Collaboration], Phys. Rev. D **64**, 112007 (2001).

[45] A. A. Aguilar-Arevalo et al. [MiniBooNE Collaboration] (2020), `arXiv:2006.16883`.

[46] K. Abe, R. Akutsu, A. Ali, C. Alt, C. Andreopoulos, L. Anthony, M. Antonova, S. Aoki, A. Ariga, T. Arihara, et al., Nature **580**, 339 (2020).

[47] M. A. Acero et al. (NOvA Collaboration), Phys. Rev. Lett. **123**, 151803 (2019).

[48] K. J. Kelly, P. A. N. Machado, S. J. Parke, Y. F. Perez-Gonzalez, and R. Z. Funchal, Phys. Rev. D **103**, 013004 (2021).

[49] B. Abi et al. (DUNE Collaboration) (2020), `arXiv:2002.03005`.

[50] M. Aker, K. Altenmüller, M. Arenz, M. Babutzka, J. Barrett, S. Bauer, M. Beck, A. Beglarian, J. Behrens, T. Bergmann, et al. (KATRIN Collaboration), Phys. Rev. Lett. **123**, 221802 (2019).

[51] L. Gastaldo, K. Blaum, A. Doerr, C. E. Düllmann, K. Eberhardt, S. Eliseev, C. Enss, A. Faessler, A. Fleischmann, S. Kempf, et al., Journal of Low Temperature Physics **176**, 876 (2014).

[52] B. Alpert, M. Balata, D. Bennett, M. Biasotti, C. Boragno, C. Brofferio, V. Ceriale, D. Corsini, P. K. Day, M. De Gerone, et al., The European Physical Journal C **75**, 112 (2015).

[53] M. P. Croce, M. W. Rabin, V. Mocko, G. J. Kunde, E. R. Birnbaum, E. M. Bond, J. W. Engle, A. S. Hoover, F. M. Nortier, A. D. Pollington, et al., Journal of Low Temperature Physics **184**, 958 (2016).

[54] K. Abe et al. [T2K Collaboration], Phys. Rev. D **87**, 012001 (2013).

[55] L. Aliaga et al. [MINVERvA Collaboration], Phys. Rev. D **94**, 092005 (2016).

[56] `https://www.fnal.gov/pub/science/particle-accelerators/accelerator-complex.html`.

[57] A. A. Aguilar-Arevalo et al. [MiniBooNE Collaboration], Phys. Rev. D **79**, 072002 (2009).

[58] P. Adamson et al., Nucl. Instrum. Methods Phys. Res., Sect. A **806**, 279 (2016).

[59] E. Aprile et al. [XENON Collaboration], Phys. Rev. D **102**, 072004 (2020).

[60] W. Willis and V. Radeka, Nuclear Instruments and Methods **120**, 221 (1974).

[61] C. Rubbia (1977), CERN-EP-INT-77-08, CERN-EP-77-08.

[62] F. Hasert, H. Faissner, W. Krenz, J. Von Krogh, D. Lanske, J. Morfin, K. Schultze, H. Weerts, G. Bertrand-Coremans, J. Lemonne, et al., Physics Letters B **46**, 121 (1973).

[63] F. Hasert, S. Kabe, W. Krenz, J. Von Krogh, D. Lanske, J. Morfin, K. Schultze, H. Weerts, G. Bertrand-Coremans, J. Sacton, et al., Physics Letters B **46**, 138 (1973).

[64] R. Acciarri, C. Adams, J. Asaadi, B. Baller, T. Bolton, C. Bromberg, F. Cavanna, E. Church, D. Edmunds, A. Ereditato, et al., Journal of Instrumentation **8**, P08005 (2013).

[65] P. Abratenko et al. (MicroBooNE Collaboration), JINST **15**, P12037 (2020).

[66] P. Agnes et al. [DarkSide Collaboration], Phys. Rev. D **98**, 102006 (2018).

[67] C. E. Aalseth et al. [DarkSide Collaboration], The European Physical Journal Plus **133**, 131 (2018).

[68] T. Heindl, T. Dandl, M. Hofmann, R. Krcken, L. Oberauer, W. Potzel, J. Wieser, and A. Ulrich, EPL (Europhysics Letters) **91**, 62002 (2010), ISSN 1286-4854.

[69] A. Hitachi, T. Takahashi, N. Funayama, K. Masuda, J. Kikuchi, and T. Doke, Phys. Rev. B **27**, 5279 (1983).

[70] B. Abi et al. (DUNE Collaboration), JINST **15**, T08010 (2020).

[71] A. Bernstein et al. (2009), FERMILAB-TM-2424-E, BNL-81896-2008-IR, LBNL-1348E, `arXiv:0907.4183`.

[72] M. G. Aartsen et al. [IceCube Collaboration], Science **342** (2013).

[73] U. Mosel, Annual Review of Nuclear and Particle Science **66**, 171 (2016).

[74] L. Alvarez-Ruso, M. SajjadAthar, M. Barbaro, D. Cherdack, M. Christy, P. Coloma, T. Donnelly, S. Dytman, A. de Gouva, R. Hill, et al., Progress in Particle and Nuclear Physics **100**, 1 (2018).

[75] C. Adams et al. [MicroBooNE Collaboration], Phys. Rev. D **99**, 092001 (2019).

[76] A. Radovic, M. Williams, D. Rousseau, M. Kagan, D. Bonacorsi, A. Himmel, A. Aurisano, K. Terao, and T. Wongjirad, Nature **41**, 560 (2018).

[77] X. Qian, C. Zhang, B. Viren, and M. Diwan, JINST **15**, P05032 (2018).

[78] C. Anderson et al. [ArgoNeuT Collaboration], Phys. Rev. Lett. **108**, 161802 (2012).

[79] R. Acciarri et al. [ArgoNeuT Collaboration], Phys. Rev. D **89**, 112003 (2014).

[80] R. Acciarri et al. [ArgoNeuT Collaboration], Phys. Rev. Lett. **113**, 261801 (2014), [Erratum: Phys.Rev.Lett. 114, 039901 (2015)].

[81] R. Acciarri et al. [ArgoNeuT Collaboration], Phys. Rev. D **96**, 012006 (2017).

[82] R. Acciarri et al. [ArgoNeuT Collaboration], Phys. Rev. D **98**, 052002 (2018).

[83] R. Acciarri et al. [ArgoNeuT Collaboration], Phys. Rev. D **102**, 011101 (2020).

[84] R. Acciarri et al. [ArgoNeuT Collaboration], Phys. Rev. D **99**, 012002 (2019).

[85] R. Acciarri et al. [ArgoNeuT Collaboration], Phys. Rev. Lett. **124**, 131801 (2020).

[86] P. A. Machado, O. Palamara, and D. W. Schmitz, Annual Review of Nuclear and Particle Science **69**, 363 (2019).

[87] A.A. Aguilar-Arevalo et al. [MiniBooNE Collaboration], Nucl. Instrum. Methods Phys. Res., Sect. A **599**, 28 (2009).

[88] A. A. Aguilar-Arevalo et al. [MiniBooNE DM Collaboration], Phys. Rev. D **98**, 112004 (2018).

[89] P. Adamson et al., Phys. Rev. Lett. **107**, 181802 (2011).

[90] C. Anderson et al. [ArgoNeuT Collaboration], J. Instrum. **7**, P10019 (2012).

[91] C. Andreopoulos et al., Nucl. Instrum. Methods Phys. Res., Sect. A **614**, 87 (2010).

[92] S. Agostinelli et al., Nucl. Instrum. Methods Phys. Res., Sect. A **506**, 250 (2003).

[93] `https://larsoft.org/`. This analysis uses LArSoft v08_12_00.

[94] D. Michael, P. Adamson, T. Alexopoulos, W. Allison, G. Alner, K. Anderson, C. Andreopoulos, M. Andrews, R. Andrews, C. Arroyo, et al., Nuclear Instruments and Methods in Physics Research Section A: Accelerators, Spectrometers, Detectors and Associated Equipment **596**, 190 (2008).

[95] R. Acciarri et al. [ArgoNeuT Collaboration], Phys. Rev. D **95**, 072005 (2017).

[96] R. Acciarri et al. (2015), arXiv:1503.01520.

[97] R. Acciarri et al. (2015), arXiv:1512.06148.

[98] The MicroBooNE Collaboration (2018), MICROBOONE-NOTE-1054-PUB.

[99] P. Abratenko et al. (MicroBooNE Collaboration) (2021).

[100] B. Baller, JINST **12**, P07010 (2017).

[101] M. Antonello et al., Adv. High Energy Phys. p. 260820 (2013).

[102] O. P. G. Scanavini and T. Yang (2017), T962 DocDB 4424-v4.

[103] E. Niner (2015), FERMILAB-THESIS-2015-16.

[104] R. Acciarri et al. [MicroBooNE Collaboration], J. Instrum. **12**, P02017 (2017).

[105] C. Adams, M. Alrashed, R. An, J. Anthony, J. Asaadi, A. Ashkenazi, M. Auger, S. Balasubramanian, B. Baller, C. Barnes, et al., Journal of Instrumentation **14**, P04004 (2019).

[106] M. Collaboration (2018), MICROBOONE-NOTE-1043-PUB.

[107] C. Adams, M. Alrashed, R. An, J. Anthony, J. Asaadi, A. Ashkenazi, M. Auger, S. Balasubramanian, B. Baller, C. Barnes, et al. (The MicroBooNE Collaboration 1), Phys. Rev. D **99**, 091102 (2019).

[108] P. Abratenko, C. Adams, M. Alrashed, R. An, J. Anthony, J. Asaadi, A. Ashkenazi, M. Auger, S. Balasubramanian, B. Baller, et al. (MicroBooNE Collaboration), Phys. Rev. Lett. **123**, 131801 (2019).

[109] P. Abratenko, M. Alrashed, R. An, J. Anthony, J. Asaadi, A. Ashkenazi, S. Balasubramanian, B. Baller, C. Barnes, G. Barr, et al. (MicroBooNE Collaboration), Phys. Rev. Lett. **125**, 201803 (2020).

[110] P. Abratenko, M. Alrashed, R. An, J. Anthony, J. Asaadi, A. Ashkenazi, S. Balasubramanian, B. Baller, C. Barnes, G. Barr, et al. (MicroBooNE Collaboration), Phys. Rev. D **102**, 112013 (2020).

[111] C. Adams, R. An, J. Anthony, J. Asaadi, M. Auger, S. Balasubramanian, B. Baller, C. Barnes, G. Barr, M. Bass, et al., The European Physical Journal C **79**, 248 (2019).

[112] P. Abratenko, M. Alrashed, R. An, J. Anthony, J. Asaadi, A. Ashkenazi, S. Balasubramanian, B. Baller, C. Barnes, G. Barr, et al. (The MicroBooNE Collaboration), Phys. Rev. D **101**, 052001 (2020).

[113] J. S. Marshall and M. A. Thomson, Eur. Phys. J. C **75**, 439 (2015).

[114] R. Acciarri, C. Adams, R. An, J. Asaadi, M. Auger, L. Bagby, B. Baller, G. Barr, M. Bass, F. Bay, et al., Journal of Instrumentation **12**, P03011 (2017).

[115] M. collaboration, P. Abratenko, M. Alrashed, R. An, J. Anthony, J. Asaadi, A. Ashkenazi, S. Balasubramanian, B. Baller, C. Barnes, et al. (2021), `arXiv:2010.08653`.

[116] M. collaboration, P. Abratenko, M. Alrashed, R. An, J. Anthony, J. Asaadi, A. Ashkenazi, S. Balasubramanian, B. Baller, C. Barnes, et al. (2020), `arXiv:2012.08513`.

[117] P. Abratenko et al. (MicroBooNE Collaboration) (2020), `arXiv:2011.01375`.

[118] P. Abratenko et al. (MicroBooNE Collaboration) (2020), `arXiv:2012.07928`.

[119] P. Abratenko et al. (MicroBooNE Collaboration) (2021), `arXiv:2101.05076`.

[120] R. Acciarri, C. Adams, R. An, J. Anthony, J. Asaadi, M. Auger, L. Bagby, S. Balasubramanian, B. Baller, C. Barnes, et al., Journal of Instrumentation **12**, P08003 (2017).

[121] C. Adams, R. An, J. Anthony, J. Asaadi, M. Auger, L. Bagby, S. Balasubramanian, B. Baller, C. Barnes, G. Barr, et al., Journal of Instrumentation **13**, P07006 (2018).

[122] C. Adams, R. An, J. Anthony, J. Asaadi, M. Auger, S. Balasubramanian, B. Baller, C. Barnes, G. Barr, M. Bass, et al., Journal of Instrumentation **13**, P07007 (2018).

[123] M. Collaboration (2021), MICROBOONE-NOTE-1095-PUB.

[124] S. Amerio et al. (ICARUS Collaboration), Nucl. Instrum. Meth. A **527**, 329 (2004).

[125] R. Acciarri et al. (SBND Collaboration), JINST **15**, P06033 (2020).

[126] R. Acciarri et al. (SBND Collaboration) (2020).

[127] B. Abi et al. (DUNE Collaboration), JINST **15**, T08008 (2020).

[128] B. Abi et al. (DUNE Collaboration), JINST **15**, P12004 (2020).

[129] Aguilar-Arevalo, A.A. et al. [MiniBooNE Collaboration], Phys. Rev. Lett. **120**, 141802 (2018).

[130] M. Martini, M. Ericson, G. Chanfray, and J. Marteau, Phys. Rev. C **80**, 065501 (2009).

[131] J. Spitz, Phys. Rev. D **89**, 073007 (2014).

[132] S. Axani, G. Collin, J. Conrad, M. Shaevitz, J. Spitz, and T. Wongjirad, Phys. Rev. D **92**, 092010 (2015).

[133] J. Spitz, Phys. Rev. D **85**, 093020 (2012).

[134] C. Rott, S. In, J. Kumar, and D. Yaylali, J. of Cosmol. and Astropart. Phys. **11**, 039 (2015).

[135] K. Abe et al. [T2K Collaboration], Nucl. Instrum. Methods Phys. Res., Sect. A **659**, 106 (2011).

[136] K. Abe et al. [T2K Collaboration], Phys. Rev. Lett. **112**, 061802 (2014).

[137] P. Huber, M. Mezzetto, and T. Schwetz, JHEP **0803**, 021 (2008).

[138] L. Aliaga et al. [MINVERvA Collaboration], Nucl. Instrum. Methods Phys. Res., Sect. A **743**, 130 (2014).

[139] B. T. Flemming et al. [MicroBooNE Collaboration] (2012), FERMILAB-DESIGN-2012-04.

[140] C. Adams et al. (2013), FERMILAB-PROPOSAL-1053.

[141] S. Badro et al. (2014), arXiv:1412.3086.

[142] Private communication with N. Jachowicz.

[143] C. Volpe et al., Phys. Rev. C **62**, 015501 (2000).

[144] M. Martini, M. Ericson, and G. Chanfray, Phys. Rev. C **84**, 055502 (2011).

[145] M. Martini, M. Ericson, and G. Chanfray, Phys. Rev. D **87**, 013009 (2013).

[146] Z. Pavlovic (2008), Ph.D. thesis, University of Texas at Austen.

[147] A.A. Aguilar-Arevalo et al. [MiniBooNE Collaboration], Phys. Rev. Lett. **100**, 032301 (2008).

[148] A.A. Aguilar-Arevalo et al. [MiniBooNE Collaboration], Phys. Rev. Lett. **103**, 061802 (2009).

[149] A.A. Aguilar-Arevalo et al. [MiniBooNE Collaboration], Phys. Rev. Lett. **103**, 081801 (2009).

[150] A.A. Aguilar-Arevalo et al. [MiniBooNE Collaboration], Phys. Rev. D **81**, 092005 (2010).

[151] A.A. Aguilar-Arevalo et al. [MiniBooNE Collaboration], Phys. Rev. D **83**, 052007 (2011).

[152] A.A. Aguilar-Arevalo et al. [MiniBooNE Collaboration], Phys. Rev. D **83**, 052009 (2011).

[153] A.A. Aguilar-Arevalo et al. [MiniBooNE Collaboration], Phys. Rev. D **88**, 032001 (2013).

[154] A.A. Aguilar-Arevalo et al. [MiniBooNE Collaboration], Phys. Rev. Lett. **100**, 032301 (2008).

[155] V. Pandey, N. Jachowicz, T. V. Cuyck, J. Ryckebusch, and M. Martini, Phys. Rev. C **92**, 024606 (2015).

[156] S. Ajimura et al. (2017), arXiv:1705.08629.